SPR 396-2 OCTOBER 2015

Performance Evaluation of Arizona's LTPP SPS-2 Project:

Strategic Study of Structural Factors for Rigid Pavements

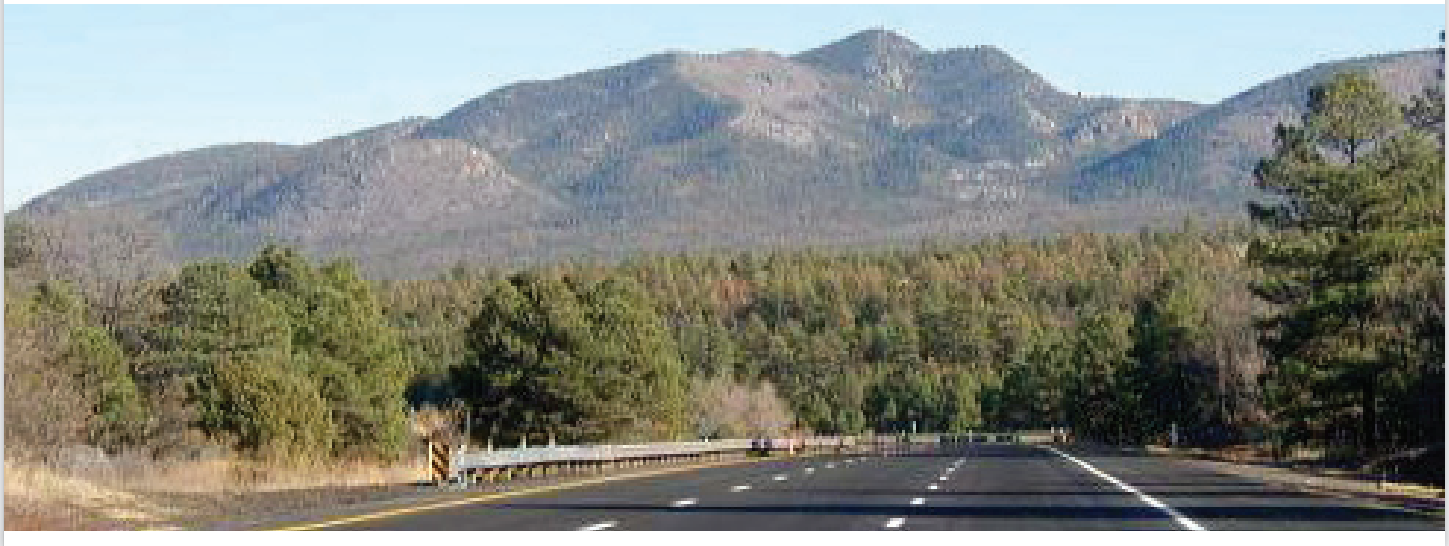

Arizona Department of Transportation Research Center

ADOT

Performance Evaluation of Arizona's LTPP SPS-2 Project: Strategic Study of Structural Factors for Rigid Pavements

SPR-396-2

October 2015

Prepared by:
Peter Schmalzer, Steven Karamihas,
Hans Meyer, Kevin Senn, and Jason Puccinelli
Nichols Consulting Engineers
1885 S. Arlington Ave., Suite 111
Reno, NV 89509

Prepared for:
Arizona Department of Transportation
206 S. 17th Ave.
Phoenix, AZ 85007
In cooperation with
U.S. Department of Transportation
Federal Highway Administration

This report was funded in part through grants from the Federal Highway Administration, U.S. Department of Transportation. The contents of this report reflect the views of the authors, who are responsible for the facts and the accuracy of the data, and for the use or adaptation of previously published material, presented herein. The contents do not necessarily reflect the official views or policies of the Arizona Department of Transportation or the Federal Highway Administration, U.S. Department of Transportation. This report does not constitute a standard, specification, or regulation. Trade or manufacturers' names that may appear herein are cited only because they are considered essential to the objectives of the report. The U.S. government and the State of Arizona do not endorse products or manufacturers.

Technical Report Documentation Page

1. Report No. FHWA-AZ-15-396(2)	2. Government Accession No	3. Recipient's Catalog No.
4. Title and Subtitle Performance Evaluation of Arizona's LTPP SPS-2 Project: Strategic Study of Structural Factors for Rigid Pavements		5. Report Date October 2015
		6. Performing Organization Code
7. Author(s) Peter Schmalzer, Steven Karamihas, Hans Meyer, Kevin Senn, and Jason Puccinelli		8. Performing Organization Report No.
9. Performing Organization Name and Address Nichols Consulting Engineers 1885 S. Arlington Avenue Suite 111 Reno, Nevada 89509-3370		10. Work Unit No. (TRAIS)
		11. Contract or Grant No. SPR 000-1(177) 396/R0396 20P
12. Sponsoring Agency Name and Address Arizona Department of Transportation 206 S. 17th Avenue Phoenix, Arizona 85007		13. Type of Report and Period Covered FINAL
		14. Sponsoring Agency Code
15. Supplementary Notes Prepared in cooperation with the Federal Highway Administration.		

16. Abstract

As part of the Long Term Pavement Performance (LTPP) Program, Arizona Department of Transportation (ADOT) constructed 21 Specific Pavement Studies 2 (SPS-2) test sections on Interstate 10 near Buckeye, Arizona, to study a variety of structural sections in new portland cement concrete construction. Opened to traffic in 1994, this project is actively being monitored at regular intervals. Surface distress, profile, and deflection data collected throughout the life of the pavement were used to evaluate the performance of various rigid pavement design features, layer configurations, and thickness. This report documents the analyses conducted as well as practical findings and lessons learned that will be of interest to ADOT.

17. Key Words LTPP, pavement performance, profile, distress, FWD, rigid, PCC, deflections, roughness, basin-data, LTE		18. Distribution Statement This document is available to the US public through the National Technical Information Service, Springfield, Virginia 22161.		23. Registrant's Seal
19. Security Classification Unclassified	20. Security Classification Unclassified	21. No. of Pages 214	22. Price	

SI* (MODERN METRIC) CONVERSION FACTORS

APPROXIMATE CONVERSIONS TO SI UNITS

Symbol	When You Know	Multiply By	To Find	Symbol
		LENGTH		
in	inches	25.4	millimeters	mm
ft	feet	0.305	meters	m
yd	yards	0.914	meters	m
mi	miles	1.61	kilometers	km
		AREA		
in^2	square inches	645.2	square millimeters	mm^2
ft^2	square feet	0.093	square meters	m^2
yd^2	square yard	0.836	square meters	m^2
ac	acres	0.405	hectares	ha
mi^2	square miles	2.59	square kilometers	km^2
		VOLUME		
fl oz	fluid ounces	29.57	milliliters	mL
gal	gallons	3.785	liters	L
ft^3	cubic feet	0.028	cubic meters	m^3
yd^3	cubic yards	0.765	cubic meters	m^3
		NOTE: volumes greater than 1000 L shall be shown in m^3		
		MASS		
oz	ounces	28.35	grams	g
lb	pounds	0.454	kilograms	kg
T	short tons (2000 lb)	0.907	megagrams (or "metric ton")	Mg (or "t")
		TEMPERATURE (exact degrees)		
°F	Fahrenheit	5 (F-32)/9 or (F-32)/1.8	Celsius	°C
		ILLUMINATION		
fc	foot-candles	10.76	lux	lx
fl	foot-Lamberts	3.426	$candela/m^2$	cd/m^2
		FORCE and PRESSURE or STRESS		
lbf	poundforce	4.45	newtons	N
lbf/in^2	poundforce per square inch	6.89	kilopascals	kPa

APPROXIMATE CONVERSIONS FROM SI UNITS

Symbol	When You Know	Multiply By	To Find	Symbol
		LENGTH		
mm	millimeters	0.039	inches	in
m	meters	3.28	feet	ft
m	meters	1.09	yards	yd
km	kilometers	0.621	miles	mi
		AREA		
mm^2	square millimeters	0.0016	square inches	in^2
m^2	square meters	10.764	square feet	ft^2
m^2	square meters	1.195	square yards	yd^2
ha	hectares	2.47	acres	ac
km^2	square kilometers	0.386	square miles	mi^2
		VOLUME		
mL	milliliters	0.034	fluid ounces	fl oz
L	liters	0.264	gallons	gal
m^3	cubic meters	35.314	cubic feet	ft^3
m^3	cubic meters	1.307	cubic yards	yd^3
		MASS		
g	grams	0.035	ounces	oz
kg	kilograms	2.202	pounds	lb
Mg (or "t")	megagrams (or "metric ton")	1.103	short tons (2000 lb)	T
		TEMPERATURE (exact degrees)		
°C	Celsius	1.8C+32	Fahrenheit	°F
		ILLUMINATION		
lx	lux	0.0929	foot-candles	fc
cd/m^2	$candela/m^2$	0.2919	foot-Lamberts	fl
		FORCE and PRESSURE or STRESS		
N	newtons	0.225	poundforce	lbf
kPa	kilopascals	0.145	poundforce per square inch	lbf/in^2

*SI is the symbol for the International System of Units. Appropriate rounding should be made to comply with Section 4 of ASTM E380.
(Revised March 2003)

Contents

List of Figures

List of Tables

List of Abbreviations, Acronyms, and Symbols

AASHTO	American Association of State Highway and Transportation Officials
AC	asphalt concrete
ADOT	Arizona Department of Transportation
ASR	alkali-silica reaction
BTB	bituminous-treated base
DGAB	dense-graded aggregate base
ESAL	equivalent single axle load
FHWA	Federal Highway Administration
ft	foot
FWD	falling weight deflectometer
HRI	Half-car Roughness Index
I	Interstate
in/mi	inches per mile
IRI	International Roughness Index
JA	joint approach
JL	joint leave
LCB	lean concrete base
LTE	load transfer efficiency
LTPP	Long Term Pavement Performance
MRI	mean roughness index
PATB	permeable asphalt-treated base
PCC	portland cement concrete
PCCP	portland cement concrete pavement
PSD	power spectral density
PSG	pseudo strain gradient
psi	pounds per square inch
RMSE	root-mean square error
RN	Ride Number
SEE	standard estimate of error
SHRP	Strategic Highway Research Program
SMP	Seasonal Monitoring Program
SPS	Specific Pavement Studies
TDR	time, domain, reflectometry

Acknowledgments

The project team would like to acknowledge the Arizona Department of Transportation (ADOT) for sponsoring this project. In addition, the authors thank the ADOT Research Center and the Technical Advisory Committee for their input as well as the leadership of project manager Christ Dimitroplos. The comprehensive information stored in the Long Term Pavement Performance database allowed this research to be conducted.

EXECUTIVE SUMMARY

As part of the Long Term Pavement Performance (LTPP) Program, the Arizona Department of Transportation (ADOT) constructed 21 Specific Pavement Studies 2 (SPS-2) test sections on Interstate 10 (I-10) near Buckeye, Arizona. Construction of all 21 sections was completed in January 1994.

The SPS-2 project studied a variety of structural sections in new portland cement concrete (PCC) construction. The SPS-2 project discussed in this report consists of 21 test sections: 12 core sections and nine supplemental sections. The 12 core sections represented the standard experimental matrix for the Strategic Highway Research Program (SHRP) requirements. ADOT added the nine supplemental test sections to evaluate features that were not included in the SHRP experiment design; these nine supplemental test sections consisted of four additional sections of random skew jointed portland cement concrete pavement (PCCP), three State 406 bituminous-treated base (BTB) sections, and two asphalt concrete (AC) sections

This report provides general information about the project location, including climate, traffic, and subgrade conditions, as well as details about the layer configurations of each test section. All 21 SPS-2 test sections were constructed consecutively and exposed to the same traffic loading, climate, and subgrade conditions, which allowed for direct comparisons between layer configurations and design features without the confounding effects introduced by different in situ conditions. This report also provides the interim findings of the SPS-2 project after 20 years of monitoring. The performance lives for many of the sections are expected to be significantly longer.

Deflection analyses concluded that most structural factors such as wider slabs and thicker sections performed as expected, with small to quantifiable benefits observed. By comparing changes in stiffness, load transfer efficiency, and structural distresses, both the deflection and distress analyses concluded that the test sections with lean concrete base performed worse than test sections with permeable asphalt-treated base, dense-graded aggregate base, and BTB. The results of these analyses also found a similar performance in both AC sections, indicating that the conditions present throughout the site are consistent.

Profile analysis results showed that roughness and roughness progression alone cannot be used to represent the health of a test section. Several test sections did not exhibit changes in roughness in proportion to the amount of longitudinal and transverse cracking present. The researchers also noted inconsistent progression in the International Roughness Index in the analysis, and they determined that warp and curl attributed to most of the irregularities. Objective profile analyses were applied to quantify the level of curl and warp on each section. These automated algorithms estimated the gross strain gradient needed to deform each slab into the shape present in the measured profile and produced a pseudo strain gradient (PSG) value. For the jointed concrete test sections, variations in average PSG over time explained many of the changes in roughness over time.

Certain sections received maintenance work. In PCC sections, work consisted of partial depth patching; in AC sections, pothole patching occurred. These maintenance events potentially mask the extent and severity of actual pavement distresses in the short term. However, in this study, the impact and overall quantity of the maintenance work on distresses were not significant and were considered negligible.

CHAPTER 1. INTRODUCTION

Understanding how design features contribute to long-term pavement performance can be extremely valuable to pavement managers looking to optimize resources and improve overall performance. This study's objectives were to document the overall performance trends of the Specific Pavement Studies 2 (SPS-2) project, identify key differences in performance between the various pavement configurations, and document key findings that would be useful to the Arizona Department of Transportation (ADOT).

This report provides the results of surface distress, deflection, and profile analyses for the Long Term Pavement Performance (LTPP) SPS-2 site near Buckeye, Arizona (the SPS-2 project). The SPS-2 sites were designed to study rigid pavement structural factors, including concrete slab thickness, concrete strength, base material, permeability, and lane width (Szrot 1994). The SPS-2 project (040200) discussed in this report consists of 21 test sections: 12 core sections and nine supplemental sections. The 12 core sections represented the standard experimental matrix for the Strategic Highway Research Program (SHRP) requirements. ADOT added the nine supplemental test sections to evaluate features that were not included in the SHRP experiment design; these nine supplemental test sections consisted of four additional sections of random skew jointed portland cement concrete pavement (PCCP), three State 406 bituminous-treated base (BTB) sections, and two asphalt concrete (AC) sections.

The SPS-2 project was constructed on eastbound Interstate 10 (I-10) in Maricopa County, Arizona (Figure 1), and was incorporated in the ADOT rehabilitation project IM-10-2(46), which spanned 22.39 miles of pavement on I-10 approximately 35 miles west of Phoenix. Average elevation of the project is 1100 ft, with a latitude of 33° 27' 11" and longitude of -112° 44' 23".

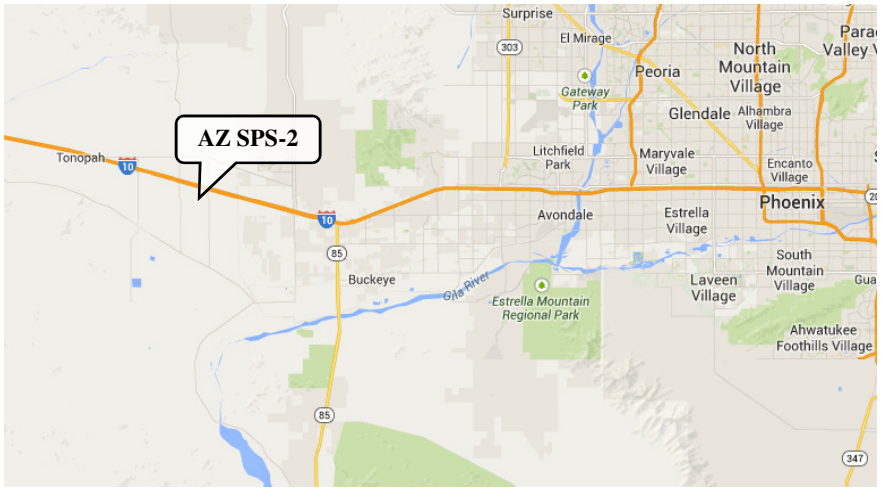

Figure 1. Location of SPS-2 Test Sections
(Courtesy of Google Maps)

Table 1 summarizes the structural design of the test sections. Sections 040213 through 040224, the core sections, made up a standard half factorial matrix of structural factors; the California SPS-2 contained the other half of the factorial matrix for core sections. Sections 040262 through 040265 consisted of random skew jointed PCCP, using a half factorial again, investigating slab width, base type, and slab thickness. Sections 040266 through 040268 consist of different slab thicknesses placed on the State 406 BTB mix. Finally, Sections 040260 and 040261 consisted of two nominally identical AC sections built at either end of the project.

The SPS-2 project was constructed in a 3-mi segment of this 22.39-mi rehabilitation project and extended from Milepost 106 to Milepost 109. The soil was covered with various desert-type brush and small trees. Each test section is 500 ft long, which does not include transitional segments between sections and destructive sampling areas outside the monitoring limits. The alignment consisted of four lanes following a fairly straight and level terrain. Figure 2 shows the layout of the SPS-2 project.

Table 1. Arizona SPS-2 Site Structural Features

Section	Slab Strength (psi)	Slab Width (ft)	Layer Thickness (inches)			Layer Type		
			Layer 1	Layer 2	Layer 3	Layer 1	Layer 2	Layer 3
040213	550	14	8	6	—	PCC	DGAB	—
040214	900	12	8	6	—	PCC	DGAB	—
040215	550	12	11	6	—	PCC	DGAB	—
040216	900	14	11	6	—	PCC	DGAB	—
040217	550	14	8	6	—	PCC	LCB	—
040218	900	12	8	6	—	PCC	LCB	—
040219	550	12	11	6	—	PCC	LCB	—
040220	900	14	11	6	—	PCC	LCB	—
040221	550	14	8	4	4	PCC	PATB	DGAB
040222	900	12	8	4	4	PCC	PATB	DGAB
040223	550	12	11	4	4	PCC	PATB	DGAB
040224	900	14	11	4	4	PCC	PATB	DGAB
040260	N/A	N/A	8.5	4	—	AC	DGAB	—
040261	N/A	N/A	8.5	4	—	AC	DGAB	—
040262	550	14	8	6	—	PCC	DGAB	—
040263	550	14	8	4	4	PCC	PATB	DGAB
040264	550	12	11	4	4	PCC	PATB	DGAB
040265	550	12	11	6	—	PCC	DGAB	—
040266	550	14	12.5	4	—	PCC	BTB	—
040267	550	14	11	4	—	PCC	BTB	—
040268	550	14	8	4	—	PCC	BTB	—

DGAB: dense-graded aggregate base.
LCB: lean concrete base.
N/A: Not available.
PATB: permeable asphalt-treated base.

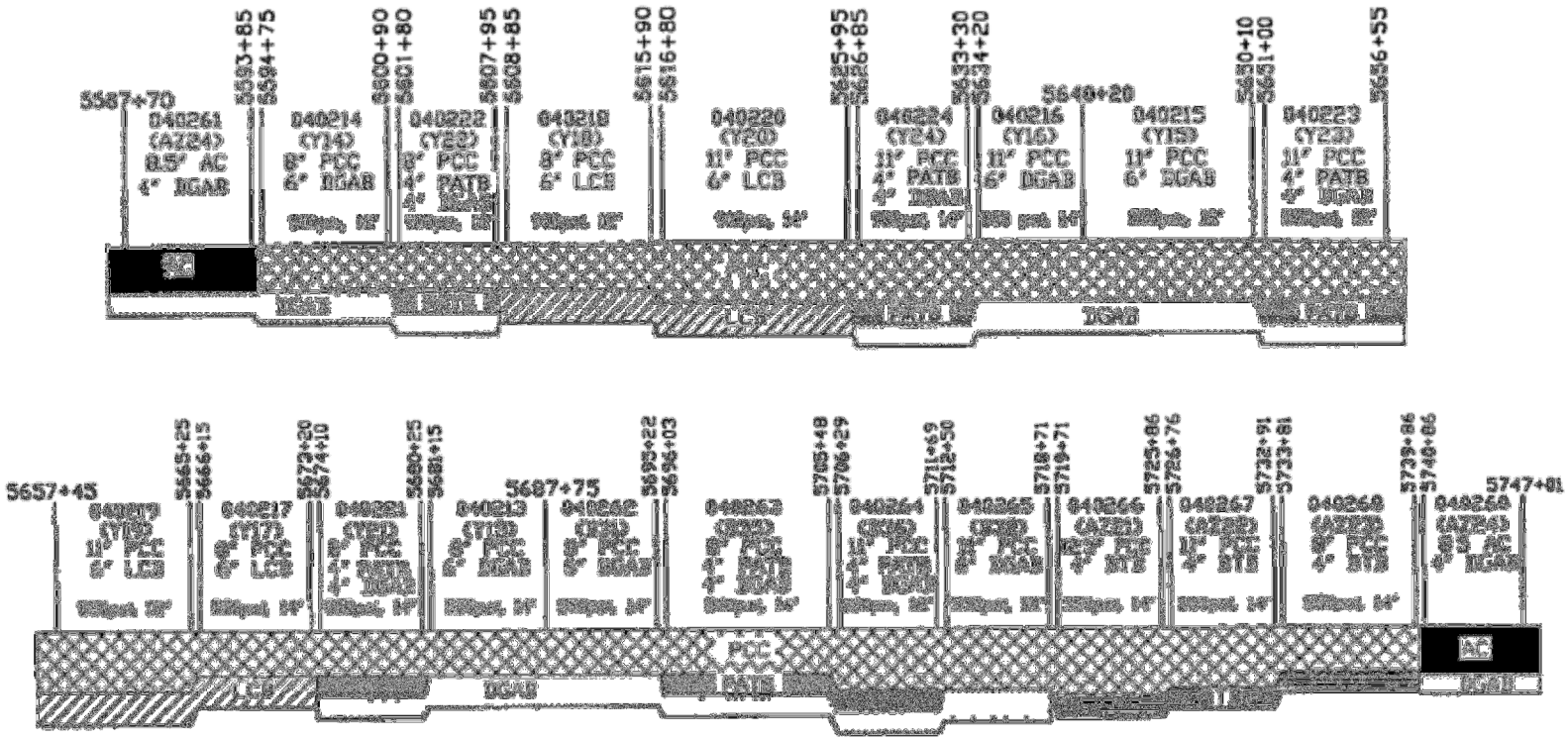

Figure 2. Layout of the SPS-2 Project

The subgrade is a coarse-grained silty sand with gravel and some sections of clayey sand with gravel. The subgrade was prepared by excavating a 3000-ft section of roadway alignment 1 ft below grade and hauling the material away to waste; the adjacent 3000-ft section material was then placed into the previous 3000-ft excavated section, and then water and compactive effort was applied. This process was continued along the alignment.

The SPS-2 project site climate is considered to be a dry, no-freeze environment by LTPP definitions.

Table 2 summarizes the climatic data in the area, summarized from 12 years of data collected by an on-site automated weather station.

Table 2. Climatic Information for SPS-2

	Average	Maximum	Minimum
Annual average daily mean temperature (°F)	73	74	71
Annual average daily maximum temperature (°F)	87	88	84
Annual average daily minimum temperature (°F)	58	60	57
Absolute maximum annual temperature (°F)	98	99	96
Absolute minimum annual temperature (°F)	47	48	47
Number of days per year above 90° F	168	182	148
Number of days per year below 32° F	7	15	1
Annual average freezing index (°F-days)	0	0	0
Annual average precipitation (inches)	6.6	10.6	2.1
Annual average daily mean solar radiation (W/ft^2)	22.7	24.5	22.1
Annual average daily max relative humidity (%)	53	65	43
Annual average daily min relative humidity (%)	17	21	13

Table 3 summarizes the total equivalent single axle loads (ESALs) computed from traffic loading information collected at the SPS-2 project site. For 1993 and from 1997 to 2002, no monitoring traffic data was available; ADOT has provided estimated ESAL values for these years. From 2003 to 2006, neither monitored nor estimated ESAL values were available; ADOT traffic estimates have been provided to illustrate the expected traffic growth as modeled by the agency, but these values are not necessarily correlated to monitored traffic data.

Table 3. Traffic Loading Summary

Year	Monitored ESALs	Estimated ESALs
1993	N/A	900,000
1994	1,527,400	N/A
1995	779,800	N/A
1996	1,264,400	N/A
1997	N/A	1,400,000
1998	N/A	1,300,000
1999	N/A	1,255,000
2000	N/A	1,386,000
2001	N/A	1,530,000
2002	N/A	2,831,000
2003	N/A	N/A
2004	N/A	N/A
2005	N/A	N/A
2006	N/A	N/A
2007	2,634,500	N/A
2008	2,495,500	N/A
2009	1,824,500	N/A
2010	1,546,000	N/A
2011	1,835,500	N/A

N/A: Not available.

Section 040215 was included in the LTPP Seasonal Monitoring Program (SMP) and was subjected to an increased frequency of performance monitoring (typically monthly falling weight deflectometer (FWD), profile, and distress monitoring). The test section was also instrumented with subsurface moisture sensors in the base and subgrade layers; subsurface temperature sensors in the AC, base, and subgrade layers; an air temperature thermometer; and a precipitation gauge.

The objective of the SMP monitoring was to provide a source of data for studying daily and seasonal variation in layer properties and their effect on pavement response and long-term performance. The SMP monitoring was conducted once every month from September 1995 to August 1996 and from December 1997 to November 1998, and once every two months from December 2001 to October 2004.

After original construction in 1994, some of the test sections received maintenance at ADOT's discretion:

- Section 040213: In 2009, partial depth patching of PCCP at joints and other locations.
- Section 040217: In 2009, partial depth patching of PCCP at joints and other locations.

- Section 040218: In 2007, partial depth patching of PCCP at joints.
- Section 040221: In 2007, partial depth patching of PCCP at joints; in 2009, partial depth patching of PCCP at joints and other locations.
- Section 040260: In 2005, 2007, and 2009, pothole patching.
- Section 040261: In 2004, 2009, and 2011, pothole patching.
- Section 040262: In 2009, partial depth patching of PCCP other than at joints.
- Section 040267: In 2008, surface grinding.

The researchers analyzed the SPS-2 project with three primary measures to evaluate pavement performance: deflection, distress, and profile. The remaining chapters of this report address each analysis, including a description of the research approach along with performance comparisons between test sections, overall trends, a summary of the results, and key findings.

CHAPTER 2. SPS-2 DEFLECTION ANALYSIS

The project factors studied in the 12 core sections of the SPS-2 project include base type (dense-graded aggregate base (DGAB), lean concrete base (LCB), and permeable asphalt-treated base (PATB)); concrete flexural strength (550 psi and 900 psi); slab width (12 or 14 ft); and slab thickness (8 or 11 inches). All of the core sections were unreinforced and doweled, with a 15-ft joint spacing. The full factorial would require 24 sections, however only half of the cells were populated, as shown in Table 4. This half-factorial experimental design meant that only the influence of base type can be directly compared among sections at the project; investigations of slab thickness, flexural strength, and lane width include confounding factors.

Table 4. Core Experiment Factorial

Base Type	Slab Thickness	Flexural Strength	Lane Width	Section ID
DGAB	8 inches	550 psi	12 ft	
			14 ft	040213
		900 psi	12 ft	040214
			14 ft	
	11 inches	550 psi	12 ft	040215
			14 ft	
		900 psi	12 ft	
			14 ft	040216
LCB	8 inches	550 psi	12 ft	
			14 ft	040217
		900 psi	12 ft	040218
			14 ft	
	11 inches	550 psi	12 ft	040219
			14 ft	
		900 psi	12 ft	
			14 ft	040220
PATB	8 inches	550 psi	12 ft	
			14 ft	040221
		900 psi	12 ft	040222
			14 ft	
	11 inches	550 psi	12 ft	040223
			14 ft	
		900 psi	12 ft	
			14 ft	040224

The researchers conducted three additional experiments on the supplemental sections, although no formal experimental design documentation exists. The first experiment investigated factors affecting the

performance of random skew joints. The concrete mix used was the same as the nominal 550 psi flexural strength mix in the core experiment. The joints were skewed by 2 ft across the slab width and were undoweled. The joint spacing pattern was 14 ft, 13 ft, 15 ft, and 12 ft. The researchers investigated slab width (12 and 14 ft), base type (DGAB and PATB), and slab thickness (8 inches and 11 inches). Again, a half-factorial design was used, as shown in Table 5.

Table 5. Skew Joint Experiment Factorial

Base Type	Slab Thickness	Slab Width	Section ID	Corresponding Core Section
DGAB	8	12		
		14	040262	040213
	11	12	040265	040215
		14		
PATB	8	12		
		14	040263	040221
	11	12	040264	040223
		14		

The second experiment investigated the influence of slab thickness on the performance of concrete sections built on the State 406 BTB mix. The joint spacing was fixed at 15 ft, and dowels were used. The concrete mix is the same as the nominal 550 psi mix used in the core experiment. Table 6 shows the experiment factorial. Corresponding core experiment sections only exist for the 8-inch slab thickness since 14-ft-wide, 550-psi, and 11-inch-thick slabs weren't constructed for the core experiment.

Table 6. State 406 BTB Mix Experiment Factorial

Base Type	Slab Width	Slab Thickness	Section ID	Corresponding Core Sections
BTB	14 ft	12.5 inches	040266	
		11 inches	040267	
		8 inches	040268	040213 (DGAB) 040217 (LCB) 040221 (PATB)

The third experiment consisted of two nominally identical AC sections built at either end of the project. The structural sections consisted of 8.5 inches of AC on 4 inches of DGAB. Table 7 shows the experiment factorial.

Table 7. AC Experiment Factorial

Begin Station	End Station	Section ID
5587+70	5588+20	040261
5740+86	5741+36	040260

Section 040215 was also included in the SMP. In addition to the project on-site automated weather station, this section also has subsurface temperature measurements; moisture instruments; and an increased frequency of performance monitoring, including FWD testing.

SECTION ANALYSES

Section 040215 (SMP Section)

Section 040215 fills the DGAB, 11-inch slab thickness, 12-ft lane, and 550-psi flexural strength cell of the core experiment matrix. It is located roughly in the center of the project: 5625 ft from the start of the project and 8655 ft from the end of the project. The PCC was poured on September 13, 1993. Table 8 shows the as-built structural section. No maintenance has been performed on this section.

Table 8. Section 040215 Layer Structure

Layer Number	Layer Type	Thickness (inches)	Layer Description
3	PCC	11	550-psi flexural strength mix
2	DGAB	6.3	Brown crushed gravel, 1-inch top size, Non Plastic, 8% passing #200
1	Subgrade		Dark brown silty sand with gravel, AASHTO Soil Classification A-2-4, Plasticity Index = 3, 24% passing #200

Moisture

Table 9 shows the depths of 10 time, domain, and reflectometry (TDR) probes installed in Section 040215. Only the first probe is in the DGAB layer; the other probes are in the subgrade.

In 2007 Nichols Consulting Engineers and Texas A&M University analyzed the data using a process documented in *LTPP Computed Parameter: Moisture Content* (Zollinger et al. 2008). Figure 3 shows the results for the first two TDR probes (representing the DGAB layer and the upper subgrade, respectively); also shown is total daily precipitation data gathered from the on-site automated weather station.

Table 9. TDR Probe Depths

Probe Number	Depth (inches)
1	13.6
2	19.6
3	25.6
4	31.6
5	37.6
6	43.6
7	49.6
8	55.7
9	67.5
10	83.5

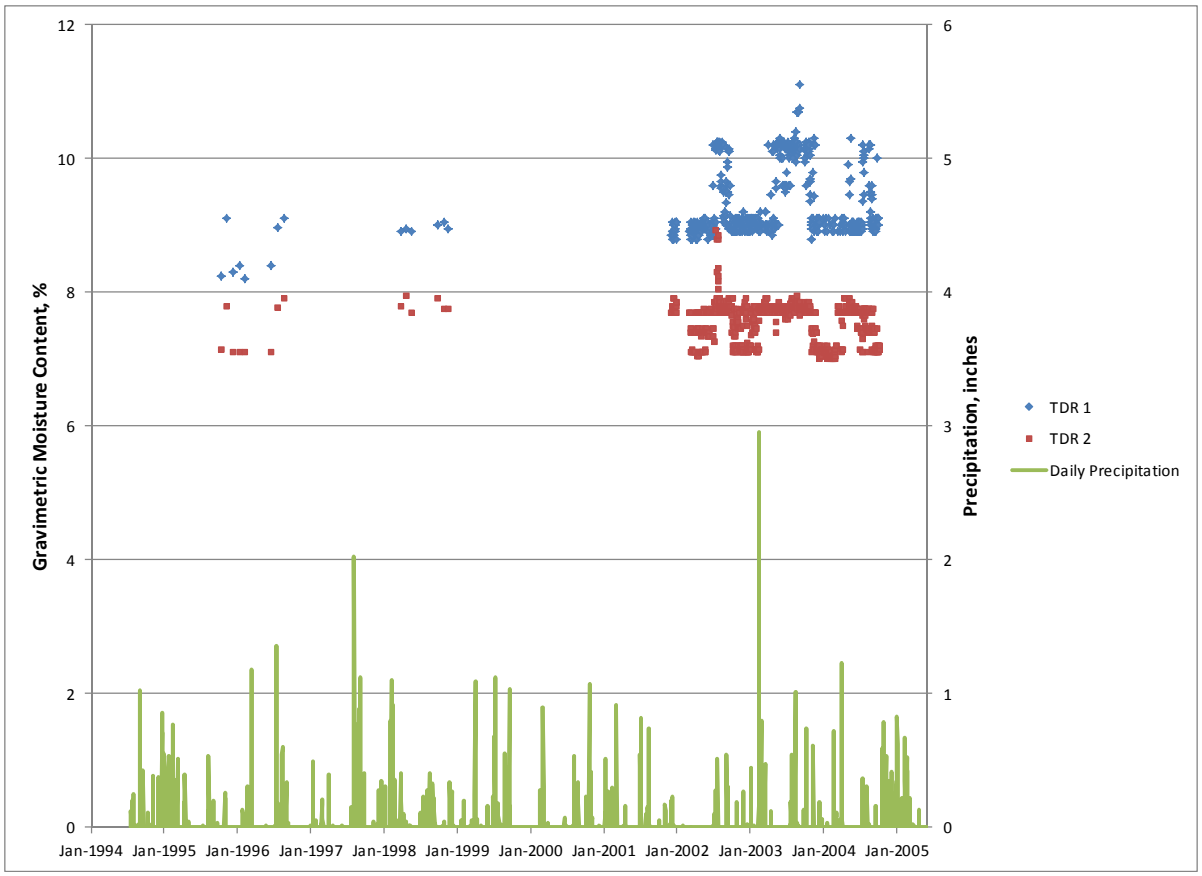

Figure 3. Subsurface Moisture and Precipitation

TDR data is spotty until the December 2001 through September 2004 monitoring period, when data shows a relatively constant moisture content of about 9 percent for the DGAB layer during the winter

months, with increases during the summer months. The magnitude of these increases does not appear to be well-correlated to precipitation measured on-site.

FWD Data

The researchers performed post-construction FWD testing on 50 occasions between February 1993 and February 2011. This data is concentrated in three periods: March 1995 to August 1996, November 1997 through January 1999 and December 2001 through December 2004.

Load Transfer Efficiency

The researchers computed load transfer efficiency (LTE) as a simple ratio of the deflection measured on the unloaded slab to the loaded slab. Figure 4 shows the results at drop height 4 for both the joint approach (JA) and joint leave (JL) tests as a function of date. LTE variability decreases over time, although there is no apparent trend in the average value. The peak LTE value occurs on August 14, 2003, which is the closest FWD test in time to the peak DGAB moisture content shown in Figure 3; but otherwise there is no apparent correlation between the data sets.

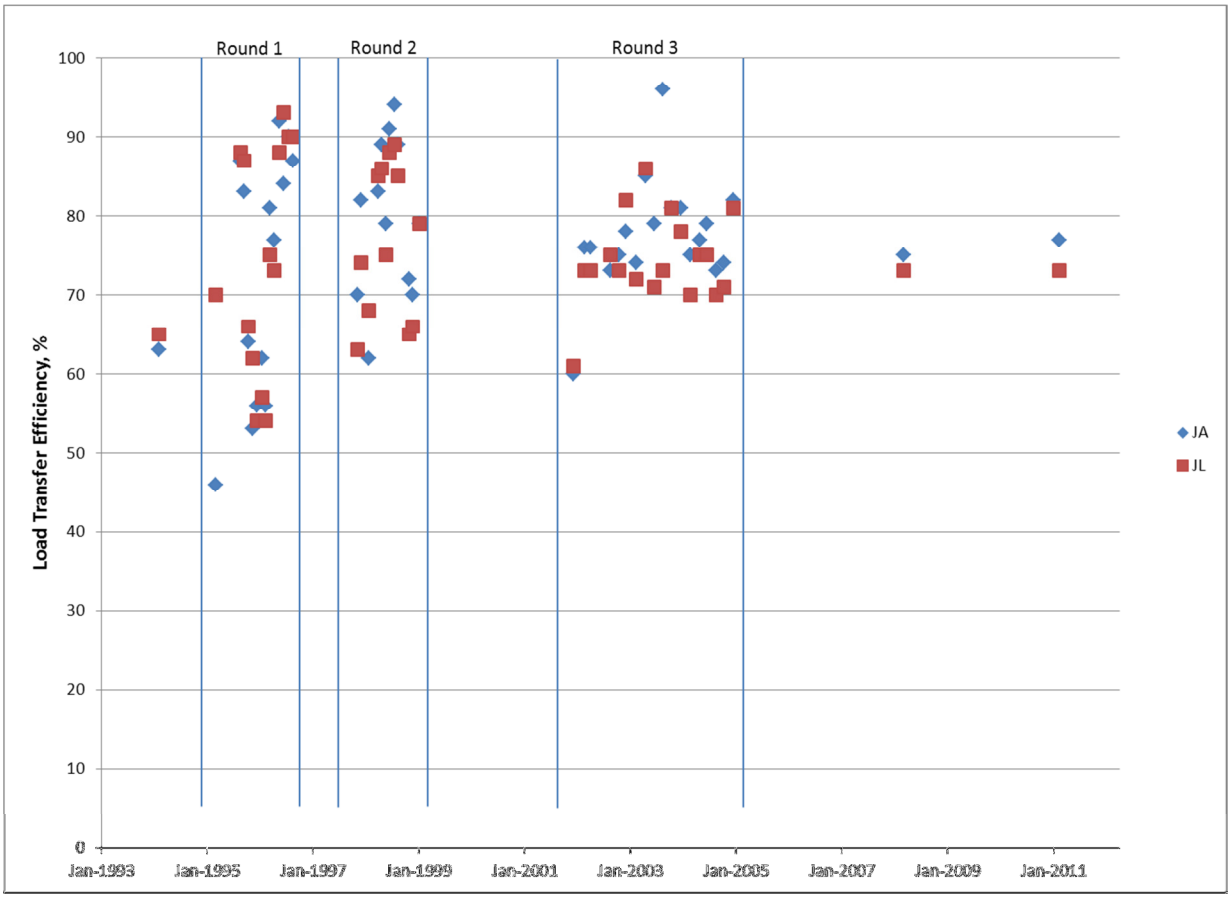

Figure 4. Load Transfer Efficiency vs. Date

Figure 5 shows LTE data versus day of year. In this plot, January 1 is day 1 and December 31 is day 365 (or 366 for leap years). There is a strong sine-like trend of LTE versus day of year for Round 1. This trend is weaker for the Round 2 data and is not apparent for the Round 3 data.

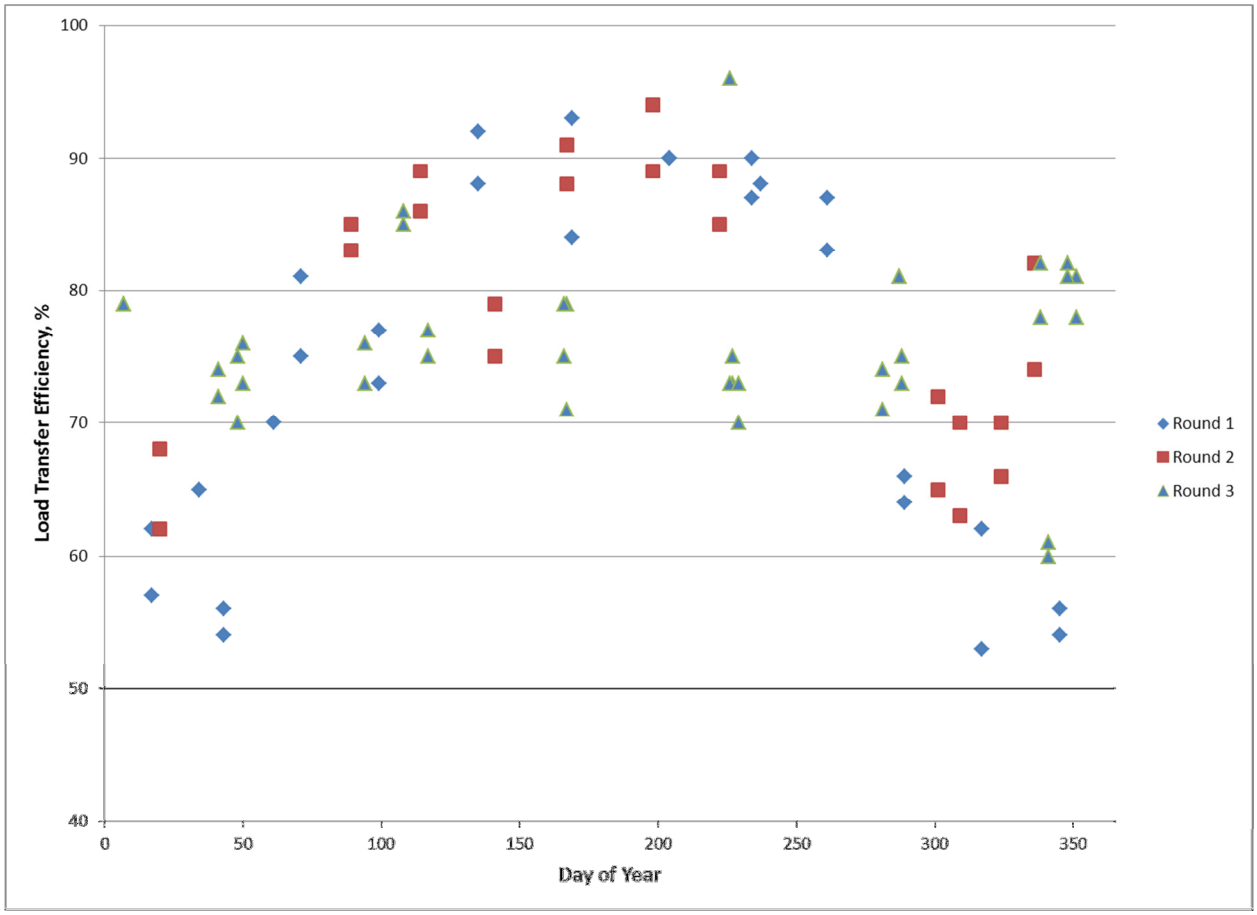

Figure 5. Load Transfer Efficiency vs. Day of Year

Figure 6 shows LTE data versus slab mid-depth temperature. The linear fit of the Round 1 data is relatively good, with an R Squared of 0.71. The goodness of fit is weaker for the Round 2 data and negligible for the Round 3 data. These results indicate that temperature variability is responsible for much of the variability in LTE observed early in this section's life, but that the effect of temperature on LTE decreases over time. Interestingly, in Round 3, LTE stabilizes within an intermediate range between the extremes seen in Round 1. If the decrease in the temperature effect is due to a decrease in friction or aggregate interlock across the joint, LTE should converge at a value near the lower extreme of the Round 1 values.

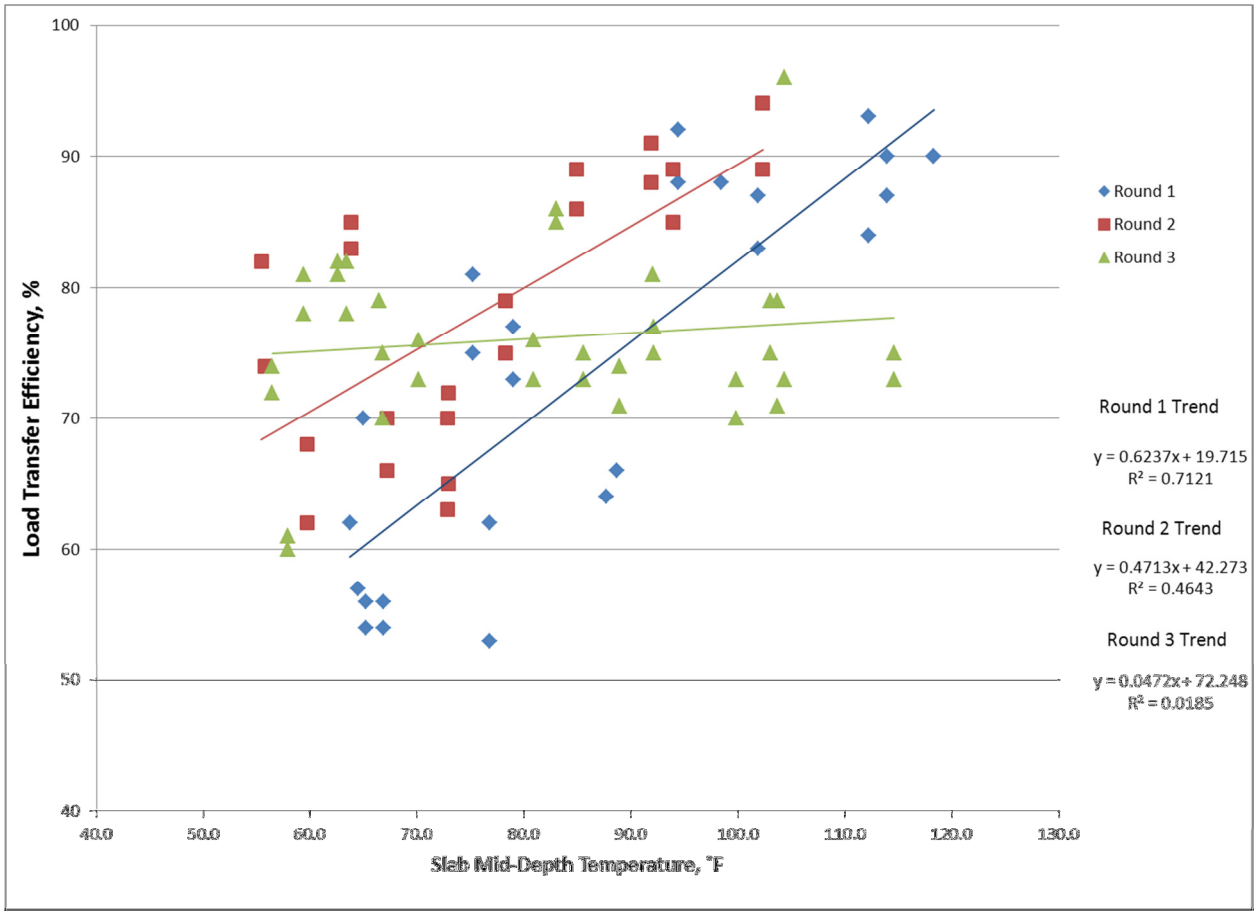

Figure 6. Load Transfer Efficiency vs. Temperature

Figure 7 shows LTE data versus slab temperature gradient. Temperature gradients were determined using a simple linear regression on the subsurface temperature data collected at the time of joint testing. In this plot, negative gradients correspond to decreasing temperature with increasing depth within the slab. There is a possible trend of LTE increasing with increasing negative temperature gradient in Round 1; however if this exists, it is probably an indirect effect of a correlation between temperature and temperature gradient at this site. There is no apparent trend between LTE and temperature gradient in the Round 2 and Round 3 data sets, indicating that the effect of temperature on LTE at this site is due to expansion of the slab, not curl.

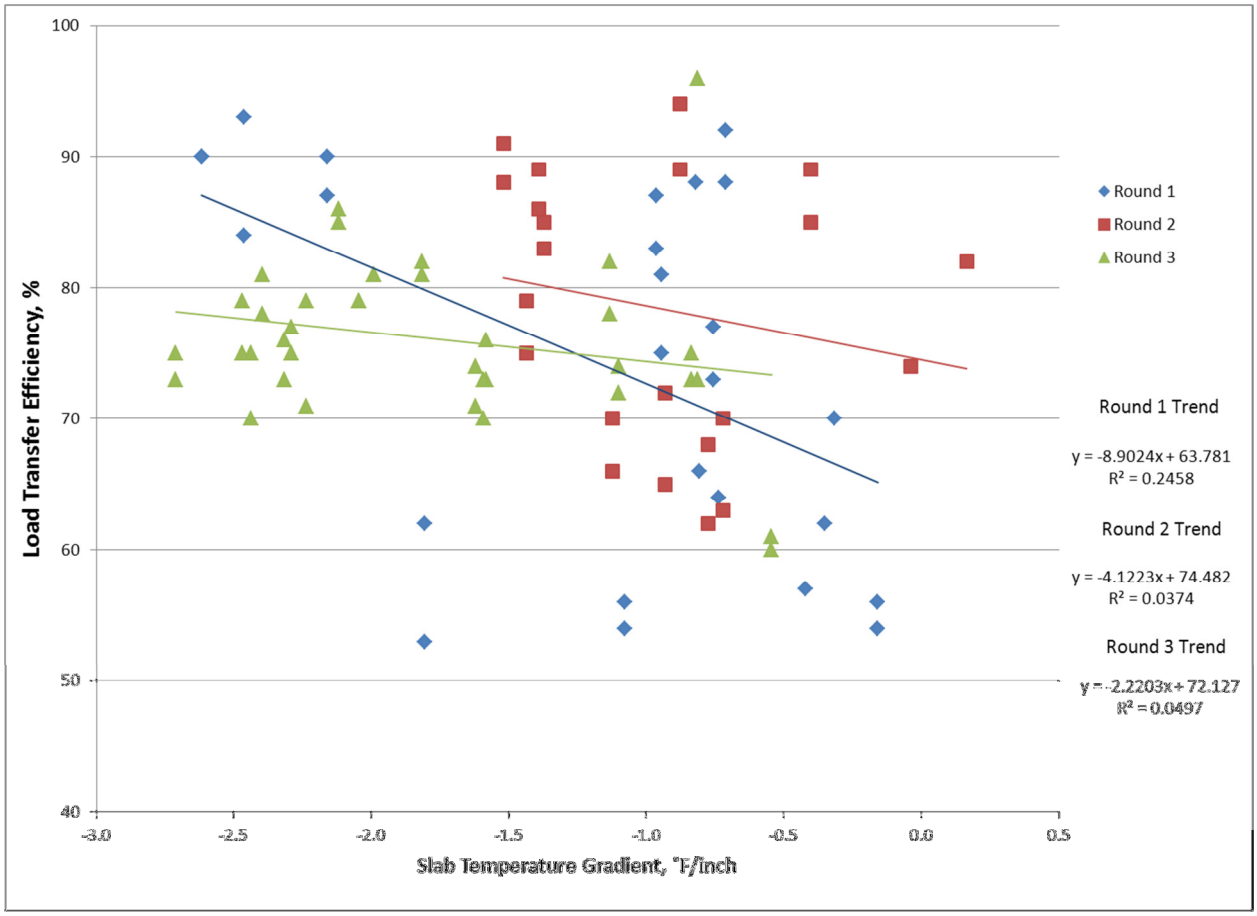

Figure 7. Load Transfer Efficiency vs. Temperature Gradient

Basin Analyses

The researchers analyzed the results of mid-slab basin tests using the empirical procedures described in the *AASHTO Guide for Design of Pavement Structures* (AASHTO 1993) and the *Supplement to the AASHTO Guide for Design of Pavement Structures* (AASHTO 1998) to determine the elastic modulus of the PCC layer (E_{pcc}) and the modulus of subgrade reaction (k).

The AASHTO 1993 guide uses the standard AREA function (sometimes known as $AREA_4$), shown in Equation 1.

— — — (Eq. 1)

Where: d_0 = deflection measured at the center of the load plate

d_{12} = deflection measured 12 inches from the center of load plate

d_{24} = deflection measured 24 inches from the center of load plate

d_{36} = deflection measured 36 inches from the center of load plate

$AREA_4$ is then used to compute the dense liquid radius of relative stiffness (l_k):

$$l_k = \left[\frac{\ln\frac{36-AREA_4}{1812.279133}}{-2.559340}\right]^{4.387009} \quad \text{(Eq. 2)}$$

l_k then can be used to determine k and E_{pcc}:

$$k = \left(\frac{P}{8d_0 l_k^2}\right)\left\{1 + \left(\frac{1}{2\pi}\right) \times \left[ln\left(\frac{a}{2l_k}\right) + \gamma - 1.25\right]\left(\frac{a}{l_k}\right)^2\right\} \quad \text{(Eq. 3)}$$

Where: d_0 = deflection measured at the center of the load plate (inches)

P = load (pounds)

γ = Euler's constant (0.57721566790)

a = load plate radius (inches)

$$l_k = \sqrt[4]{\frac{E_{pcc}D_{pcc}^3}{12(1-\mu_{pcc}^2)k}} \quad \text{(Eq. 4)}$$

Where: E_{pcc} = modulus of the PCC slab (psi)

D_{pcc} = thickness of the PCC slab (inches)

μ_{pcc} = Poisson's ratio of the PCC slab

The AASHTO 1998 supplement recommends using a different AREA function, known as $AREA_7$:

$$AREA_7 = 4 + 6\left(\frac{d_8}{d_0}\right) + 5\left(\frac{d_{12}}{d_0}\right) + 6\left(\frac{d_{18}}{d_0}\right) + 9\left(\frac{d_{24}}{d_0}\right) + 18\left(\frac{d_{36}}{d_0}\right) + 12\left(\frac{d_{60}}{d_0}\right) \quad \text{(Eq. 5)}$$

Note that this equation requires a deflection sensor at 8 inches from the center of the load plate, which is not present for some of the earlier data collected on this section. $AREA_7$ is then used to compute the estimated dense liquid radius of relative stiffness (l_{est}):

$$l_{est} = \left[\frac{ln\left(\frac{60-AREA_7}{289.708}\right)}{-0.698}\right]^{2.566} \quad \text{(Eq. 6)}$$

l_{est} is then used to estimate k (k_{est}):

$$k_{est} = \frac{P \times 0.1245 e^{\left[-0.14707 e^{(-0.0756 l_{est})}\right]}}{d_0 l_{est}^2} \quad \text{(Eq. 7)}$$

k_{est} is then adjusted for finite slab size:

$$k = \frac{k_{est}}{AF_l^2 AF_{d_0}} \quad \text{(Eq. 8)}$$

AF_l and AF_{d0} are correction factors for finite slab size:

$$AF = 1 - 0.89434 e^{-0.61662\left(\frac{L}{l_{est}}\right)^{1.04831}} \quad \text{(Eq. 9)}$$

$$AF_{d_0} = 1 - 1.15085e^{-0.79432\left(\frac{L}{l_{est}}\right)^{0.80151}} \quad \text{(Eq. 10)}$$

In Equations 9 and 10, L is determined using Equation 11, which only holds if the slab width is more than half of the slab length, as is the case for all sections in this project:

$$L = \sqrt{L_l L_w} \quad \text{(Eq. 11)}$$

Where: L_l = slab length (inches)

L_w = slab width (inches)

E_{pcc} can then be determined using Equation 4, using the AF_l factor to correct l_{est}.

Results computed using the AASHTO 1993 and 1998 methods were spot-checked using the MODCOMP6 layered-elastic backcalculation program, with the layer model shown in Table 10.

Figure 8 shows E_{pcc} data for all three analysis procedures for the 16,000-pound nominal load level along with the results from the laboratory static modulus test (LTPP P64/ASTM C469). Both laboratory static modulus tests were performed on 4-inch-diameter cores. The first sample was obtained on October 5, 1993, and tested on October 11, 1993; the second sample was obtained on August 31, 1994, and tested on September 28, 1994. The intervals from the slab pour to test are 28 days and 380 days, respectively.

Table 10. Section 040215 Layer Model

Layer	Layer Type	Seed Modulus (ksi)	Poisson's Ratio	Thickness (inches)
1	PCC	4000	0.15	11.2
2	DGAB	30	0.45	6.3
3	Subgrade	30	0.45	

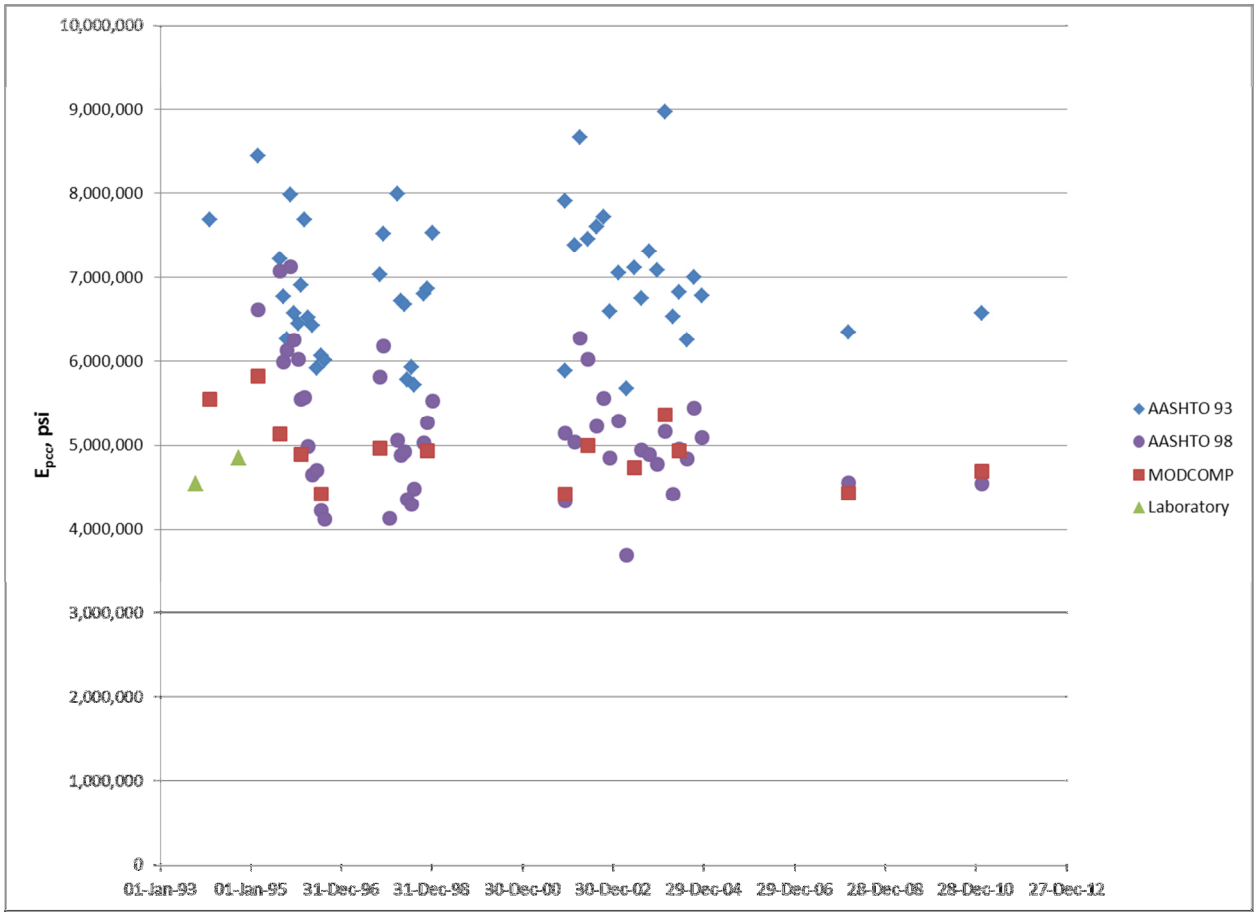

Figure 8. Section 040215 E_{pcc} vs. Date

The E_{pcc} values determined using the AASHTO 1993 procedure are high and highly variable. The backcalculated results are less variable and agree better with the laboratory results and typical values for concrete. Figure 9 shows AASHTO 1993 versus backcalculated E_{pcc} values.

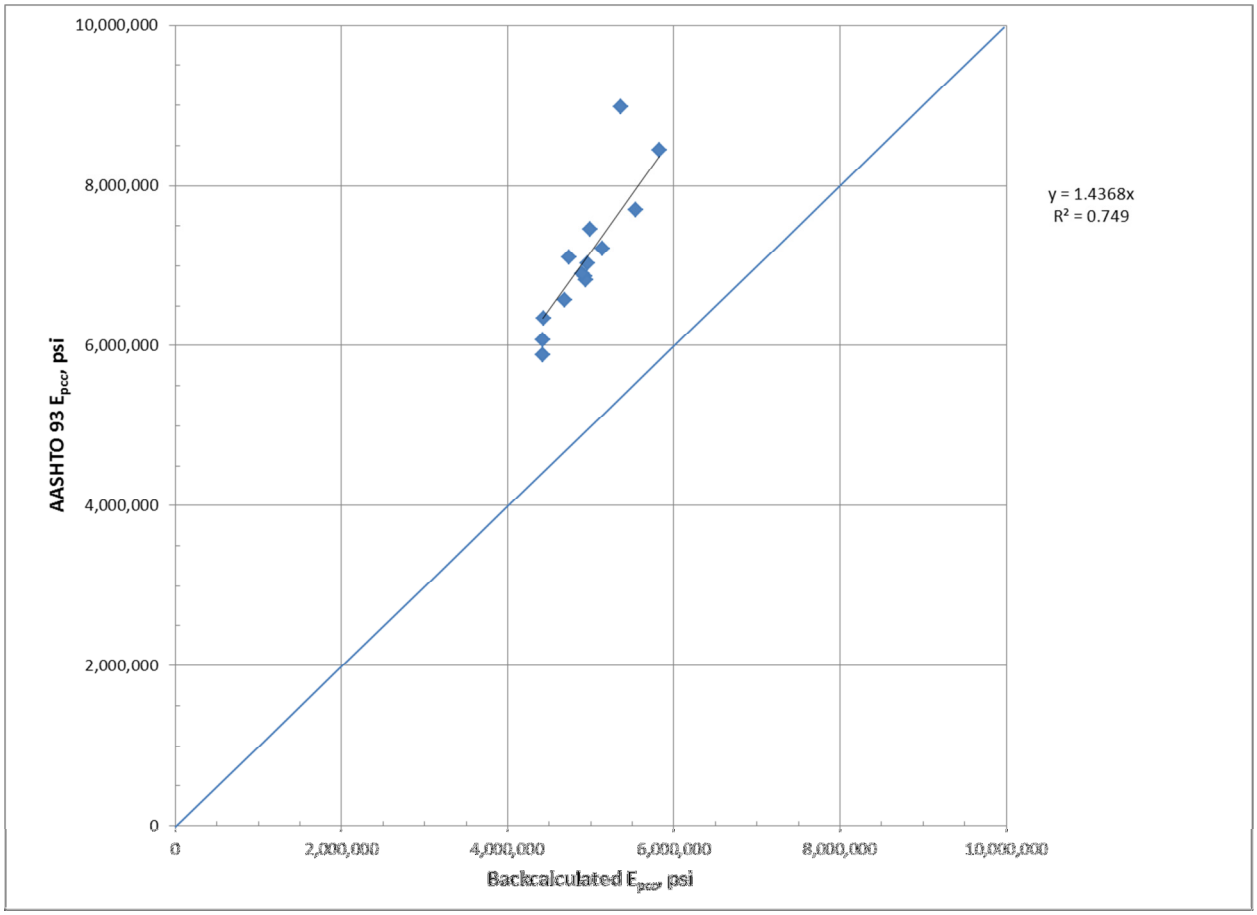

Figure 9. Section 040215 AASHTO 1993 vs. Backcalculated E_{pcc}

The AASHTO 1998 results are significantly less biased relative to the backcalculated values, but slightly more variable, as shown in Figure 10.

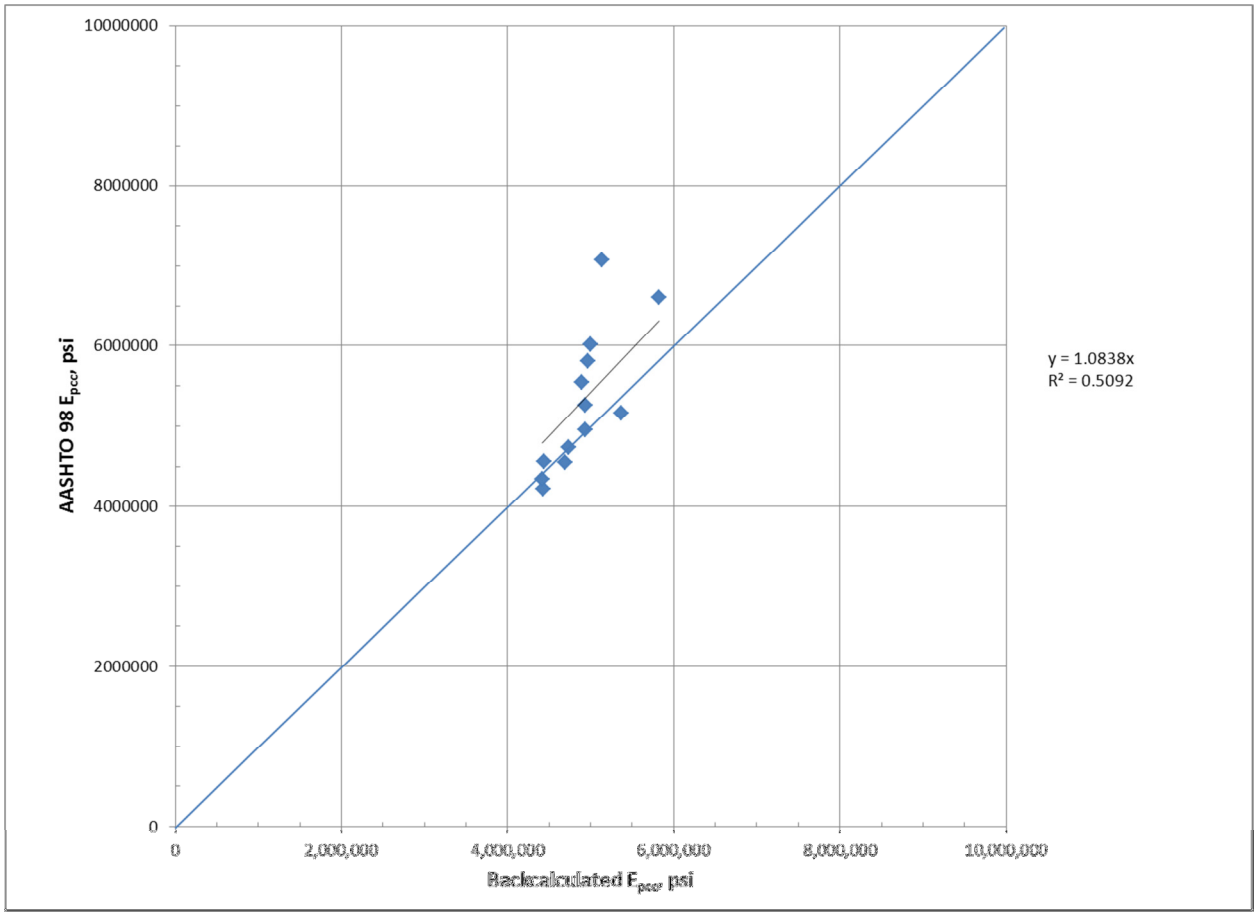

Figure 10. Section 040215 AASHTO 1998 vs. Backcalculated E_{pcc}

Both the AASHTO 1993 and 1998 analysis procedures yield a composite modulus of subgrade reaction, which includes contribution from the base and subgrade layers. The backcalculated results yield individual stiffness values for the base and subgrade layers. Equation 12 was used to convert the backcalculated base and subgrade modulus values to an equivalent composite modulus of subgrade reaction (k-). This equation is from Volume 2 of the 1985 *AASHTO Guide for Design of Pavement Structures* (AASHTO 1985) and was used to develop Figure 3.3 in the AASHTO 1993 guide. The backcalculated moduli were reduced by a factor of three for consistency with the data used to develop this equation.

(Eq. 12)

Where: t = thickness of base course (inches)

E_b = resilient modulus of base course (psi)

E_s = resilient modulus of subgrade (psi)

Figure 11 shows the composite k-values computed using the AASHTO 1993, 1998, and backcalculation procedures.

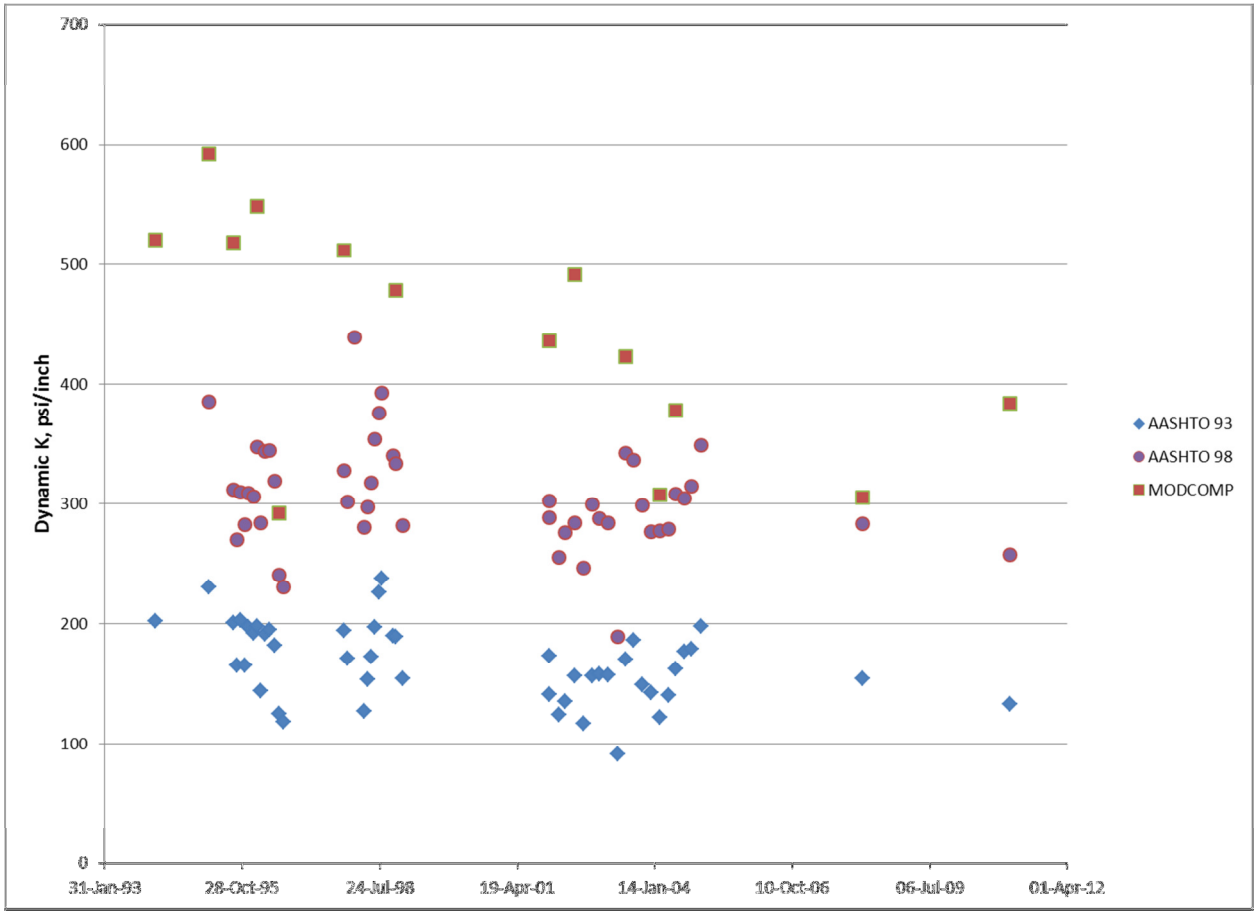

Figure 11. Section 040215 K-Values vs. Date

The AASHTO 1993 and 1998 k-values are well-correlated, however, the relationship has a definite nonzero intercept, as shown in Figure 12.

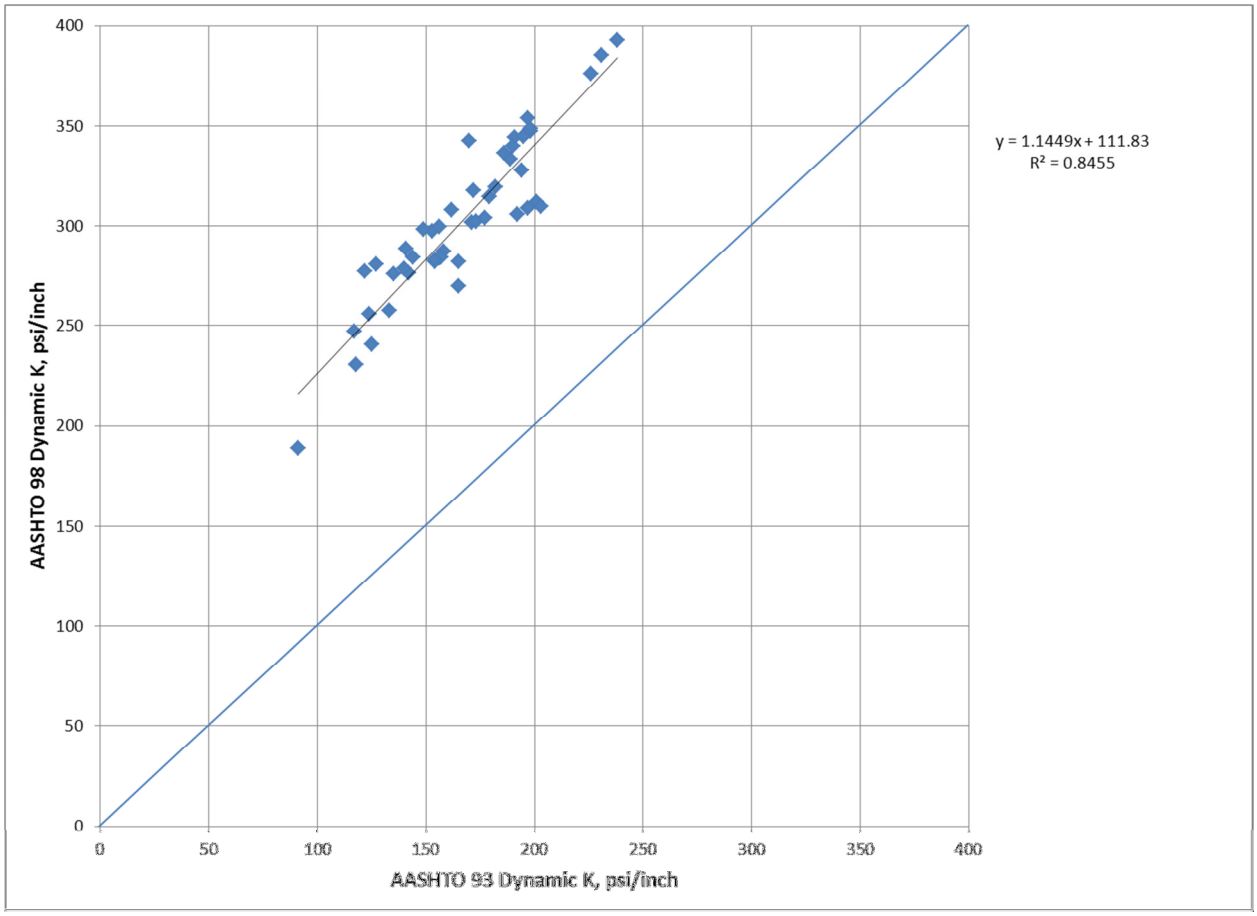

Figure 12. AASHTO 1998 vs. AASHTO 1993 K-Values

The average value of $1/(AF_I\text{^}2 * AF_{d0})$ (i.e., the correction factor from Equation 8) is 1.306, showing that the difference between these procedures is not just due to the correction for finite slab size.

The AASHTO 1998 and backcalculated values also show some correlation, as shown in Figure 13. It is unclear how much of the bias between the data sets is due to Equation 12.

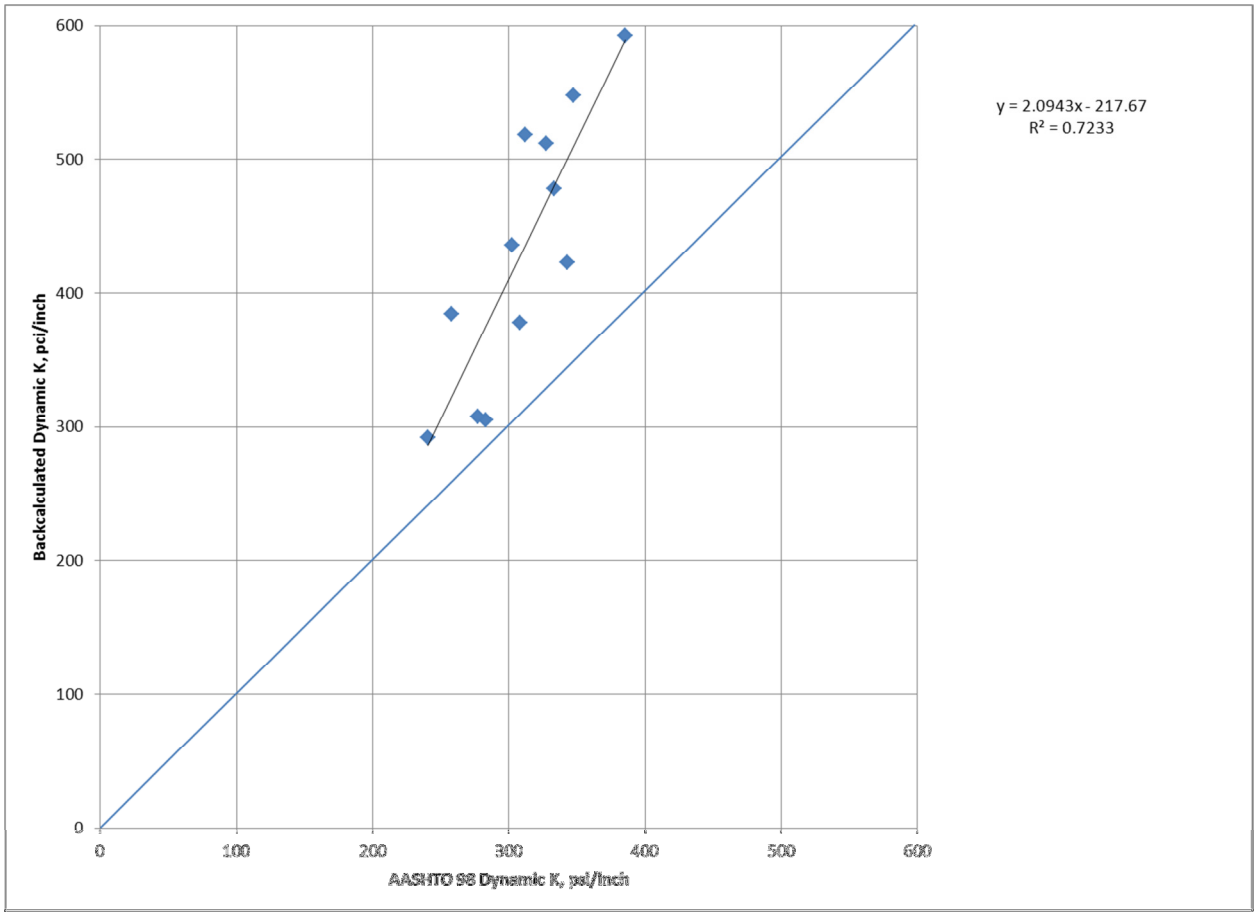

Figure 13. AASHTO 1998 vs. Backcalculated K-Values

In general, the backcalculation procedure assigns most of the variability in structural response of this section over time to variations in the base and subgrade stiffness, which makes sense given the much higher sensitivity of unbound materials than PCC to environmental effects. The AASHTO procedures assign this variability to both the slab stiffness and subgrade stiffness, which makes less sense. The backcalculated results also show a general trend of decreasing k-value over time, which is not apparent from the AASHTO results. However, confidence in the backcalculated k-values is limited because of the questionable nature of the tools available to convert resilient moduli to composite k-value.

In the remainder of this report, only AASHTO 1998 results are presented, where the data available is compatible with its use. For data sets where testing does not include a sensor at 8 inches from the center of the load plate, the AASHTO 1993 data is presented as correlated to the AASHTO 1998 procedure using the relationships developed above. A limited number of backcalculated results are also presented as a spot-check for each section.

Section 040213

Section 040213 is in the thin, wide, low-strength DGAB cell of the experimental matrix.

LTE Data

Figure 14 shows LTE data versus date. Results from the JA and JL tests are in good agreement, and no trend in performance with time is apparent. All testing was performed in the winter, with dates ranging from November 8 to March 6. Slab mid-depth temperatures ranged from 57˚ F to 81˚ F. A moderate gradient of LTE with temperature was observed, with a slope of 0.43 percent/˚F and an R^2 of 0.45.

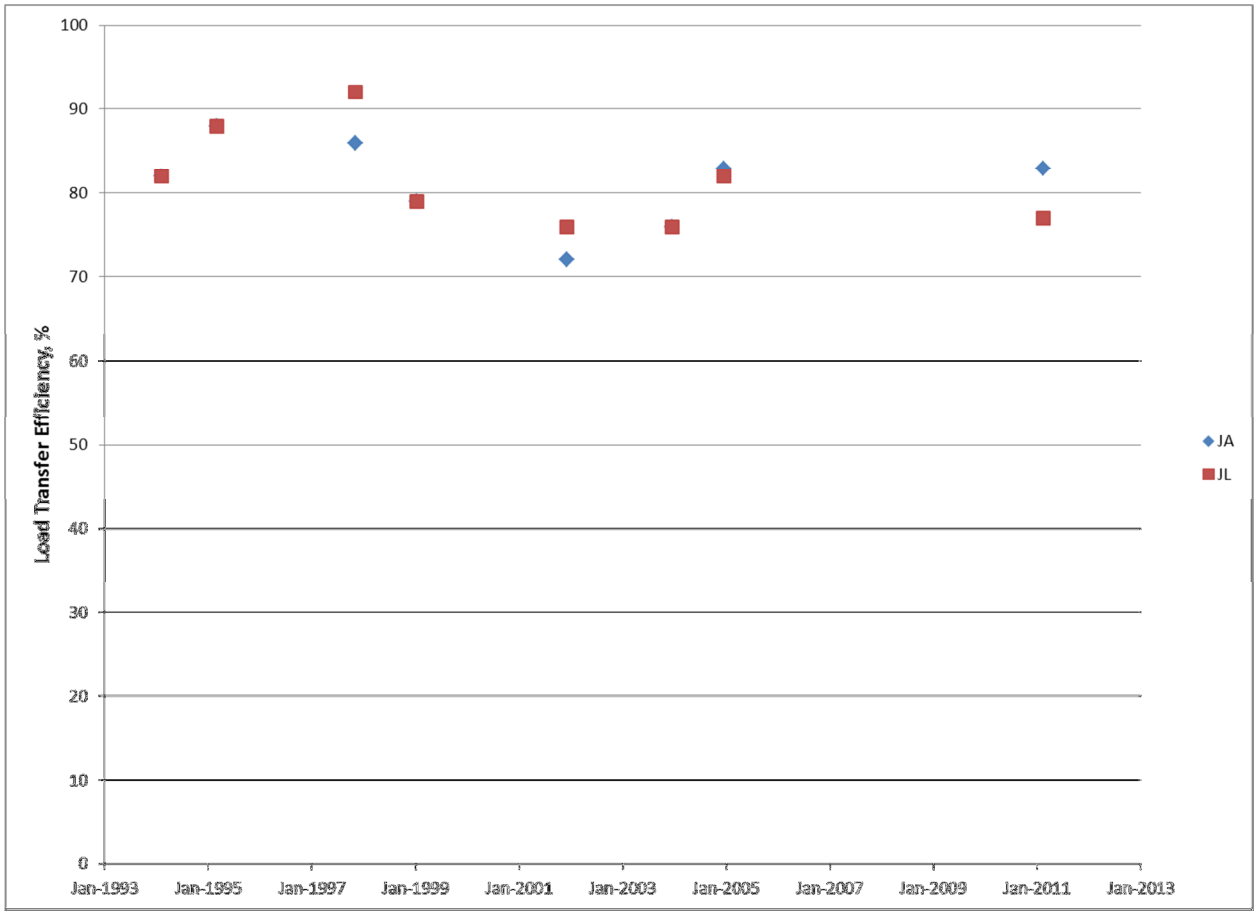

Figure 14. Section 040213 Load Transfer Efficiency vs. Date

Basin Data

Figure 15 presents E_{pcc} data versus date. The AASHTO 1993 procedure, using the correction factors developed for the SMP section, was used for the first data point because the FWD did not have a sensor

at 8 inches at that time. Despite the correction factors, the computed E_{pcc} is well above the expected range. Backcalculation was performed using MODCOMP for selected dates, using the layer model shown in Table 11. Both the AASHTO 1998 and backcalculated data agree that there is a trend of decreasing E_{pcc} over time at this section.

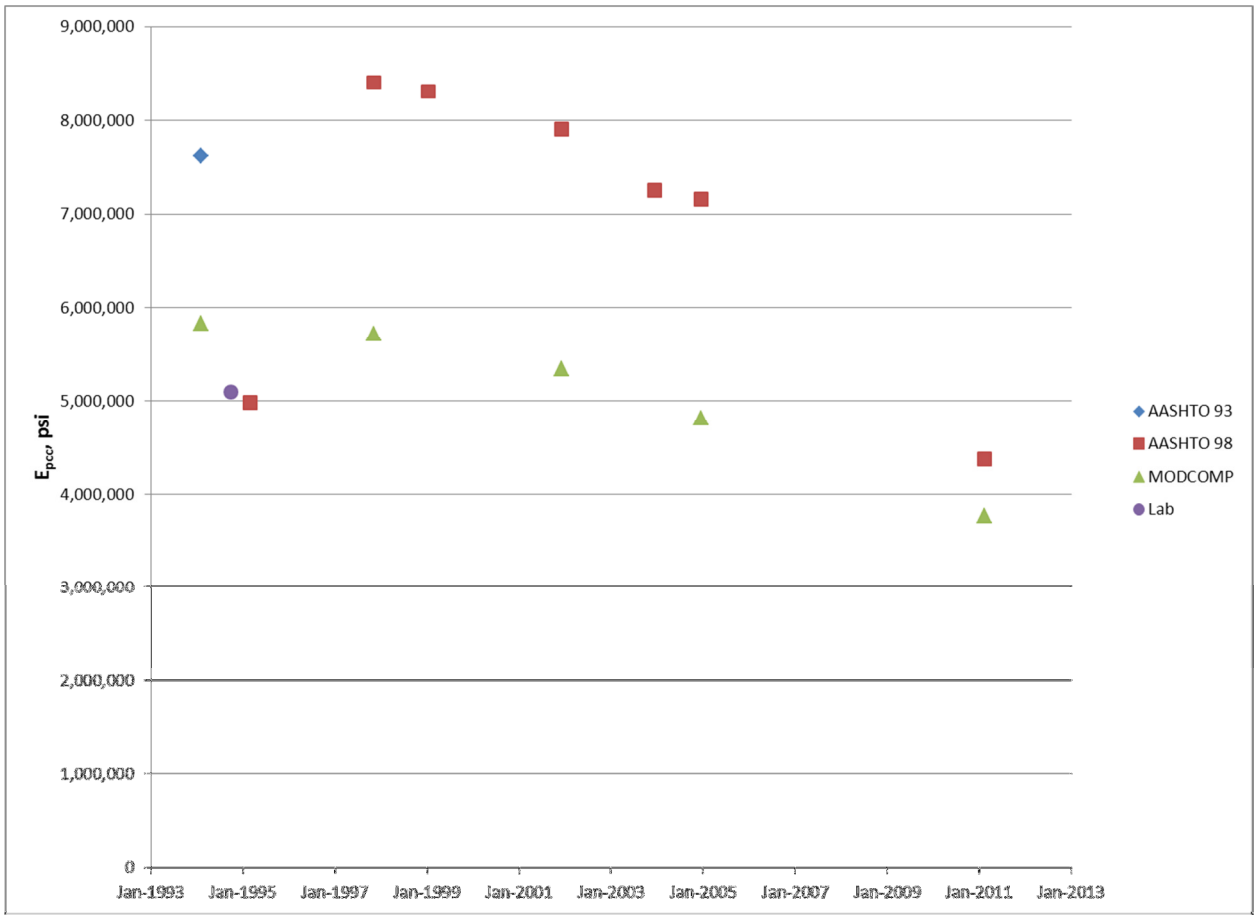

Figure 15. Section 040213 E_{pcc} vs. Date

Table 11. Section 040213 Layer Model

Layer	Layer Type	Seed Modulus (ksi)	Poisson's Ratio	Thickness (inches)
1	PCC	4000	0.15	7.9
2	DGAB	30	0.45	5.8
3	Subgrade	30	0.45	

Figure 16 shows k-values versus date. As with the other sections, the backcalculated k-value is significantly higher than that computed using the AASHTO 1998 procedure. There is a possible decreasing trend of k-value with time in the backcalculated values, whereas the AASHTO 1998 data shows an increase in k-value early in the pavement's life and then a gradual decrease.

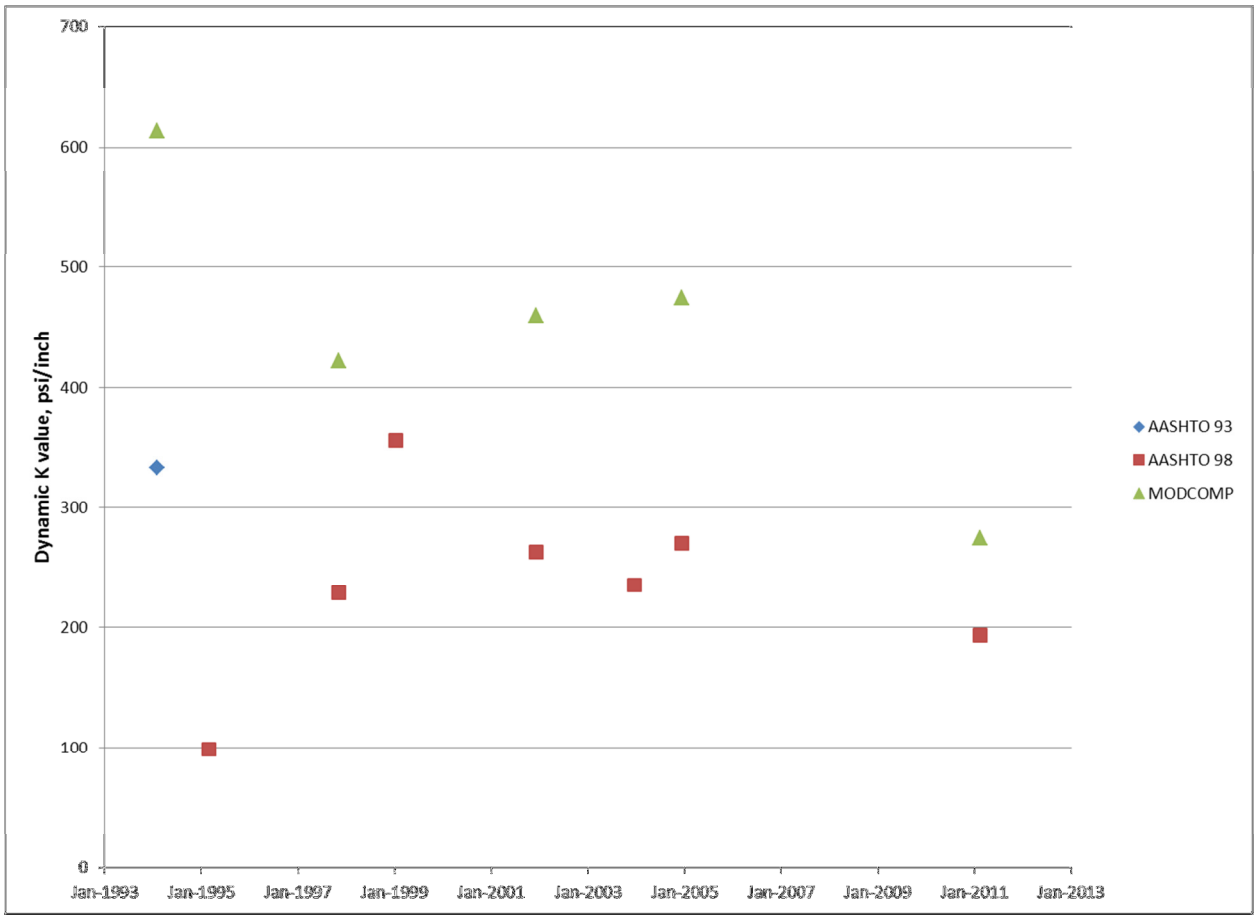

Figure 16. Section 040213 K-Values vs. Date

Section 040214

Section 040214 is in the thin, narrow, high-strength DGAB cell of the experimental matrix.

LTE Data

Figure 17 shows LTE data versus date. JA and JL test results are in reasonably good agreement. All testing was performed in the winter, with dates ranging from November 3 to February 21. Slab mid-depth temperatures ranged from 51˚ F to 85˚ F with an average temperature of 66˚ F. A moderate gradient of LTE with temperature was observed, with a slope of 0.39 percent/˚F and an R^2 of 0.43. There

appears to be a slight decrease in LTE with time. The final test was performed with a slab temperature of 63˚ F, so this decrease is unlikely to be a temperature effect.

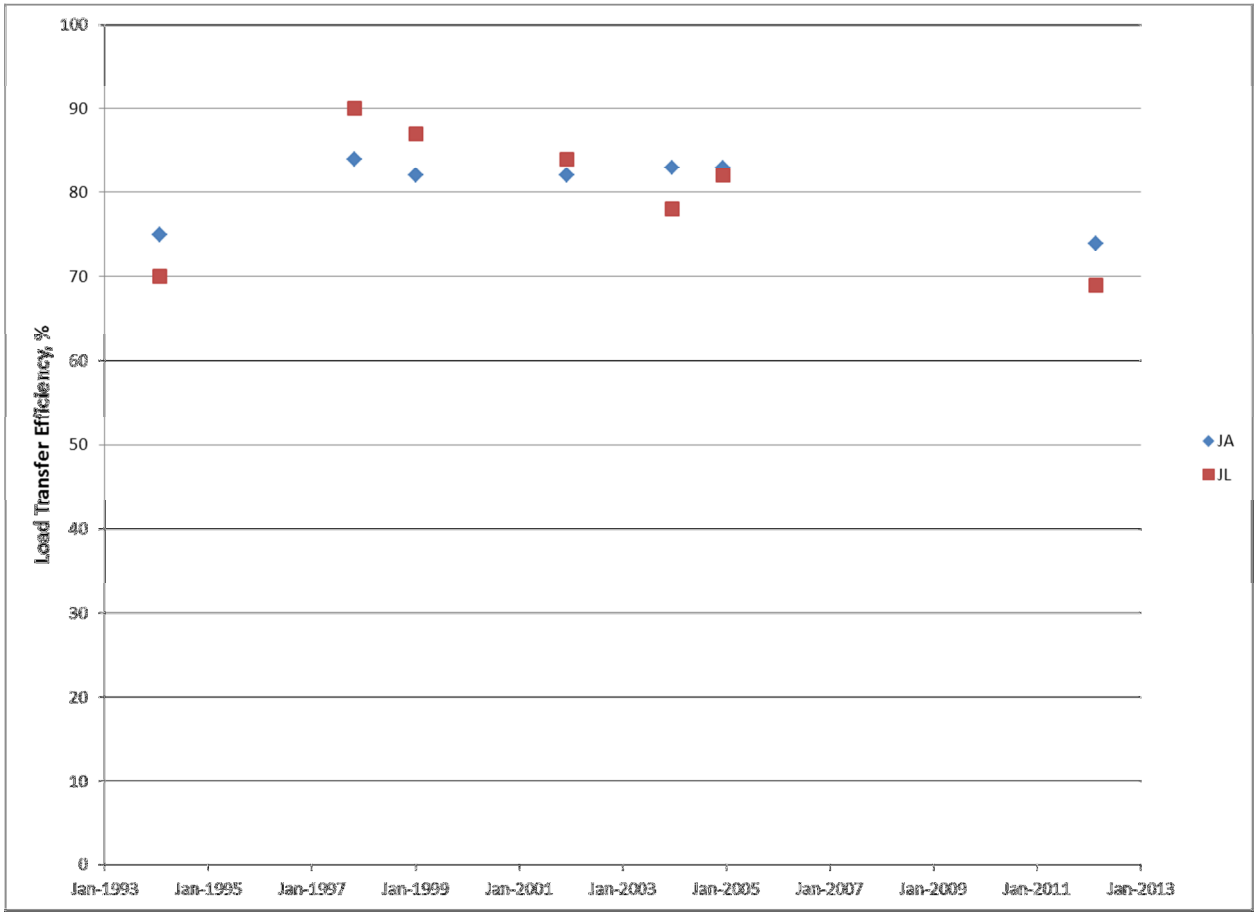

Figure 17. Section 040214 Load Transfer Efficiency vs. Date

Basin Data

Figure 18 presents E_{pcc} versus date data. The AASHTO 1993 procedure, using the correction factors developed for the SMP section, was used for the first data point because the FWD did not have a sensor at 8 inches at that time. Despite the correction factors, the computed E_{pcc} is well above the expected range. Backcalculation was performed using MODCOMP for selected dates, using the layer model shown in Table 12. Both the AASHTO 1998 and backcalculated data agree that there is a trend of decreasing E_{pcc} over time at this section.

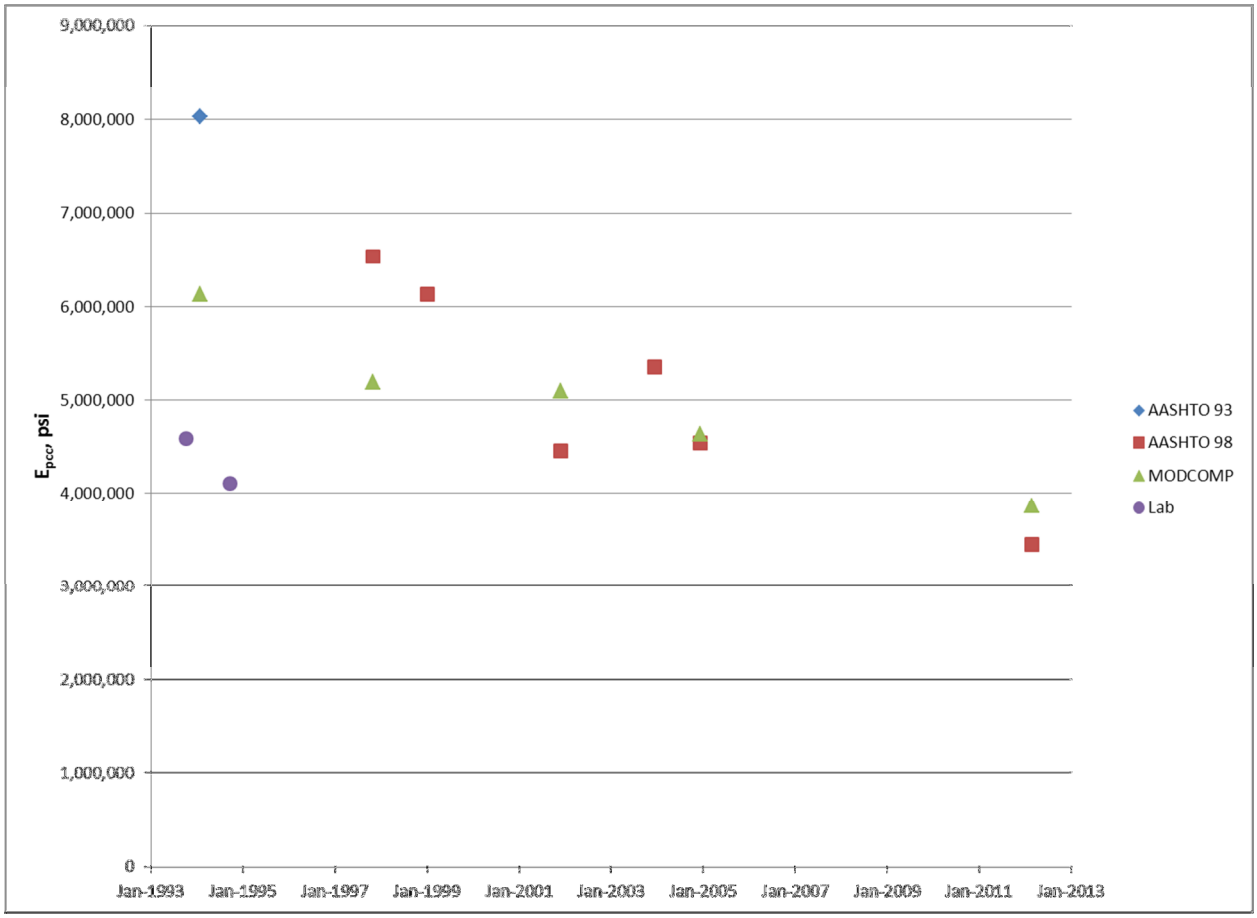

Figure 18. Section 040214 E_{pcc} vs. Date

Table 12. Section 040214 Layer Model

Layer	Layer Type	Seed Modulus (ksi)	Poisson's Ratio	Thickness (inches)
1	PCC	4000	0.15	8.3
2	DGAB	30	0.45	6.1
3	Subgrade	30	0.45	

k-value versus date Figure 19 shows k-values versus date data. The backcalculated k starts out well above the AASHTO 1998 K, but gets closer over time. Both data sets show a trend of decreasing k-value over time.

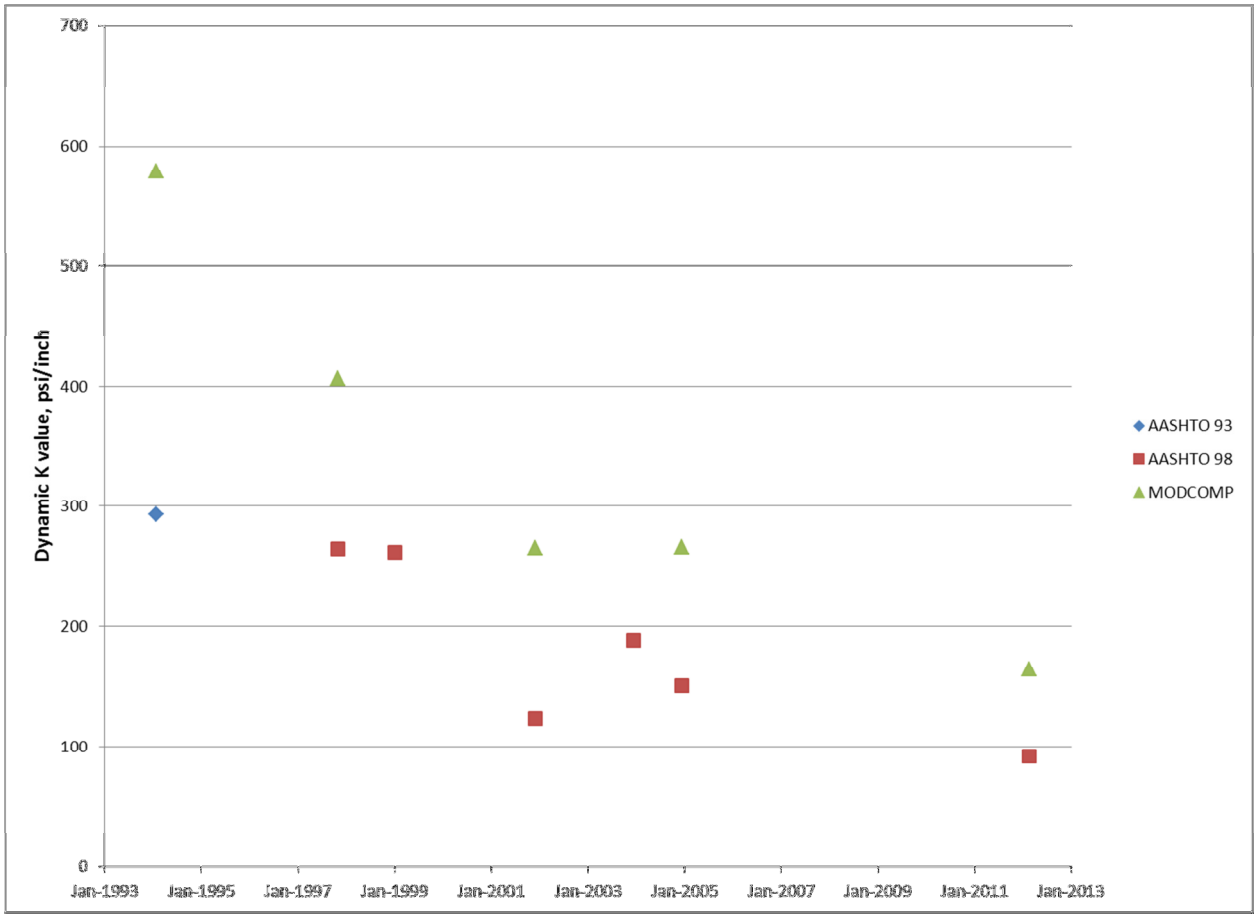

Figure 19. Section 040214 K-Values vs. Date

Section 040216

Section 040216 is in the thick, wide, high-strength DGAB cell of the experimental matrix.

LTE Data

Figure 20 shows LTE data versus date. JA and JL test results are in reasonably good agreement except for the last data point. All testing was performed in the winter, with dates ranging from November 4 to March 1. Slab mid-depth temperatures ranged from 51˚ F to 80˚ F with an average temperature of 63˚ F. A gradient of LTE with temperature was observed, with a slope of 0.83 percent/˚F and an R^2 of 0.65. The final test point shows a substantial reduction in LTE. This test was performed with a slab temperature of 51˚ F, which is the lowest temperature in the data series. This indicates that the decrease in LTE may be due to temperature effects, not age effects.

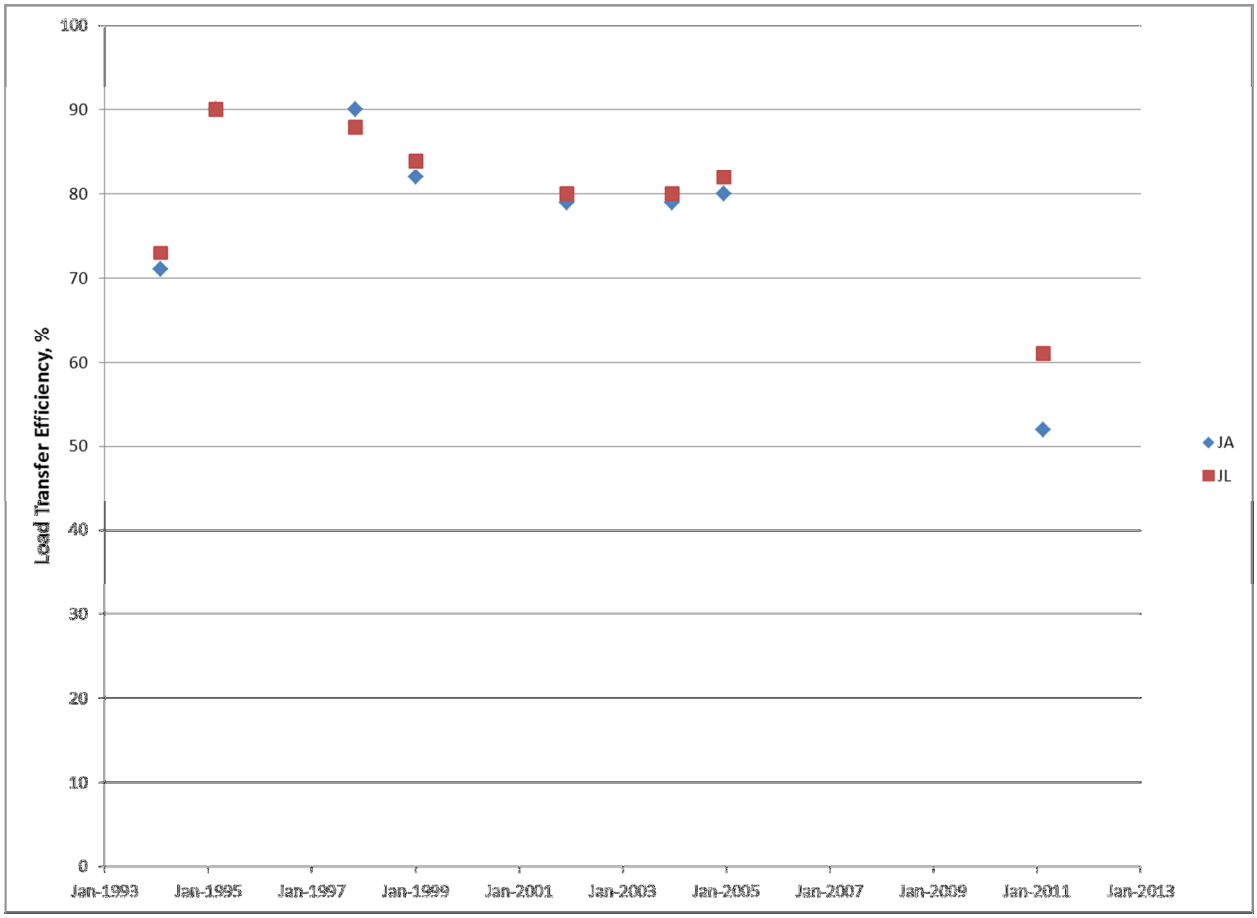

Figure 20. Section 040216 Load Transfer Efficiency vs. Date

Basin Data

Figure 21 presents E_{pcc} data versus date. The AASHTO 1993 procedure, using the correction factors developed for the SMP section, was used for the first data point, as the FWD did not have a sensor at 8 inches at that time. Despite the correction factors, the computed E_{pcc} is well above the expected range. Backcalculation was performed using MODCOMP for selected dates, using the layer model shown in Table 13. Both the AASHTO 1998 and backcalculated data agree that there is a slight trend of decreasing E_{pcc} over time at this section.

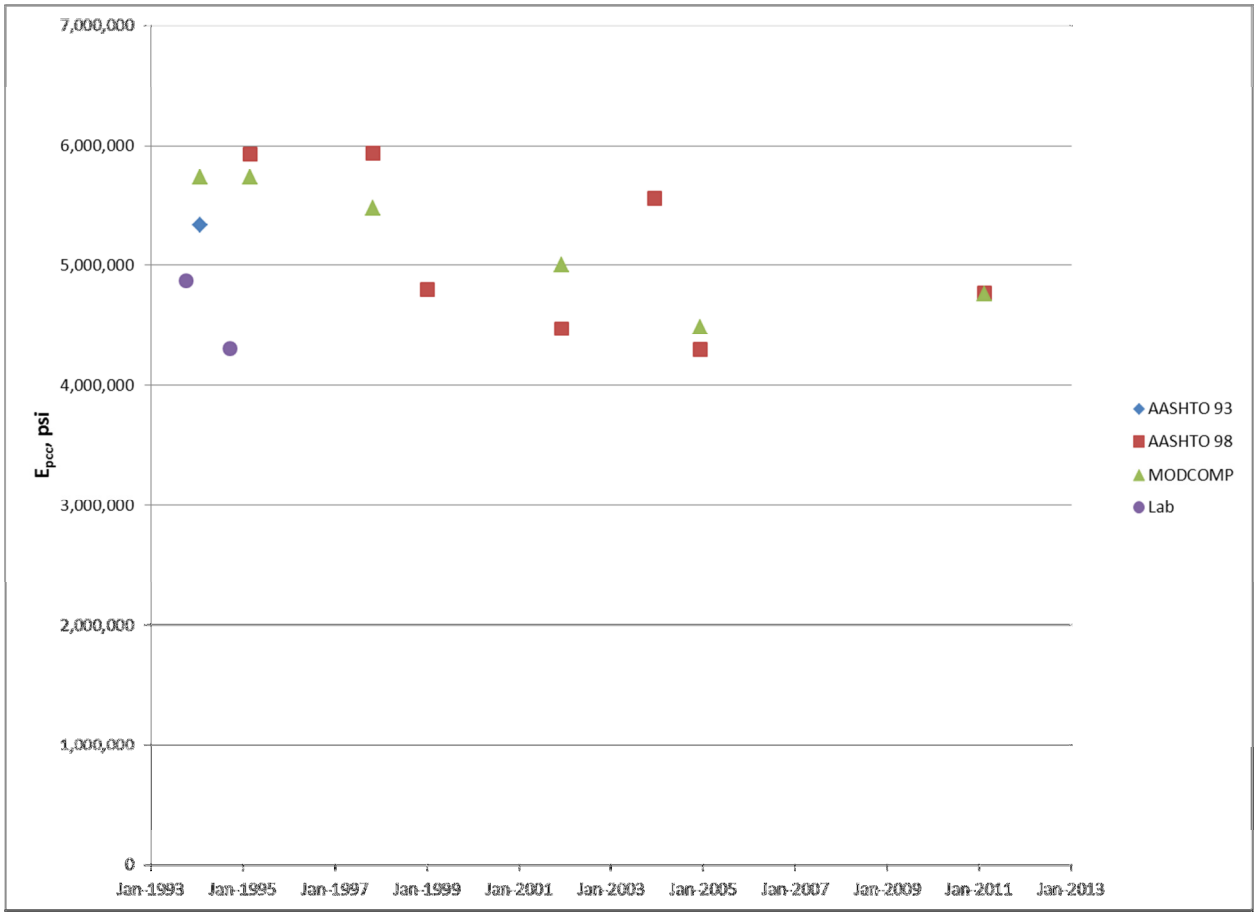

Figure 21. Section 040216 E_{pcc} vs. Date

Table 13. Section 040216 Layer Model

Layer	Layer Type	Seed Modulus (ksi)	Poisson's Ratio	Thickness (inches)
1	PCC	4000	0.15	11.2
2	DGAB	30	0.45	6.3
3	Subgrade	30	0.45	

Figure 22 shows k-values versus date. The backcalculated k-value is significantly higher than the AASHTO 1998 k-value, however both agree that the k-value declined from the initial construction date to about 2005, but recovered by the final test in 2012. However, because of the gap in data between 2005 and 2012, the 2012 results may be outliers, and the apparent recovery in k-value may be spurious.

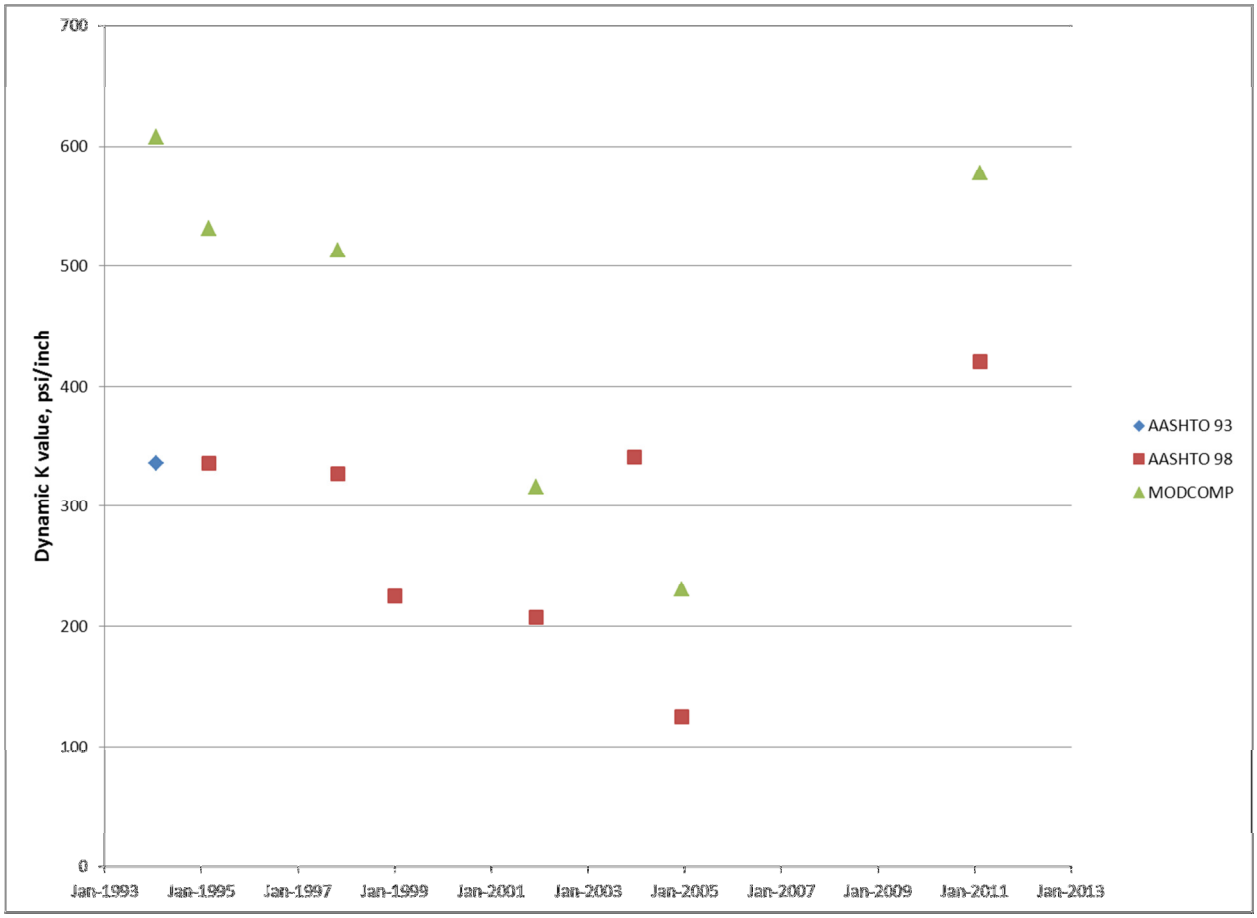

Figure 22. Section 040216 K-Values vs. Date

Section 040217

Section 040217 is in the thin, wide, low-strength LCB cell of the experimental matrix.

LTE Data

Figure 23 shows LTE data versus date. The JL results are consistently higher than the JA results except for the first data point. All testing was performed in the winter, with dates ranging from November 5 to March 2. Slab mid-depth temperatures ranged from 52˚ F to 81˚ F, with an average temperature of 67˚ F. No gradient of LTE with temperature was observed; a regression of LTE versus mid-slab temperature had a slope of -0.20 percent/˚F and an R^2 of 0.04. The data shows a decrease in LTE during the first two test points and then a consistent value for the remainder.

Figure 23. Section 040217 Load Transfer Efficiency vs. Date

Basin Data

Figure 22 presents E_{pcc} data versus date. The AASHTO 1993 procedure, using the correction factors developed for the SMP section, was used for the first data point because the FWD did not have a sensor at 8 inches at that time. Despite the correction factors, the computed E_{pcc} is well above the expected range. Backcalculation was performed using MODCOMP for selected dates, using the layer model shown in Table 14. Both the AASHTO 1998 and backcalculated data agree that there is a slight trend of decreasing E_{pcc} over time at this section.

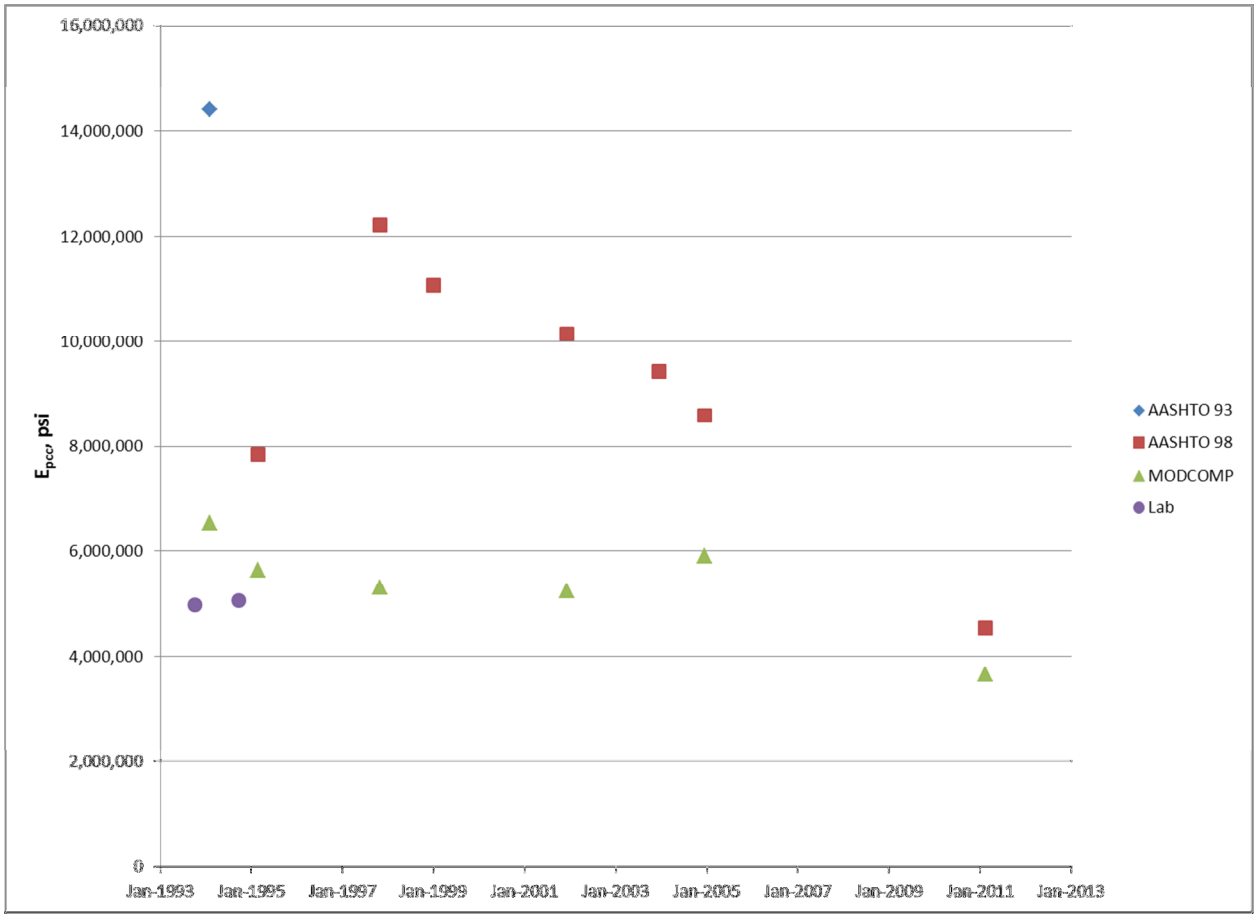

Figure 24. Section 040217 E_{pcc} vs. Date

Table 14. Section 040217 Layer Model

Layer	Layer Type	Seed Modulus (ksi)	Poisson's Ratio	Thickness (inches)
1	PCC	4000	0.15	8.1
2	LCB	500	0.20	6.1
3	Subgrade	30	0.45	

Figure 25 shows k-values versus date. The backcalculated k-value is significantly higher than the AASHTO 1998 k-value. Both analyses show an increase in k-value from the initial construction to 2005, with a slight decrease between 2005 and 2012.

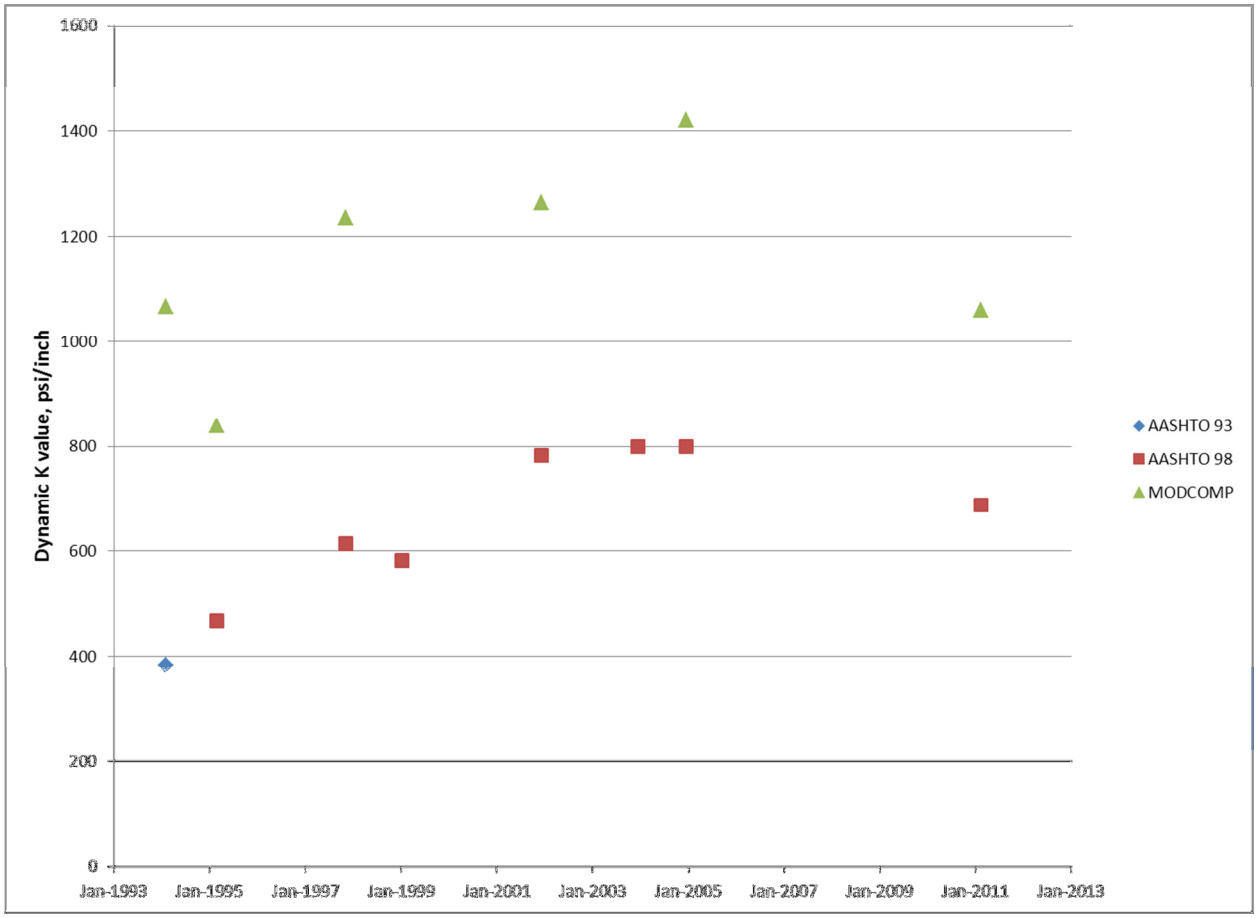

Figure 25. Section 040217 K-Values vs. Date

Section 040218

Section 040218 is in the thin, narrow, high-strength LCB cell of the experimental matrix.

LTE Data

Figure 26 shows LTE data versus date. All testing was performed in the winter, with dates ranging from November 4 to February 9. Slab mid-depth temperatures ranged from 45˚ F to 75˚ F with an average temperature of 64˚ F. No gradient of LTE with temperature was observed; a regression of LTE versus mid-slab temperature had a slope of -0.34 percent/˚F and an R^2 of 0.08. The data is variable, with an apparent decrease in LTE after construction and then a return to the initial value.

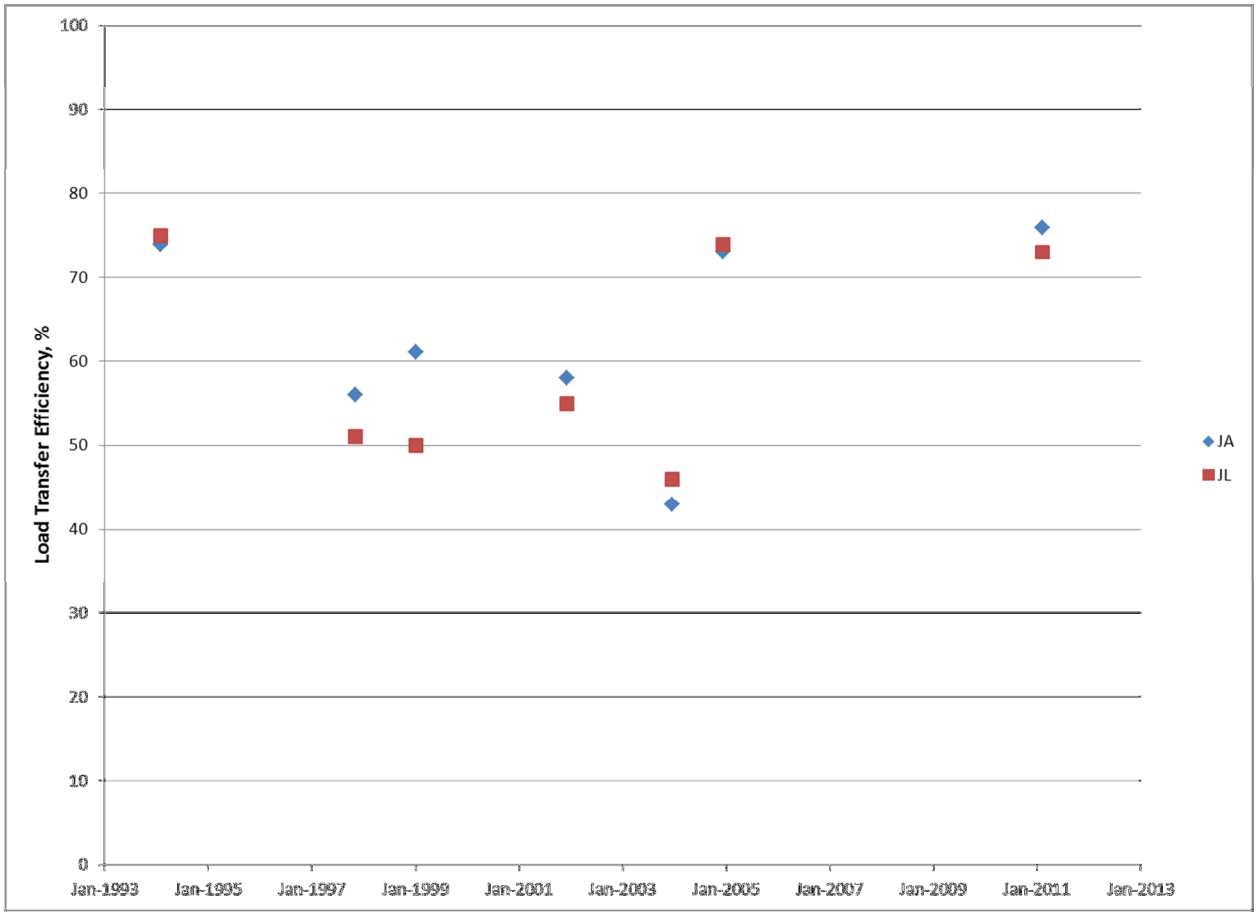

Figure 26. Section 040218 Load Transfer Efficiency vs. Date

Basin Data

Figure 27 presents E_{pcc} data versus date. The AASHTO 1993 procedure, using the correction factors developed for the SMP section, was used for the first data point because the FWD did not have a sensor at 8 inches at that time. Despite the correction factors, the computed E_{pcc} is well above the expected range. Backcalculation was performed using MODCOMP for selected dates, using the layer model shown in

Table 15. The backcalculated results for the December 2004 and February 2011 have excessive root-mean square errors (RMSEs) of 14.8 percent and 16.5 percent, respectively, whereas the remaining results all have RMSEs of less than 5 percent. Normally data with such a high RMSE would be discarded, but this data was retained because it is otherwise consistent with the values computed for this section and other sections, and these are the only data points characterizing the most recent 10 years of the pavement's life. The high RMSE indicates that the pavement is not behaving in a manner consistent with layered-elastic theory. Both the AASHTO 1998 and backcalculated data agree that there is a slight trend of decreasing E_{pcc} over time at this section.

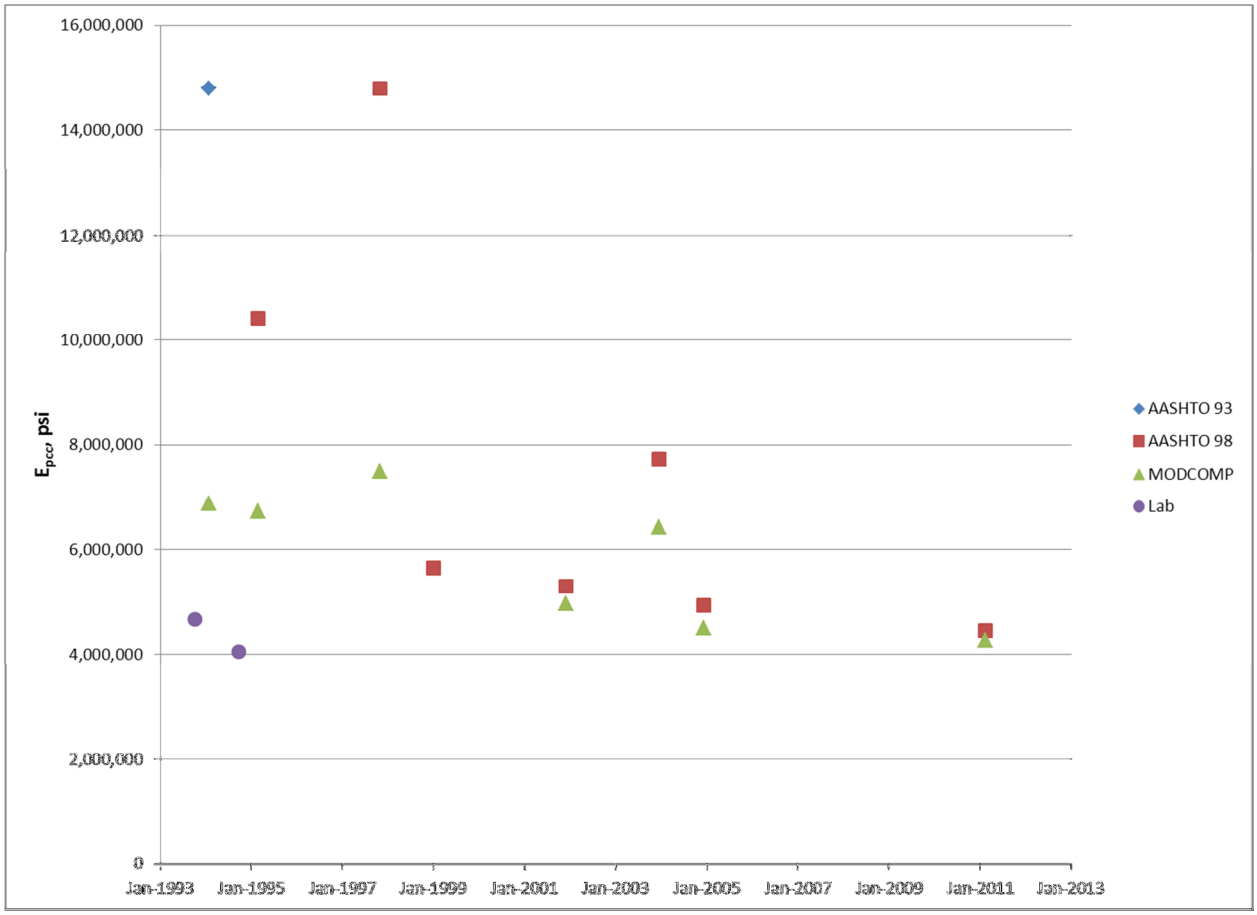

Figure 27. Section 040218 E_{pcc} vs. Date

Table 15. Section 040218 Layer Model

Layer	Layer Type	Seed Modulus (ksi)	Poisson's Ratio	Thickness (inches)
1	PCC	4000	0.15	8.3
2	LCB	500	0.20	6.2
3	Subgrade	30	0.45	

Figure 28 shows k-values versus date. The backcalculated k-value is significantly higher than the AASHTO 1998 k-value during the early performance period, with a large degree of convergence by 2012. The backcalculated data shows a strong trend of decreasing k-value over time; however, the trend in the AASHTO 1998 data is weak to nonexistent.

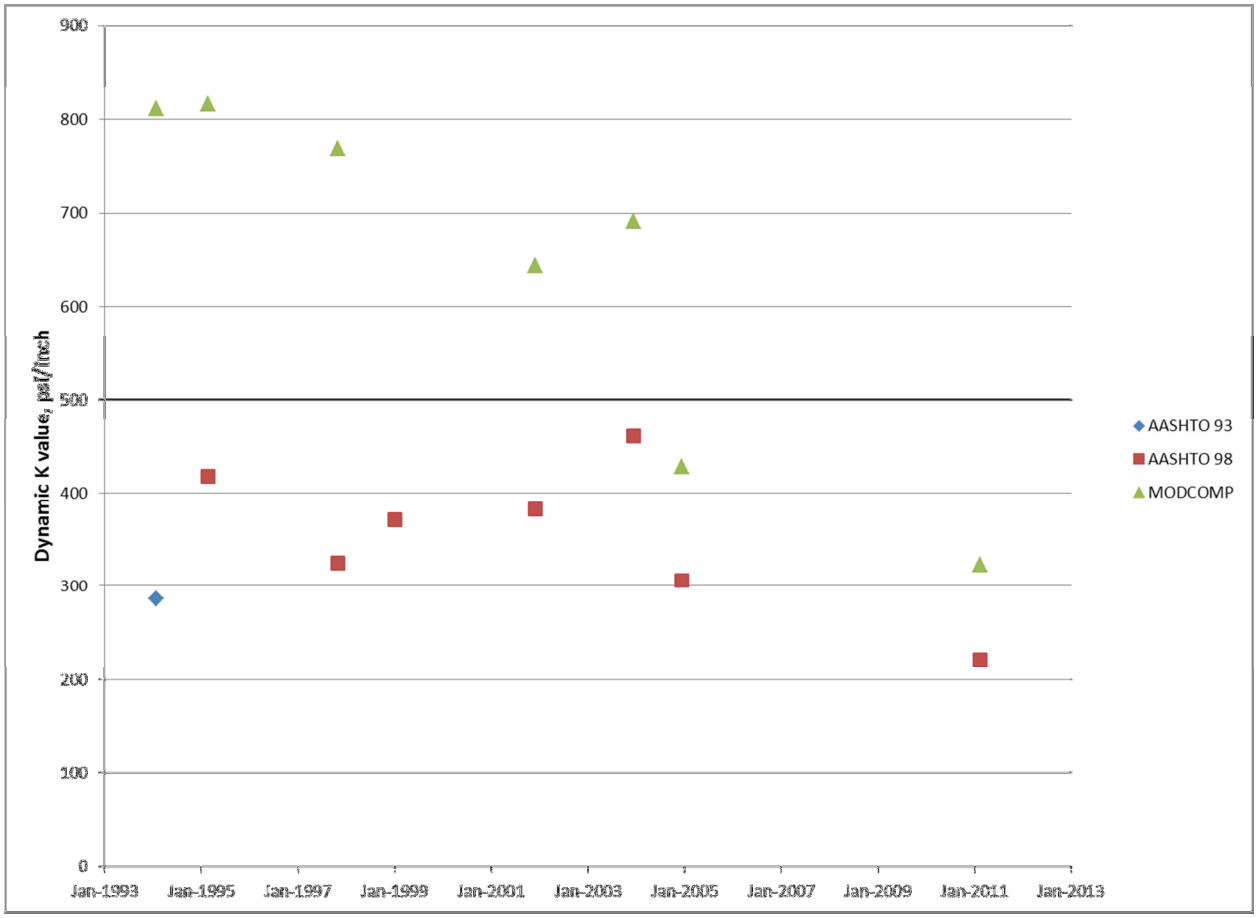

Figure 28. Section 040218 K-Values vs. Date

Section 040219

Section 040219 is in the thick, narrow, low-strength LCB cell of the experimental matrix.

LTE Data

Figure 29 shows LTE data versus date. All testing was performed in the winter, with dates ranging from November 6 to March 5. Slab mid-depth temperatures ranged from 54˚ F to 69˚ F with an average temperature of 63˚ F. No gradient of LTE with temperature was observed; a regression of LTE versus mid-slab temperature had a slope of -0.64 percent/˚F and an R^2 of 0.08. The data is variable but shows a decrease in LTE, which occurs more rapidly in the JA data than the JL data.

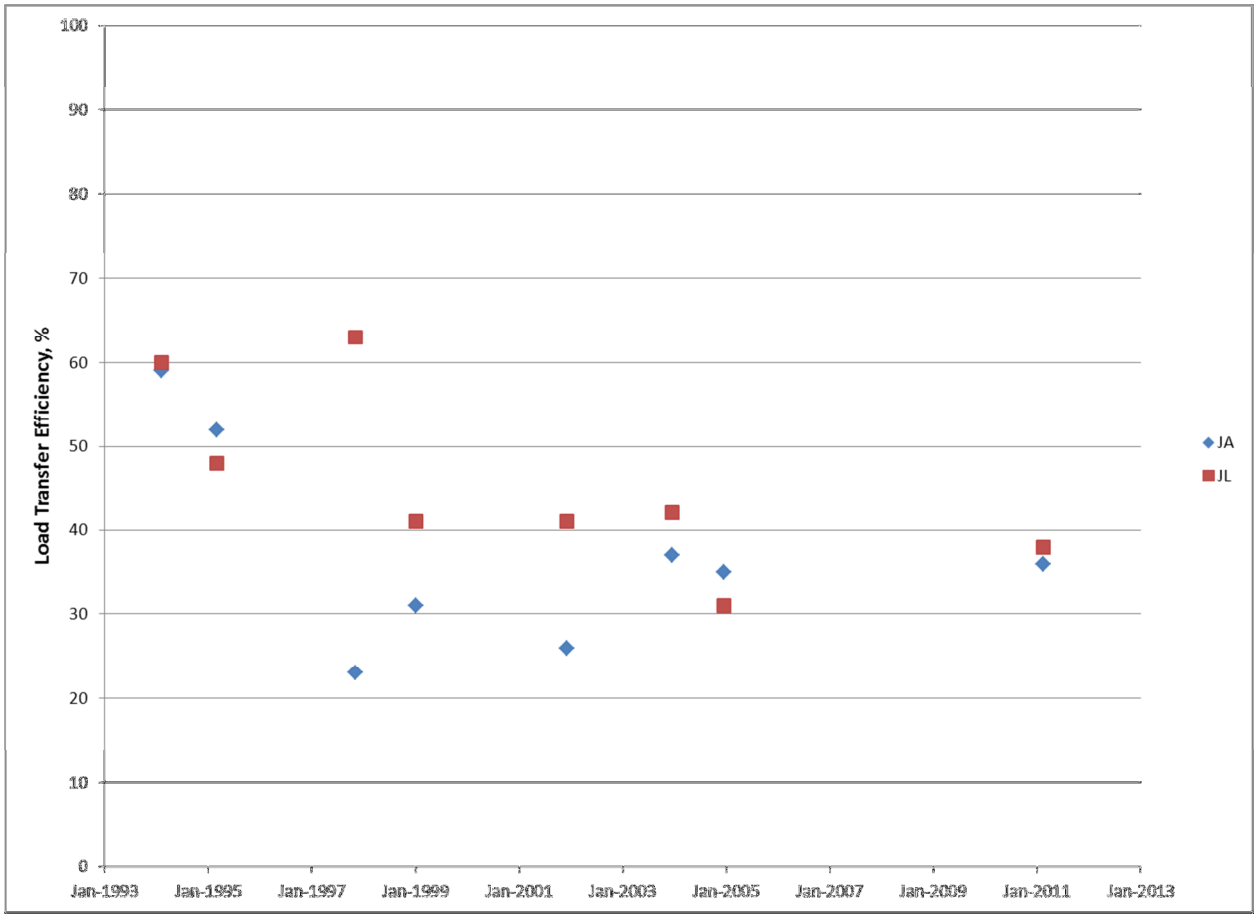

Figure 29. Section 040219 Load Transfer Efficiency vs. Date

Basin Data

E_{pcc} versus date data is presented in Figure 30. The AASHTO 1993 procedure, using the correction factors developed for the SMP section, was used for the first data point because the FWD did not have a sensor at 8 inches at that time. Backcalculation was performed using MODCOMP for selected dates, using the layer model shown in Table 16. The backcalculated results for the November 1997 and January 1999 data exhibit excessive RMSEs of 7.4 percent and 8.0 percent, respectively, whereas the remaining results all have RMSEs of less than 5 percent. The corresponding AASHTO 1998 results are well above the expected range. The high RMSE indicates that the pavement is not behaving in a manner consistent with layered-elastic theory.

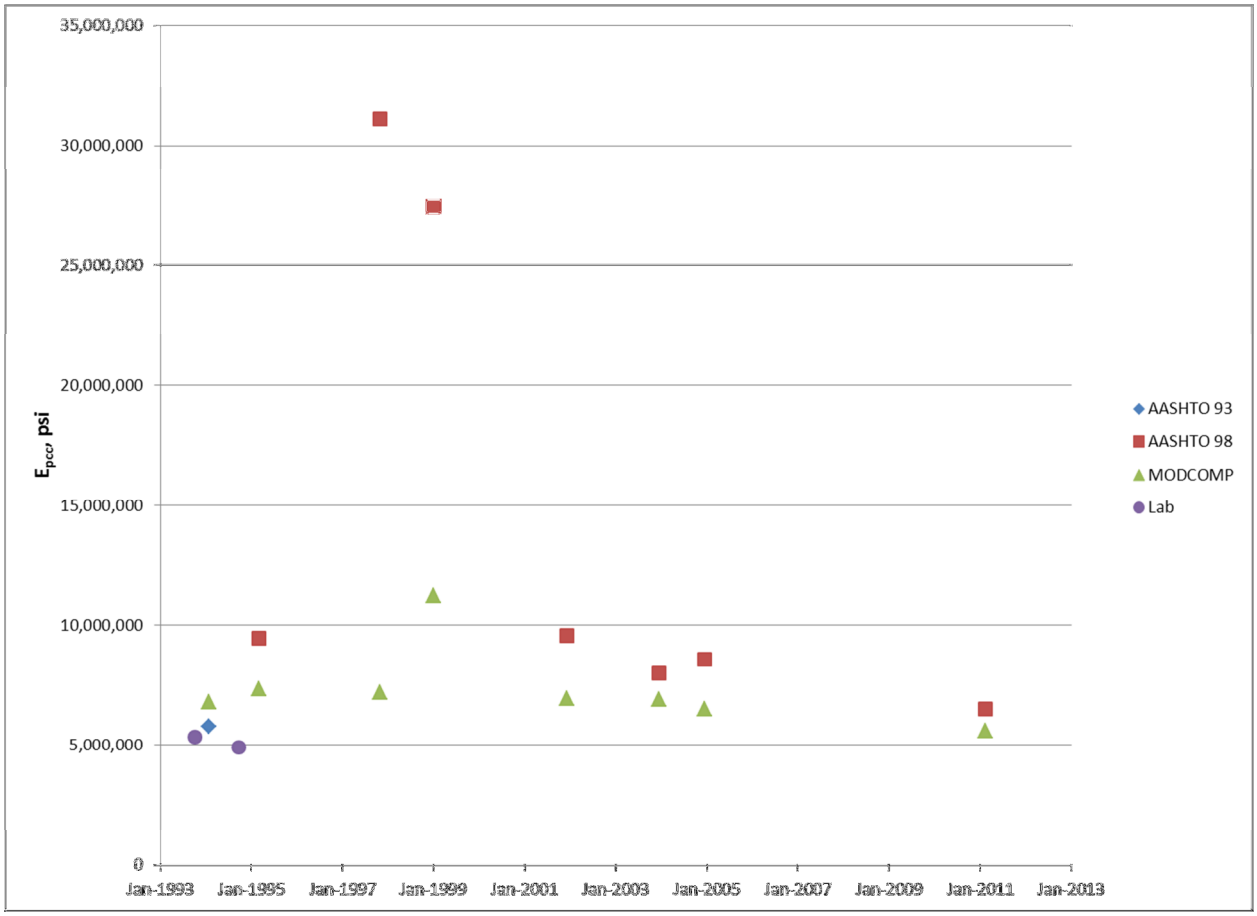

Figure 30. Section 040219 E_{pcc} vs. Date

Table 16. Section 040219 Layer Model

Layer	Layer Type	Seed Modulus (ksi)	Poisson's Ratio	Thickness (inches)
1	PCC	4000	0.15	10.8
2	LCB	500	0.20	6.2
3	Subgrade	30	0.45	

Figure 31 shows k-values versus date. The backcalculated k-values are significantly greater than the AASHTO 1998 k-values. The AASHTO 1998 data shows low k-values from 1997 to 2000 corresponding to the excessively high E_{pcc} values. The backcalculated data is much more consistent.

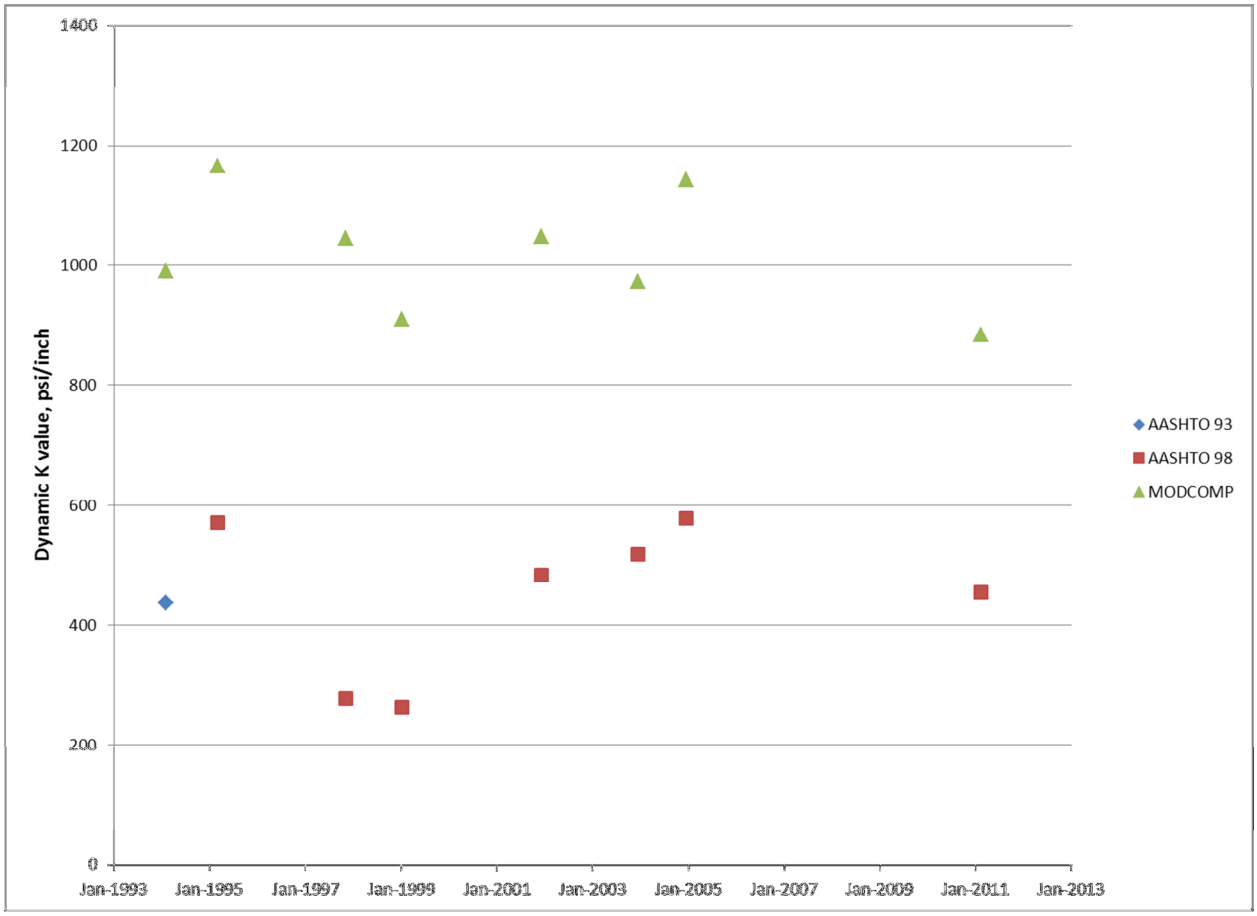

Figure 31. Section 040219 K-Values vs. Date

Section 040220

Section 040220 is in the thick, wide, high-strength LCB cell of the experimental matrix.

LTE Data

Figure 32 shows LTE data versus date. All testing was performed in the winter, with dates ranging from November 4 to February 28. Slab mid-depth temperatures ranged from 51˚ F to 81˚ F, with an average temperature of 65˚ F. No gradient of LTE with temperature was observed; a regression of LTE versus mid-slab temperature had a slope of 0.48 percent/˚F and an R^2 of 0.16. The data shows an initial decrease in LTE followed by some recovery. The JL data is significantly higher than JA data during the period of lowest LTE, but the JA and JL data reconverge as LTE increases.

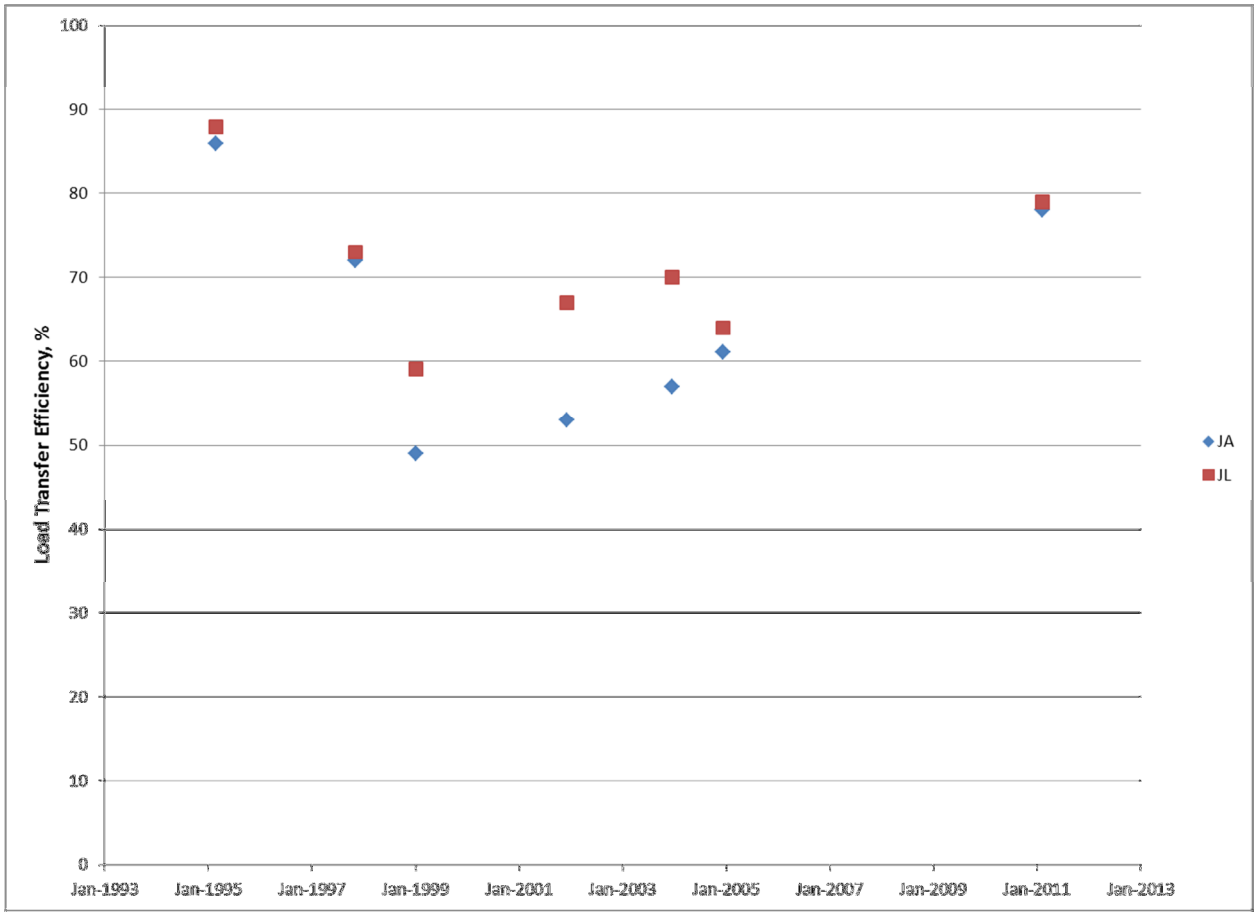

Figure 32. Section 040220 Load Transfer Efficiency vs. Date

Basin Data

Figure 33 presents E_{pcc} data versus date. The AASHTO 1993 procedure, using the correction factors developed for the SMP section, was used for the first data point because the FWD did not have a sensor at 8 inches at that time. Backcalculation was performed using MODCOMP for selected dates, using the layer model shown in Table 17. The backcalculated results for the December 2004 data exhibit an excessive RMSE of 7.9 percent; the remaining results all have RMSEs of less than 5 percent. The high RMSE indicates that the pavement is not behaving in a manner consistent with layered-elastic theory.

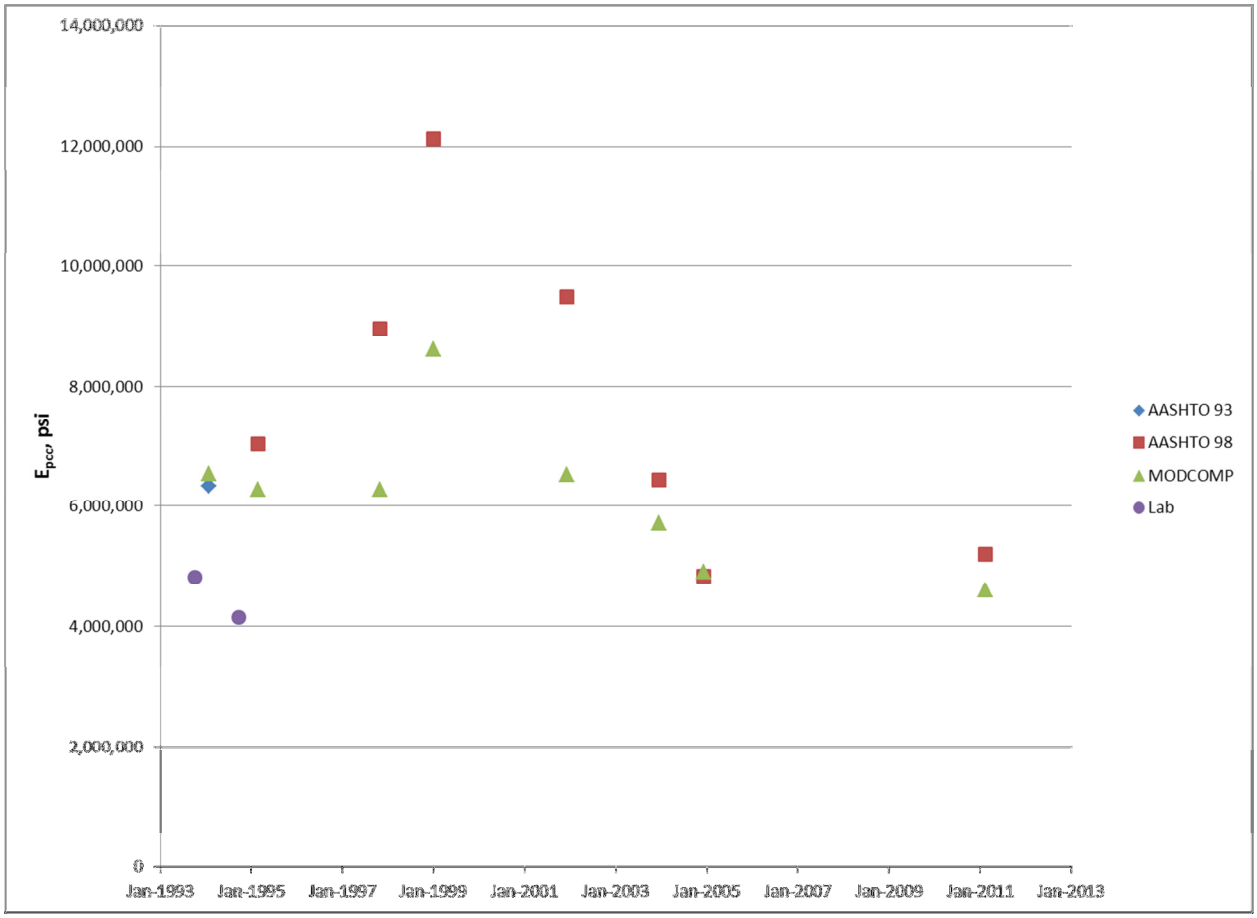

Figure 33. Section 040220 E_{pcc} vs. Date

Table 17. Section 040220 Layer Model

Layer	Layer Type	Seed Modulus (ksi)	Poisson's Ratio	Thickness (inches)
1	PCC	4000	0.15	11.2
2	LCB	500	0.20	6.2
3	Subgrade	30	0.45	

Figure 34 shows k-values versus date. The backcalculated k-values are significantly higher than the AASHTO 1998 k-values. The backcalculated results show a period of low k-value during 2004 to 2005. This trend is noticeable but much diminished in the AASHTO 1998 data.

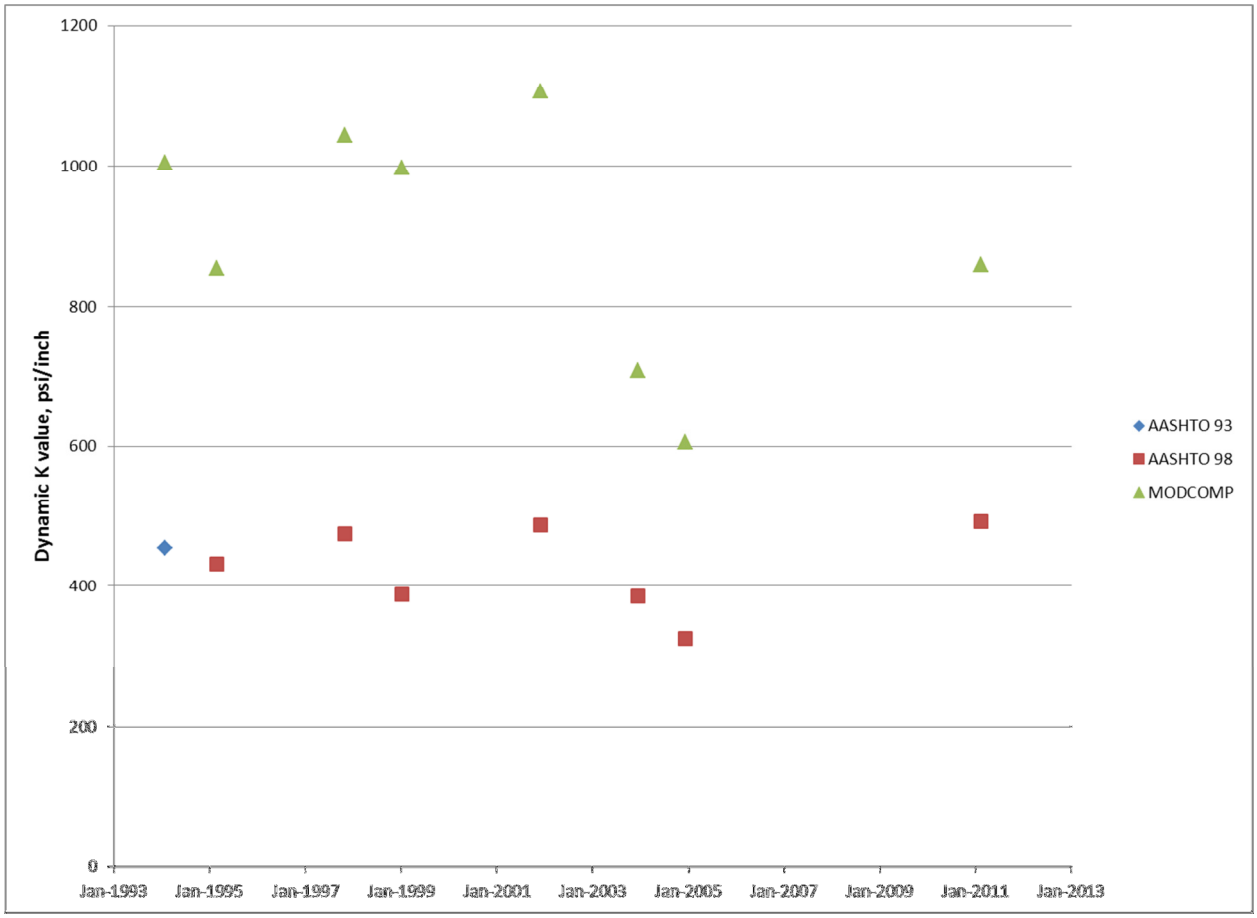

Figure 34. Section 040220 K-Values vs. Date

Section 040221

Section 040221 is in the thin, wide, low-strength PATB cell of the experimental matrix.

LTE Data

Figure 35 shows LTE data versus date. All testing was performed in the winter, with dates ranging from November 6 to February 15. Slab mid-depth temperatures ranged from 49˚ F to 80˚ F, with an average temperature of 62˚ F. No gradient of LTE with temperature was observed; a regression of LTE versus mid-slab temperature had a slope of 0.53 percent/˚F and an R^2 of 0.17. The data shows a consistent decline in LTE over time, with JL higher than JA except for the first test instance.

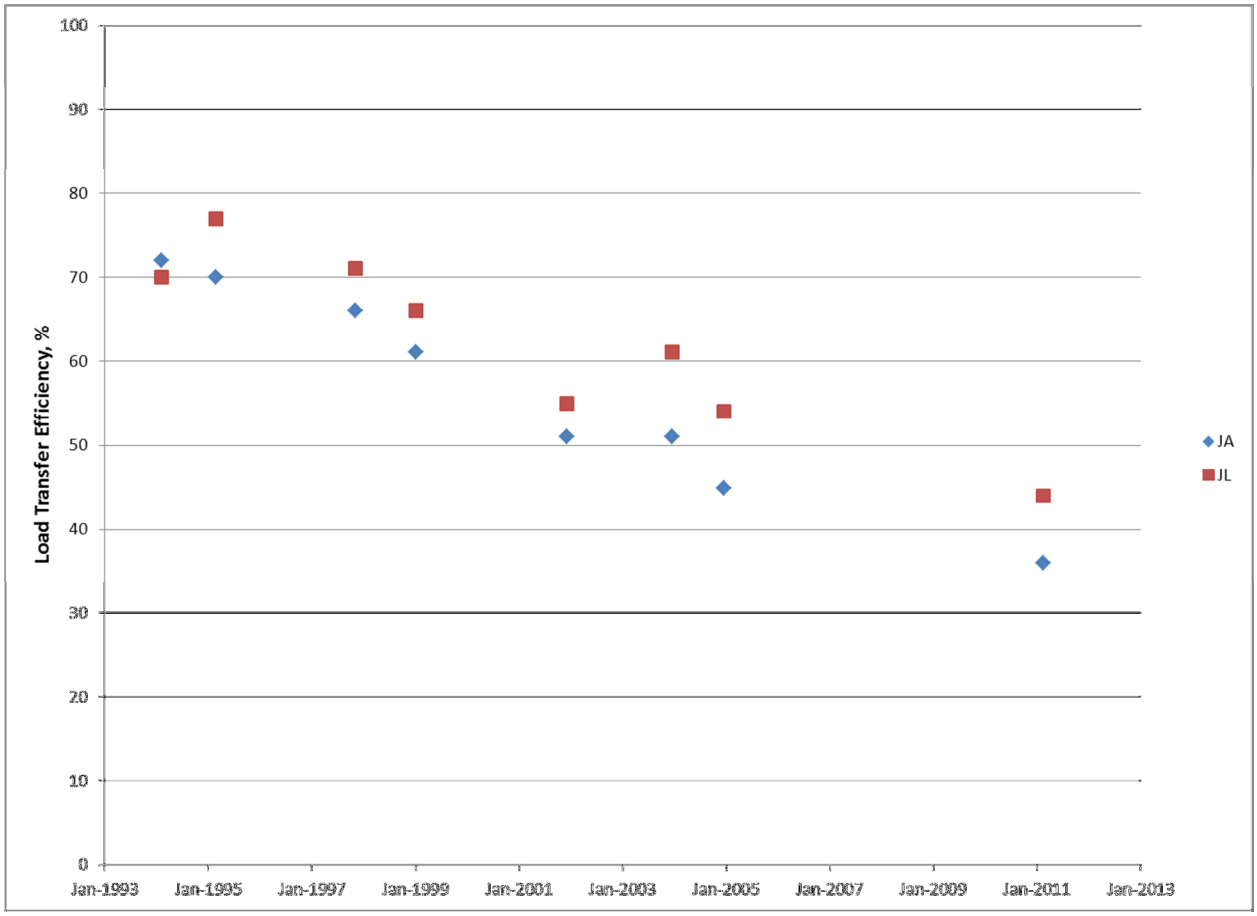

Figure 35. Section 040221 Load Transfer Efficiency vs. Date

Basin Data

Figure 36 presents E_{pcc} data versus date. The AASHTO 1993 procedure, using the correction factors developed for the SMP section, was used for the first data point because the FWD did not have a sensor at 8 inches at that time. Backcalculation was performed using MODCOMP for selected dates, using the layer model shown in Table 18 The AASHTO 1998 and backcalculated data is well-correlated, although the AASHTO 1998 results are significantly higher.

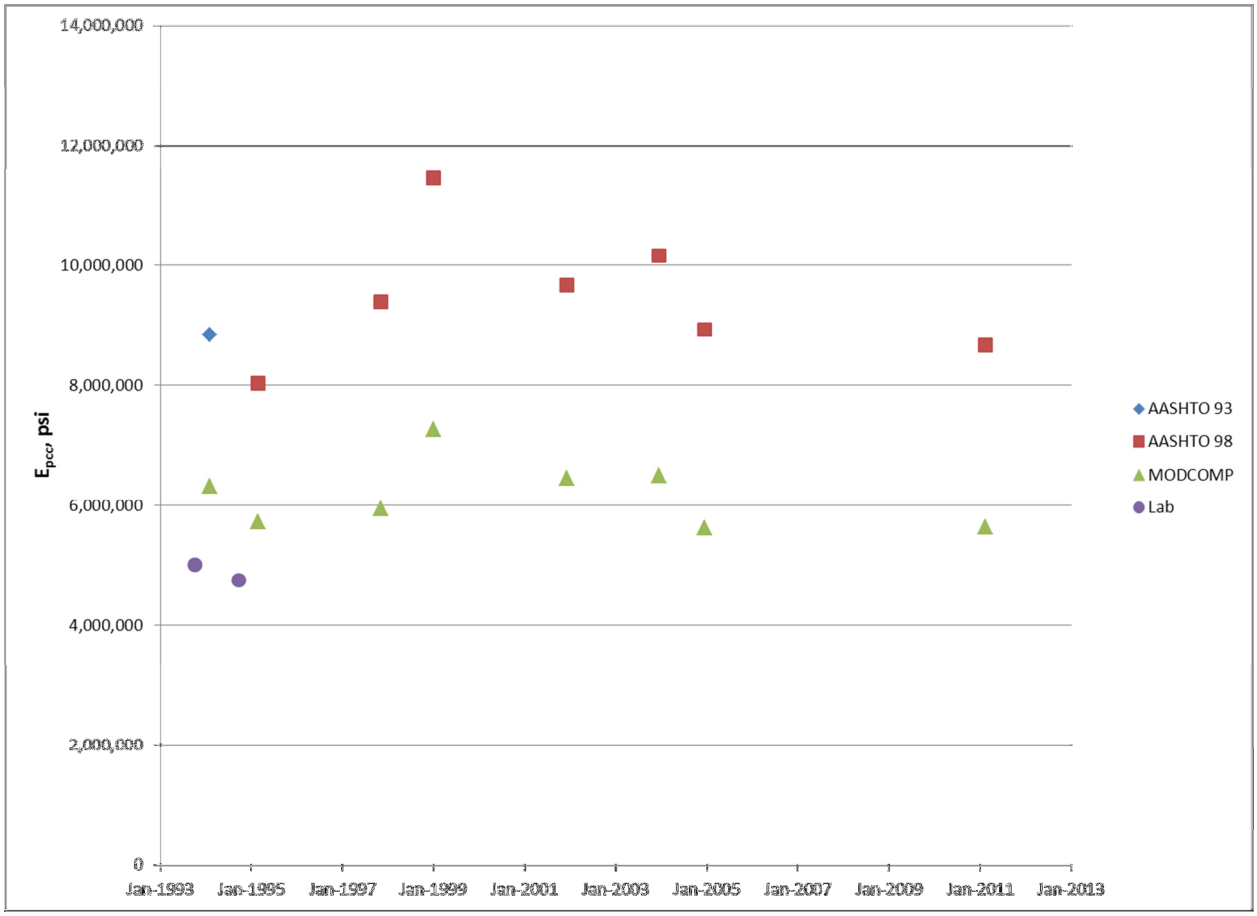

Figure 36. Section 040221 E_{pcc} vs. Date

Table 18. Section 040221 Layer Model

Layer	Layer Type	Seed Modulus (ksi)	Poisson's Ratio	Thickness (inches)
1	PCC	4000	0.15	8.1
2	PATB	100	0.35	4.2
3	Subgrade	30	0.45	

Figure 37 shows k-values versus date. As with the E_{pcc} data, the backcalculated and AASHTO 1998 data are well-correlated, although in this case, the backcalculated data is significantly higher.

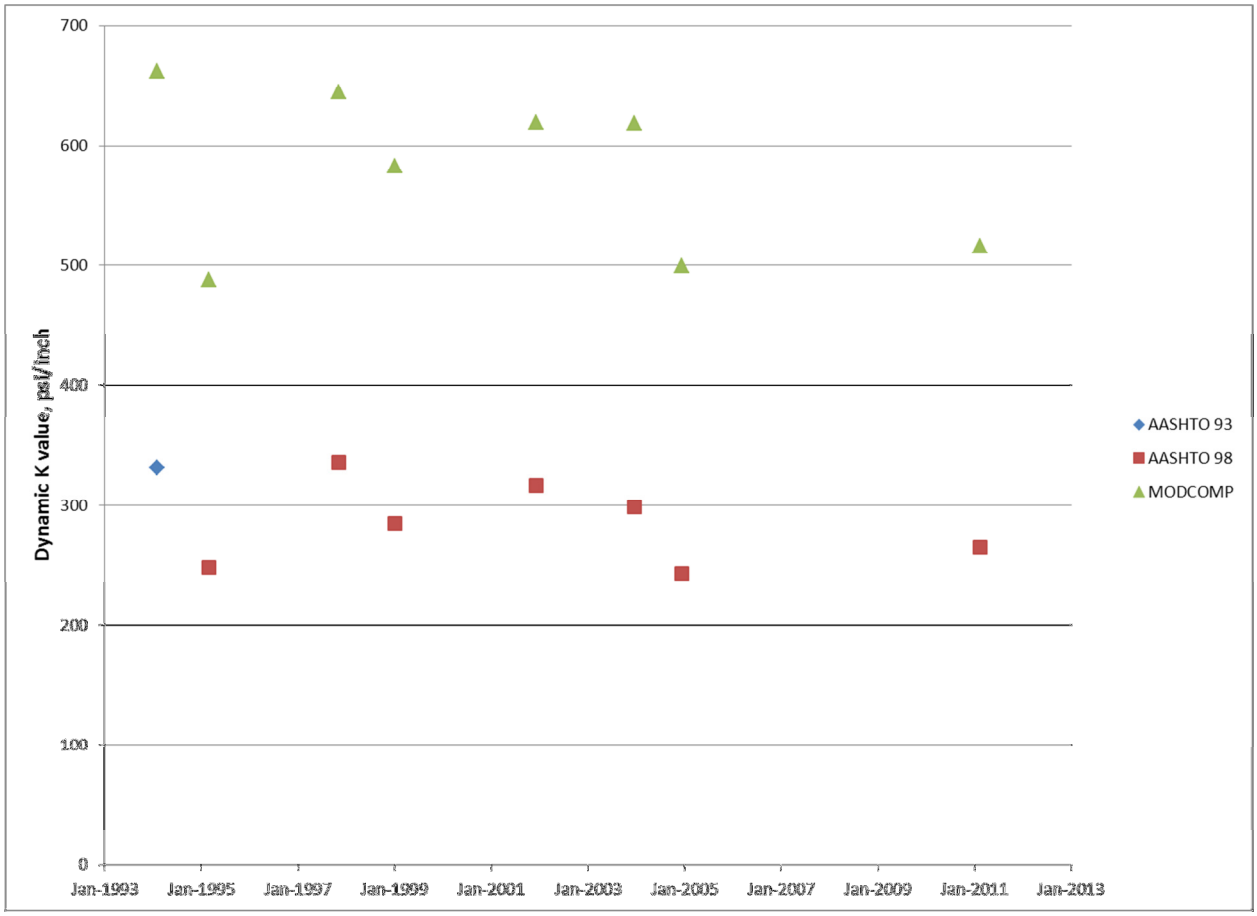

Figure 37. Section 040221 K-Values vs. Date

Section 040222

Section 040222 is in the thin, narrow, high-strength PATB cell of the experimental matrix.

LTE Data

Figure 38 shows LTE data versus date. All testing was performed in the winter, with dates ranging from November 3 to February 27. Slab mid-depth temperatures ranged from 55˚ F to 83˚ F with an average temperature of 66˚ F. A moderate gradient of LTE with temperature was observed; a regression of LTE versus mid-slab temperature had a slope of 1.14 percent/˚F and an R^2 of 0.63. The data shows a consistent decline in LTE over time, with JL higher than JA except for the first test time. As mid-slab temperatures also decrease with increasing date for this section, it is possible that the apparent temperature dependency for this section is an artifact.

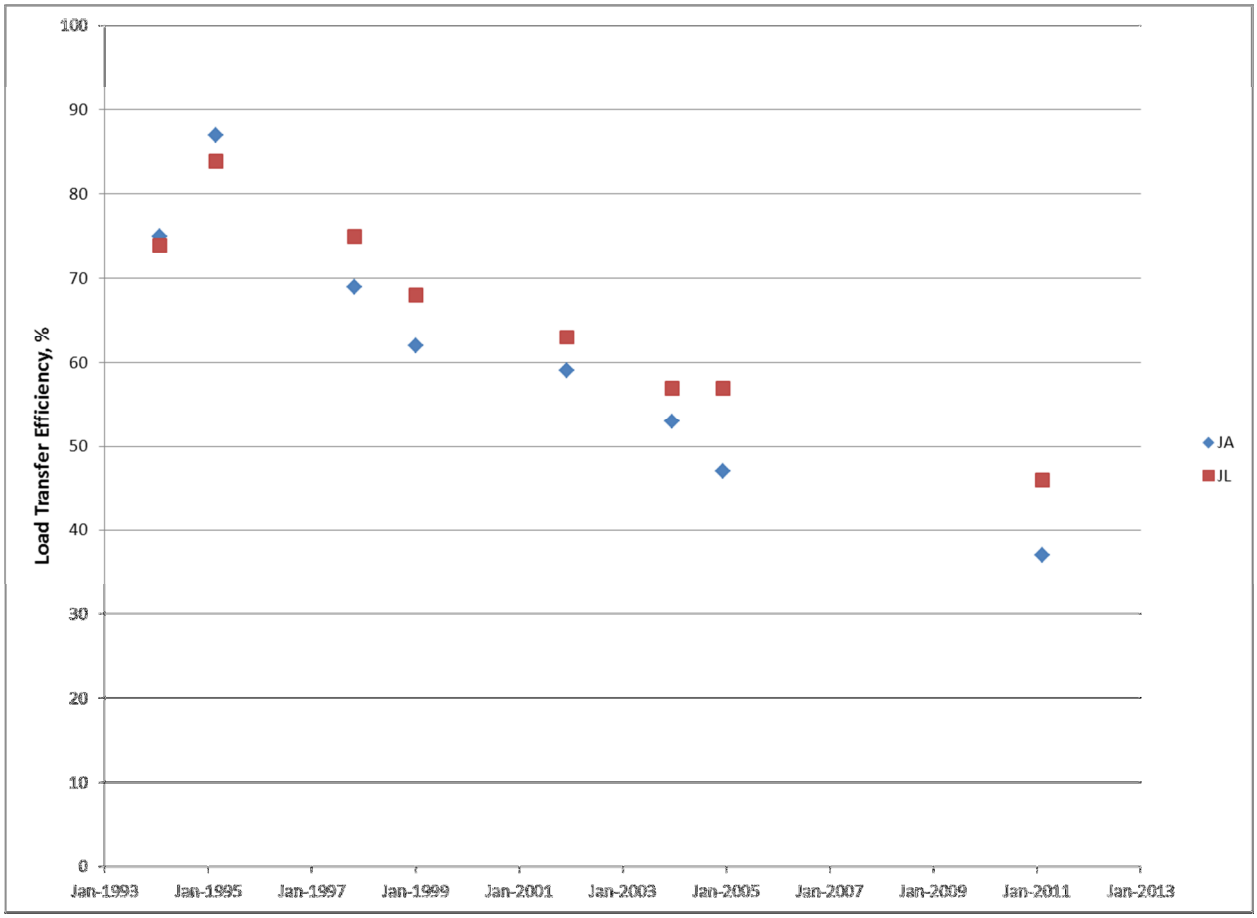

Figure 38. Section 040222 Load Transfer Efficiency vs. Date

Basin Data

Figure 39 presents E_{pcc} data versus date. The AASHTO 1993 procedure, using the correction factors developed for the SMP section, was used for the first data point because the FWD did not have a sensor at 8 inches at that time. No laboratory static modulus data is available for this section. Backcalculation was performed using MODCOMP for selected dates, using the layer model shown in Table 19. The AASHTO 1998 data shows high values of E_{pcc} during the 1998 to 2004 period, whereas the backcalculated results are more stable over time.

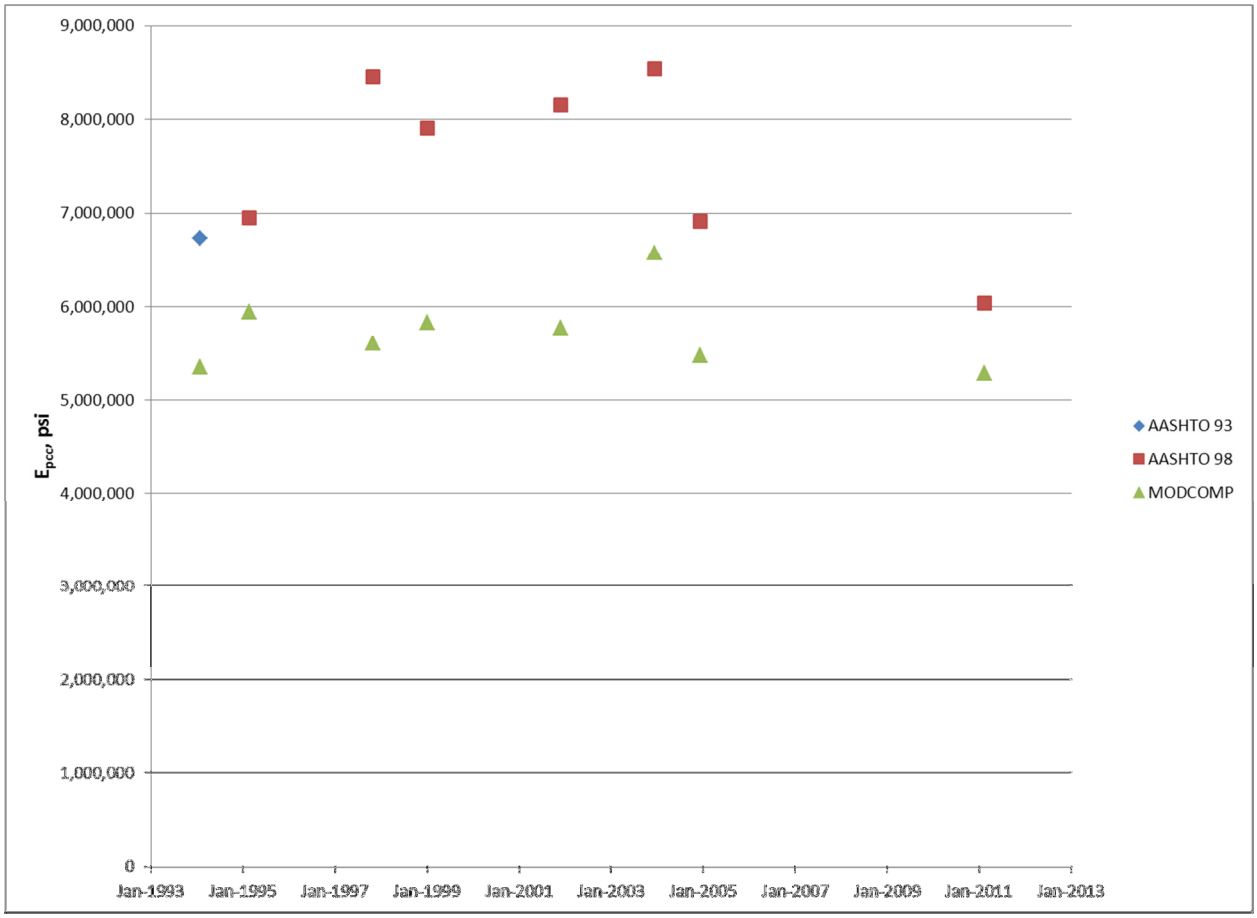

Figure 39. Section 040222 E_{pcc} vs. Date

Table 19. Section 040222 Layer Model

Layer	Layer Type	Seed Modulus (ksi)	Poisson's Ratio	Thickness (inches)
1	PCC	4000	0.15	8.6
2	PATB	100	0.35	3.9
3	Subgrade	30	0.45	

Figure 40 shows k-values versus date. Both the AASHTO 1998 and the backcalculated k-values are well correlated, although the backcalculated values are significantly higher. Both data sets show a slight trend of decreasing k-value over time.

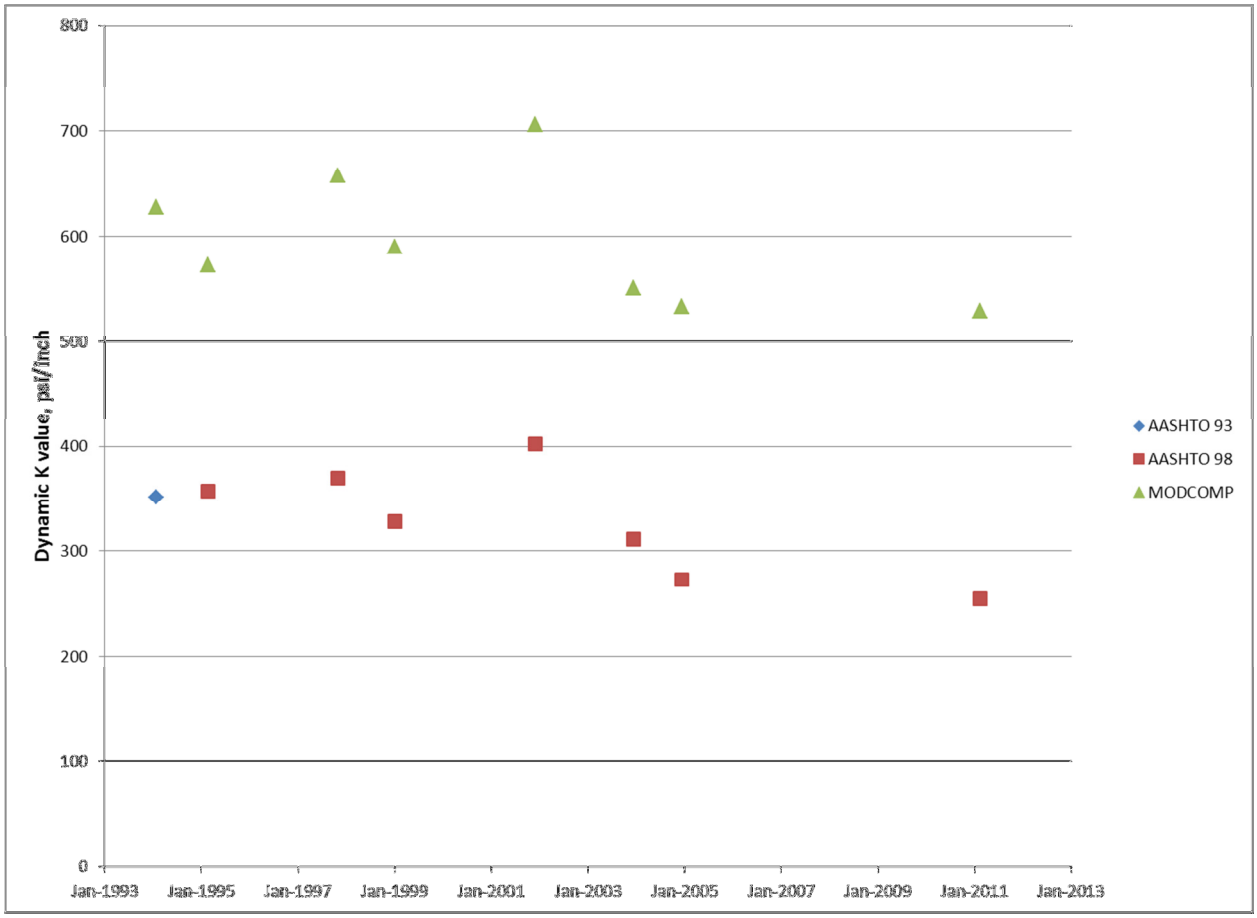

Figure 40. Section 040222 K-Values vs. Date

Section 040223

Section 040223 is in the thick, narrow, low-strength PATB cell of the experimental matrix.

LTE Data

Figure 41 shows LTE data versus date. All testing was performed in the winter, with dates ranging from November 3 to February 27. Slab mid-depth temperatures ranged from 52˚ F to 79˚ F, with an average temperature of 63˚ F. No gradient of LTE with temperature was observed; a regression of LTE versus mid-slab temperature had a slope of 0.02 percent/˚F and an R^2 of 0.01.

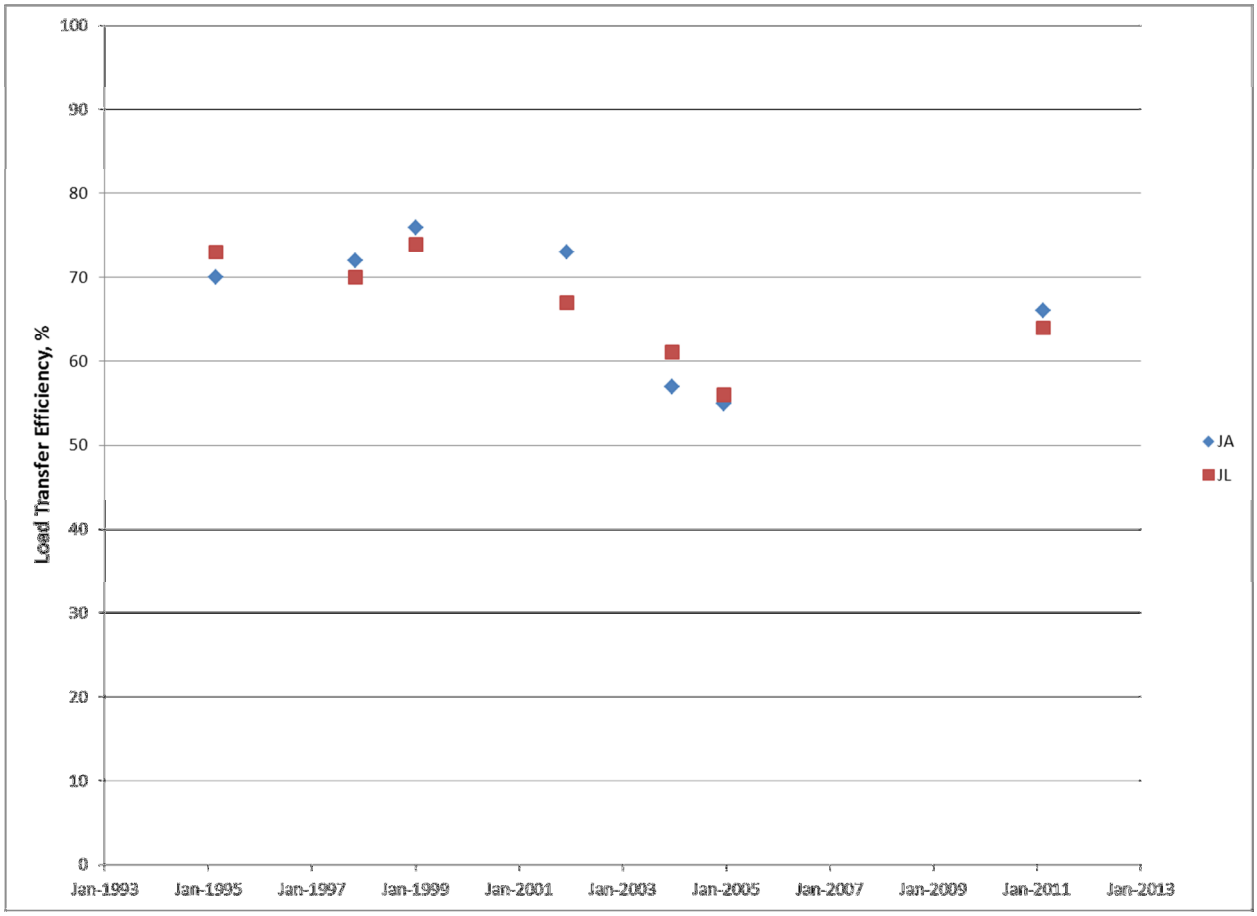

Figure 41. Section 040223 Load Transfer Efficiency vs. Date

Basin Data

Figure 42 presents E_{pcc} data versus date. The AASHTO 1993 procedure, using the correction factors developed for the SMP section, was used for the first data point because the FWD did not have a sensor at 8 inches at that time. Backcalculation was performed using MODCOMP for selected dates, using the layer model shown in Table 20. Both the backcalculated and AASHTO 1998 results show a decrease in E_{pcc} in 1997, although this decrease is exaggerated in the AASHTO 1998 data set.

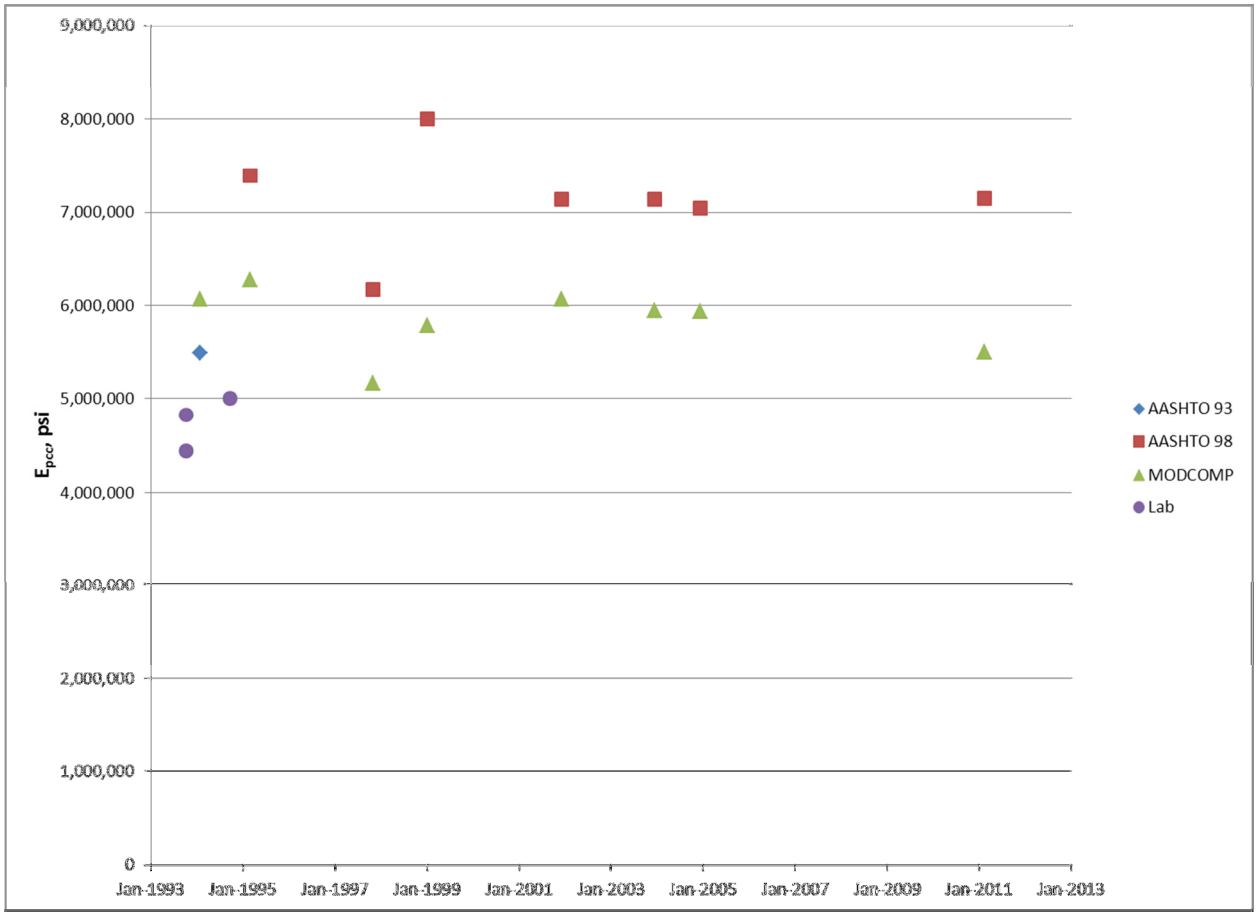

Figure 42. Section 040223 E_{pcc} vs. Date

Table 20. Section 040223 Layer Model

Layer	Layer Type	Seed Modulus (ksi)	Poisson's Ratio	Thickness (inches)
1	PCC	4000	0.15	11.1
2	PATB	100	0.35	4.1
3	Subgrade	30	0.45	

Figure 43 shows k-values versus date. The backcalculated results are significantly higher than the AASHTO 1998 results. Excepting the final test in 2011, the backcalculated results show a gradual trend of decreasing k-value over time.

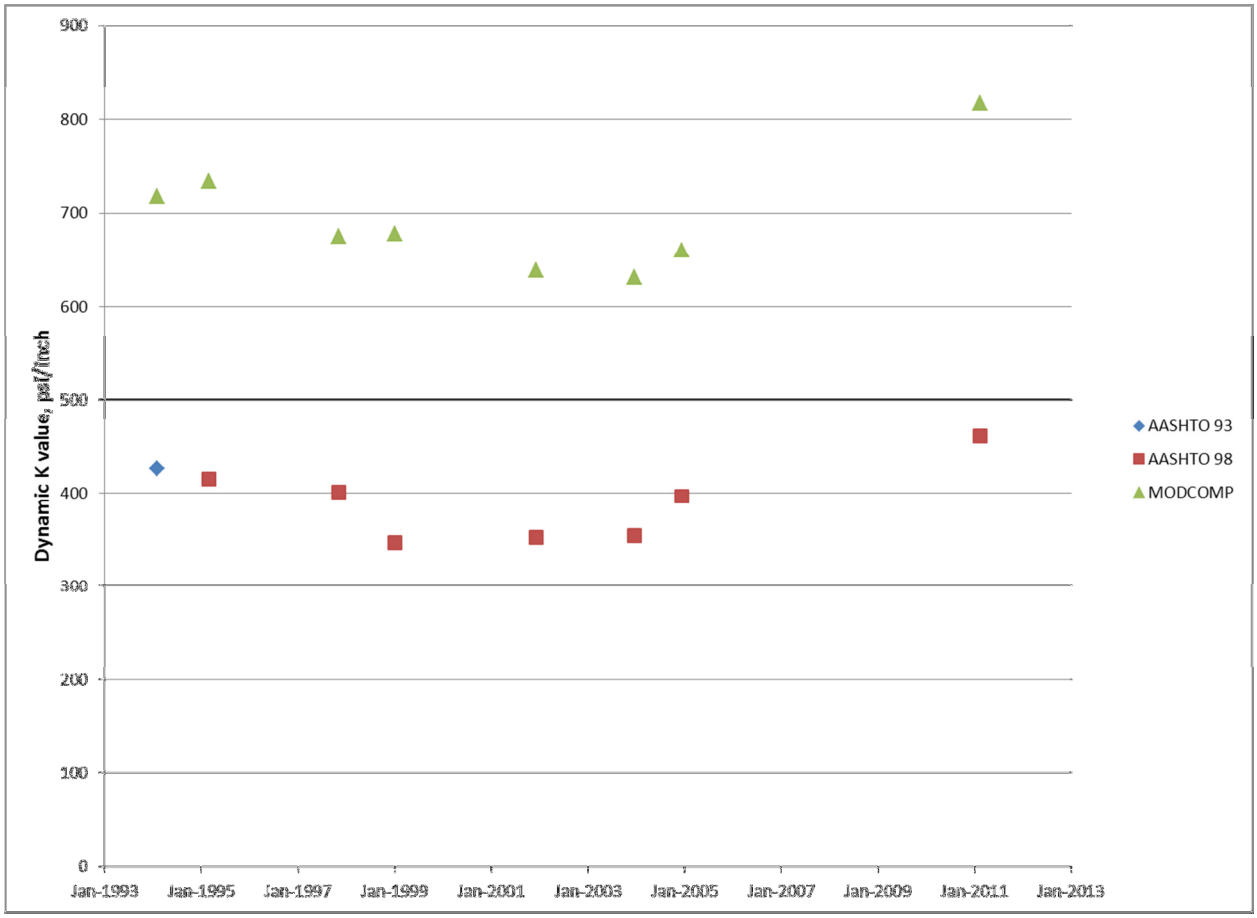

Figure 43. Section 040223 K-Values vs. Date

Section 040224

Section 040224 is in the thick, wide, high-strength PATB cell of the experimental matrix.

LTE Data

Figure 44 shows LTE data versus date. All testing was performed in the winter, with dates ranging from November 4 to March 1. Slab mid-depth temperatures ranged from 52˚ F to 79˚ F, with an average temperature of 63˚ F. No gradient of LTE with temperature was observed; a regression of LTE versus mid-slab temperature had a slope of 0.21 percent/˚F and an R^2 of 0.08.

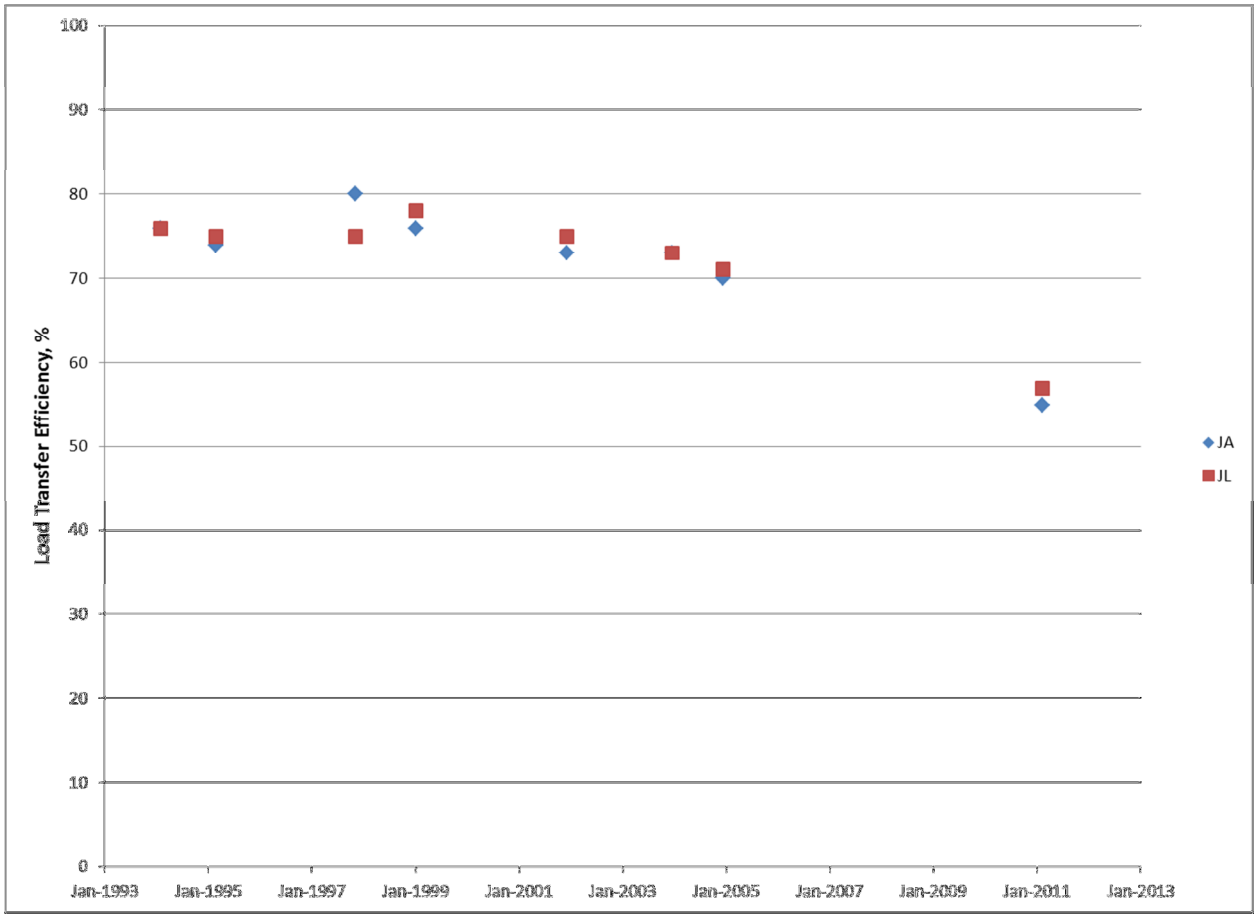

Figure 44. Section 040224 Load Transfer Efficiency vs. Date

Basin Data

Figure 45 presents E_{pcc} data versus date. The AASHTO 1993 procedure, using the correction factors developed for the SMP section, was used for the first data point because the FWD did not have a sensor at 8 inches at that time. Backcalculation was performed using MODCOMP for selected dates, using the layer model shown in Table 21. Both the backcalculated and AASHTO 1998 results show a gradual trend of decreasing E_{pcc} over time, with an outlier in 2004. This increase in E_{pcc} in 2004 is exaggerated in the AASHTO 1998 data.

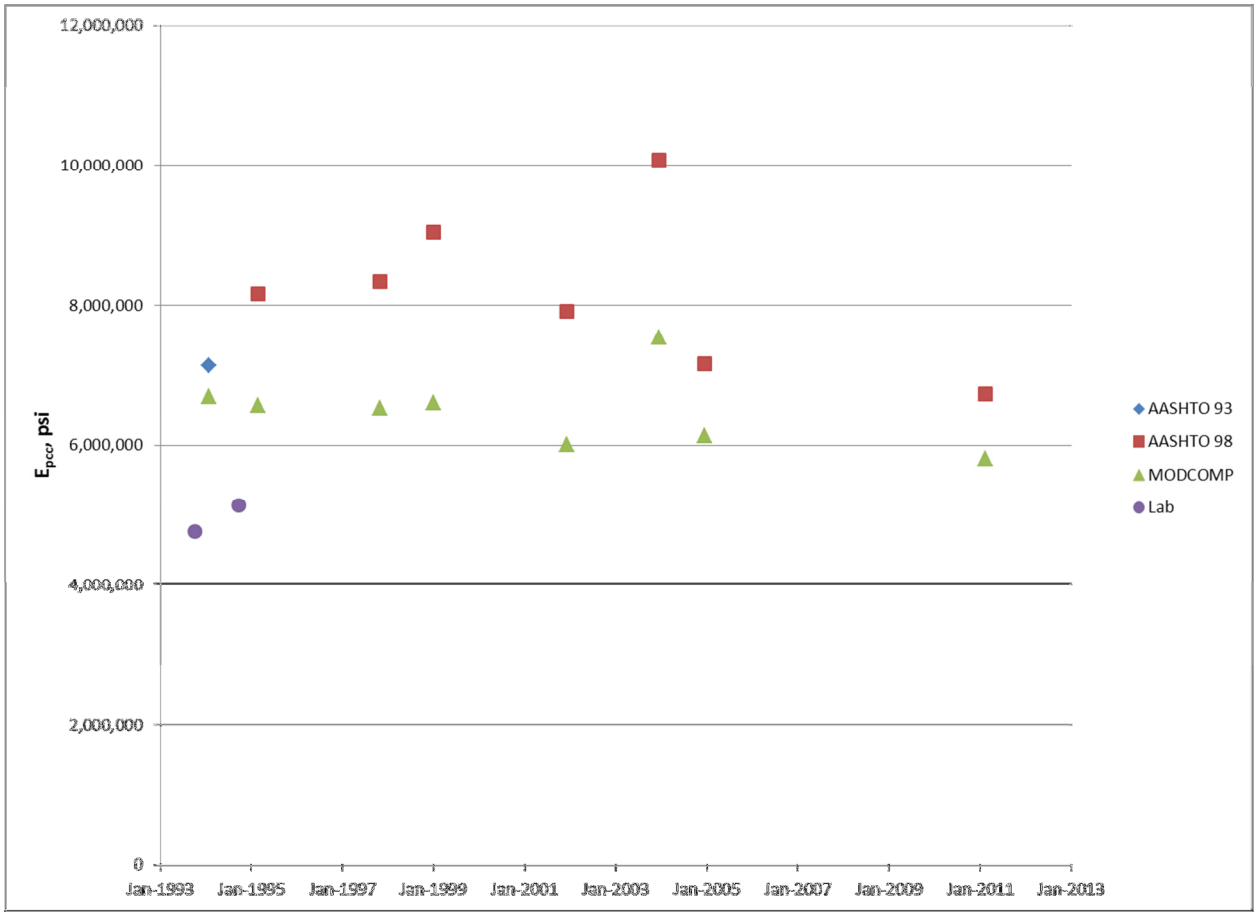

Figure 45. Section 040224 E_{pcc} vs. Date

Table 21. Section 040224 Layer Model

Layer	Layer Type	Seed Modulus (ksi)	Poisson's Ratio	Thickness (inches)
1	PCC	4000	0.15	10.6
2	PATB	100	0.35	4.4
3	Subgrade	30	0.45	

Figure 46 shows k-values versus date. The backcalculated k-values are significantly higher than the AASHTO 1998 k-values. Both result sets show a trend of decreasing k-value over time, although this trend is stronger in the backcalculated results.

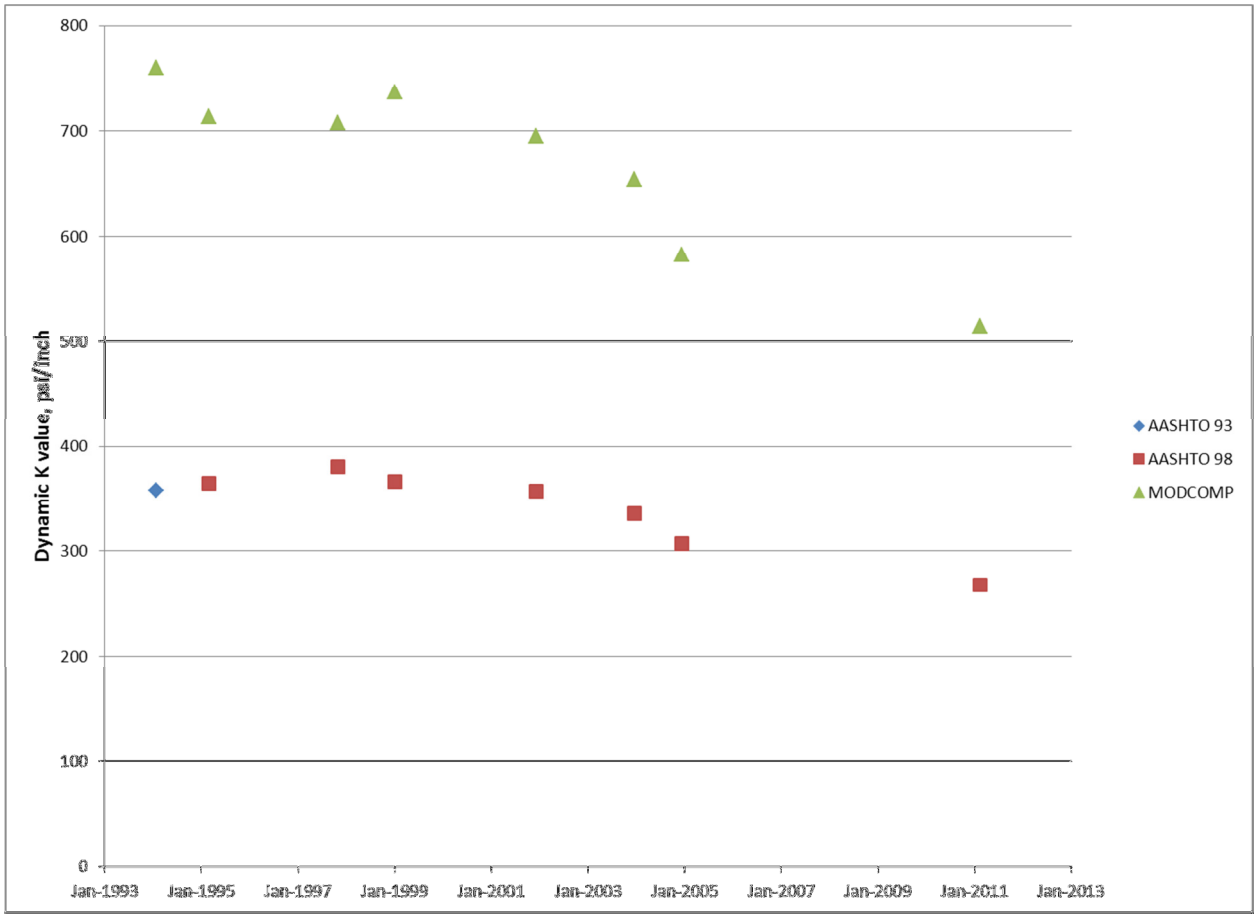

Figure 46. Section 040224 K-Values vs. Date

Section 040262

Section 040262 is a supplemental section built with undoweled skew joints and a thin, wide, low-strength slab on DGAB.

LTE Data

Figure 47 shows LTE data versus date. All testing was performed in the winter, with dates ranging from November 7 to February 16. Slab mid-depth temperatures ranged from 62˚ F to 73˚ F, with an average temperature of 68˚ F. No gradient of LTE with temperature was observed; a regression of LTE versus mid-slab temperature had a slope of 1.4 percent/˚F and an R^2 of 0.08. Any potential temperature effect would be masked by the limited range of test temperatures. LTE is significantly higher for the JL than the JA test at all test dates except for the final date.

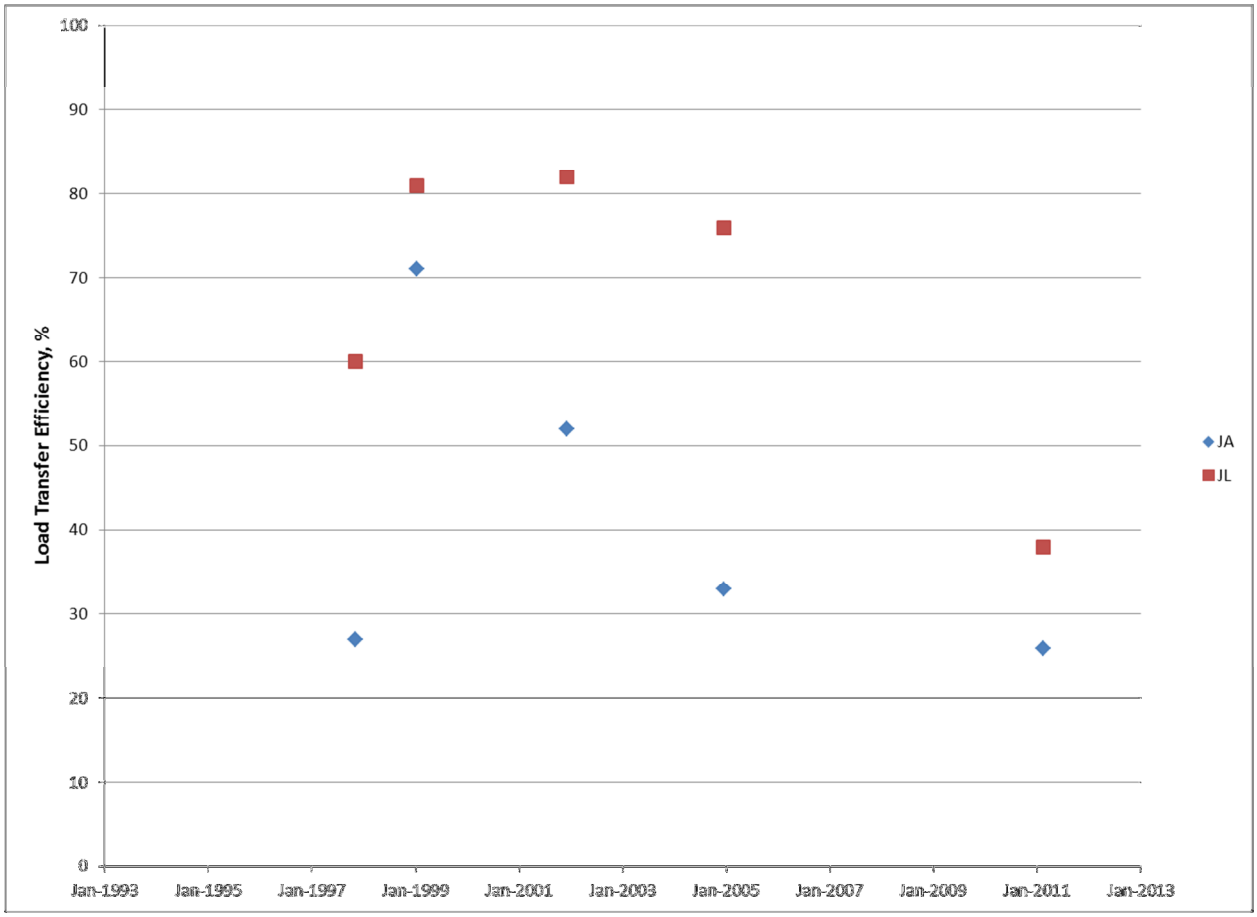

Figure 47. Section 040262 Load Transfer Efficiency vs. Date

Basin Data

Figure 48 presents E_{pcc} data versus date. The AASHTO 1993 procedure, using the correction factors developed for the SMP section, was used for the first data point because the FWD did not have a sensor at 8 inches at that time. Backcalculation was performed using MODCOMP for selected dates, using the layer model shown in Table 22. The backcalculated E_{pcc} values are consistent over time, with a possible slight decreasing trend. The AASHTO 1998 E_{pcc} values are significantly higher for the initial test but converge with the backcalculated values over time.

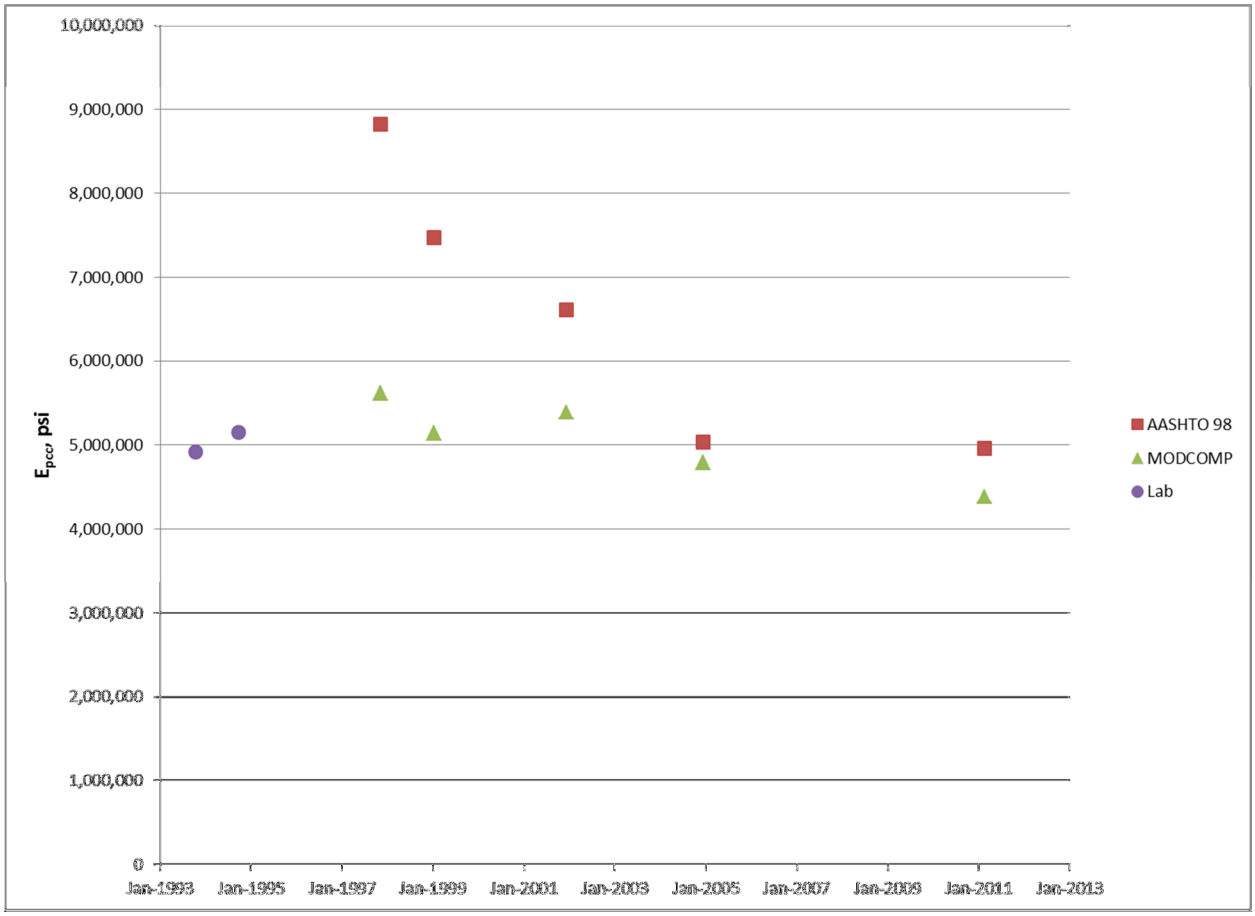

Figure 48. Section 040262 E_{pcc} vs. Date

Table 22. Section 040262 Layer Model

Layer	Layer Type	Seed Modulus (ksi)	Poisson's Ratio	Thickness (inches)
1	PCC	4000	0.15	8.1
2	DGAB	30	0.45	6.1
3	Subgrade	30	0.45	

Figure 49 shows k-values versus date. The backcalculated k-values are significantly higher than the AASHTO 1998 k-values. Both result sets show a trend of decreasing k-value over time, although this trend is stronger in the backcalculated results.

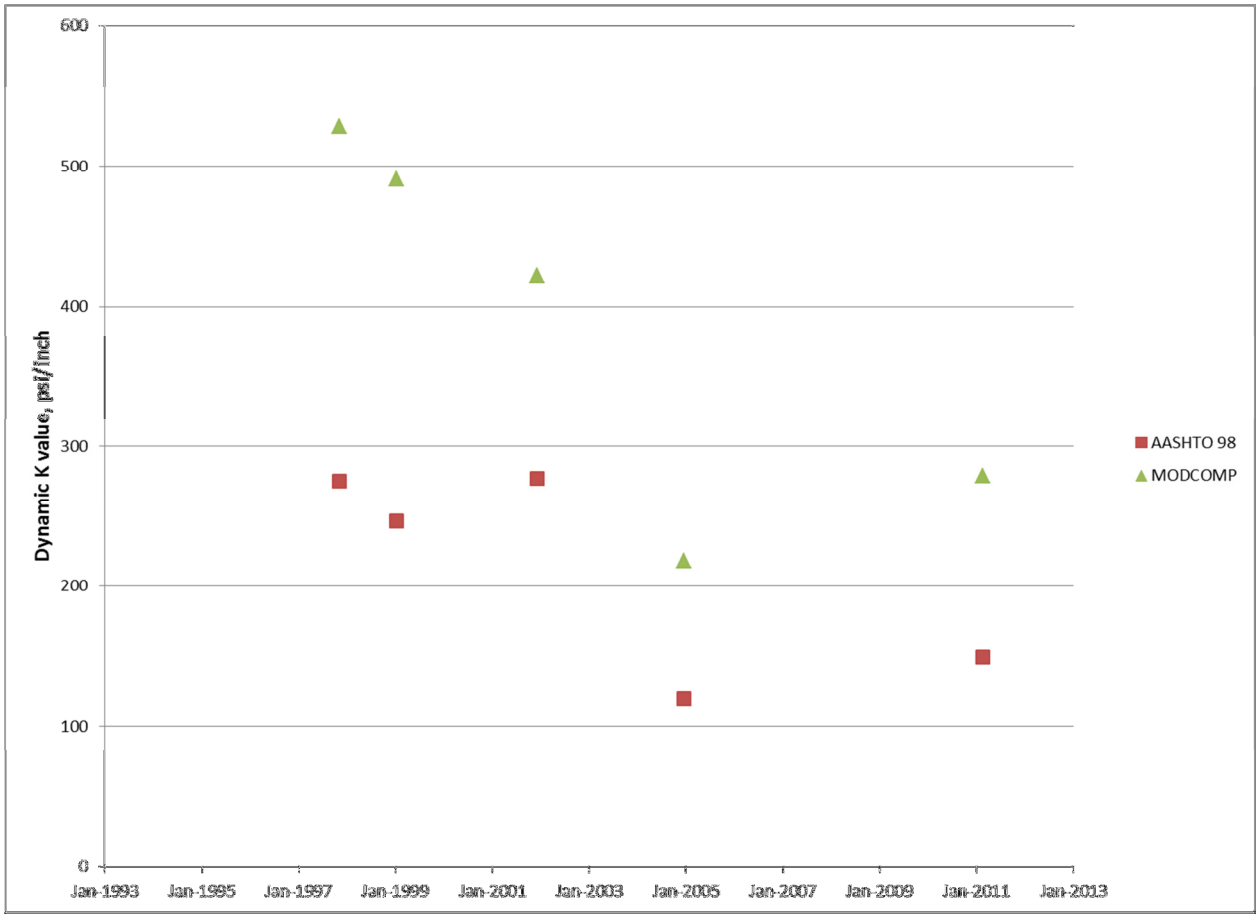

Figure 49. Section 040262 K-Values vs. Date

Section 040263

Section 040263 is a supplemental section built with undoweled skew joints and a thin, wide, low-strength slab on PATB.

LTE Data

Figure 50 shows LTE data versus date. All testing was performed in the winter, with dates ranging from November 7 to February 16. Slab mid-depth temperatures ranged from 58˚ F to 81˚ F with an average temperature of 71 ˚F. A slight gradient of LTE with temperature was observed; a regression of LTE versus mid-slab temperature had a slope of 0.23 percent/˚F and an R^2 of 0.61. LTE is similar and low for both the JL and JA test at all test dates.

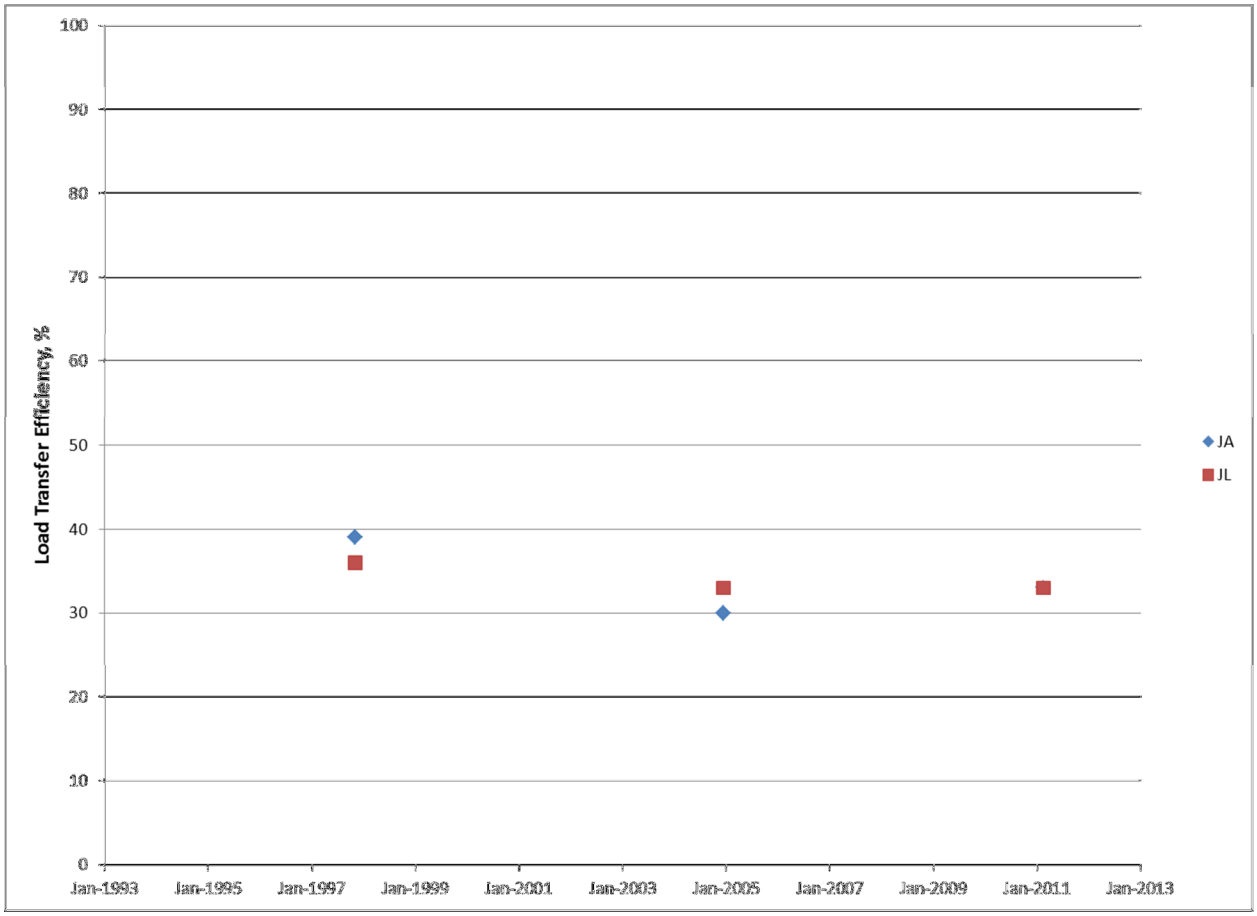

Figure 50. Section 040263 Load Transfer Efficiency vs. Date

Basin Data

Figure 51 presents E_{pcc} data versus date. Backcalculation was performed using MODCOMP, using the layer model shown in Table 23. The AASHTO 1998 E_{pcc} results are significantly higher than the backcalculated results, which show a decreasing trend in E_{pcc} between 2001 and 2011, although the data is sparse.

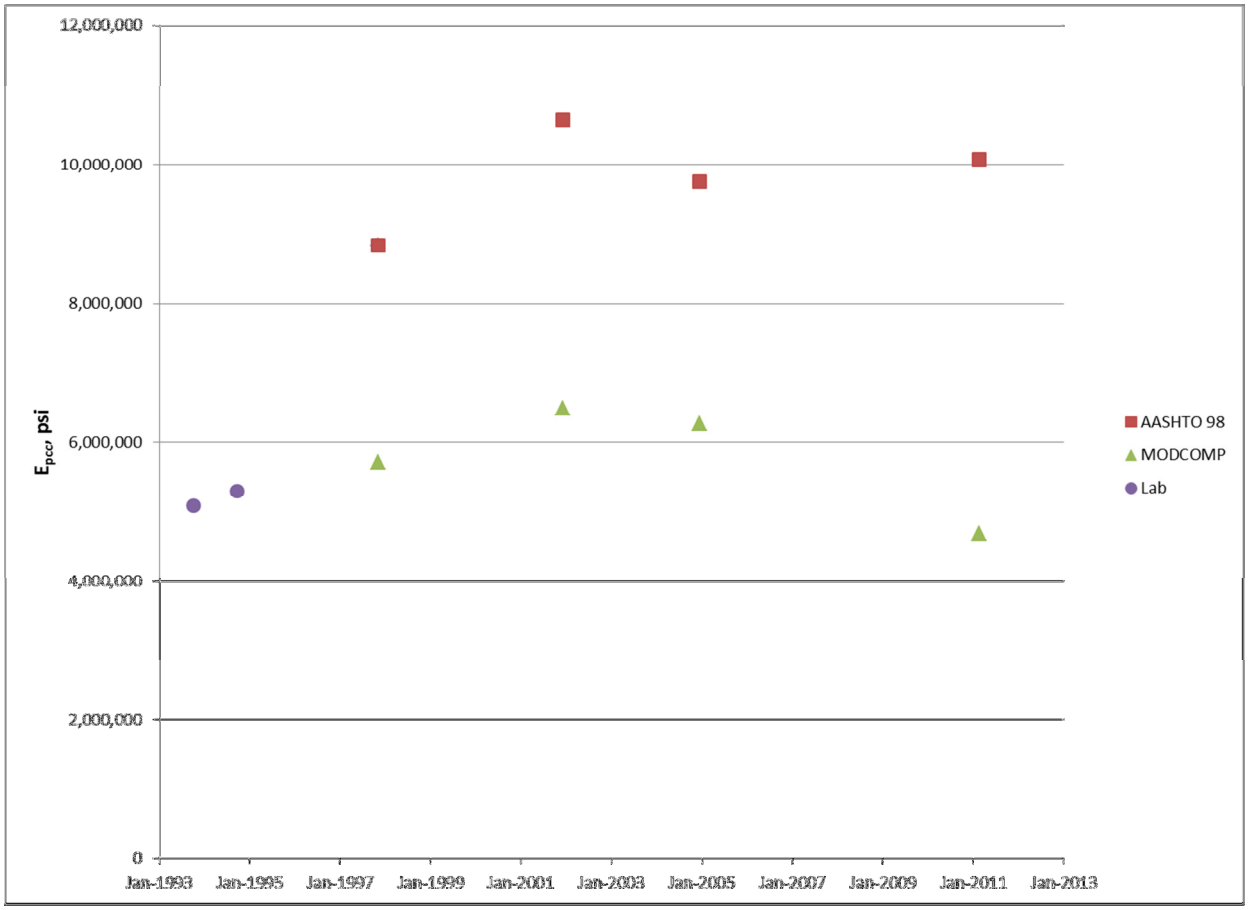

Figure 51. Section 040263 E_{pcc} vs. Date

Table 23. Section 040263 Layer Model

Layer	Layer Type	Seed Modulus (ksi)	Poisson's Ratio	Thickness (inches)
1	PCC	4000	0.15	8.2
2	PATB	100	0.35	4.4
3	Subgrade	30	0.45	

Figure 52 shows k-values versus date. The backcalculated results are significantly higher than the AASHTO 1998 results, which show a possible slight decrease in K value over time, possibly caused by a misassignment of the decreasing slab stiffness seen in the backcalculated results.

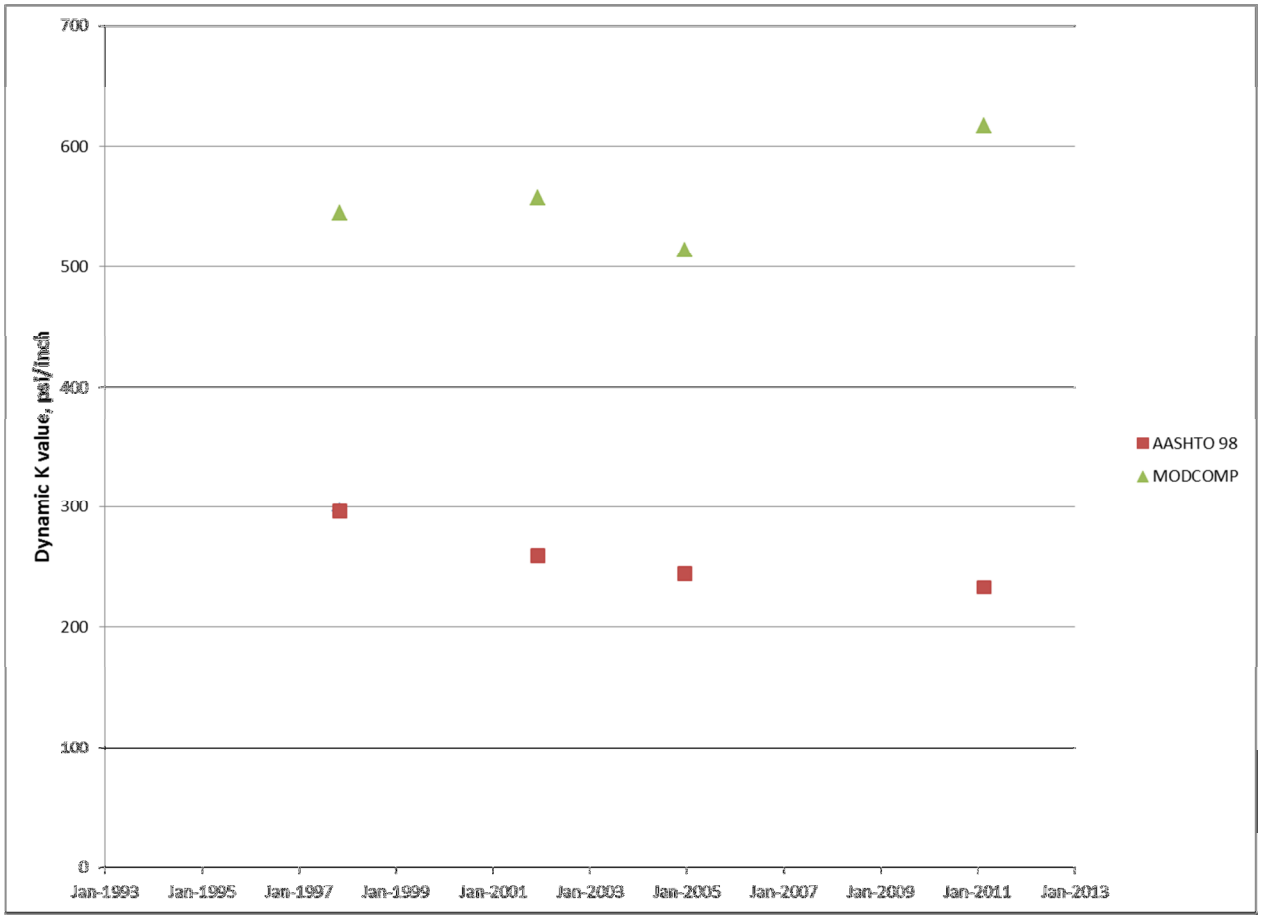

Figure 52. Section 040263 K-Values vs. Date

Section 040264

Section 040264 is a supplemental section built with undoweled skew joints and a thick, narrow, low-strength slab on PATB.

LTE Data

Figure 53. Section 040264 Load Transfer Efficiency vs. Date shows LTE data versus date. All testing was performed in the winter, with dates ranging from November 7 to February 16. Slab mid-depth temperatures ranged from 58˚ F to 68˚ F with an average temperature of 62˚ F. No gradient of LTE with temperature was observed; a regression of LTE versus mid-slab temperature had a slope of 2.3 percent/˚F and an R^2 of 0.15. LTE determined using the JL test data declines significantly over time. LTE determined using the JA test is consistently low.

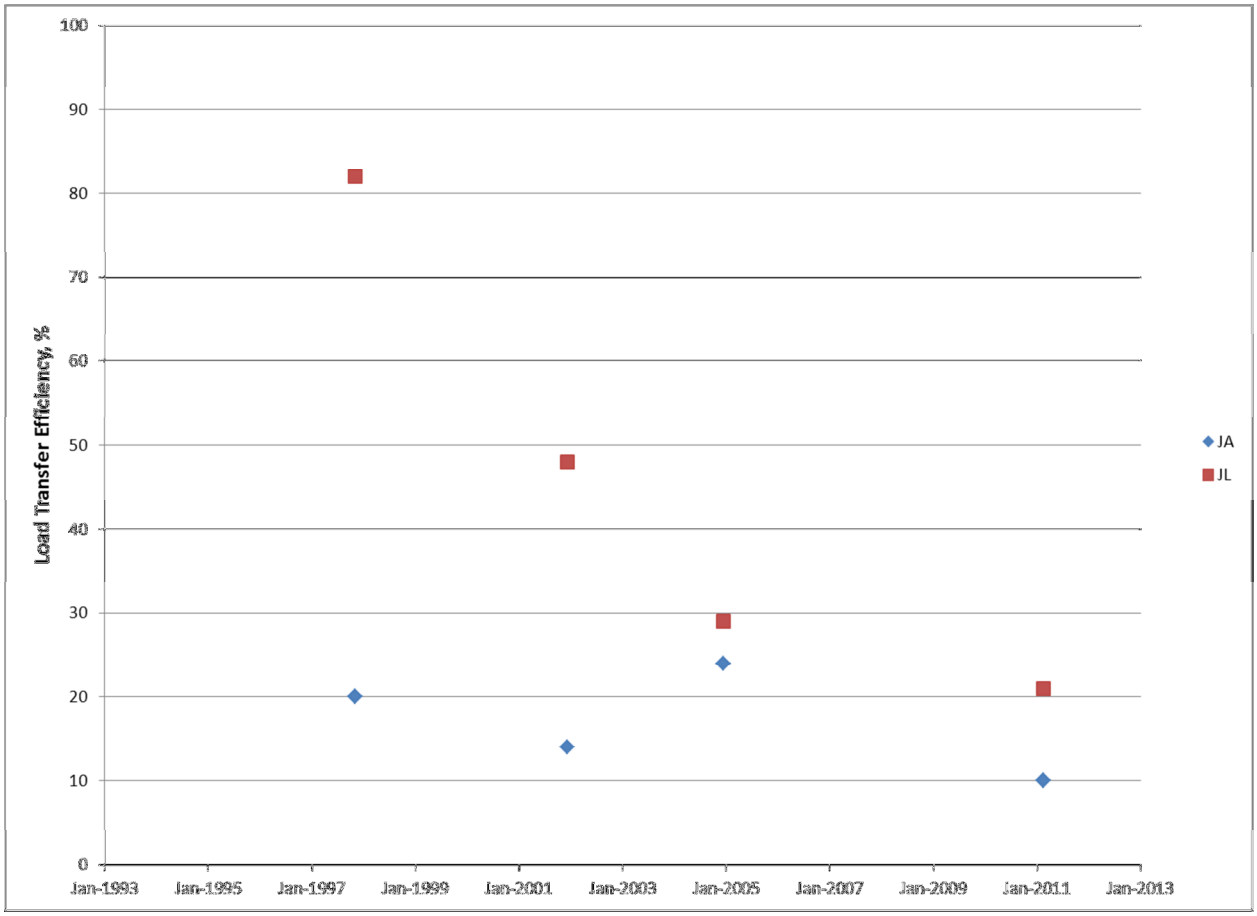

Figure 53. Section 040264 Load Transfer Efficiency vs. Date

Basin Data

Figure 54 presents E_{pcc} data versus date. Backcalculation was performed using MODCOMP, using the layer model shown in Table 24. All of the backcalculation results have RMSEs in excess of 8 percent, and therefore these results should not be considered reliable.

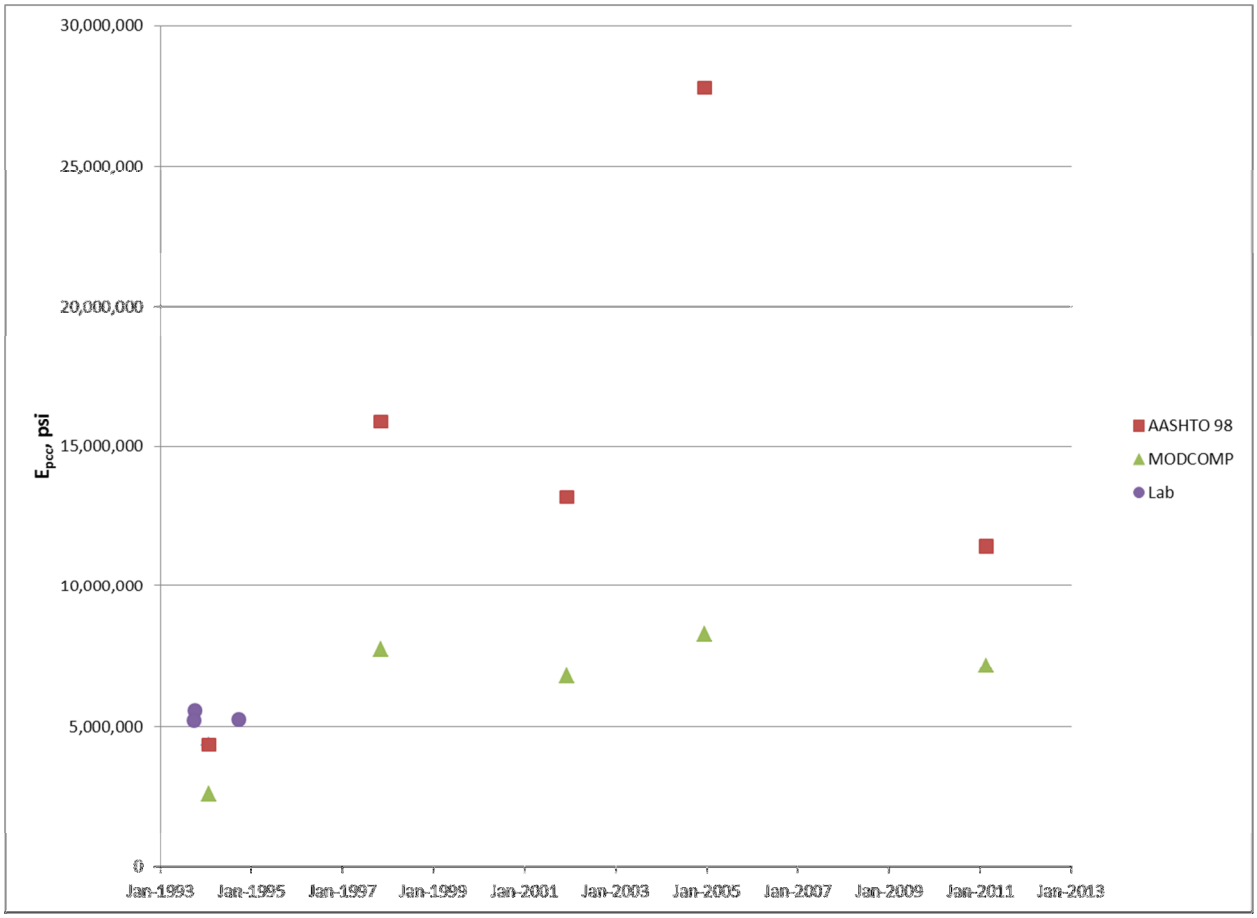

Figure 54. Section 040264 E_{pcc} vs. Date

Table 24. Section 040264 Layer Model

Layer	Layer Type	Seed Modulus (ksi)	Poisson's Ratio	Thickness (inches)
1	PCC	4000	0.15	11.5
2	PATB	100	0.35	3.8
3	Subgrade	30	0.45	

Figure 55 shows k-values versus date. Due to the high RMSEs, the backcalculated results should not be considered reliable. Both the backcalculated results and the AASHTO 1998 results show a k-value that decreases immediately after construction and then remains relatively constant.

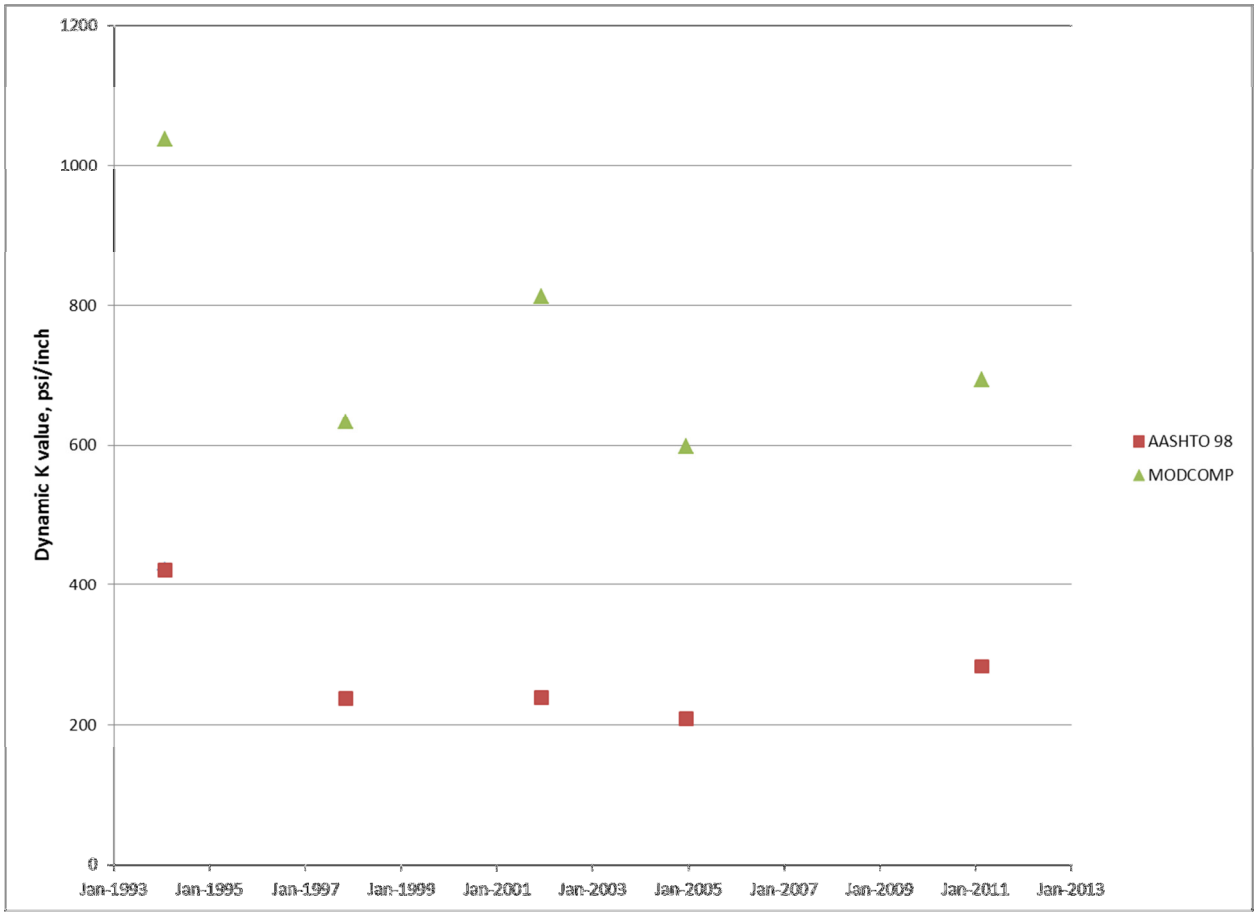

Figure 55. Section 040264 K-Values vs. Date

Section 040265

Section 040265 is a supplemental section built with undoweled skew joints and a thick, narrow, low-strength slab on DGAB.

LTE Data

Figure 56 shows LTE data versus date. All testing was performed in the winter, with dates ranging from November 6 to February 17. Slab mid-depth temperatures ranged from 57˚ F to 78˚ F with an average temperature of 67˚ F. A gradient of LTE with temperature was observed; a regression of LTE versus mid-slab temperature had a slope of 1.9 percent/˚F and an R^2 of 0.52. LTE determined using the JL test data declines significantly over time. LTE determined using the JA test is significantly lower than JL for the first three test dates, but converge at the last test date data point.

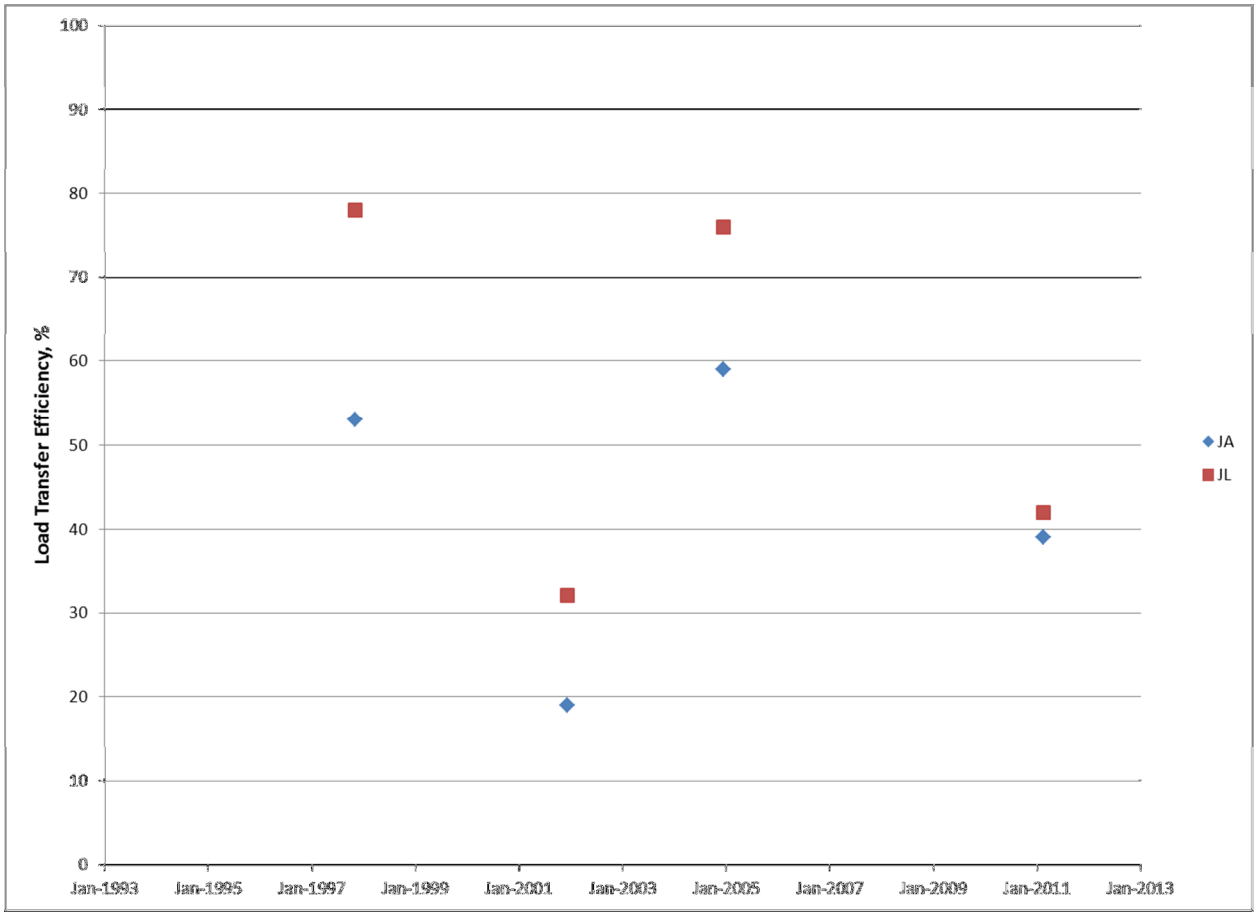

Figure 56. Section 040265 Load Transfer Efficiency vs. Date

Basin Data

Figure 57 presents E_{pcc} data versus date. Backcalculation was performed using MODCOMP, using the layer model shown in Table 25**Error! Reference source not found.**. The backcalculated results for the first test date (February 3, 1994) include an abnormally low modulus value for the PCC layer and a high modulus value for the DGAB layer, and should not be considered reliable. After the initial test, both sets of results show similar E_{pcc} values, which decline gradually over time.

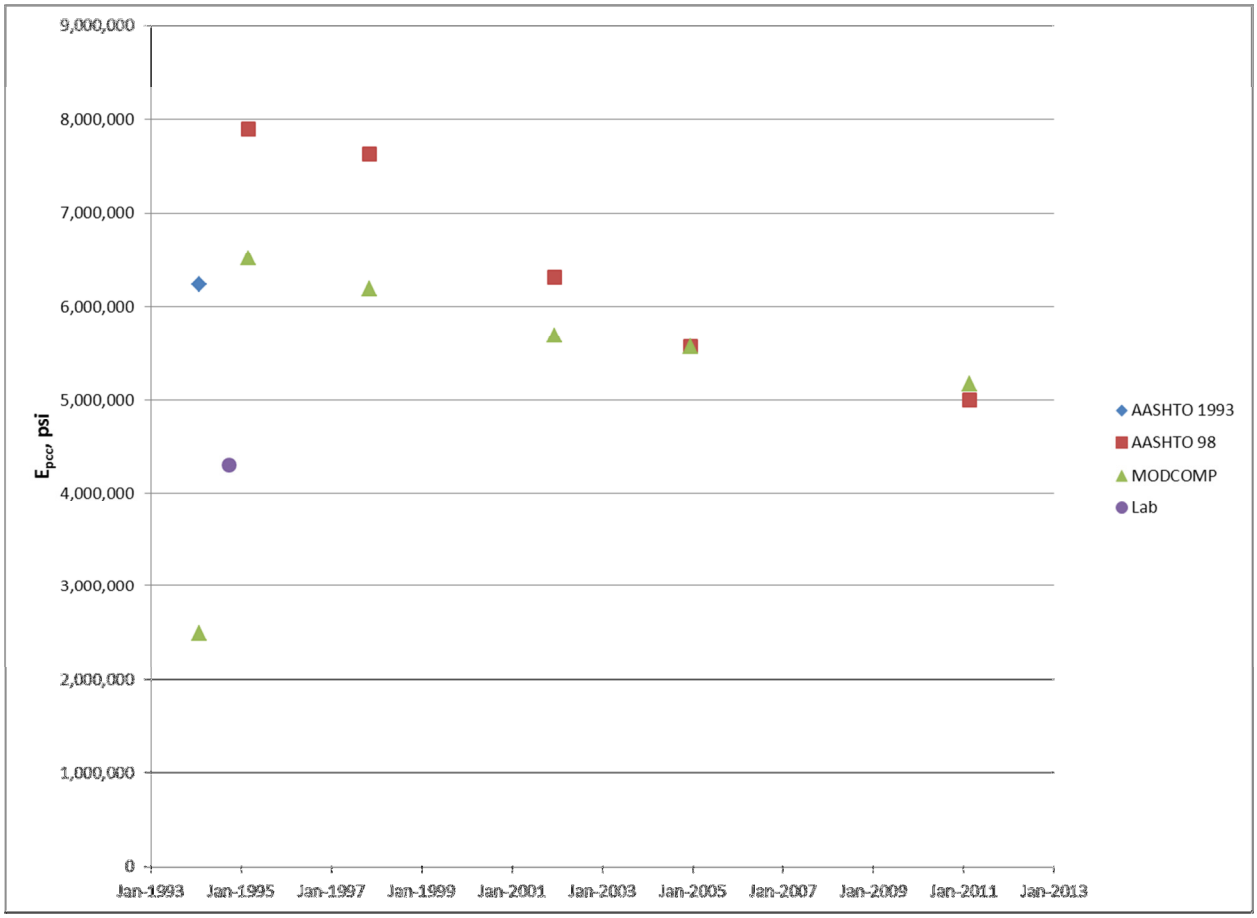

Figure 57. Section 040265 E_{pcc} vs. Date

Table 25. Section 040265 Layer Model

Layer	Layer Type	Seed Modulus (ksi)	Poisson's Ratio	Thickness (inches)
1	PCC	4000	0.15	10.8
2	DGAB	30	0.45	6.8
3	Subgrade	30	0.45	

Figure 58 shows k-values versus date. As with the backcalculated initial E_{pcc} result, the initial backcalculated k-value is probably not valid. The abnormally low E_{pcc} value and high k-value are probably due to compensating layer effect. After the initial test value, the backcalculated results show a gradual decrease in k-value over time. The AASHTO 1998 results are relatively constant.

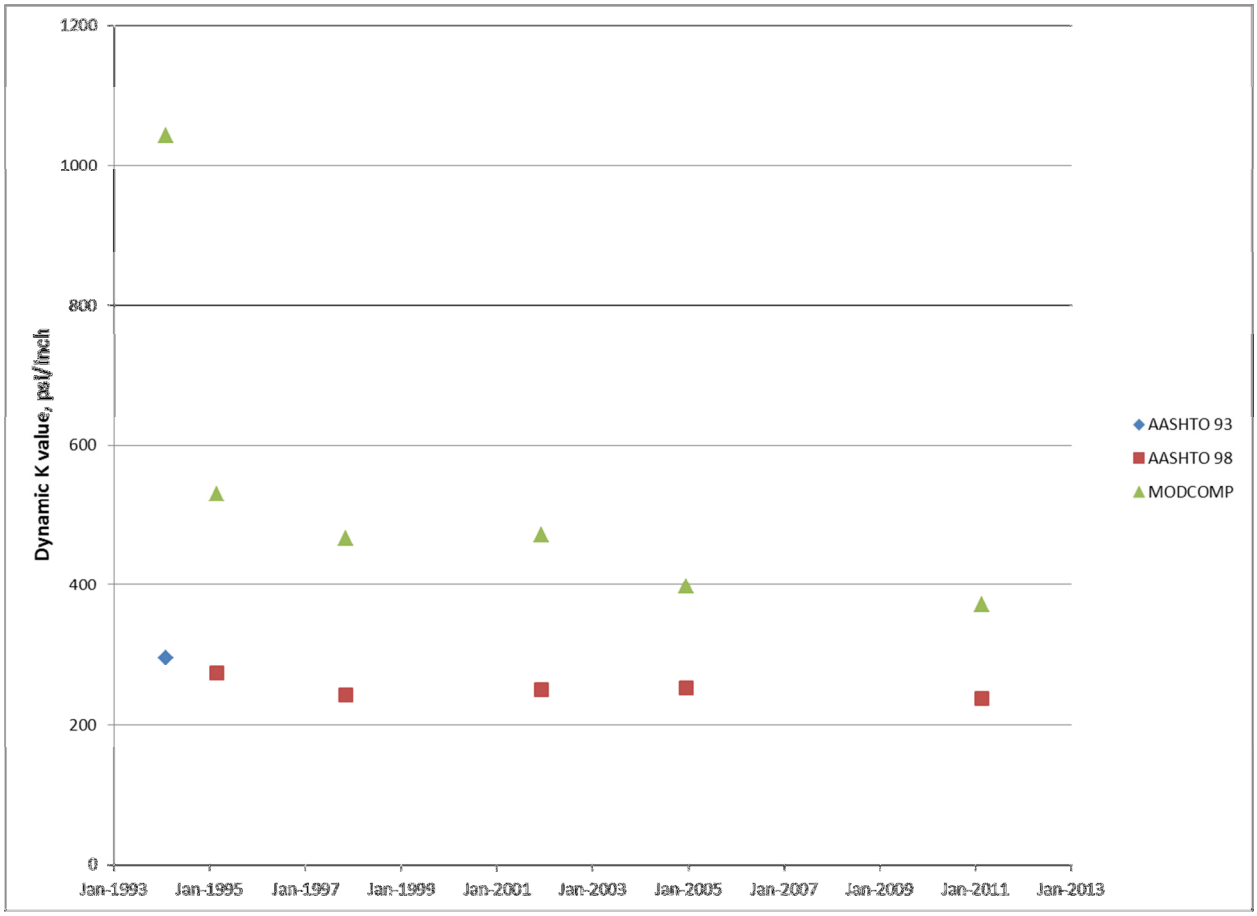

Figure 58. Section 040265 K-Values vs. Date

Section 040266

Section 040266 is a supplemental section built with doweled joints and a nominally 12.5-inch-thick, wide, low-strength slab on the State 406 BTB.

LTE Data

Figure 59 shows LTE data versus date. All testing was performed in the winter, with dates ranging from November 7 to February 18. Slab mid-depth temperatures ranged from 61˚ F to 75˚ F with an average temperature of 66˚ F. No gradient of LTE with temperature was observed; a regression of LTE versus mid-slab temperature had a slope of 0.1 percent/˚F and an R^2 of 0.06. LTE is relatively constant over time, and both the JA and JL results are similar.

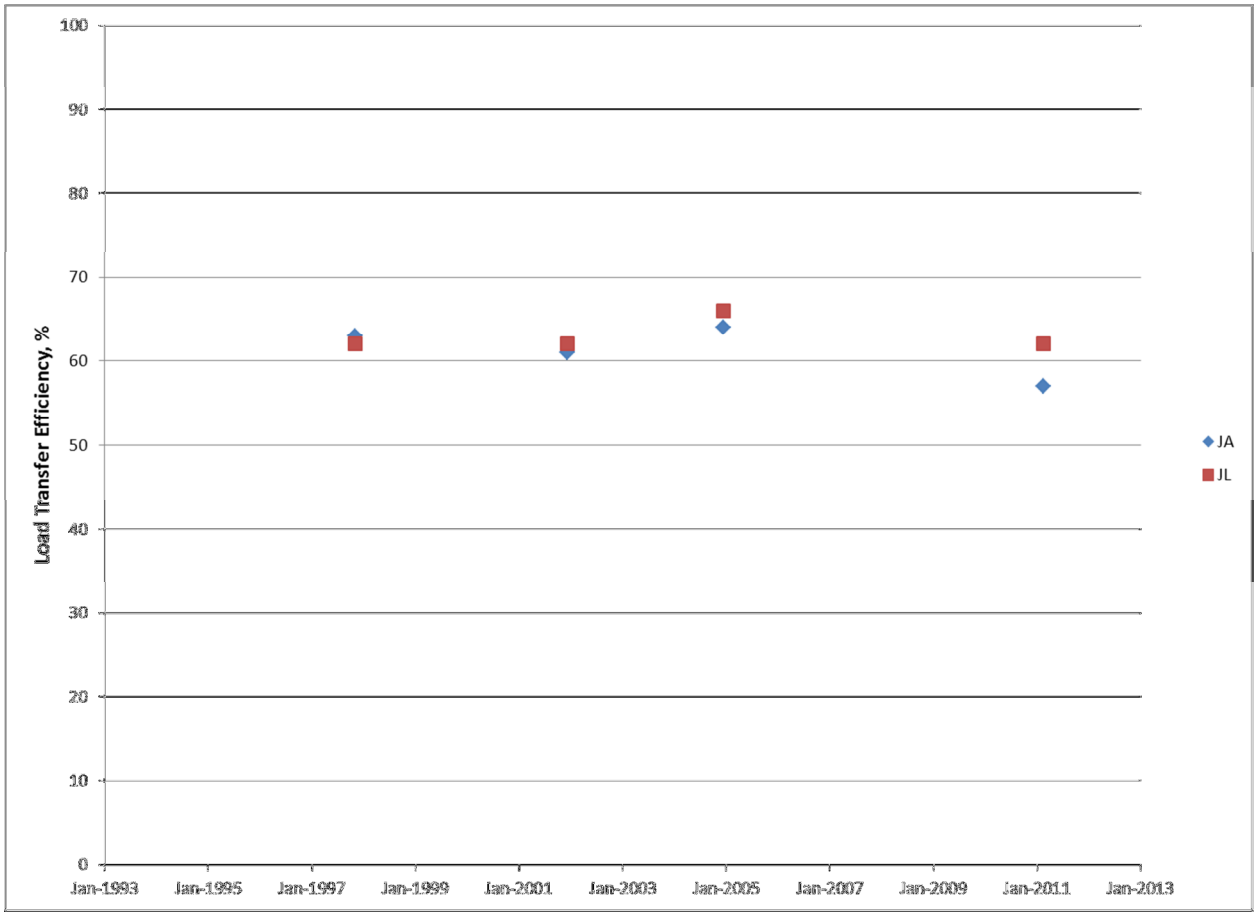

Figure 59. Section 040266 Load Transfer Efficiency vs. Date

Basin Data

Figure 60 presents E_{pcc} data versus date. Backcalculation was performed using MODCOMP, using the layer model shown in Table 26. The backcalculated results for the first test date (February 3, 1994) include an abnormally low modulus value for the PCC layer and a high modulus value for the DGAB layer, and should not be considered reliable. After the initial test, both the backcalculated and AASHTO 1998 results show relatively consistent E_{pcc} over time.

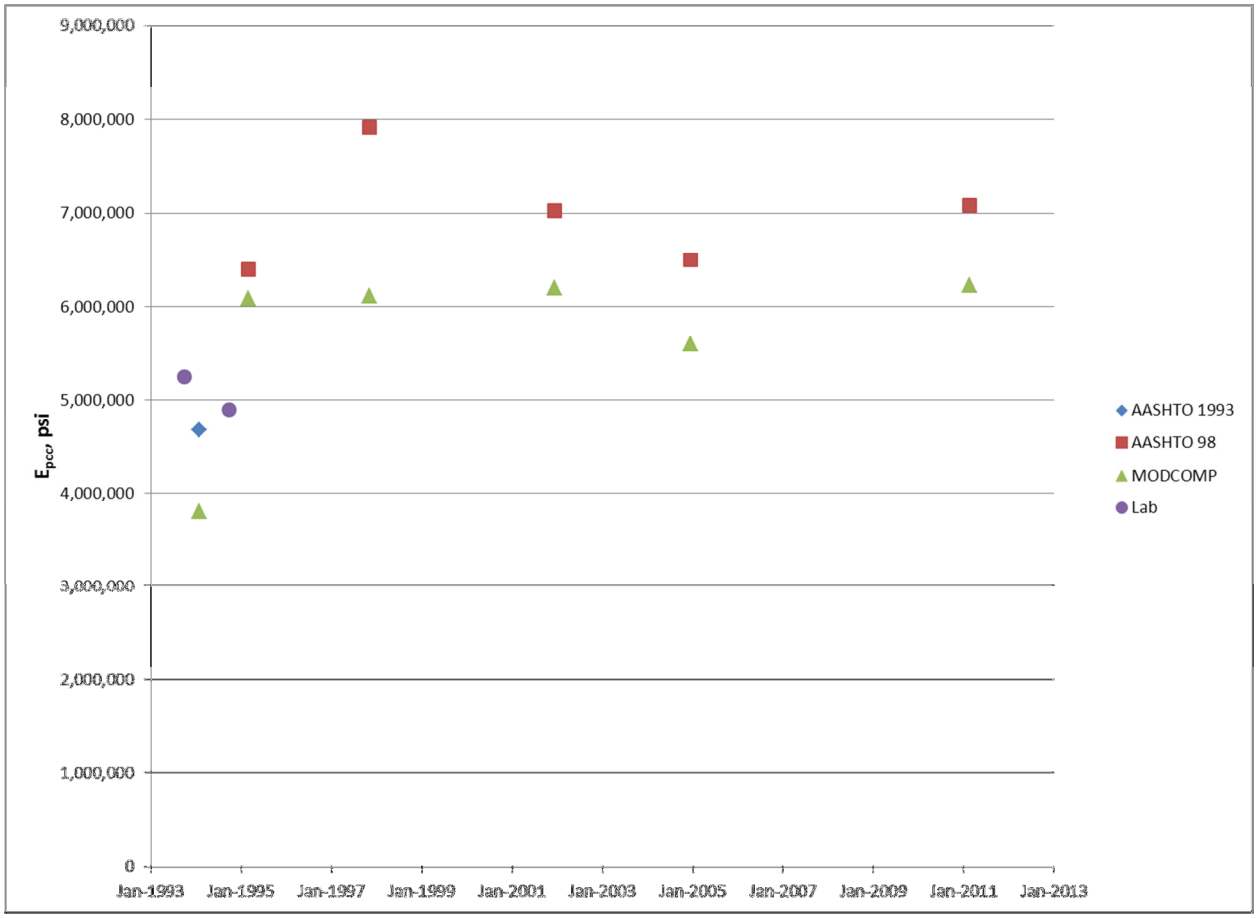

Figure 60. Section 040266 E_{pcc} vs. Date

Table 26. Section 040266 Layer Model

Layer	Layer Type	Seed Modulus (ksi)	Poisson's Ratio	Thickness (inches)
1	PCC	4000	0.15	12.3
2	BTB	100	0.35	3.9
3	Subgrade	30	0.45	

Figure 61 shows k-values versus date. The backcalculated results are significantly higher than the AASHTO 1998 results. After eliminating the first result, which was probably related to compensating layer effect, the backcalculated results show a gradual trend of decreasing k-value versus time.

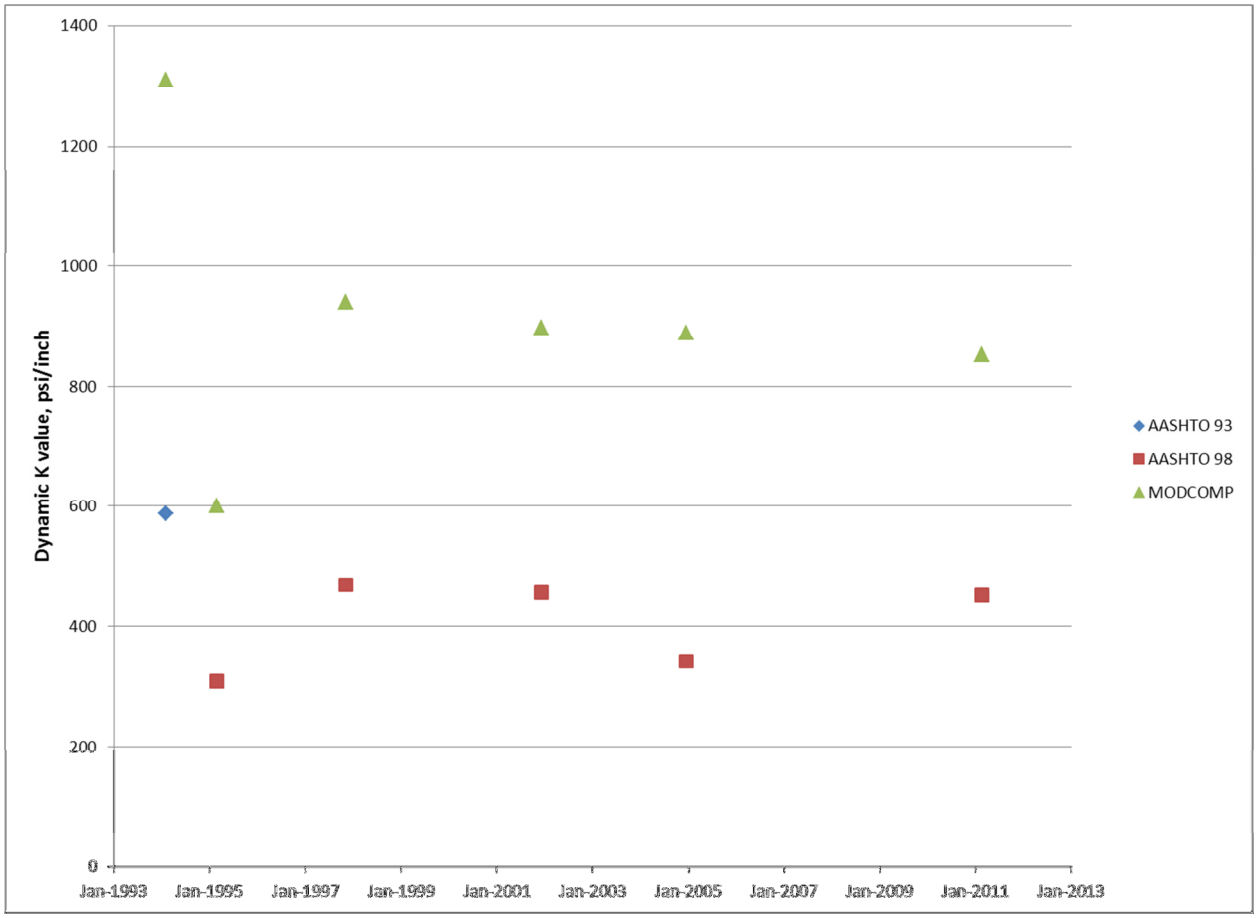

Figure 61. Section 040266 K-Values vs. Date

Section 040267

Section 040267 is a supplemental section built with doweled joints and a nominally 11-inch-thick, wide, low-strength slab on the State 406 BTB.

LTE Data

Figure 62 shows LTE data versus date. All testing was performed in the winter, with dates ranging from November 7 to February 18. Slab mid-depth temperatures ranged from 62˚ F to 75˚ F with an average temperature of 66˚ F. No gradient of LTE with temperature was observed; a regression of LTE versus mid-slab temperature had a slope of 0.05 percent/˚F and an R^2 of 0.003. LTE is relatively constant over time, and both the JA and JL results are similar.

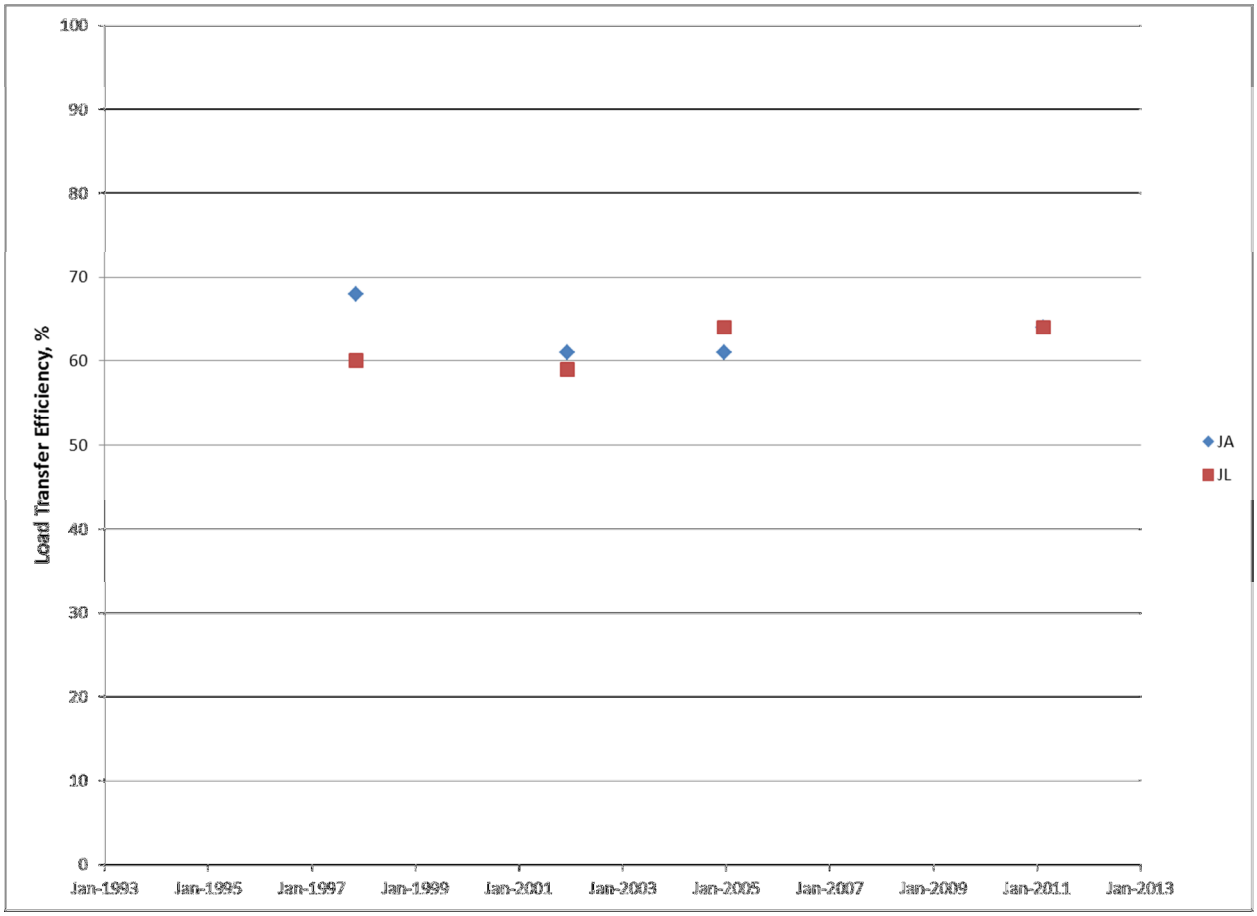

Figure 62. Section 040267 Load Transfer Efficiency vs. Date

Basin Data

Figure 63 presents E_{pcc} versus date data. Backcalculation was performed using MODCOMP, using the layer model shown in Table 27. The backcalculated results for the first test date (February 3, 1994) include an abnormally low modulus value for the PCC layer and a high modulus value for the DGAB layer, and should not be considered reliable.

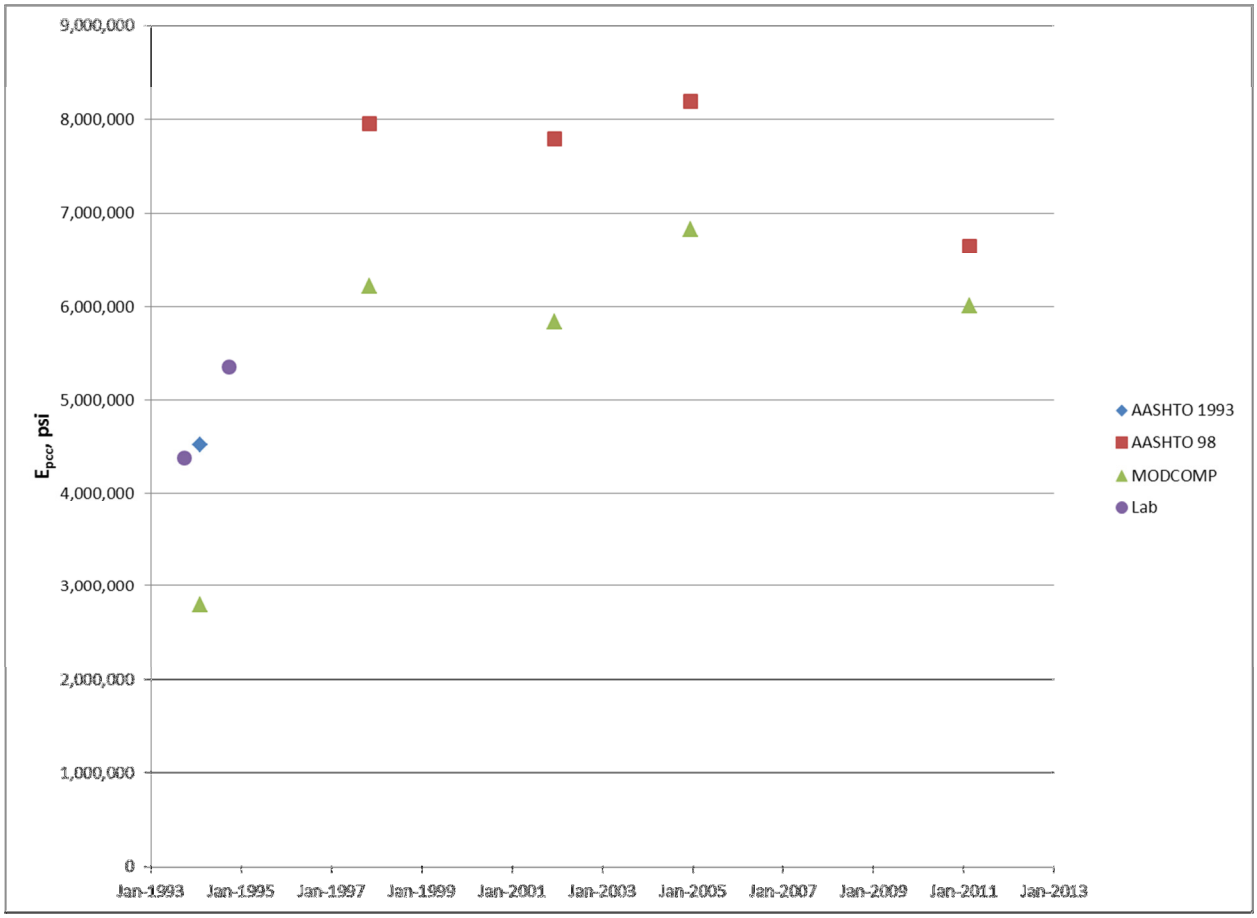

Figure 63. Section 040267 E_{pcc} vs. Date

Table 27. Section 040267 Layer Model

Layer	Layer Type	Seed Modulus (ksi)	Poisson's Ratio	Thickness (inches)
1	PCC	4000	0.15	11.3
2	BTB	100	0.35	3.9
3	Subgrade	30	0.45	

Figure 64 shows k-values versus date. The backcalculated k-values are significantly higher than the AASHTO 1998 results. The backcalculated results show a possible trend of decreasing k-value versus time, however the data is sparse.

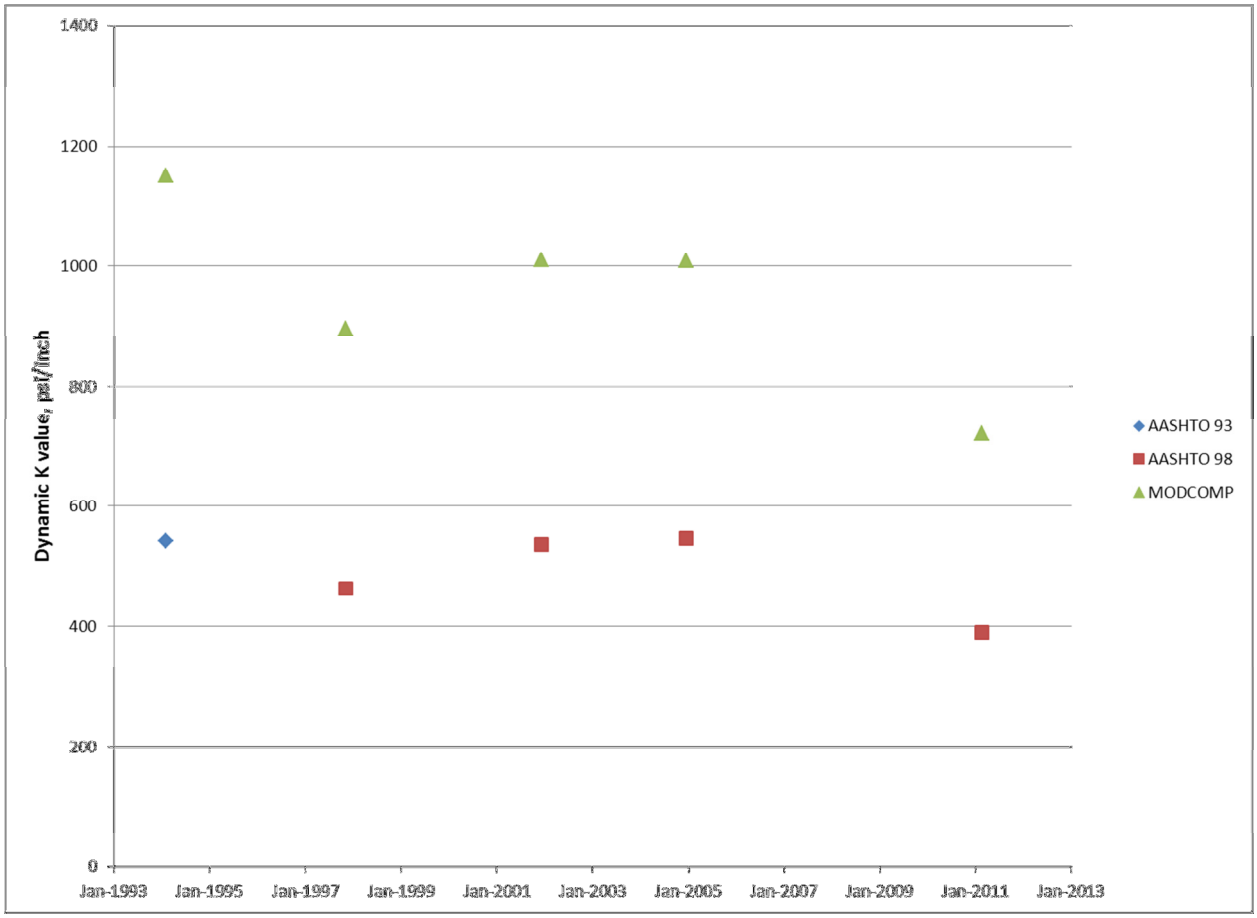

Figure 64. Section 040267 K-Values vs. Date

Section 040268

Section 040268 is a supplemental section built with doweled joints and a nominally 8-inch-thick, wide, low-strength slab on the State 406 BTB.

LTE Data

Figure 65 shows LTE data versus date. All testing was performed in the winter, with dates ranging from November 10 to February 22. Slab mid-depth temperatures ranged from 50˚ F to 73˚ F with an average temperature of 66˚ F. No gradient of LTE with temperature was observed; a regression of LTE versus mid-slab temperature had a slope of 0.38 percent/˚F and an R^2 of 0.40. LTE is relatively constant over time, and both the JA and JL results are similar.

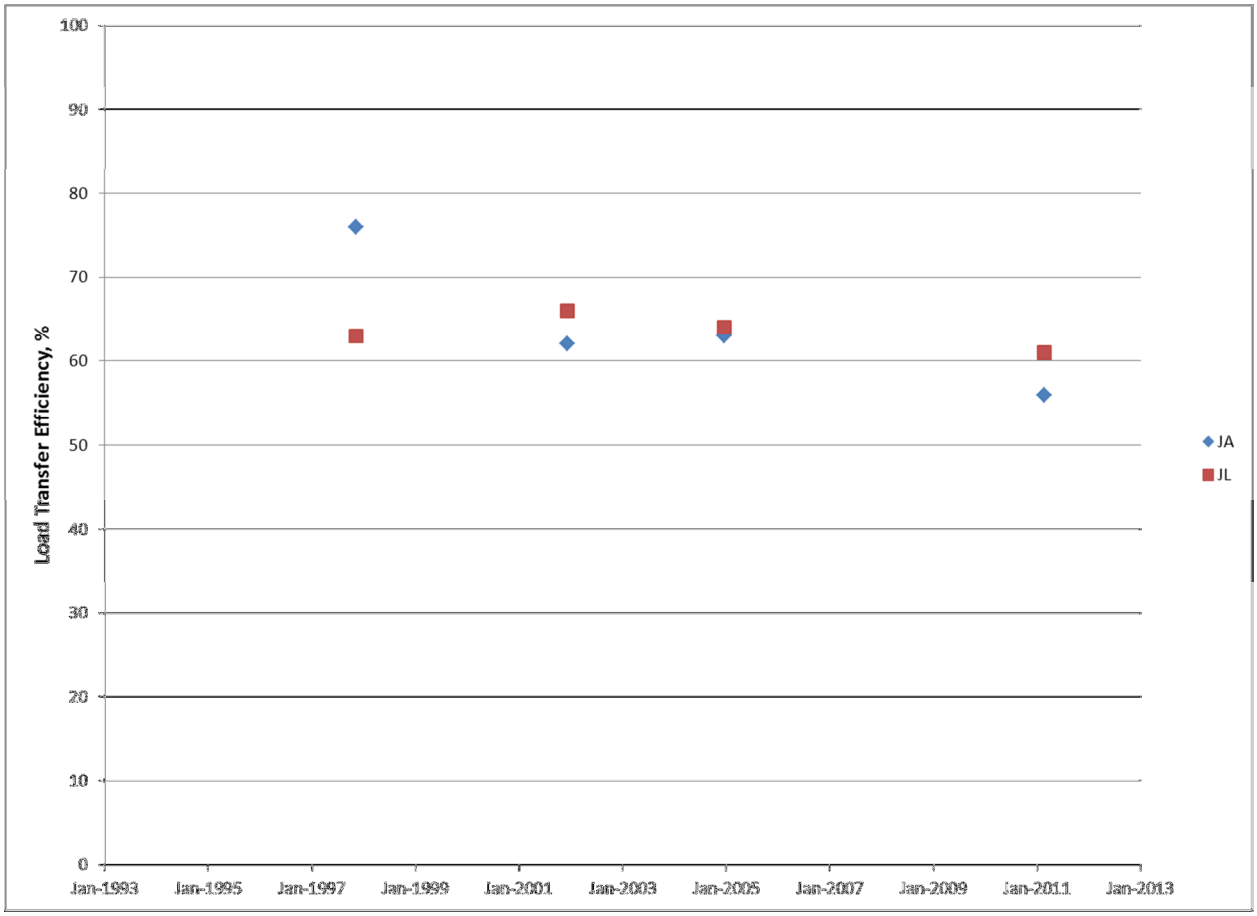

Figure 65. Section 040268 Load Transfer Efficiency vs. Date

Basin Data

Figure 66 presents E_{pcc} versus date data. Backcalculation was performed using MODCOMP, using the layer model shown in Table 28. The backcalculated results for the first test date (February 3, 1994) have an RMSE of 9.8 percent and should not be considered reliable. The backcalculated results and AASHTO 1998 results are well-correlated, however the AASHTO 1998 results are significantly higher.

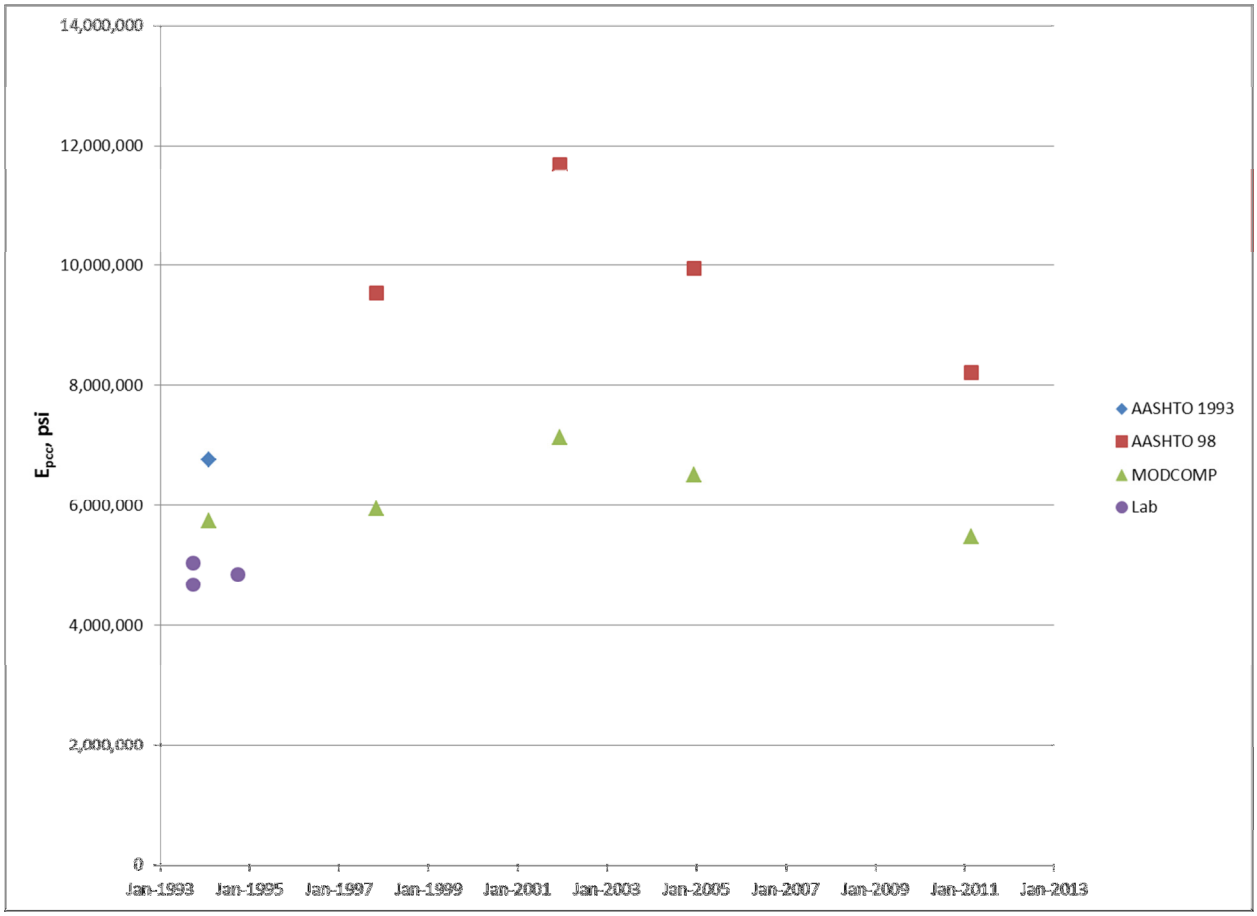

Figure 66. Section 040268 E_{pcc} vs. Date

Table 28. Section 040268 Layer Model

Layer	Layer Type	Seed Modulus (ksi)	Poisson's Ratio	Thickness (inches)
1	PCC	4000	0.15	8.5
2	BTB	100	0.35	3.8
3	Subgrade	30	0.45	

Figure 67 shows k-values versus date. The backcalculated results are significantly higher than the AASHTO 1998 results, however both show a significant trend of decreasing k-value versus time.

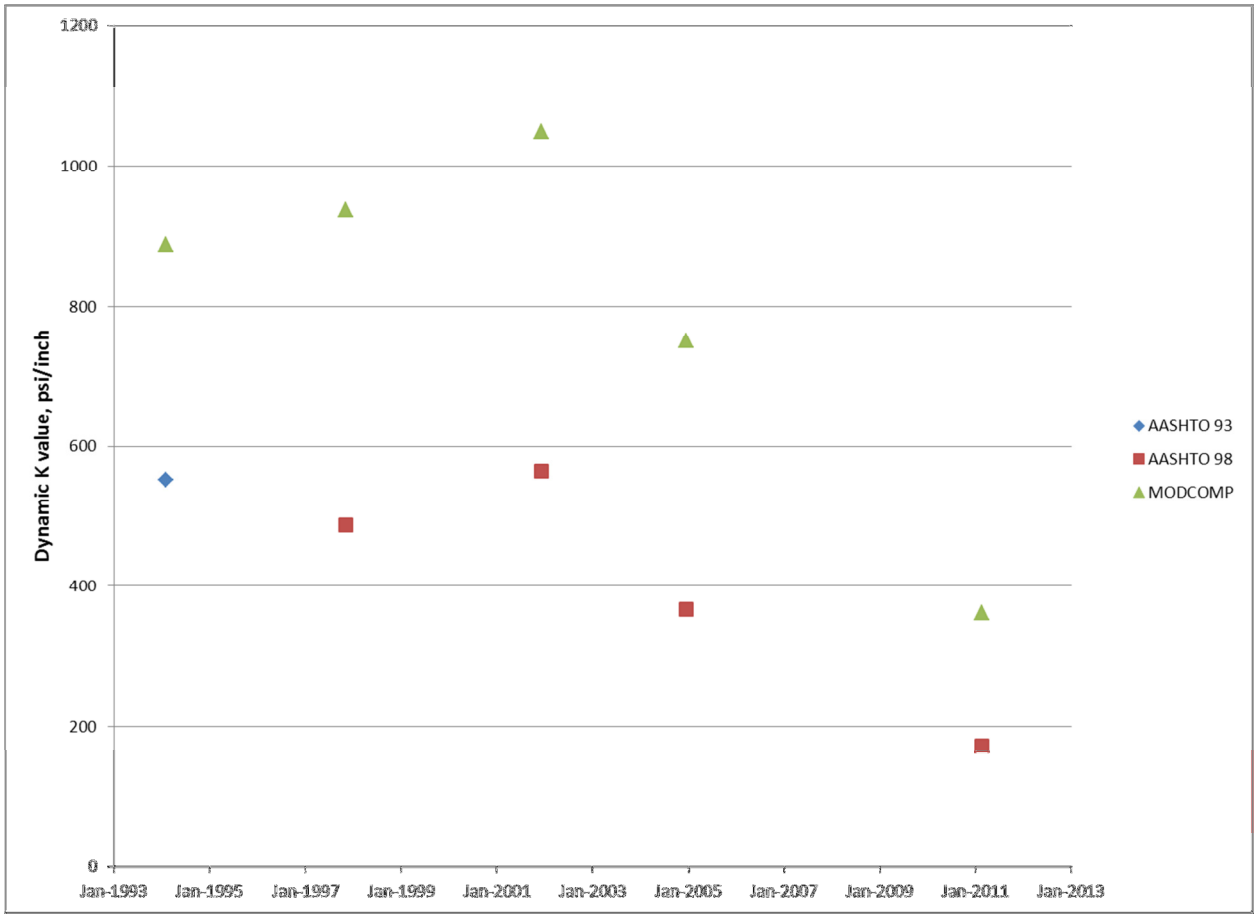

Figure 67. Section 040268 K-Values vs. Date

Section 040260

Section 040260 is a supplemental flexible pavement section with a nominal structural section of 8.5 inches of AC on 4 inches of DGAB. Backcalculation was performed using MODCOMP, using the layer model shown in Table 29.

Table 29. Section 040260 Layer Model

Layer	Layer Type	Seed Modulus (ksi)	Poisson's Ratio	Thickness (inches)
1	AC	400	0.35	9.4
2	DGAB	30	0.45	4.0
3	Subgrade	30	0.45	

All of the moduli of AC layers have been temperature-corrected to 77° F using the following LTPP-derived equation:

$$E_{ref} = E_{calc} \times 10^{k(T_{ref} - T_{calc})} \quad \text{(Eq. 13)}$$

Where: E_{ref} = modulus at the reference temperature

E_{calc} = backcalculated modulus

k = -0.0195 for testing in the wheelpath, -0.021 for testing in the mid-lane

T_{ref} = reference temperature (°C)

All temperatures are based on the measured AC mid-depth temperature, where available. For tests where the mid-depth temperature was not available, the researchers followed the BELLS2 estimation procedure. The BELLS2 procedure was developed to estimate the mid-depth temperature of asphalt pavement and requires surface temperature at the time of testing, time of day, and the previous day's average air temperature as inputs.[1]

Figure 68 shows backcalculated results for the AC layer. Only data from the mid-lane test location is presented, for consistency with the rigid section results. RMSEs are generally high for this data; the average RMSE for the November 6, 1997, December 17, 2004, and February 22, 2011, tests are in excess of 4 percent and vary from 7.7 percent to 8.3 percent. This figure also includes AC modulus determined at 77° F using the LTPP P07 test protocol. The date used to plot this laboratory value is the sampling date for the cores; however, these cores were stored for approximately 10 years before testing.

[1] Lukanen, Erland O., Richard Stubstad, and Robert Briggs. June 2000. *Temperature Predictions and Adjustment Factors for Asphalt Pavement*. Publication FHWA-RD-98-085. McLean, Virginia: Federal Highway Administration.

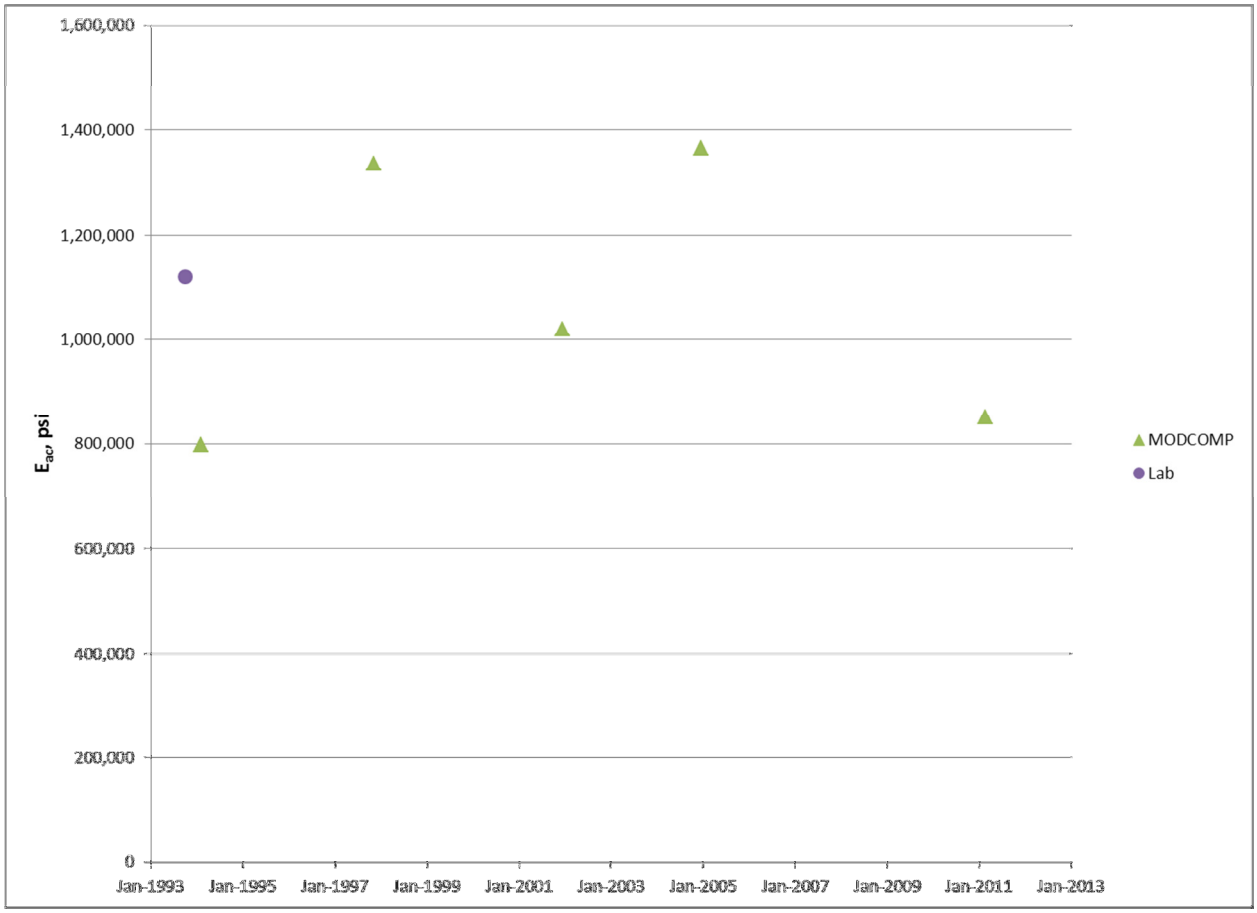

Figure 68. Section 040260 E_{ac} vs. Date

The researchers used the backcalculated base and subgrade resilient moduli to determine k-values, using Eq. 12 for consistency with the rigid pavement section results. Figure 69 shows k-value results. The data shows an increasing trend in k-value from the time of initial construction to approximately 2001, with k-value decreasing thereafter.

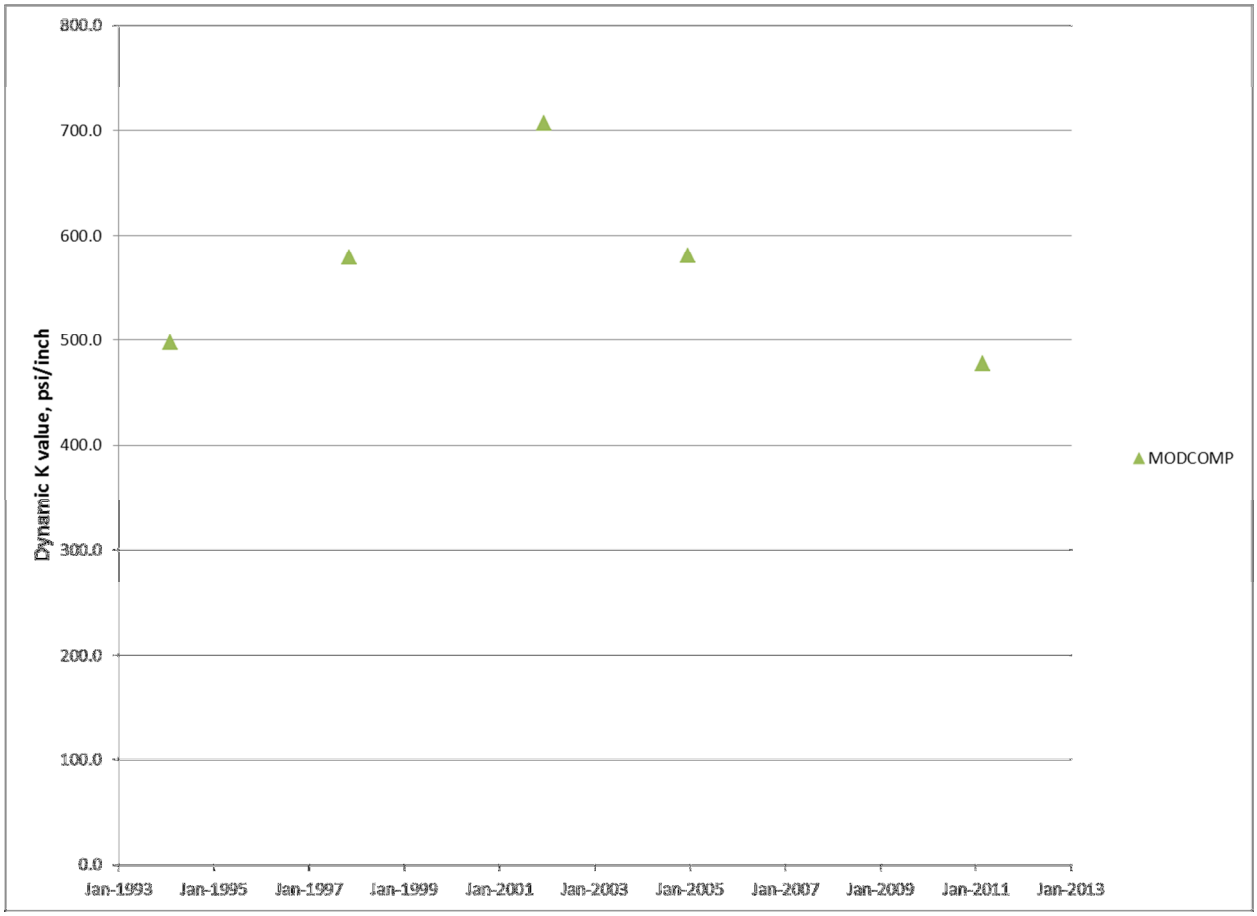

Figure 69. Section 040260 K-Values vs. Date

Section 040261

Section 040261 is a supplemental flexible pavement section with a nominal structural section of 8.5 inches of AC on 4 inches of DGAB. Backcalculation was performed using MODCOMP, using the layer model shown in Table 30.

Table 30. Section 040261 Layer Model

Layer	Layer Type	Seed Modulus (ksi)	Poisson's Ratio	Thickness (inches)
1	AC	400	0.35	8.9
2	DGAB	30	0.45	4.0
3	Subgrade	30	0.45	

All of the moduli of AC layers have been temperature-corrected to 77° F using Eq. 13. Results are shown in Figure 70. All results presented are for the mid-lane test position, with the exception of February 1, 1994, which is from the outer wheelpath because mid-lane data wasn't available for that date. RMSEs are generally high; only the November 3, 1997, results have an average RMSE of less than 4 percent. Errors for the remaining dates vary from 4.12 percent to 9.97 percent. The laboratory test data presented is for the test performed at 77° F. This data is plotted at the time of sampling; however, the test date is approximately 10 years later.

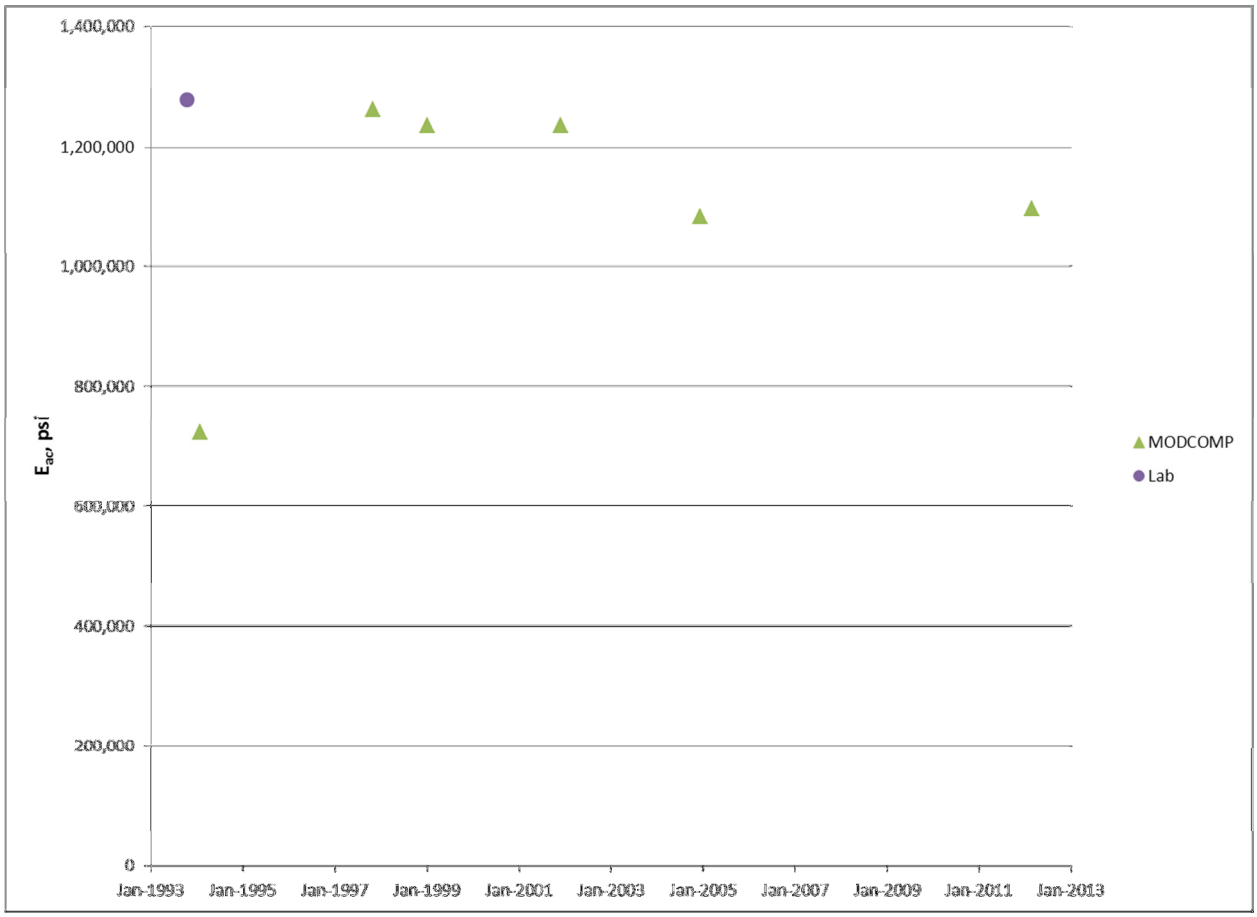

Figure 70. Section 040261 E_{ac} vs. Date

Figure 71 shows k-values versus date. The data shows an increasing trend in k-value from initial construction until approximately 2005. Then k-value appears to decrease, although there is only one data point available after 2005, which could be an outlier.

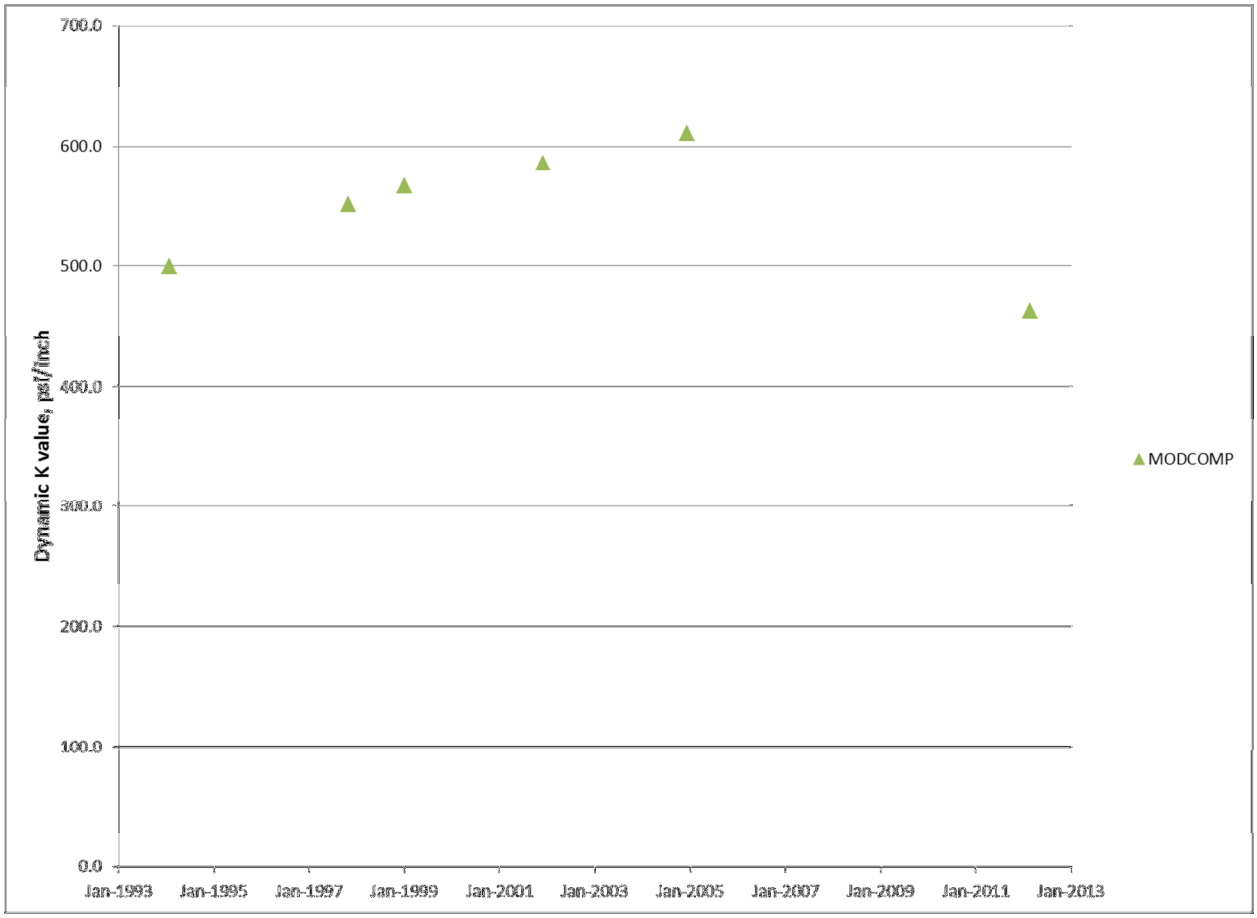

Figure 71. Section 040261 K-Values vs. Date

SUMMARY OF RESULTS

Table 31 summarizes results from the core sections, Table 32 summarizes results from the undoweled skew joint sections, Table 33 summarizes results from the State 406 BTB sections, and Table 34 summarizes results from the flexible sections. Due to the unreliability of the AASHTO 1993 and 1998 results for this project, only the backcalculated results are presented. Three summaries of each parameter are included: the average of all results, the average of results for tests performed before 1996 ("initial") and the average of results for tests performed after 2004 ("final"). Results for the core experiment have also been aggregated by experiment factor, as shown in Table 35.

.

Table 31. Core Section Results

Section	Thick (inches)	Width (ft)	FS (psi)	Base Type	E_{pcc} (ksi)			Dynamic K			LTE, JA			LTE, JL		
					All	Initial*	Final**	All	Initial*	Final**	All	Initial*	Final**	All	Initial*	Final**
040213	8	14	550	DGAB	5096	5776	4293	449	518	375	81	85	83	82	87	80
040214	8	12	900	DGAB	4982	5661	4244	336	493	215	80	80	79	80	80	76
040215	11	12	550	DGAB	4950	5131	4857	442	497	344	77	73	77	75	74	74
040216	11	14	900	DGAB	5199	5647	4624	463	551	404	78	84	66	80	84	72
040217	8	14	550	LCB	5375	5819	4780	1148	1047	1240	50	56	48	57	62	55
040218	8	12	900	LCB	5897	7037	4386	640	799	376	63	65	75	61	63	74
040219	11	12	550	LCB	7307	7109	6043	1020	1067	1013	37	45	36	46	57	35
040220	11	14	900	LCB	6183	6365	4753	898	968	733	65	79	70	71	81	72
040221	8	14	550	PATB	6181	5999	5626	579	598	508	57	69	41	62	73	49
040222	8	12	900	PATB	5730	5633	5381	596	619	531	61	77	42	66	78	52
040223	11	12	550	PATB	5841	5836	5718	694	708	738	67	71	61	66	72	60
040224	11	14	900	PATB	6487	6601	5971	671	727	549	72	77	63	73	75	64

FS = flexural strength.

*Results for tests performed before 1996.

**Results for tests performed after 2004.

Table 32. Skew-Joint Section Results

Section	Thick (inches)	Width (ft)	FS (psi)	Base Type	E_{pcc} (ksi)			Dynamic K			LTE, JA			LTE, JL		
					All	Initial*	Final**	All	Initial*	Final**	All	Initial*	Final**	All	Initial*	Final**
040262	8	14	550	DGAB	5238	5625	4790	415	529	218	42	27	30	67	60	57
040263	8	14	550	PATB	5533	5714	5151	496	545	459	34	39	32	34	36	33
040264	11	12	550	PATB	6811	6208	7723	721	741	646	17	20	17	45	82	25
040265	11	12	550	DGAB	5272	5067	5370	547	680	385	43	53	49	57	78	59

FS = flexural strength.

*Results for tests performed before 1996.

**Results for tests performed after 2004.

Table 33. State 406 BTB Section Results

Section	Thick (inches)	Width (ft)	FS (psi)	Base Type	E_{pcc} (ksi)			Dynamic K			LTE, JA			LTE, JL		
					All	Initial*	Final**	All	Initial*	Final**	All	Initial*	Final**	All	Initial*	Final**
040266	12.5	14	550	BTB	5669	5331	5911	915	951	871	61	63	61	63	62	64
040267	11	14	550	BTB	5538	4503	6419	958	1024	865	64	68	63	62	60	64
040268	8	14	550	BTB	6159	5845	5992	798	913	557	64	76	60	64	63	63

FS = flexural strength.

*Results for tests performed before 1996.

**Results for tests performed after 2004.

Table 34. Flexible Section Results

Section	Thick (Inches)	Width (ft)	FS (psi)	Base Type	E_{ac} (ksi)			Dynamic K			LTE, JA			LTE, JL		
					All	Initial*	Final**	All	Initial*	Final**	All	Initial*	Final**	All	Initial*	Final**
040260	8	16		DGAB	1074	1067	1109	568	538	529						
040261	8	16		DGAB	1106	993	1090	546	525	537						

FS = flexural strength.

*Results for tests performed before 1996.

**Results for tests performed after 2004.

Table 35. Results by Experiment Factor

Factor	Value	Average E_{pcc} (ksi)			Average Dynamic K			Average LTE, JA			Average LTE, JL		
		All	Initial*	Final**	All	Initial*	Final**	All	Initial*	Final**	All	Initial*	Final**
Flexural Strength	550 psi	5792	5945	5219	722	739	703	61	67	57	65	71	59
	900 psi	5746	6157	4893	601	693	468	70	77	66	72	77	68
Slab Thickness	8 inch	5544	5987	4785	625	679	541	65	72	61	68	74	64
	11 inch	5994	6115	5328	698	753	630	66	71	62	68	74	63
Slab Width	12 ft	5784	6068	5105	621	697	536	64	68	61	66	71	61
	14 ft	5754	6034	5008	701	735	635	67	75	62	71	77	65
Base Type	DGAB	5057	5554	4504	423	515	334	79	80	76	79	81	75
	LCB	6190	6583	4990	926	970	840	54	61	57	59	66	59
	PATB	6060	6017	5674	635	663	582	64	74	51	67	74	56

*Results for tests performed before 1996.

**Results for tests performed after 2004.

Tables 31 through 35 include some intriguing trends, but statistical significance is limited due to the small number of sections and large variability relative to the differences between factors. A rigorous analysis of the experimental factors would require inclusion of additional SPS-2 projects. However the k-value and LTE (both JA and JL) for the DGAB sections are significantly different from both the LCB and PATB sections at the 5 percent level. The differences between the LCB and PATB sections are not statistically significant.

The difference in E_{pcc} between the high- and low-strength sections is very small and not statistically significant. While both mixes lose stiffness over time, the high-strength mix appears to lose more stiffness, which may be associated with the map cracking seen on these sections. There is an even larger decline in subgrade support for the high-strength sections. While this trend is exacerbated by the exceptionally poor performance of Section 040218, it persists even with the exclusion of the data from Section 040218. LTE is better for the high-strength sections.

Slab thickness performs largely as expected. Thin sections have a higher decline in E_{pcc} than thick sections. Subgrade support is higher for thick sections, which is typically due to the lower deviator stress and higher confining pressure generated by the higher stiffness and weight of the thicker slab. Again, this trend persists even with the exclusion of Section 040218. LTE values are very similar for both thick and thin slabs.

Slab width shows small benefits to the wider slab for subgrade support and LTE. E_{pcc} is very similar for both wide and narrow slabs. The improvement in LTE can be explained by the extra two dowel bars. Some improvement in LTE may also be due to the increased interface for aggregate interlock, although no such improvement was seen for the thick versus thin sections. The improvement in subgrade support is more difficult to explain.

The initial E_{pcc} shows some dependence on base type, and the slabs on stiffer base materials appear to be themselves stiffer. This is probably due to the compensating layer effect in backcalculation, which suggests that the subgrade support values for the LCB and PATB materials have been correspondingly underestimated. Over the monitoring period, slabs on LCB show a 24 percent decline in $E_{pcc,}$ those on DGAB show a 19 percent decline, and those on PATB show a 6 percent decline. Subgrade support for the DGAB declines 35 percent over the monitoring period, while the LCB declines 13 percent and the PATB declines 12 percent. LTE is consistently best for the DGAB sections. LCB is initially worse than PATB, but slightly better at the end of the monitoring period.

For the undoweled skew-joint sections, E_{pcc} declines less for the thicker and narrower sections than for the thinner and wider sections. The effect of base type on E_{pcc} cannot be discerned. Both DGAB sections exhibit a much larger decline in subgrade modulus than the PATB sections. The DGAB sections have better LTE than the PATB sections as measured by the JL test. LTE as measured by the JA test is similar for both base types. This may indicate the formation of voids under the leave edge of the slab due to erosion of the DGAB material.

The State 406 BTB mix appears to perform better than the PATB, although caution should be used in drawing conclusions as only one pair of sections is directly comparable. Section 040268 with BTB performs better than Section 040221 with PATB in all measured parameters. There is little evidence of an effect of thickness on performance, with the exception of a larger decline in subgrade support for the thinnest section.

The flexible sections perform quite similarly and exhibit remarkably constant response over time despite the large increase in distress, although Figures 68 and 70 suggest that AC modulus and subgrade support increase initially and then decrease. Subgrade support is similar to the rigid DGAB sections in the initial period but does not decrease over time to the extent that it does for the rigid sections.

CONCLUSIONS

- The effect of flexural strength on performance is equivocal. The high-strength sections appear to have slightly improved LTE but lose stiffness more rapidly than the low-strength sections.
- Thicker sections perform better than thin sections with regard to slab stiffness and subgrade support. LTE performance is similar.
- Wide sections perform slightly better than narrow sections with regard to LTE and subgrade support. Declines in slab stiffness over time are similar.
- LTE is highest for slabs on DGAB. LTE is similar for slabs on LCB and PATB.
- For undoweled slabs on DGAB, LTE from the JL test is higher than for the JA test. For doweled slabs and undoweled slabs on PATB, both tests yield similar results.
- Slabs on LCB had the greatest decline in stiffness. Slabs on PATB had the least decline.
- Subgrade support for the rigid sections on DGAB declines significantly over time. For the two flexible sections on DGAB, subgrade support increases for approximately 10 years after construction and then decreases. Subgrade support for PATB and LCB sections have small declines over time.
- The State 406 BTB mix appears to perform better than the PATB, although the basis for comparison is very limited.
- A relationship between slab mid-depth temperature and LTE was observed for Section 040215 (the SMP section). This effect was strongest in the data collected before 1997 and decreases over time. The relationship appears to be smooth, as opposed to the stepwise, “lock-up” concept, whereby the joint is either wide, allowing for no aggregate interlock, or compressed, allowing for full aggregate interlock. No relationship between slab temperature gradient and LTE was observed. Relationships for the other sections are not discernible due to lack of data.
- The AASHTO 1993 FWD analysis procedure significantly overestimates E_{pcc} for all of the sections.

- The AASHTO 1998 FWD analysis procedure produces reasonable estimates of E_{pcc} for the DGAB sections, but unreasonably high estimates for the LCB, PATB, and BTB sections. This procedure also assigns much of the variability in deflection response over time for all sections to changes in E_{pcc} rather than k-value. K-value is also probably underestimated as more of the stiffness of the overall structure is allocated to the PCC layer rather than the underlying layers.

- Layered-elastic backcalculation yields relatively constant estimates of E_{pcc} and E_{ac} that are consistent with the laboratory static modulus test results for the rigid sections and laboratory resilient modulus test results for the flexible sections. Most of the change in deflection response over time is attributed to the base and subgrade layers, which is reasonable. But better tools are necessary for converting from resilient modulus of multiple layers to a single k-value.

CHAPTER 3. SPS-2 DISTRESS ANALYSIS

This chapter describes analyses and results from evaluating distress data collected on the Arizona SPS-2 project using LTPP manual survey techniques (Miller and Bellinger 2003). Surface distress provides powerful information regarding the nature and extent of pavement deterioration, which can be used to quantify performance trends as well as to investigate the contribution of design features on service life.

All 21 SPS-2 test sections were constructed consecutively and exposed to the same traffic loading, climate, and subgrade conditions. This allows for direct comparisons between layer configurations and design features without confounding effects introduced by different in situ conditions.

PCC DISTRESS TYPES

Deterioration in concrete surfaces appears in multiple types of distress, as defined below (Huang 1993):

- **Corner break:** A crack that intersects the joint at a distance less than 6 ft on either side measured from the corner of the slab. Load repetitions plus the loss of support, poor load transfer across the joint, and thermal curling and moisture warping usually cause corner breaks.

- **Durability or "D" cracking:** A series of closely spaced, crescent-shaped hairline cracks that appear at the concrete surface adjacent to and roughly parallel to joints and crack, and along the slab edge. The fine surface cracks contain calcium hydroxide residue, which causes a dark coloring of the crack in the immediate surrounding area. "D" cracking is caused by freeze-thaw expansive pressures of certain types of coarse aggregates.

- **Faulting of transverse joints and cracks:** A difference of elevation across a joint or crack. Faulting is caused in part by a buildup of loose materials under the trailing slab near the joint or crack or by a depression of the leading slab. The buildup of eroded or infiltrated materials is caused by pumping due to heavy loadings. The upward warp and curl of the slab near the joint or crack due to moisture and temperature gradients contribute to the pumping condition. Lack of load transfer contributes greatly to faulting.

- **Joint seal damage:** Evident in stripping and extrusion of joint sealant, weed growth, hardening of the filler, loss of bond to the slab edge, and lack or absence of sealant in the joint.

- **Longitudinal cracking:** Cracks that generally occur parallel to the centerline of the pavement. They are often caused by a combination of heavy load repetition, loss of foundation support, curling and warping, and improper construction.

- **Lane-to-shoulder dropoff:** Longitudinal joint faulting is a difference in elevation at the longitudinal joint between two traffic lanes. Where the longitudinal joint has faulted, the length of the affected area and the maximum joint faulting should be recorded.

- **Map cracking:** A network of shallow, fine, or hairline cracks that extend only through the upper surface of the concrete. Map cracking is usually caused by overfinishing of the concrete and can

lead to scaling of the surface, which is the breakdown of the slab surface to a depth of approximately 0.25 to 0.5 inch.

- **Patch deterioration:** A portion of the original concrete slab that has been removed and replaced by concrete or other epoxy materials. Poor construction of the patch, loss of support, heavy load repetitions, lack of load transfer devices, improper or absent joints, and moisture or thermal gradients can all cause patch deterioration.

- **Pumping and water bleeding:** Material ejected with water through joints or cracks, caused by the deflection of slab under moving loads. As the water is ejected, it carries particles of gravel, sand, clay, or silt, resulting in a progressive loss of pavement support. Surface staining or accumulation of base or subgrade material on the pavement surface close to joints and cracks is evidence of pumping. (Pumping can occur without this evidence, particularly when stabilized bases are used.) Water that is ejected by heavy traffic loads after a rainstorm also suggests pumping. Water bleeding occurs when water seeps out of joints or cracks.

- **Transverse cracking:** Cracks that are usually caused by a combination of heavy load repetitions and stresses from temperature gradient, moisture gradient, and drying shrinkage.

- **Spalling (transverse and longitudinal joint or crack):** Cracking, breaking, or chipping of the slab edges within 1 ft of the joint or crack. A joint spall usually does not extend vertically through the whole slab thickness, but instead extends to intersect the joint at an angle. Spalling usually results from excessive stresses at the joint or crack, caused by the infiltration of incompressible materials and by subsequent expansion or traffic loading. It can also be caused by the disintegration of concrete, weak concrete at the joint caused by overworking, or poorly designed or constructed load transfer devices.

These distress types are categorized based on cause or failure mechanism. Table 36 summarizes rigid pavement distress types and their associated failure mechanisms.

Table 36. Rigid Pavement Distress Types and Failure Mechanism

Distress Type	Primary Failure Mechanism	
	Traffic/Loading Related	Climate/Materials Related
Corner break	X	
Durability "D" cracking		X
Faulting of transverse joints and cracks	X	
Joint seal damage		X
Longitudinal cracking	X	X
Lane-to-shoulder dropoff	X	
Map cracking		X
Patch deterioration	X	X
Pumping and water bleeding	X	X
Transverse cracks	X	X
Spalling (joints and cracks)		X
Spalling (corner)		X

AC DISTRESS TYPES

For the supplemental asphalt surfaces (Sections 040260 and 040261), multiple distress types cause deterioration (Huang 1993):

- **Fatigue cracking:** A series of interconnecting cracks caused by repeated traffic loading. Cracking initiates at the bottom of the asphalt layer where tensile stress is the highest under the wheel load. With repeated loading, the cracks propagate to the surface.

- **Longitudinal wheelpath cracking:** Cracking parallel to the centerline occurring in the wheelpath. This cracking can be the early stages of fatigue cracking or can initiate from construction-related issues such as paving seams and segregation of the mix during paving. In the latter case, cracking is typically very straight (no meandering).

- **Longitudinal non-wheelpath cracking:** Cracking parallel to the centerline occurring outside the wheelpath. This cracking is not load-related and can initiate from paving seams or where mix segregation issues occurred during paving. Cracking can also be caused by tensile forces experienced during temperature changes. Pavements with oxidized or hardened asphalt are more prone to this type of cracking.

- **Transverse cracking:** Cracking that is predominantly perpendicular to the pavement centerline. This distress type initiates from tensile forces experienced during temperature changes. Pavements with oxidized/hardened asphalt are more prone to this type of cracking.

- **Block cracking:** Cracking that forms a block pattern and divides the surface into approximately rectangular pieces. This distress type initiates from tensile forces experienced during temperature changes and indicates the AC has significantly oxidized or hardened.
- **Raveling:** Wearing away of the surface caused by dislodging of aggregate particles and loss of asphalt binder. Raveling is caused by moisture stripping and asphalt hardening.
- **Bleeding:** Excessive bituminous binder on the surface that can lead to loss of surface texture or a shiny, glass-like, reflective surface. Bleeding is a result of high asphalt content or low air void content in the mix.
- **Rutting:** A surface depression in the wheelpaths. Rutting can result from consolidation or lateral movement of material due to traffic loads. It can also signify plastic movement of the asphalt mix because of inadequate compaction, excessive asphalt, or a binder that is too soft given the climatic conditions.

The distress types defined above can be grouped into two general categories based on cause or failure mechanism: structural and environmental factors. Table 37 summarizes flexible pavement distress types and their associated failure mechanisms.

Table 37. Flexible Pavement Distress Types and Failure Mechanisms

Distress Type	Primary Failure Mechanism	
	Traffic/Load Related	Climate/Materials Related
Fatigue cracking	X	
Longitudinal wheelpath cracking	X	
Longitudinal non-wheelpath cracking		X
Transverse cracking		X
Block cracking		X
Raveling		X
Bleeding		X
Rutting	X	X

RESEARCH APPROACH

Investigators began their analysis with a review of all distress data collected at each test section to identify suspect or inconsistent information. They used photos and distress maps to verify quantities reported in the database. Because of the subjective nature of the data collection technique (raters must select distress type and severity based on a set of rules), variation is expected in distress data.

Most distress data collected for LTPP purposes are reported at three severity levels: low, moderate, and high. Inconsistencies between severity levels within a distress type create one of the largest sources of variability in distress data (Rada et al. 1999). In addition, conducting analyses on three separate severity levels for each distress type becomes increasingly complex, with results that are difficult to interpret. To reduce variability and to consolidate the information for analyses, the researchers summed the quantities from the three severity levels into one composite value.

For PCCPs, longitudinal and transverse cracking can be the result of both structural (traffic/load) and environmental (climate/materials) related failure; because of this, the comparisons used between PCC test sections analyze the resistance to these failures globally and not as a specific result of either load or climate/material factors. For AC comparisons, longitudinal and transverse cracking are examined as a specific result of a structural- or environmental-related failure. Although the structural and environmental distress factors are clearly significant aspects of the performance of the Arizona SPS-2 project in terms of structural and functional service life, the analyses also incorporated patching and other surface defects (i.e., map cracking, water bleeding, and pumping).

The experimental design of the SPS-2 project is such that replicate data was not collected. Therefore, standard statistical comparisons (i.e., t-tests) to determine the significance of findings could not be conducted. Instead, the evaluation consisted of graphical comparisons between test sections from data collected at the same time.

OVERALL PERFORMANCE TREND OBSERVATIONS

While gathering pavement distress data, researchers became aware of a few significant trends affecting the overall pavement performance of the project. These observations were clearly driving issues for this project and were intrinsically important pieces of the distress performance**.**

Transverse and longitudinal cracking are most prevalent in the LCB base test sections when compared to the other bases, with the exception of Section 040220 (the 11-inch-thick, 900-psi section). The 11-inch-thick, 900-psi sections have relatively small cracking regardless of the base type used in the design.

Heavy map cracking with staining and spalling beginning to form was noted in Sections 040216 and 040218, both of which had 900-psi strength pavement. Most of the 900-psi sections do exhibit well-defined map cracking, especially in the wheelpaths; this defect may be a result of alkali-silica reaction (ASR), and more investigation should be done.

In comparison with the rest of the core SPS-2 project, the 14-ft-wide, 11-inch-thick, 900-psi strength sections (040216, 040220, 040224) exhibited significantly smaller amounts of damage accumulation,

with the exception of map cracking, which greatly affected the 900-psi strength sections. This performance is as expected, considering the test sections were the widest, thickest, and strongest in terms of flexural strength of the core experiment.

Tables 38 and 39 provide the dates when surveys were performed at each test section. Figures 72 through 92 show the overall distress trends for each section by year. The performance trends are relatively consistent and within the expected range of variation. Fluctuations in scaling, polished aggregate, and map cracking are attributable to rater variability and the irregular surface characteristics observed in the sections. Other drops in the distress graph are typically indicative of the distress forming into a different distress (i.e., transverse and longitudinal cracking into map cracking). The maintenance work (i.e., partial depth patching, pothole patching) performed on the project did not significantly mask the severity and extent of distresses.

Table 38. Manual Distress Survey Dates by Core Section

Survey Date	040213	040214	040215	040216	040217	040218	040219	040220	040221	040222	040223	040224
Feb. 27-28, 1995	X	X	X	X	X	X		X	X	X	X	X
Aug. 25, 1995			X									
Nov. 13, 1995			X									
Feb. 12, 1996			X									
April 8, 1996			X									
July 22, 1996			X									
Aug. 21, 1996			X									
Nov. 3-4, 1997	X	X	X	X	X	X	X	X	X	X	X	X
Jan. 20, 1998			X									
Jan. 6-8, 1999	X	X		X	X	X	X	X	X	X	X	X
March 14-15, 2000	X	X	X	X	X	X	X	X	X	X	X	X
Dec. 3-7, 2001	X	X	X	X	X	X	X	X	X	X	X	X
Oct. 15, 2002			X									
Dec. 3-5, 2002	X	X	X	X	X	X	X	X	X	X	X	X
June 16, 2003			X									
Dec. 15-18, 2003	X	X	X	X	X	X	X	X	X	X	X	X
June 14, 2004			X									
Oct. 7, 2004			X									
Dec. 9-14, 2004	X	X	X	X	X	X	X	X	X	X	X	X
March 3-5, 2008	X	X	X	X	X	X	X	X	X	X	X	X
Jan. 19-20, 2010	X	X	X	X	X	X	X	X	X	X	X	X
Feb. 9-16, 2011	X		X	X	X	X	X	X	X	X	X	X
Feb. 21-23, 2012	X	X	X	X	X	X	X	X	X	X	X	X

Table 39. Manual Distress Survey Dates by Supplemental Section

Survey Date	0040260	040261	040262	040263	040264	040265	040266	040267	040268
Feb. 3-March 1, 1995	x	x	x	x	x	x	x	x	x
Nov. 3-5, 1997	x	x	x	x	x	x	x	x	x
Jan. 6-11, 1999	x	x	x	x	x	x	x	x	x
March 14-17, 2000	x	x	x	x	x	x	x	x	x
Dec. 3-10, 2001	x	x	x	x	x	x	x	x	x
Dec. 9-17, 2004	x	x	x	x	x	x	x	x	x
March 3-6, 2008	x	x	x	x	x	x	x	x	x
Nov. 3-4, 1997		x	x	x	x	x	x	x	x
Jan. 19-25, 2010		x	x	x	x	x	x		
Feb. 16-22, 2011	x		x	x	x	x	x	x	x
Feb. 21-March 1, 2012	x	x	x	x	x	x	x	x	x

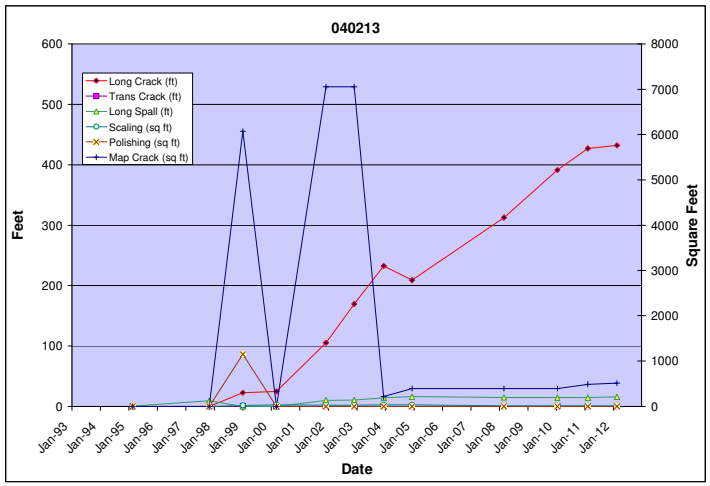

Figure 72. Distress Trends in Section 040213 by Year

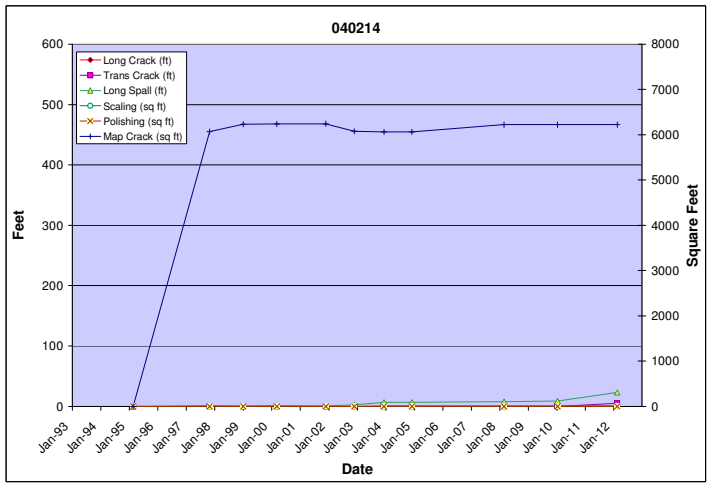

Figure 73. Distress Trends in Section 040214 by Year

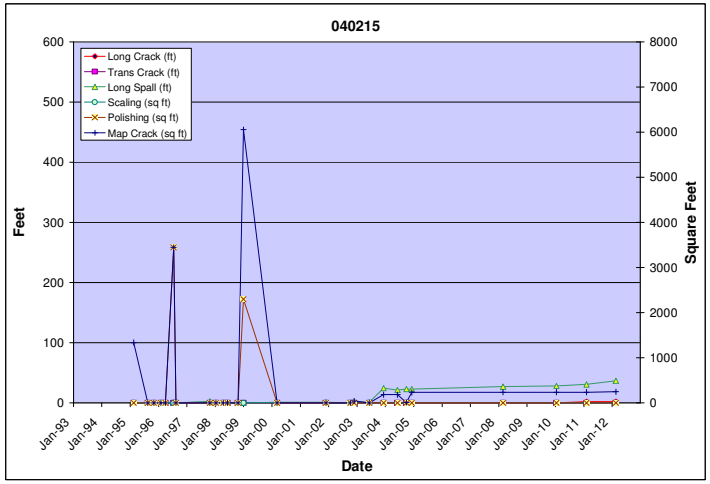

Figure 74. Distress Trends in Section 040215 by Year

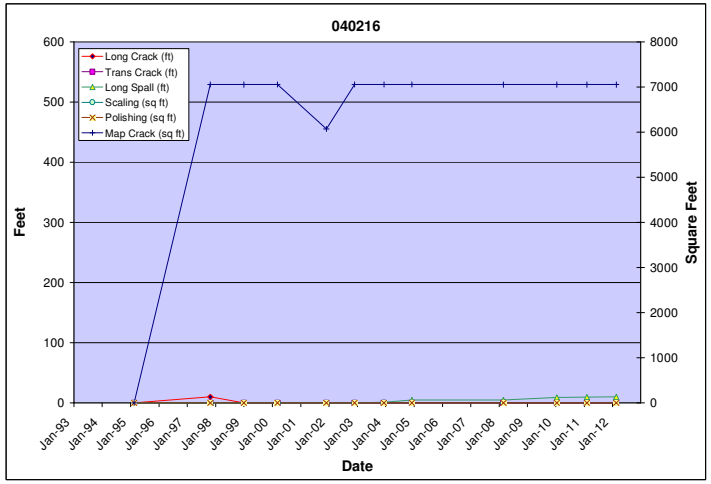

Figure 75. Distress Trends in Section 040216 by Year

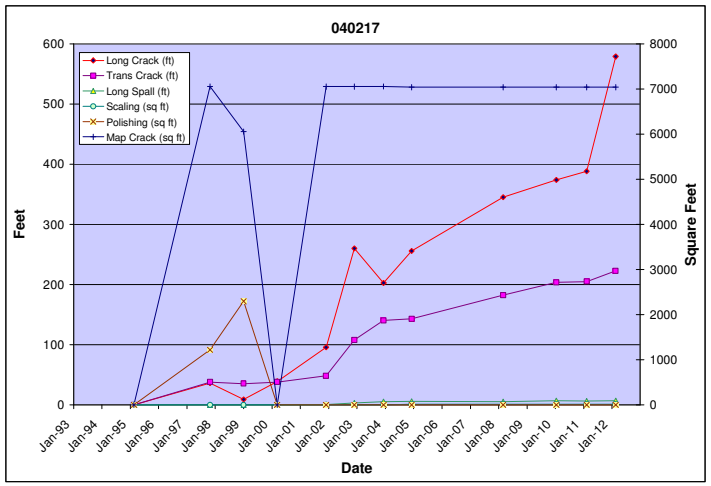

Figure 76. Distress Trends in Section 040217 by Year

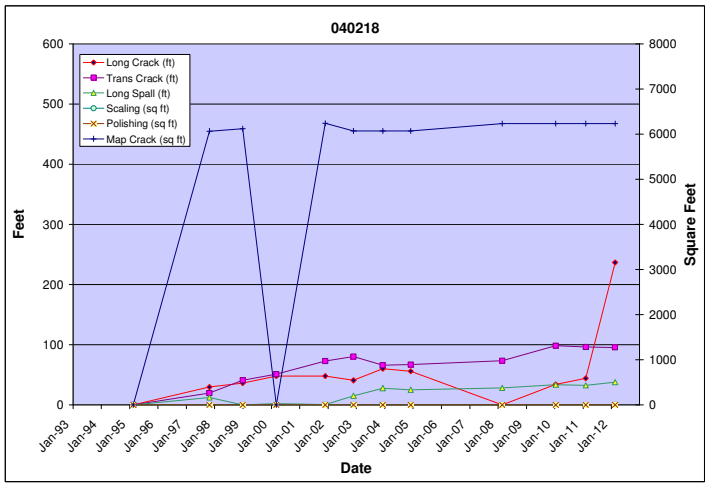

Figure 77. Distress Trends in Section 040218 by Year

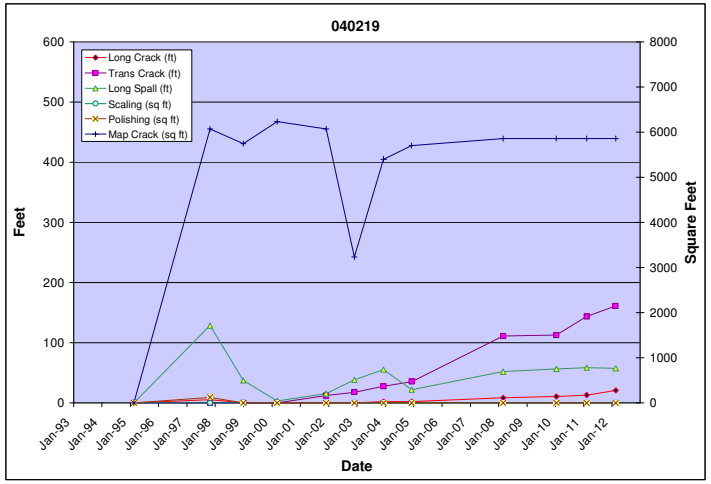

Figure 78. Distress Trends in Section 040219 by Year

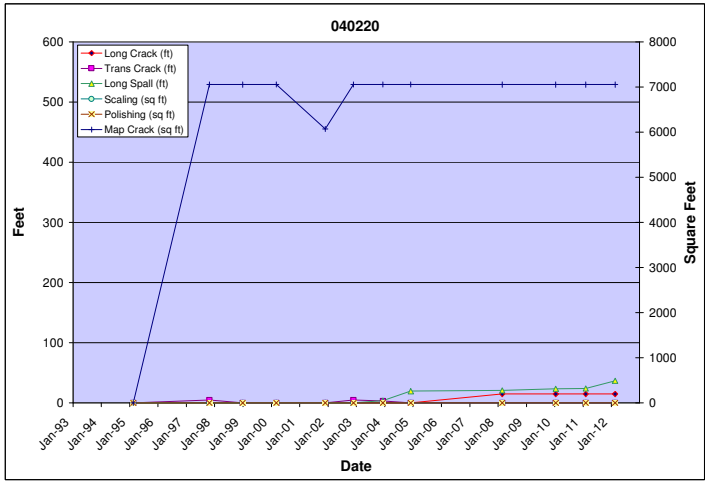

Figure 79. Distress Trends in Section 040220 by Year

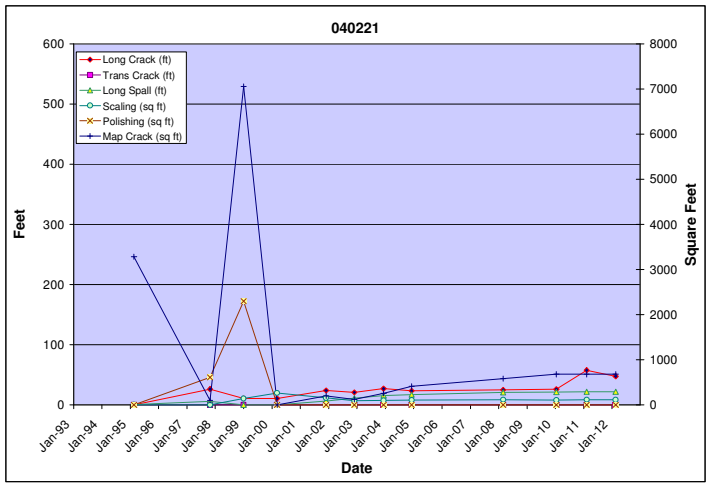

Figure 80. Distress Trends in Section 040221 by Year

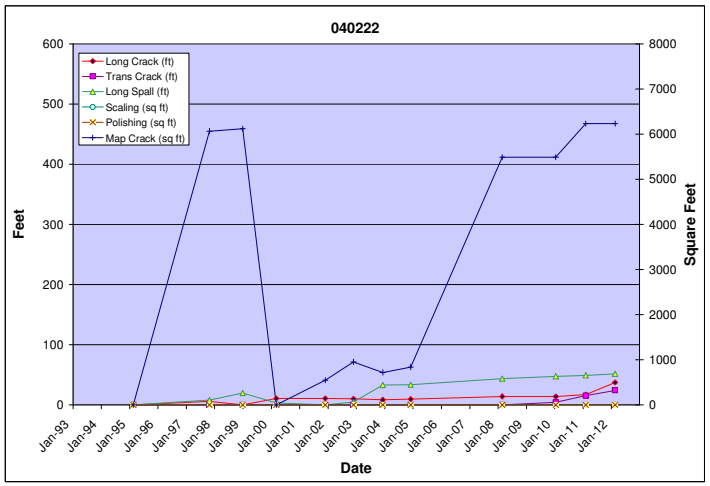

Figure 81. Distress Trends in Section 040222 by Year

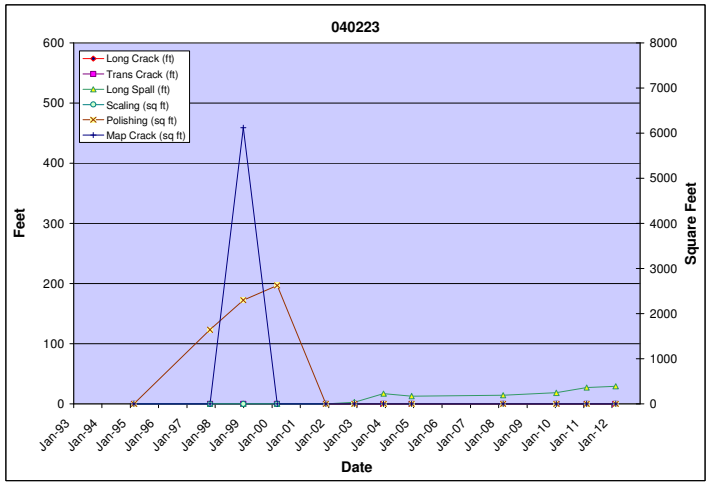

Figure 82. Distress Trends in Section 040223 by Year

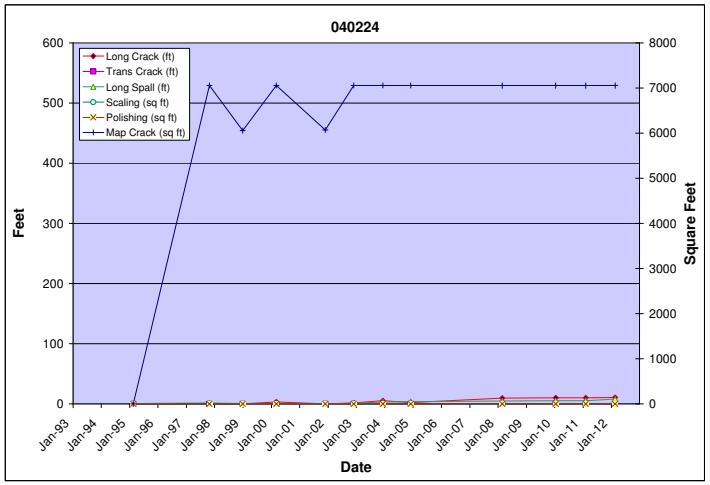

Figure 83. Distress Trends in Section 040224 by Year

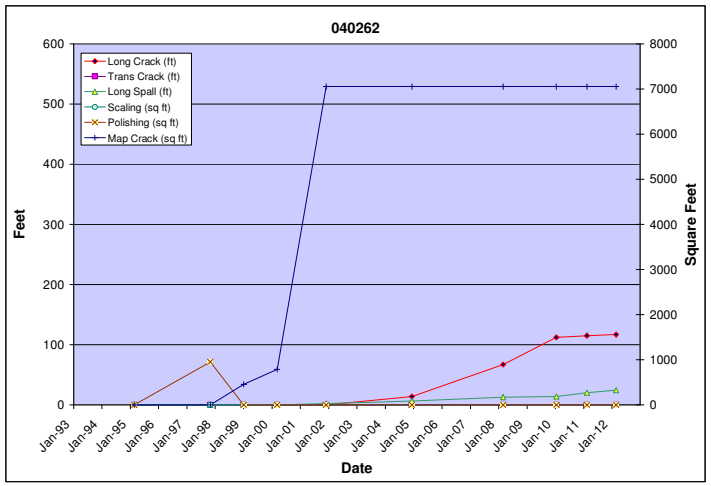

Figure 84. Distress Trends in Section 040262 by Year

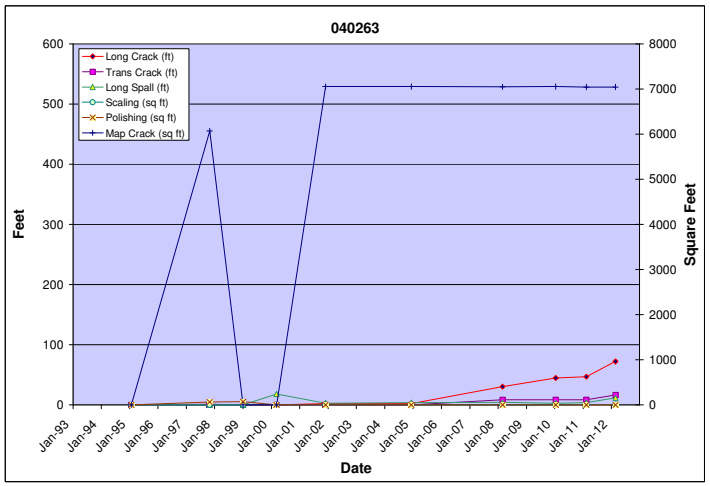

Figure 85. Distress Trends in Section 040263 by Year

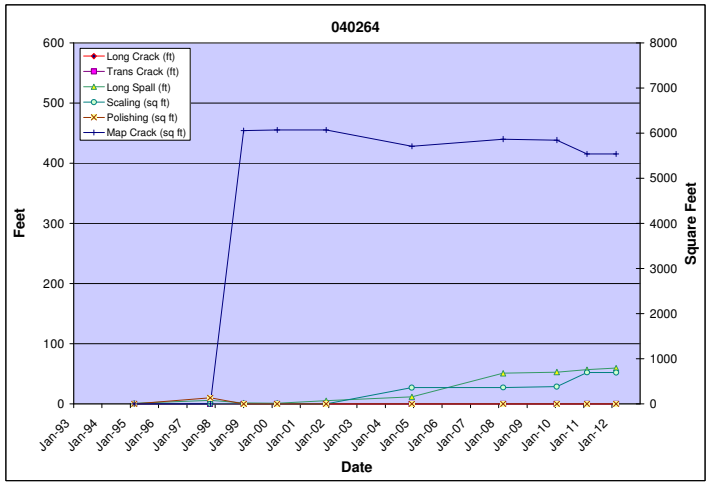

Figure 86. Distress Trends in Section 040264 by Year

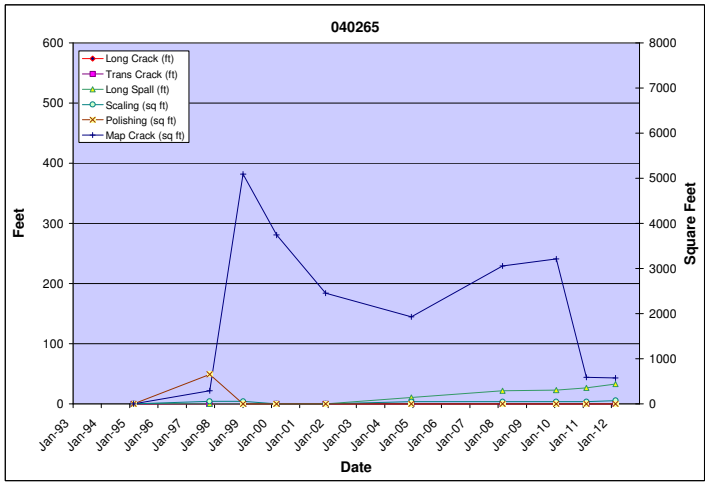

Figure 87. Distress Trends in Section 040265 by Year

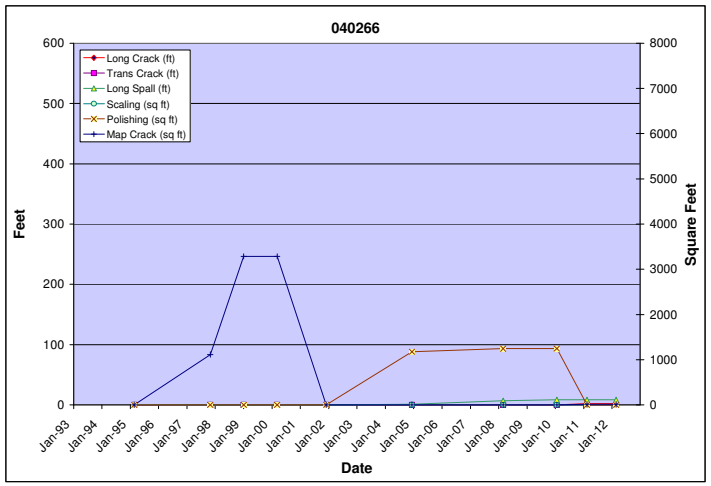

Figure 88. Distress Trends in Section 040266 by Year

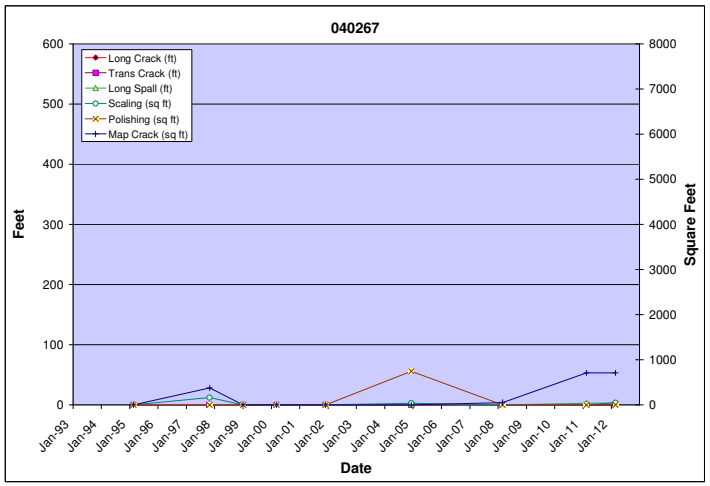

Figure 89. Distress Trends in Section 040267 by Year

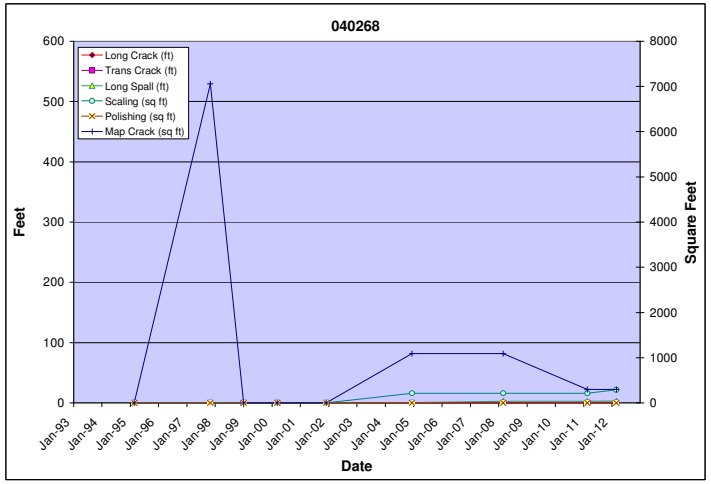

Figure 90. Distress Trends in Section 040268 by Year

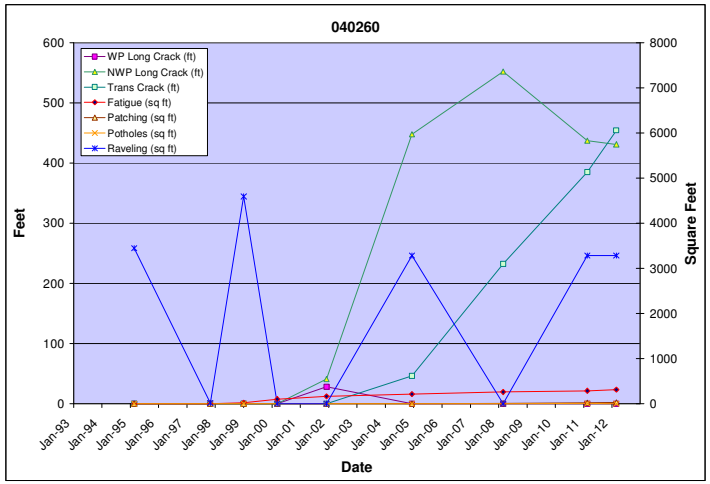

Figure 91. AC Distress Trends in Section 040260 by Year

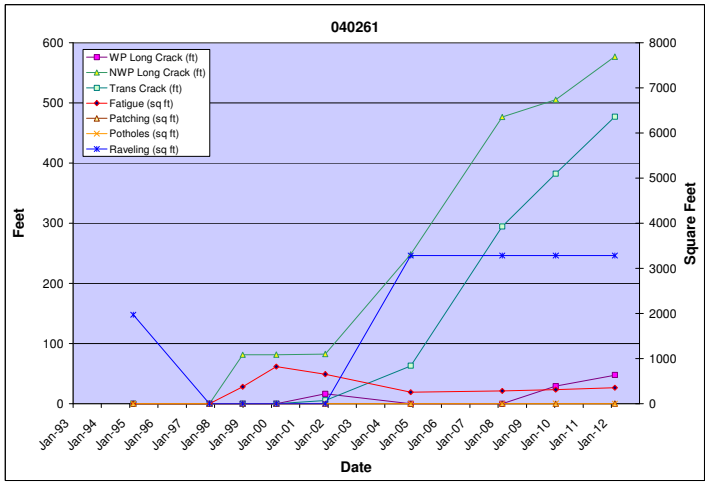

Figure 92. AC Distress Trends in Section 040261 by Year

Performance Comparisons

While all sections were still in service at the time of this report, there were some differences in performance. Using data collected from the February-March 2012 visit, researchers conducted in-depth analyses and comparisons of all SPS-2 test sections. Figure 93 summarizes the total cracking per slab width of PCC sections observed in 2012. Total cracking (both longitudinal and transverse) resulted from structural (traffic/load) and environmental (climate/materials) related failure. Figure 94 summarizes the map cracking per section area of the PCC sections observed in 2012. Regardless of other LCB section attributes, all showed high percentages of map cracking throughout the section. Figure 95 summarizes the PCC section faulting observed in 2012. The undoweled, skewed supplemental Sections 040262 and 040265 showed the highest faulting. Of the core experiment, Section 040214 exhibited the most faulting with 0.06 inches in the edge and 0.05 inches in the wheelpath.

Figure 96 summarizes the structural distresses and the environmental distresses of the two AC supplemental sections in 2012.

Following is a synopsis of the key findings and performance of each section in terms of distress deterioration and any unique circumstances.

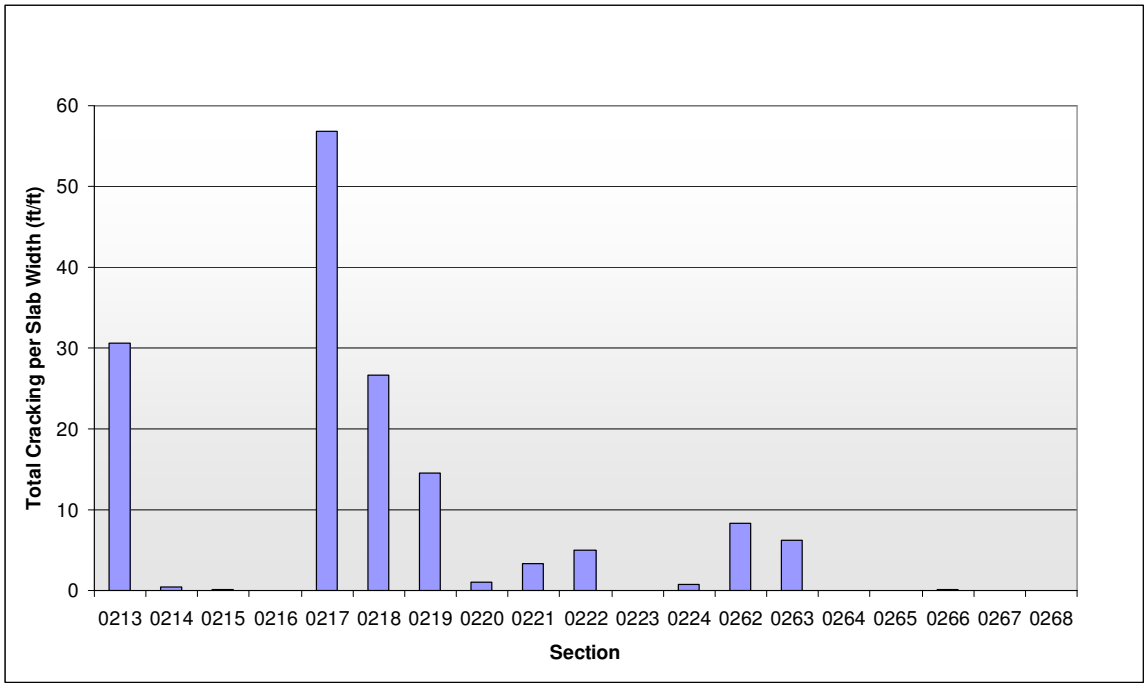

Figure 93. 2012 PCC Sections Cracking Summary

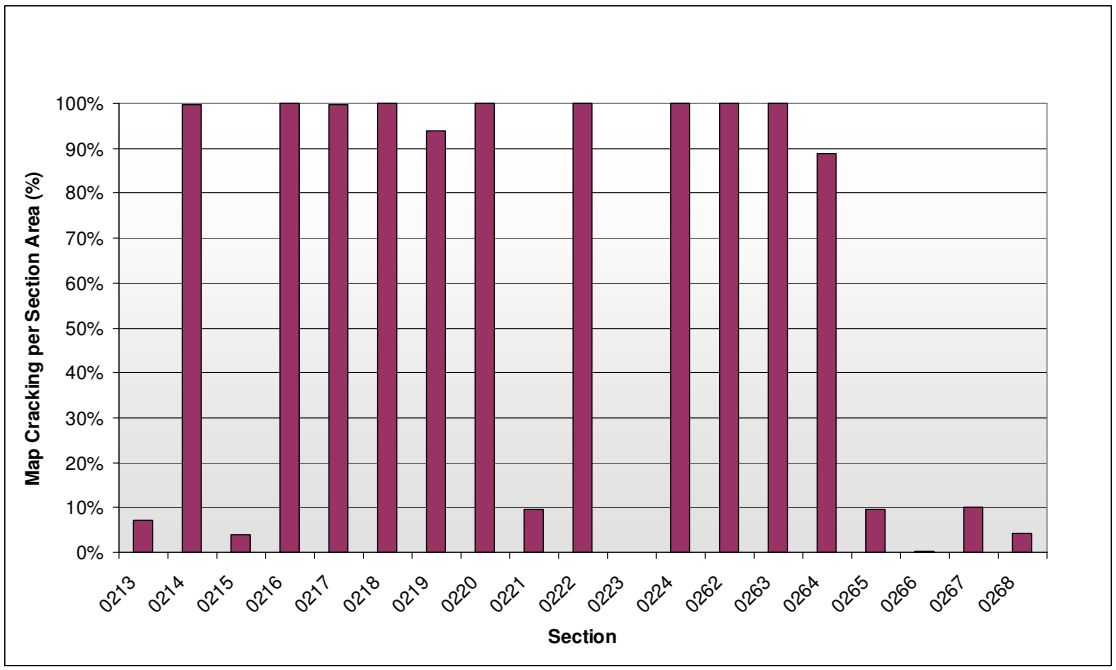

Figure 94. 2012 PCC Sections Map Cracking Summary

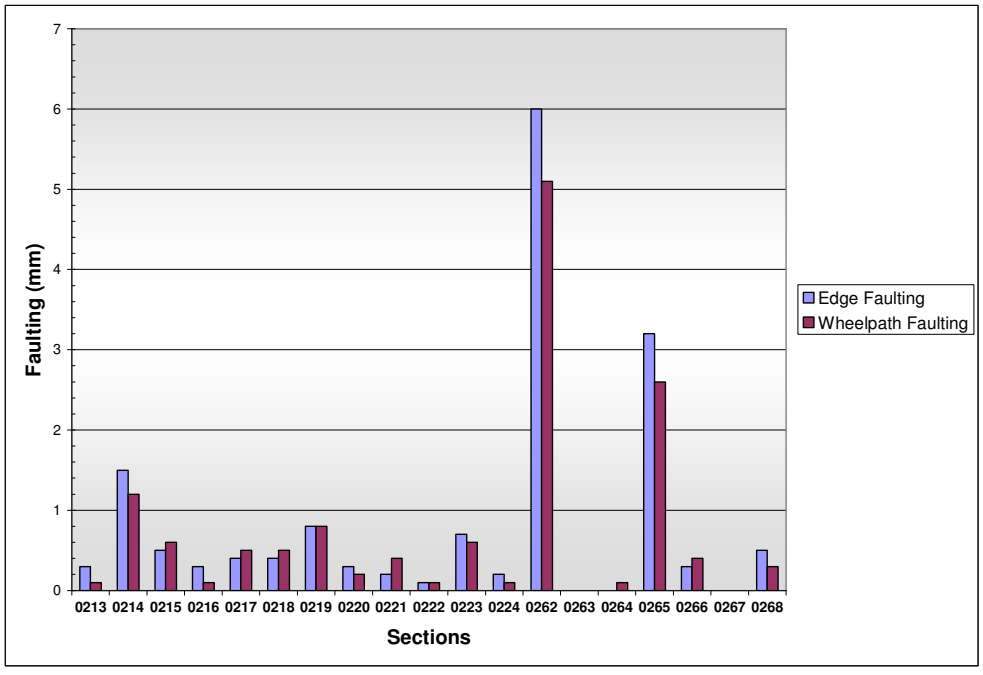

Figure 95. 2012 PCC Sections Faulting Summary

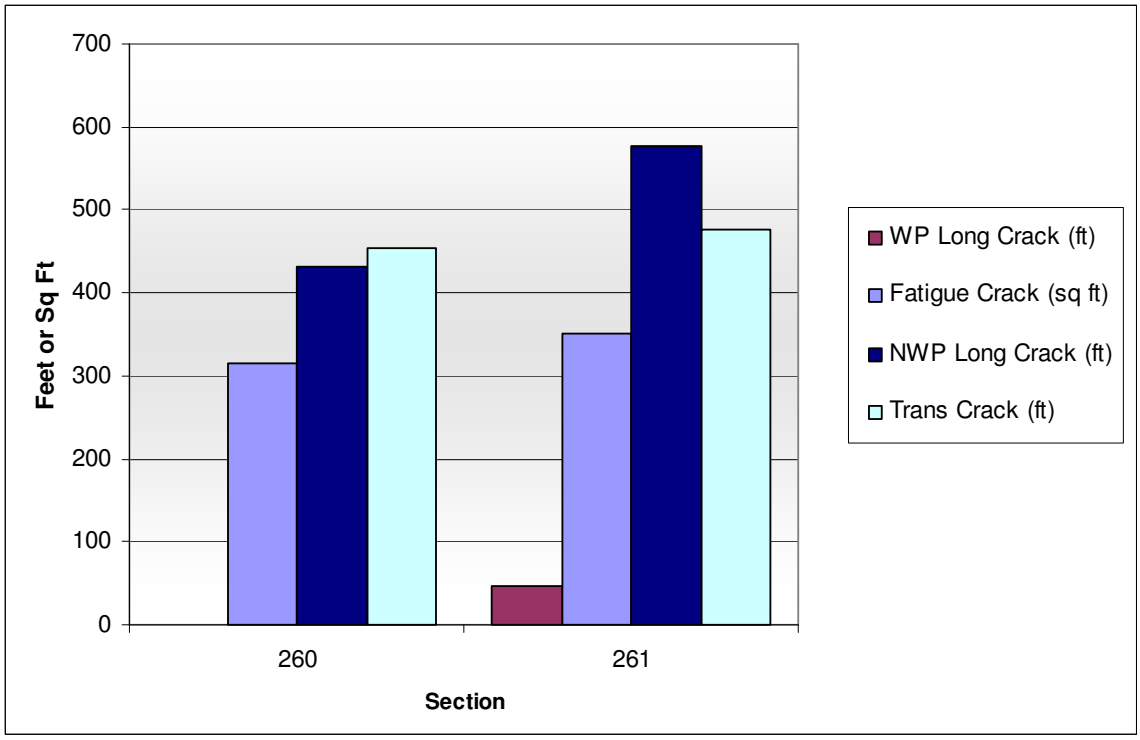

Figure 96. 2012 AC Sections Performance Summary

The following observations are for the individual sections based on structural and environmental distress trends depicted in Figures 72 to 92. The observations discuss the distress-specific trends per section. Also discussed are probable causes for sudden increases and decreases within the identified distress trends.

Core Experiment

Section 040213 (DGAB, Thin, Low Strength)

Section 040213 began to exhibit longitudinal cracking in 1998, with 22 ft observed. By 2012 the longitudinal cracking increased to 432 ft. Along with the adjacent downstream Section 040262 (DGAB), the longitudinal cracking is primarily located in the right wheelpath. The 2.2-ft^2 partial depth patching in 2009 had no effect on the distresses. The two sections also exhibited the largest lane-to-shoulder separation average (approximately 1 inch). The lane-to-shoulder separation, along with joint seal failure and longitudinal cracking occurring in the right wheelpath, suggests that the project's interlayers were affected. Lane-to-shoulder dropoff was minimal. Longitudinal spalling was observed at 15 ft in 2012. Map cracking, scaling, and polished aggregate fluctuated greatly. All three were observed in 1999. In 2003, map cracking had decreased to 213 ft^2 but then increased steadily to 515 ft^2 in 2012. In 2008, scaling had reduced to approximately 9 ft^2 and remained constant through the survey in 2012. Polished aggregate was no longer observed after the 1999 survey.

Section 040214 (DGAB, Thin, High Strength)

Section 040214 performed well against transverse and longitudinal cracking. One 5-ft transverse crack was observed in 2012, and no longitudinal cracking was observed. Approximately 1 ft of longitudinal spalling was observed in 1997 and steadily increased to 8 ft in 2010. In 2012 the longitudinal spalling spiked to 23 ft. Map cracking was observed across the entire section in 1997. The map cracking was noted as well defined in the section in 2008. In 1999 shoulder heave occurred with an average heave of about 0.25 inch. By 2012 the upward heave of the shoulder had reached an average of 0.60 inch.

Section 040215 (DGAB, Thick, Low Strength)

Section 040215 performed well against transverse and longitudinal cracking, with longitudinal cracking observed at 2 ft in 2011 and increasing by 1/3 ft in 2012. No transverse cracking was observed. Longitudinal spalling increased from 1 ft in 2000 to 37 ft in 2012. Map cracking fluctuated greatly at the beginning of the project before remaining at about 22 ft^2 from 2004 to 2012. Polished aggregate was noted in July 1996 and January 1999. Lane-to-shoulder heave increased steadily, reaching an average of 0.4 inch in 2012.

Section 040216 (DGAB, Thick, High Strength)

Section 040216 performed well against most distresses except very well-defined map cracking. A fluctuation of longitudinal cracking occurred in 1997 that was ultimately masked by the map cracking. Longitudinal spalling increased from 1 ft in 2003 to 10 ft in 2012. In 2012 the map cracking began to spall, and staining was noted around the transverse joints. No scaling or polished aggregate were observed. Lane-to-shoulder dropoff and separation were relatively small compared to other sections.

Section 040217 (LCB, Thin, Low Strength)

Section 040217 had the worst resistance to transverse and longitudinal cracking of all the PCC sections. Longitudinal cracking increased from 36 ft in 1997 to 579 ft in 2012. Transverse cracking increased from five cracks at 38 ft in 1997 to 30 cracks at 222 ft in 2012. Longitudinal spalling was noted at 7 ft in 2012. The partial depth patching that occurred in 2009 was slight — less than 1 ft^2 and only to fill largely spalled cracks — it was not recorded in the distress surveys. Map cracking was present in the entire section in 1997 and continued with two fluctuations noted in 1999 and 2000 because of rater variability. In 2012, map cracking was observed throughout the entire section along with 13 ft^2 of scaling. Lane-to-shoulder dropoff and separation were relatively small compared to the other sections.

Section 040218 (LCB, Thin, High Strength)

Section 040218 performed poorly against transverse and longitudinal cracking. Transverse cracking increased steadily from four cracks totaling 19 ft in 1997 to 22 cracks totaling 95 ft in 2012. Longitudinal cracking has fluctuated throughout the monitoring history because it was masked by map cracking. Researchers observed a sharp spike from 44 ft in 2011 to 236 ft in 2012. The partial depth patching that occurred in 2007 was slight — approximately 1 ft^2 — with only one recorded on the inside corner of a slab. Longitudinal spalling increased from 2 ft in 2000 to 37 ft in 2012. Map cracking was observed over

the entire section. In 2012 the map cracking was heavy and starting to spall, with stains on the longitudinal and transverse joints. Lane-to-shoulder dropoff and separation were relatively small compared to the other sections.

Section 040219 (LCB, Thick, Low Strength)

Section 040219 performed poorly against transverse and longitudinal cracking. Transverse cracking increased steadily from one full width crack of 12 ft in 2001 to 22 cracks totaling 161 ft in 2012. Longitudinal cracking was low, with 2 ft observed in 2003 increasing to 20 ft in 2012. Longitudinal spalling fluctuated early in the monitoring history and ultimately increased from 3 ft in 2000 to 57 ft in 2012. Map cracking was observed throughout the entire section, just under the entire area of the section. Polished aggregate was observed in 1997. Lane-to-shoulder dropoff and separation were relatively small compared to the other sections.

Section 040220 (LCB, Thick, High Strength)

Section 040220 performed well against transverse and longitudinal cracking when compared with the other LCB sections. Transverse cracking fluctuated throughout the monitoring history. Two transverse cracks were observed in 1997, 2002, and 2003, ultimately becoming indistinguishable from map cracking. Longitudinal cracking was first observed at 14 ft in 2008 and remained constant through 2012. Longitudinal spalling increased from 3 ft in 2003 to 36 ft in 2012. Lane-to-shoulder dropoff and separation were relatively small compared to the other sections. Map cracking was observed in the entire section, with a more defined pattern in the wheelpaths.

Section 040221 (PATB, Thin, Low Strength)

Section 040221 performed well against transverse and longitudinal cracking. No transverse cracking was observed. Longitudinal cracking was first observed at 26 ft in 1997 and increased to 47 ft in 2012 with some fluctuations attributable to rater variability. Longitudinal spalling increased from 6 ft in 2001 to 21 ft in 2012. Map cracking was 681 ft^2 in 2012. The section also received small amounts of fiberglass patching that was first noted in the 2004 survey. Flexible asphalt patching also occurred in 2007 and 2009; this patching was slight and did not affect the distress totals of the section. Lane-to-shoulder dropoff and separation were relatively small compared to the other sections.

Section 040222 (PATB, Thin, High Strength)

Section 040222 performed well against transverse and longitudinal cracking. Transverse cracking increased steadily from one crack of 4 ft in 2010 to seven cracks totaling 24 ft in 2012. Longitudinal cracking has remained relatively low, with 6 ft observed in 1995, increasing to 37 ft in 2012. Longitudinal spalling increased from 7 ft in 1997 to 51 ft in 2012. Map cracking was observed throughout the entire section in 2012. Map cracking in this section and in Section 040224 (the other high-strength PATB section) is not as well-defined as in the other high-strength sections. Lane-to-shoulder dropoff averaged 0.2 inch and separation averaged 0.5 inch in 2012.

Section 040223 (PATB, Thick, Low Strength)

Section 040223 performed very well against transverse and longitudinal cracking as neither of the two distresses has been observed during the monitoring history. Longitudinal spalling increased from 3 ft in 2002 to 29 ft in 2012. Early spikes in map cracking and polished aggregate were attributable to rater variability. No map cracking or polished aggregate was observed in 2012. Lane-to-shoulder dropoff and separation were relatively small compared to the other sections.

Section 040224 (PATB, Thick, High Strength)

Section 040224 performed well against transverse and longitudinal cracking. No transverse cracking was observed. Longitudinal cracking was slight, with 3 ft in 2000 increasing slowly to 10 ft in 2012. Longitudinal spalling increased from 3 ft in 2002 to 8 ft in 2012. Map cracking was observed throughout the entire section since 1997. Lane-to-shoulder dropoff and separation were relatively small compared to the other sections.

Skew-Joint Experiment

Section 040262 (DGAB, Thin, Low Strength, Undoweled)

Section 040262 exhibited 13 ft of longitudinal cracking in 2004, increasing to 116 ft. Longitudinal cracking was primarily located in the right wheelpath, similar to Section 040213. Lane-to-shoulder separation of approximately 1 inch, along with joint seal failure and longitudinal cracking occurring in the right wheelpath, suggests that the base may have been affected. No transverse cracking was observed. The partial depth patching that occurred in 2009 was slight — less than 1 ft^2 and only filling in largely spalled cracks — and therefore was not recorded in the distress surveys. Longitudinal spalling increased from 2 ft in 2001 to 24 ft in 2012. Map cracking was observed in the entire section from 2001 to 2012. This section also exhibited the worst transverse faulting, averaging 0.059 and 0.063 inches on the edge and wheelpath, respectively, in 1995 and increasing to 0.24 inch average on the edge and 0.20 inch average in the wheelpath.

Section 040263 (PATB, Thin, Low Strength, Undoweled)

Section 040263 exhibited transverse cracking that increased steadily from one 8-ft crack in 2008 to two cracks totaling 16 ft in 2012. Longitudinal cracking was first observed in 1997 at 1 ft, with no cracking noted in 1999 and 2000, and increased steadily to 72 ft in 2012. Longitudinal spalling was measured at 11 ft in 2012. Map cracking was observed throughout the section from 2001 to 2012. Small areas of scaling were observed in 2011 and 2012 totaling 6 ft^2.

Section 040264 (PATB, Thick, Low Strength, Undoweled)

Section 040264 performed very well against transverse and longitudinal cracking; neither distress was observed during the monitoring history. Longitudinal spalling increased from 1 ft in 1995 to 59 ft in 2012. Map cracking was observed throughout the entire section from 1999 to 2012. Scaling increased from 358 ft^2 in 2004 to 695 ft^2.

Section 040265 (DGAB, Thick, Low Strength)

Section 040265 performed very well against transverse and longitudinal cracking; neither distress was observed during the monitoring history. Longitudinal spalling increased from 10 ft in 2004 to 32 ft in 2012. Map cracking fluctuated greatly early in the monitoring history before remaining about 575 ft^2 in 2011 and 2012. Irregular surface characteristics were noted. This section also exhibited significant transverse faulting, which averaged 0.051 on the edge and 0.055 inches in the wheelpath in 1995. By 2012, faulting had increased to 0.13 inch average on the edge and 0.10 inch average in the wheelpath.

State 406 BTB Experiment

Section 040266 (BTB, Thick, Low Strength)

Section 040266 performed well against transverse and longitudinal cracking, with only 2 ft of longitudinal cracking in 2011 and 2012. Longitudinal spalling was noted at 8 ft in 2012. Map cracking and polished aggregate fluctuated in the monitoring history before remaining at about 10 ft^2 of map cracking in 2011 and 2012. Irregular surface characteristics were noted in surveys. Two transverse spalls totaling 7 ft were also observed in 2012. Lane-to-shoulder dropoff was minimal.

Section 040267 (BTB, Thick, Low Strength)

Section 040267 performed well against transverse and longitudinal cracking; neither distress was observed during the monitoring history. Longitudinal spalling was minimal. Map cracking and polished aggregate fluctuated in the monitoring history before remaining at 708 ft^2 of map cracking in 2011 and 2012. Irregular surface characteristics of this section were noted. The section received diamond grinding between 2004 and 2008 for the installation of weigh-in-motion sensors within the test section. The diamond grinding eliminated the previous polished aggregate ratings. Scaling was observed to be 50 ft^2 in 2012. Lane-to-shoulder dropoff was minimal.

Section 040268 (BTB, Thin, Low Strength)

Section 040268 performed well against transverse and longitudinal cracking, with only 1 ft of longitudinal cracking observed in 2011 and 2012. Longitudinal spalling was minimal, with 3 ft in 2012. Map cracking and scaling fluctuated during the monitoring history. Irregular surface characteristics were noted. In 2012, 292 ft^2 of scaling and 298 ft^2 of map cracking were observed. Lane-to-shoulder dropoff was minimal.

Flexible Experiment

Section 040260 (AC, DGAB)

Section 040260 began exhibiting transverse cracking in 2004 with 46 ft, increasing to 454 ft in 2012. Nonwheelpath longitudinal cracking was 41 ft in 2001 and increased rapidly to 431 ft in 2012. Wheelpath longitudinal cracking was 28 ft in 2001. Fatigue cracking increased from 22 ft^2 in 1999 to

315 ft^2 in 2012. Fluctuating raveling was observed throughout the section, attributable to rater variability. In 2012 raveling occurred in 3281 ft^2 of both wheelpaths.

Section 040261 (AC, DGAB)

Section 040261 began exhibiting transverse cracking in 2001 with 5 ft, increasing to 477 ft in 2012. Nonwheelpath longitudinal cracking was 81 ft in 1999 and remained relatively constant until increasing to 248 ft in 2004. In 2012, the nonwheelpath cracking reached 577 ft. Wheelpath longitudinal cracking was 16 ft in 2001, 29 ft in 2010, and 47 ft in 2012. Fatigue cracking fluctuated throughout the study and is attributed to segregation occurring in the right wheelpath in 1999. Fatigue fluctuated because of rater variability and was observed at 374 ft^2 in 1999, then spiked to 823 ft^2 in 2000 before being observed at 352 ft^2 in 2012. Rater variability also attributed to fluctuating raveling values throughout the section. From 2004 to 2012, raveling occurred in 3281 ft^2 of both wheelpaths. This section performed almost identically to Section 040260, which could indicate that the in situ conditions throughout the SPS-2 site remained relatively consistent.

KEY FINDINGS FROM THE SPS-2 DISTRESS ANALYSIS

The SPS-2experimental design did not offer replicate treatments to verify findings. Conclusions drawn from this comparison are based on one set of in situ conditions; observations from other climate or loading scenarios may differ from those noted within this report. Therefore, findings reported may be unique to the conditions and construction of this site.

The data captured at the project provides valuable insight into pavement performance, design, management, and construction, as described in the following sections.

Performance

In terms of pavement distress, Section 040223 demonstrated the top performance among all SPS-2 test sections. Section 040223 exhibited the least amount of distresses, including cracking, spalling, and faulting. Section 040215 and Section 040266 performed as well as Section 040223 in certain distresses, however both exhibited map cracking, and Section 040215 exhibited an average lane-to-shoulder dropoff of 0.4 inch. Section 040216 and the other State 406 BTB mix sections (040267 and 040268) all performed similarly as Section 040223 in most distresses, but worse than Section 040223 in surface defects such as map cracking and scaling.

Section 040217 had the greatest amount of distresses among all the test sections in the SPS-2 project. The section exhibited the largest and earliest cracking, ultimately reaching the greatest amount of both transverse (in number and length) and longitudinal cracking in the project.

Two of the undoweled skewed supplemental sections, Sections 040262 and 040265, exhibited the worst faulting performance. Section 040262 had an average joint/crack faulting of 0.22 inch, and Section 040265 had faulting of 0.11 inch.

Core Section Performance by Structural Feature

Sections with LCB material (040217, 040218, 040219, and 040220) performed more poorly in resisting longitudinal and transverse cracking than sections with PATB and DGAB material. Section 040220 performed very well as an exception to the trend. Contributing to its performance are the thick, high-strength and wide-slab PCC attributes. Sections with only DGAB material (040213, 040214, 040215, and 040216) on average performed slightly better than sections with PATB material in regards to transverse and longitudinal cracking. Section 040213 was an exception to the trend as longitudinal cracking greatly affected the right wheelpath of the PCC slab. This could be due in part to the structural strength and thickness of the section and the large lane-to-shoulder separation and dropoff of the section. Section 040223 was also an exception to the trend, performing very well in regards to all distress.

Sections with high-strength (900-psi) PCC (040214, 040216, 040218, 040220, 040222, and 040224) performed better in longitudinal and transverse cracking than sections with low-strength (550 psi) PCC of the same thickness (040213, 040215, 040217, 040219, 040221, and 040223). This trend includes a slight bias considering that the sections vary in width, where a greater width has been shown to improve the fatigue life and 2 ft of widened slab is equivalent to about 1 inch of slab thickness (Yu et al. 1995). High-strength sections also exhibited well defined and large amounts of map cracking throughout the PCC. Researchers conducted a preliminary investigation on one core taken from Section 040218 and noted that ASR was visible; however the amount was very minor and did not appear to be the cause of the map cracking at the surface. The exact cause of the defect requires more investigation.

Sections with a thick (11-inch) PCC surface (040215, 040216, 040219, 040220, 040223, and 040224) performed better in resistance to longitudinal and transverse cracking than sections with a thin (8-inch) PCC surface (040213, 040214, 040217, 040218, 040221, and 040222). Even when considering the effect of a widened slab, the thick sections showed greater performance.

As mentioned in the FWD analysis, the half-factorial experimental design would include many confounding factors in a comparison of slab width, especially when considering resistance against transverse and longitudinal cracking. In regard to lane-to-shoulder dropoff, wider slabs on average have a higher resistance compared to narrower slabs.

Supplemental Section Performance

The AC sections performed very similar to each other, suggesting that the in situ conditions throughout the SPS-2 site remained relatively consistent as the sections are on opposite ends of the project.

The skewed joint, untied sections (040262, 040263, 040264, and 040265) performed similarly against cracking to the tied, core section counterparts (040213, 040221, 040223, and 040215, respectively). The exception to the trend is Section 040262, which performed better than Section 040213. However, the sections performed worse in resistance in transverse faulting, with Section 040265 and 040262 having the highest faulting of the SPS-2 project. Irregular surface characteristics were also observed in the skewed joint sections.

The State 406 BTB mix sections (040266, 040267, and 040268) performed very well compared to the other sections in the SPS-2 project. No transverse cracking was observed. Longitudinal cracking was observed at 2 ft and 1 ft in Sections 040266 and 040268, respectively. Longitudinal spalling is less than 10 ft throughout the sections, and as of 2012, Section 040266 has two transverse spalls measured at approximately 7 ft total. Irregular surface characteristics were observed throughout the sections, with map cracking and scaling observed in the 2012 survey.

Conclusions

Additional conclusions of the distress analysis follow:

- Sections with LCB material had the worst performance for transverse and longitudinal cracking while sections built on DGAB and PATB performed relatively similar in resisting transverse and longitudinal cracking.
- Thicker sections performed better than thinner sections when comparing cracking resistance.
- Higher strength sections appeared to perform better than low strength for longitudinal and transverse cracking. However, significant map cracking was observed in these sections, especially in the vicinity of the joints. A preliminary ASR investigation based on stereo microscopy of one core indicated the primary cause was not ASR, although some ASR was observed. A more detailed petrographic evaluation conducted in accordance with ASTM C856 should be conducted to determine the cause of the map cracking as it is clearly linked to a materials-related distress.
- The advantage of the drainage in PATB sections is not apparent in the particular conditions of the SPS-2 project.
- The State 406 BTB mix performed well in regard to distress, especially against transverse and longitudinal cracking.
- Wide slabs on average have a greater resistance to lane-to-shoulder dropoff than narrow slabs with the exception of Section 040220, which exhibited an average of 0.35 inch.
- Undoweled sections performed similarly to the core sections in regard to cracking; however undoweled sections exhibited more joint and crack faulting.
- The AC supplemental section performance indicates the in situ conditions remained consistent.
- With no replicate sections, there is limited ability to assess potential variability independent of actual performance.

CHAPTER 4. SPS-2 ROUGHNESS ANALYSIS

Road profile measurements were collected on this site about once per year since the winter after the road was opened to traffic. Profile data were also collected on 16 additional dates on Section 040215 as part of the SMP. Researchers analyzed the profiles in detail using profile analysis methods employed in other Arizona SPS studies (Karamihas and Senn 2009; Karamihas and Senn 2010), which included calculating roughness index values, examining the spatial distribution of roughness within a section, viewing profiles with post-processing filters, and examining their spectral properties. The study applied the traditional analysis methods to the AC sections (040260 and 040261) to treat them as control sections for comparison to the PCC sections.

Curl and warp analysis has been previously performed on the Arizona SPS-2 site (Karamihas and Senn 2012). This study applied algorithms for estimating the level of curl and warp present in the pavement and its effect on surface roughness. Appendix C provides the detailed findings from this analysis, including updated figures containing data from visit 16 (December 8, 2011).

PROFILE DATA SYNCHRONIZATION

Profile data were collected from the entire SPS-2 site on 16 dates (Table 40). A minimum of seven repeat profile measurements were made at each visit. The measurements for all visits included Sections 040213, 040224, 040260, and 040268.

Researchers also collected profile data on 16 additional dates over Section 040215 as part of the SMP. On most of the measurement dates for this section, profiles were collected in the morning and the afternoon. In others, the profiles were collected in the early and late morning. Each group of runs is treated in this report as a distinct visit. Table 41 lists the dates and times of each group of runs. These visits cover four seasons in 1998 and 12 consecutive seasons starting in winter 2001.

DATA EXTRACTION

Profiles of individual test sections were extracted directly from the raw measurements and aligned using an automated trace comparison algorithm. This was done for two reasons. First, profiles were collected in visits 03 through 08 and S01 through S14 at a 0.98-inch sample interval and in visits 09 through 11 and S15 through S28 at a sample interval of about 0.77 inches. These data appeared in the database after the application of an 11.8-inch moving average and decimation to a sample interval of 5.91 inches. The raw data contained the more detailed profiles.

Second, this study depended on consistency of the profile starting and ending points with the construction layout and consistency of the section limits with time.

Table 40. Profile Measurement Visits of the SPS-2 Site

Visit	Date	Time	Repeats
01	Jan. 25, 1994	06:10	9
02	March 5, 1995	11:21	9
03	Jan. 27, 1997	11:23-12:49	9
04	Dec. 4, 1997	11:06-13:07	7
05	Dec. 8, 1998	10:29-11:27	7
06	Nov. 15, 1999	11:39-12:39	7
07	Nov. 30, 2000	13:38-15:01	9
08	Nov. 8, 2001	11:09-12:40	9
09	Oct. 30, 2002	12:41-14:07	9
10	Feb. 4, 2004	13:47-15:12	9
11	Dec. 12, 2004	16:16-18:37	9
12	Aug. 11, 2006	04:18-06:26	9
	Aug. 13, 2006	00:17-04:28	9
13	Dec. 30, 2007	10:06-13:21	9
14	Sept. 20, 2008	00:37-03:36	9
15	Jan. 25, 2010	16:09-19:00	9
16	Dec. 8, 2011	19:57-22:40	9

Table 41. Seasonal Visits of Section 040215

Visit	Date	Repeats	Time
S01	Jan. 15, 1998	7	11:33-11:53
S02	Jan. 15, 1998	5	16:43-16:52
S03	April 13, 1998	5	10:13-10:30
S04	April 13, 1998	5	15:20-15:31
S05	July 9, 1998	5	08:23-08:45
S06	July 9, 1998	5	12:11-12:26
S07	Sept. 30, 1998	5	11:59-12:15
S08	Sept. 30, 1998	7	14:34-15:05
S09	Dec. 9, 2001	7	09:21-09:46
S10	Dec. 9, 2001	9	14:58-15:30
S11	Jan. 24, 2002	7	10:12-10:38
S12	Jan. 24, 2002	9	14:56-15:33
S13	March 15, 2002	7	09:40-10:11
S14	March 15, 2002	7	14:30-15:01
S15	Oct. 9, 2002	9	08:43-09:34
S16	Oct. 9, 2002	9	13:47-14:35
S17	Dec. 20, 2002	9	09:05-09:43
S18	Dec. 20, 2002	9	13:24-14:08
S19	March 7, 2003	9	09:24-09:54
S20	March 7, 2003	9	13:57-14:37
S21	July 25, 2003	9	04:24-05:06
S22	July 25, 2003	9	08:34-09:12
S23	Nov. 24, 2003	9	09:32-10:17
S24	Nov. 24, 2003	9	14:23-15:04
S25	Dec. 14, 2003	9	10:33-11:10
S26	Dec. 14, 2003	9	15:16-15:56
S27	April 22, 2004	9	04:59-05:38
S28	April 22, 2004	9	09:49-10:25
S29	July 15, 2004	9	04:17-04:50
S30	July 15, 2004	9	09:02-09:40
S31	Sept. 9, 2004	9	08:35-09:05
S32	Sept. 9, 2004	9	15:53-16:25

CROSS CORRELATION

Searching for the longitudinal offset between repeat profile measurements that provides the best agreement between them is a helpful way to refine their synchronization. This can be done by inspecting filtered profile plots, but it is very time-consuming. Visual assessment is also somewhat subjective when two profiles do not agree well, which is often the case when measurements are made several years apart. An automated procedure, rather than visual inspection, was used for finding the longitudinal offset between measurements.

The procedure is based on a customized version of cross correlation (Karamihas 2004). In this procedure, a basis measurement is designated that is considered to have the correct longitudinal positioning. A candidate profile is then searched for the longitudinal offset that provides the highest cross correlation to the basis measurement. A high level of cross correlation requires a good match of profile shape, the location of isolated rough spots, and overall roughness level. Therefore, the correlation level is often only high when the two measurements are synchronized. (For these profiles great care was required because local peaks in correlation were observed each 15 ft, when joints from the two profiles were aligned. However, the highest correlation level was only observed when the profiles were truly synchronized.) When the optimal offset is found, a profile is extracted from the candidate measurement with the proper overall length and endpoint positions. For the rest of this discussion, this process will be referred to as automated synchronization.

For this application, cross correlation was performed after the International Roughness Index (IRI) filter was applied to the profiles rather than using the unfiltered profiles. This helped assign the proper weighting to relevant profile features. In particular, it increased the weighting of short-wavelength roughness that may appear at joints. This enhanced the effectiveness of the automated synchronization procedure. The long-wavelength content within the IRI output helped ensure the longitudinal positioning was nearly correct, and the short-wavelength content was able to leverage roughness near joints to fine-tune the positioning.

Synchronization

In visits 01 through 11, the profiler covered all test sections in each pass with a single, long run. In visits 12 through 16 the profiler covered portions of the site in each pass, and the site was split into either four or five groups of test sections.

Profiles of individual test sections were extracted from the raw measurements using the following steps:

1. Establish a basis measurement for each section from visit 08.

   This was done using the event markers from a raw measurement. The first repeat measurement was used for this purpose. Event markers appeared at the start of every section and appeared at the end of every section except 040214. The locations of the event markers were compared to the layout provided in the construction report (Szrot 1994). They exhibited a linear relationship with a bias of less than 0.014 percent, and no individual section starting point differed by more than 5 ft. All of the sections were assumed to begin at the appropriate event marker and continue for 500 ft.

2. Automatically synchronize the other eight repeats from visit 08 to the basis set.

3. Automatically synchronize the measurements from the previous visit to the current basis set.

4. Replace the basis set with a new set of synchronized measurements from the first repeat of the current visit.

5. Repeat steps 3 and 4 until visit 01 is complete.

Data for visits 09 through 16 were provided after visits 01 through 08 were synchronized. Visits 09 through 16 were synchronized using steps 3 through 5, but going forward in time.

LONGITUDINAL DISTANCE MEASUREMENT

The basis set of profile measurements for visit 08, established in step 1, was done using the event markers in one raw profile measurement (the first repeat). The other eight repeats from visit 08 were automatically synchronized to the basis set. When the longitudinal placement of the individual sections within each measurement were compared to the layout within the basis set, the slope of the linear fit ranged from 0.9995 to 1.0000. Thus, the longitudinal distance measurement for the nine profile measurements of visit 08 was consistent within 0.05 percent. This is a very high level of agreement in longitudinal distance measurement.

Figure 97 shows the disagreement in longitudinal distance measurement for visits 01 through 11 using the original basis set as a reference (Szrot 1994). In the figure, a range of disagreement for each visit exists because up to nine repeat profile measurements were made. The variation between repeat measurements within a visit appears as the width of each bar in the figure. Since the longitudinal distance measurement was based on the rotation of a drive wheel, the variations were most likely caused by variations in speed, lateral wander, and tire inflation pressure (Karamihas et al. 1999). If tire inflation pressure were the dominant cause, the disagreement would grow more positive with each successive repeat measurement as the tire heated up because the tire rolling radius would increase and the profiler would register less wheel rotation for the same travel distance. This appeared to be the case for visits 04 through 10, but the effect was never greater than 0.10 percent of the overall distance.

The variation between visits in Figure 97 is caused by differences in distance measurement instrument calibration. The longitudinal distance measured by a profiler is not true horizontal distance. It always includes some additional component because the profiler must travel up and down the undulations in the road. This component can be minimized by calibrating the profiler to true horizontal distance. However, if a profiler operates on a road with grade changes and roughness that are not similar to the site used for longitudinal distance measurement calibration, some error will exist. Tire inflation pressure must also be close to the level that existed during calibration for consistent results.

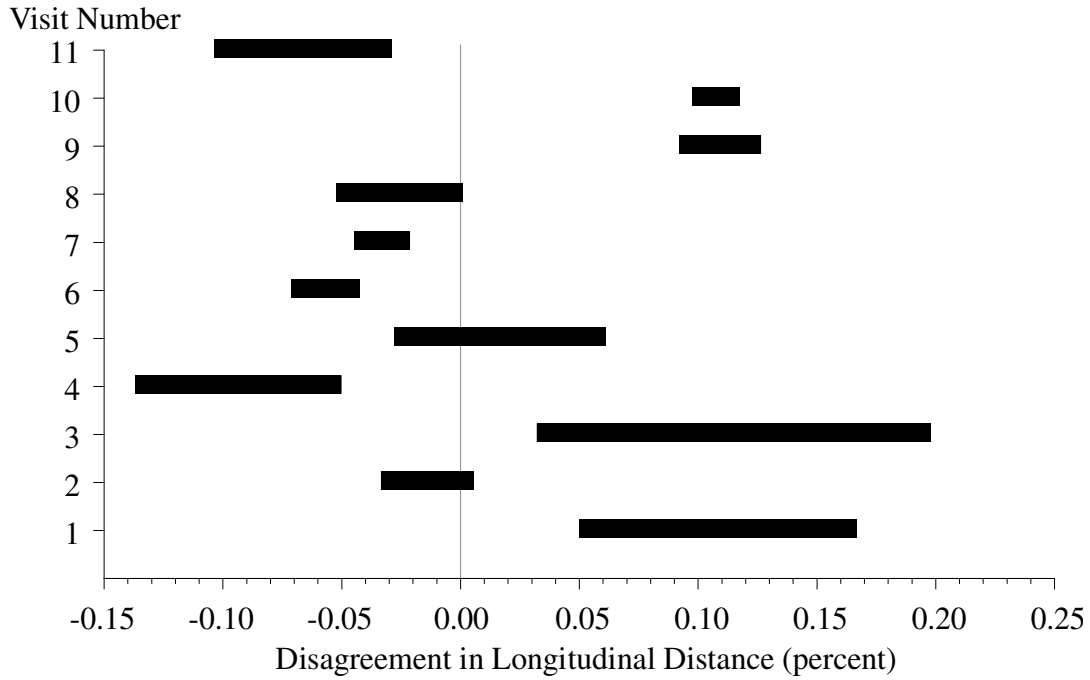

Figure 97. Consistency in Longitudinal Distance Measurement

Modest inconsistency in longitudinal distance measurement between visits is not critical as long as the profiles of individual sections are extracted using event markers rather than longitudinal distance from the start of each profile measurement. A high level of inconsistency, however, could interfere with comparisons between profile features and distress surveys. Errors in profile index values, such as the IRI, are also roughly of the same order as errors in longitudinal distance measurement (Karamihas et al. 1999). Figure 97 shows that longitudinal distance was measured with a very high level of agreement throughout all 11 visits.

DATA QUALITY SCREENING

Each visit of each test section included five, seven, or nine repeat profile measurements. Data quality screening was performed to select five repeat profile measurements per section from each visit. The five measurements among the group of available runs were selected that exhibited the best agreement with each other. In this case, agreement between any two profiles was judged by cross-correlating them after applying the IRI filter rather than the overall IRI values. This method compares the profile traces rather than the overall index. Achieving high correlation requires that the details of the profile shape affecting roughness agree as well as the overall roughness level (Evans and Eltahan 2000).

The average correlation level produced by these calculations provided a numerical assessment of the repeatability within each set of repeat measurements. Overall, most sets of selected repeat measurements exhibited good repeatability. In some cases, localized surface distress reduced repeatability in some areas. The inconsistency in profile in these areas occurred because of slight

variations in the lateral tracking position of the profiles as the profiler passed over transversely inconsistent surface features. The most prominent example of this occurred in the later visits of Section 040213 on the left side of the lane.

Appendix A describes the process of selecting five repeat measurements for each visit of each section, and provides a list of the selected profiles with a repeatability score. Appendix B provides the standard deviation of left and right IRI values for each set of repeat measurements.

SUMMARY ROUGHNESS VALUES

Figures 98 through 118 show left and right IRI versus time for all 21 test sections; "years" is defined as the number of years between the measurement date and the date the site was opened to traffic (October 1, 1993). For most of the sections, this includes 32 summary IRI values: two per visit over 16 visits. Section 040215 includes several extra IRI values from seasonal visits (Table 41).

To supplement the plots, Appendix B also lists the IRI, Half-car Roughness Index (HRI), and Ride Number (RN) of each section for each visit. These roughness values are the average of the five repeat measurements selected in the data quality screening; they are not necessarily the same five repeat measurements selected for the LTPP public database. Appendix B also provides the standard deviation of IRI over the five repeat measurements. This helps identify erratic roughness values that are the result of transverse variations in profile caused by surface distresses.

Figures 98 through 118 provide a snapshot of the roughness history of each pavement section. In Figure 98, the IRI in Section 040213 increases overall, but the roughness does not increase consistently as time progresses. For example, the IRI values in visit 01 (0.32 years) are greater than the values in visit 02 (1.42 years), and the IRI values in visit 12 (12.86 years) are much greater than in visit 11 (11.20 years) or visit 13 (14.25 years). In addition, the right IRI increases over the three visits — visit 13 (14.256 years), 14 (14.92 years), and 16 (16.32 years) — whereas the left IRI does not. The analyses described below show that the first two observations owe to diurnal changes in curl and warp, and the third does not.

In Section 040215, the IRI progression also reverses direction many times. The eras from four to six years and eight to 11 years includes several pairs of IRI values from two different times on the same day, and a series of seasonal measurements. Of the 16 diurnal pairs collected in Section 040215 (see Table 41), the later set of repeat measurements produced IRI values that were between 2.2 inches/mi above and 19.0 inches/mi below the earlier set of repeat measurements from the same day. In addition, the four seasonal visits that took place in year 9 produced a range of IRI values of 27.2 inches/mi on the left side and 20.5 inches/mi on the right side.

The analyses described below explain the inconsistent progression in IRI in all the test sections and showed that some short-term changes in IRI are due to curl and warp. The remainder of this chapter is devoted to characterizing the profile content that made up the roughness and explaining the profile features that contributed to roughness progression.

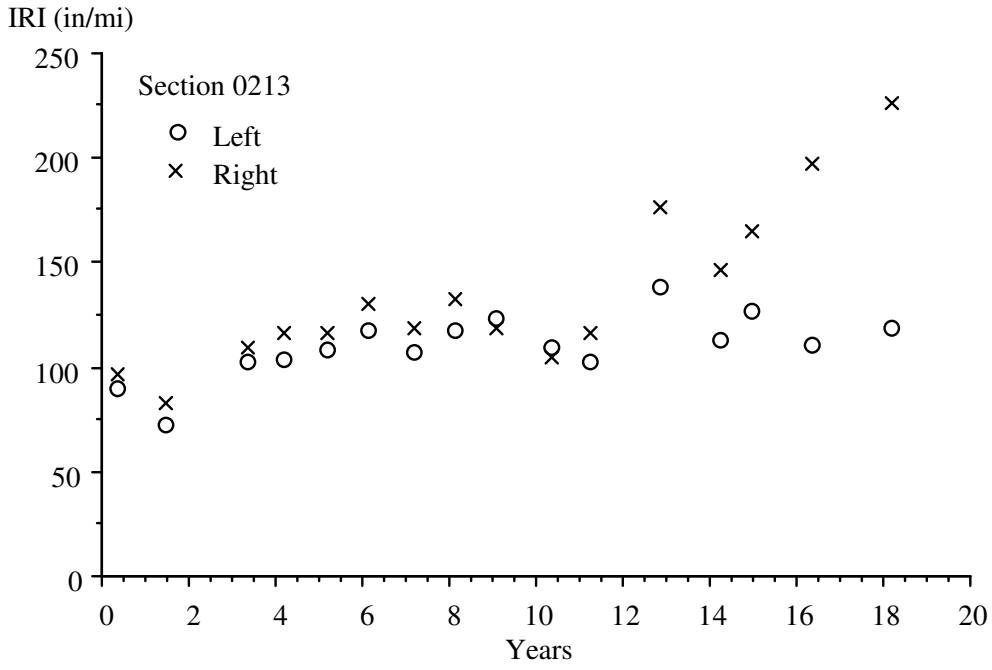

Figure 98. IRI Progression in Section 040213

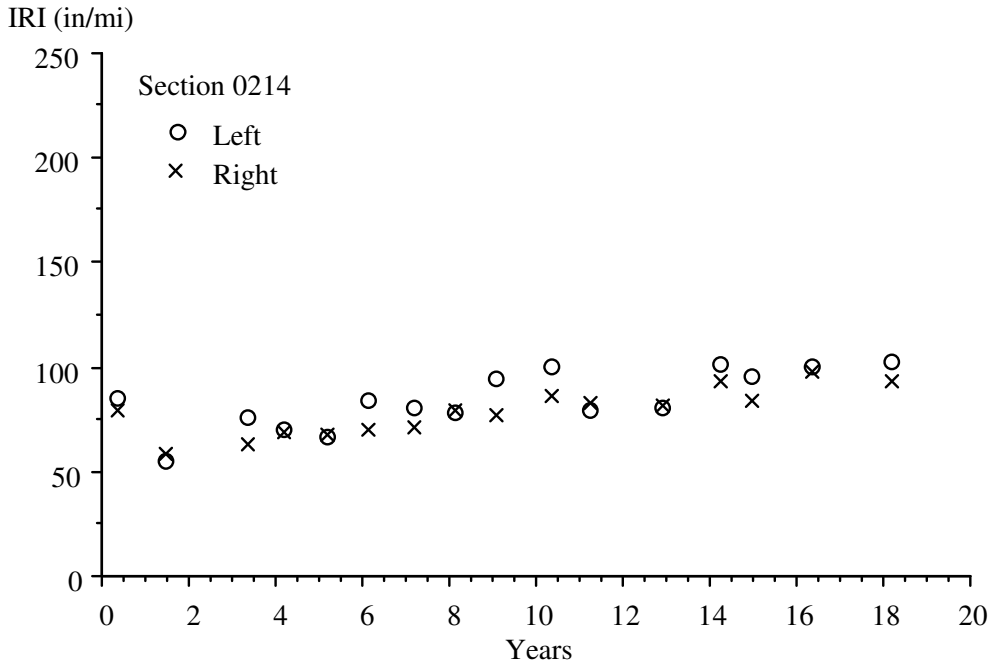

Figure 99. IRI Progression in Section 040214

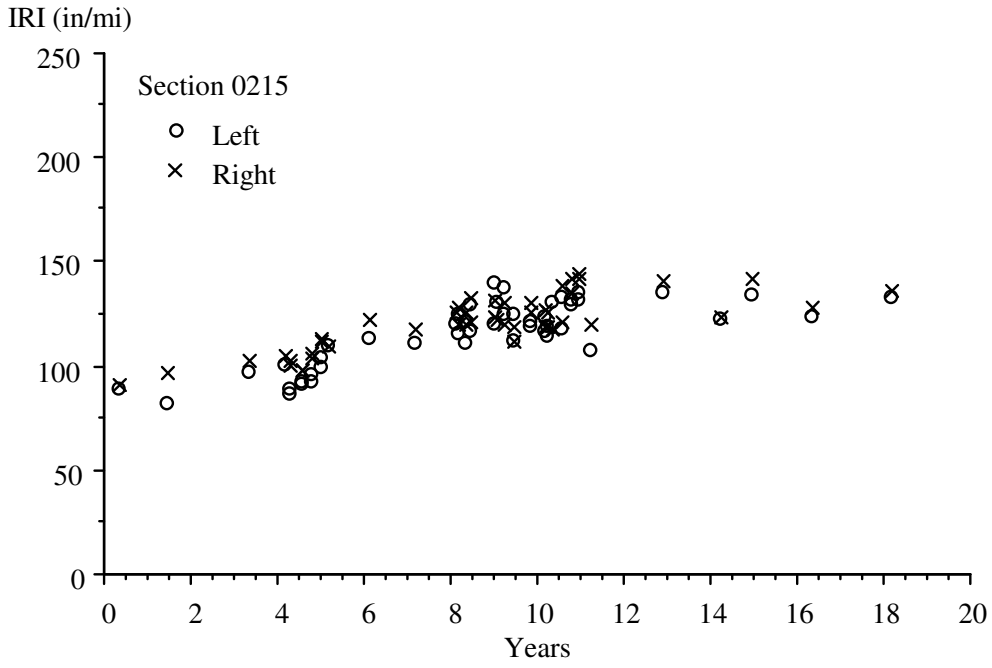

Figure 100. IRI Progression in Section 040215

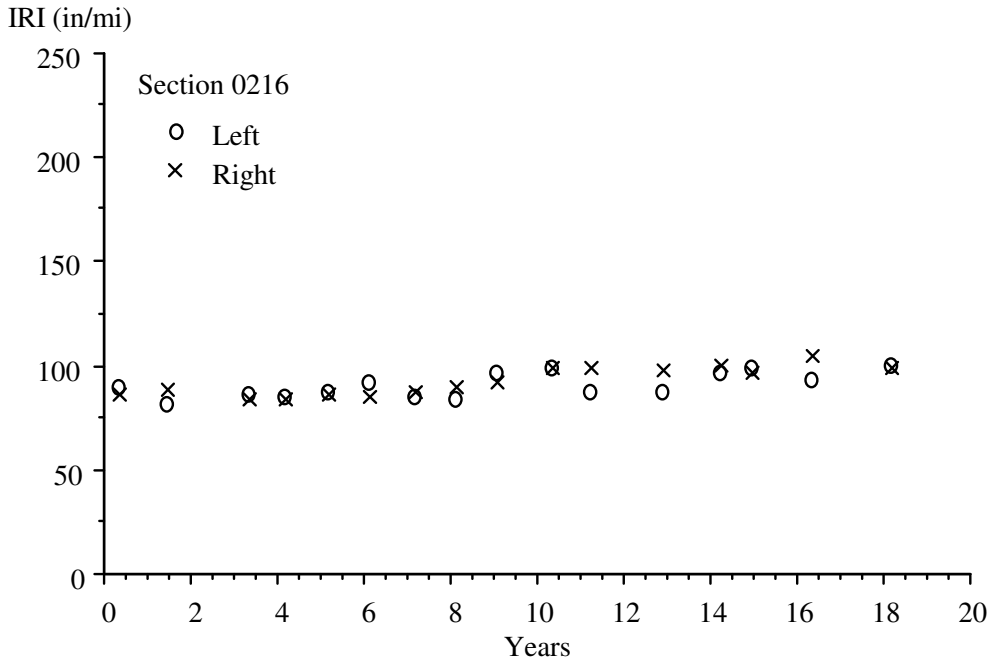

Figure 101. IRI Progression in Section 040216

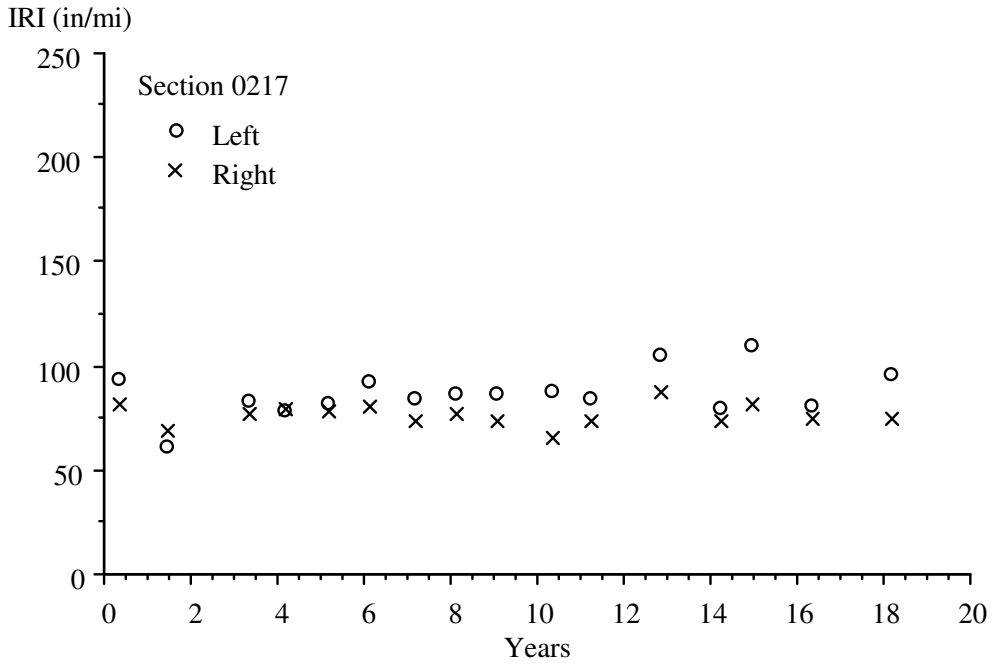

Figure 102. IRI Progression in Section 040217

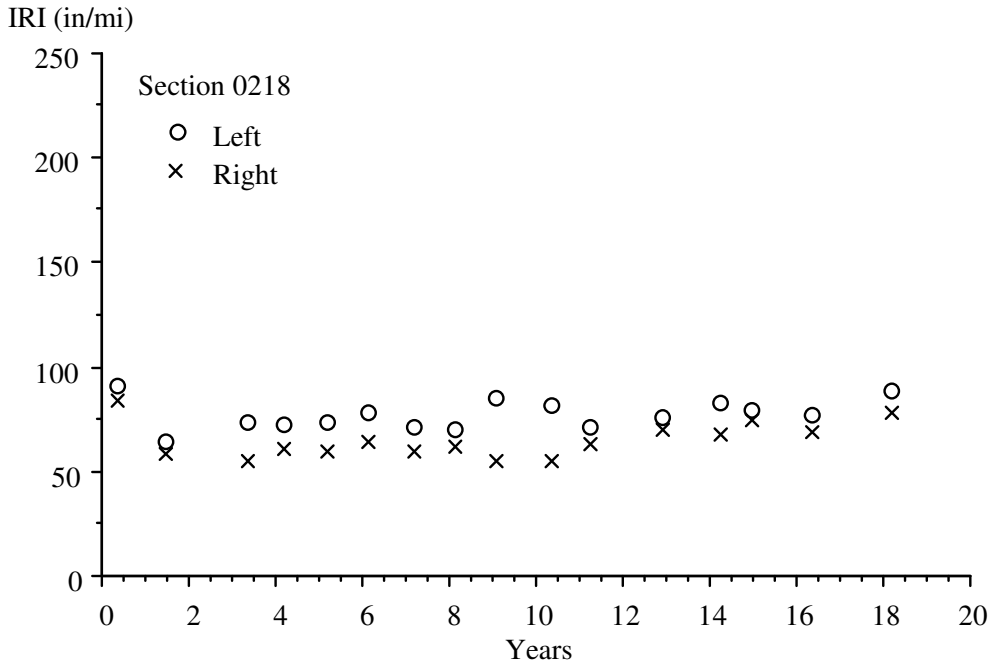

Figure 103. IRI Progression in Section 040218

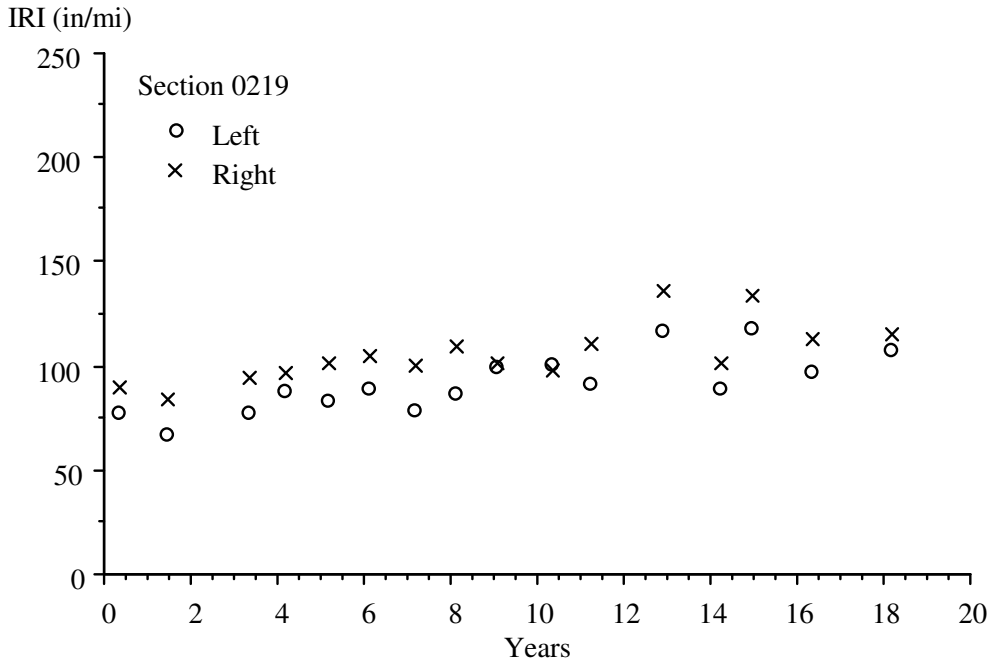

Figure 104. IRI Progression in Section 040219

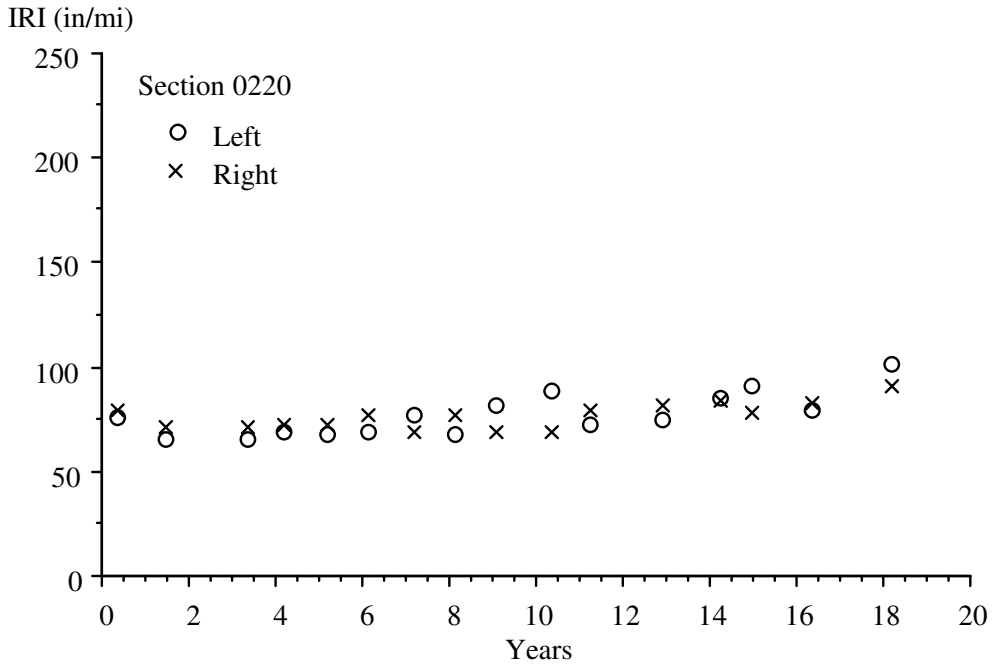

Figure 105. IRI Progression in Section 040220

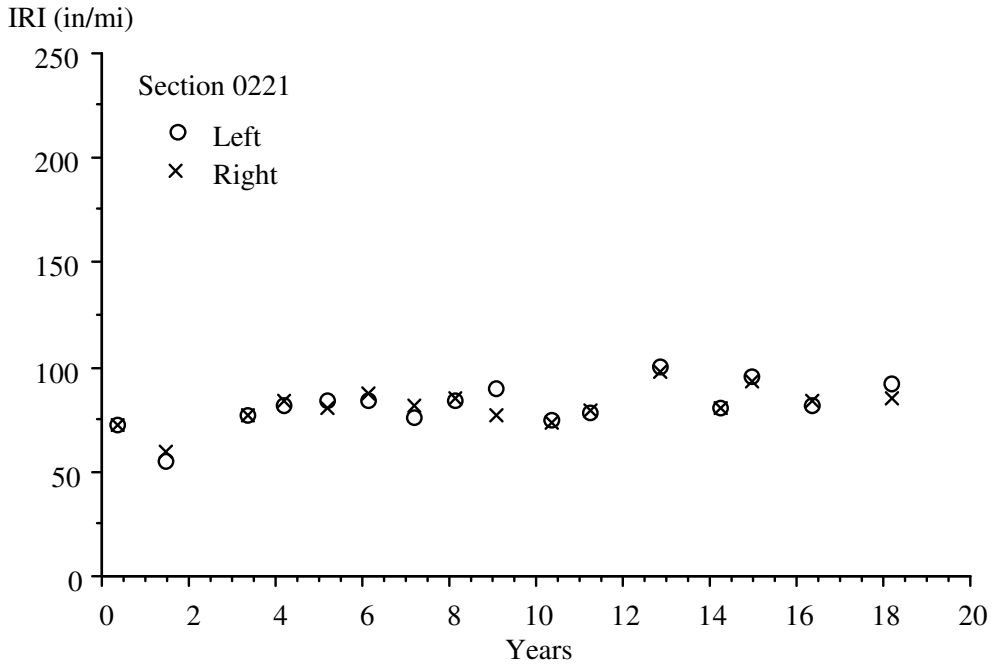

Figure 106. IRI Progression in Section 040221

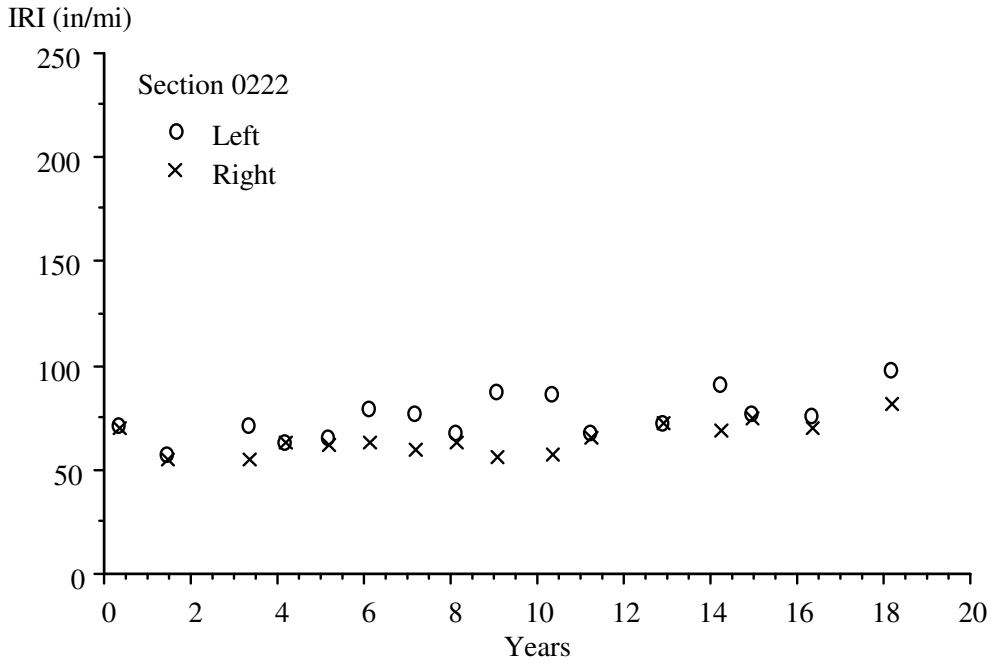

Figure 107. IRI Progression in Section 040222

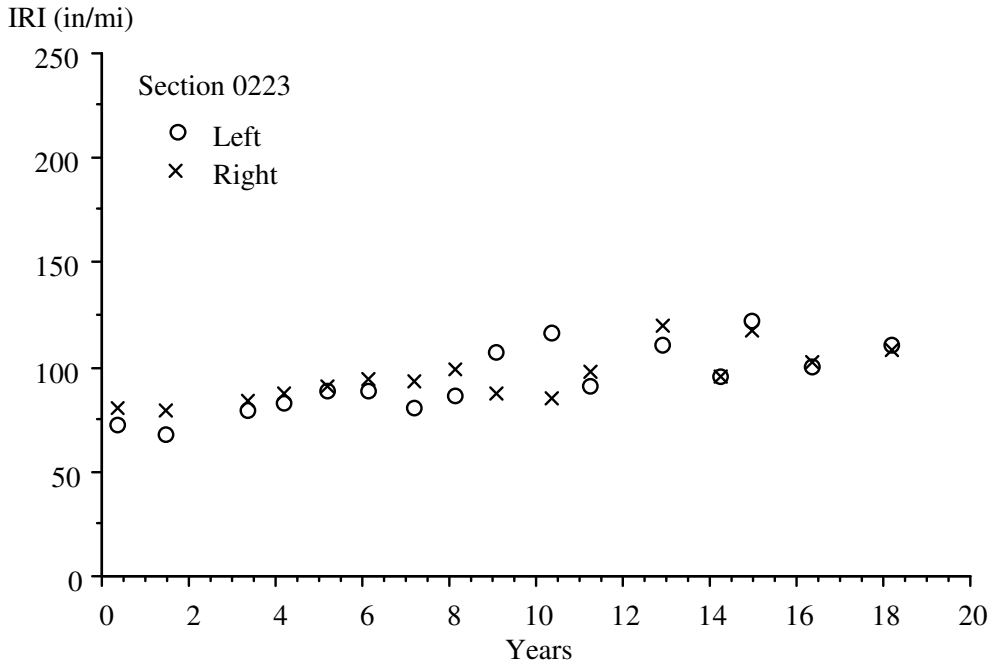

Figure 108. IRI Progression in Section 040223

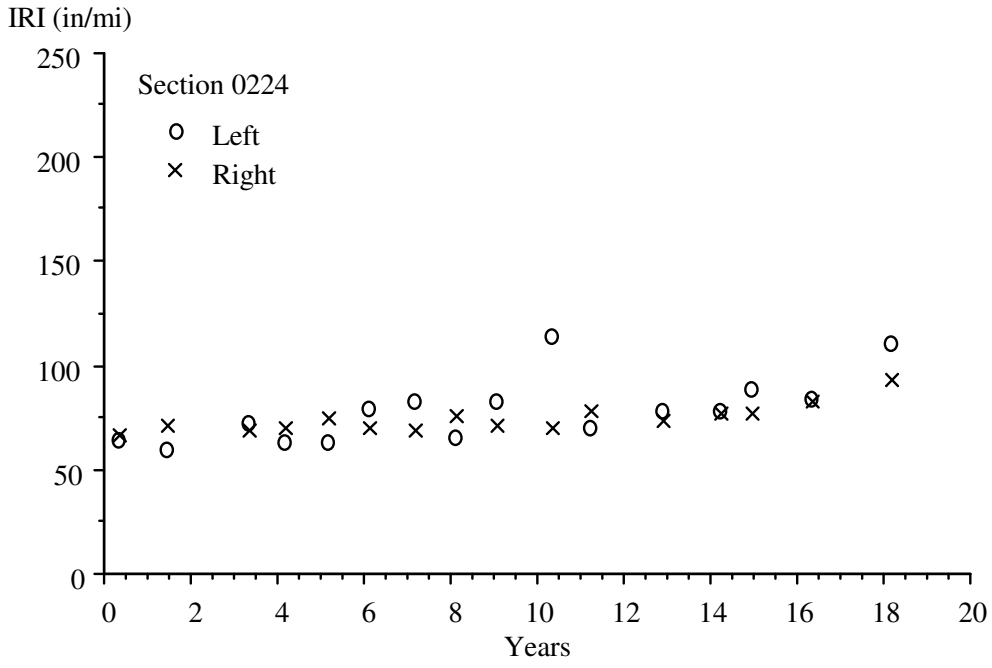

Figure 109. IRI Progression in Section 040224

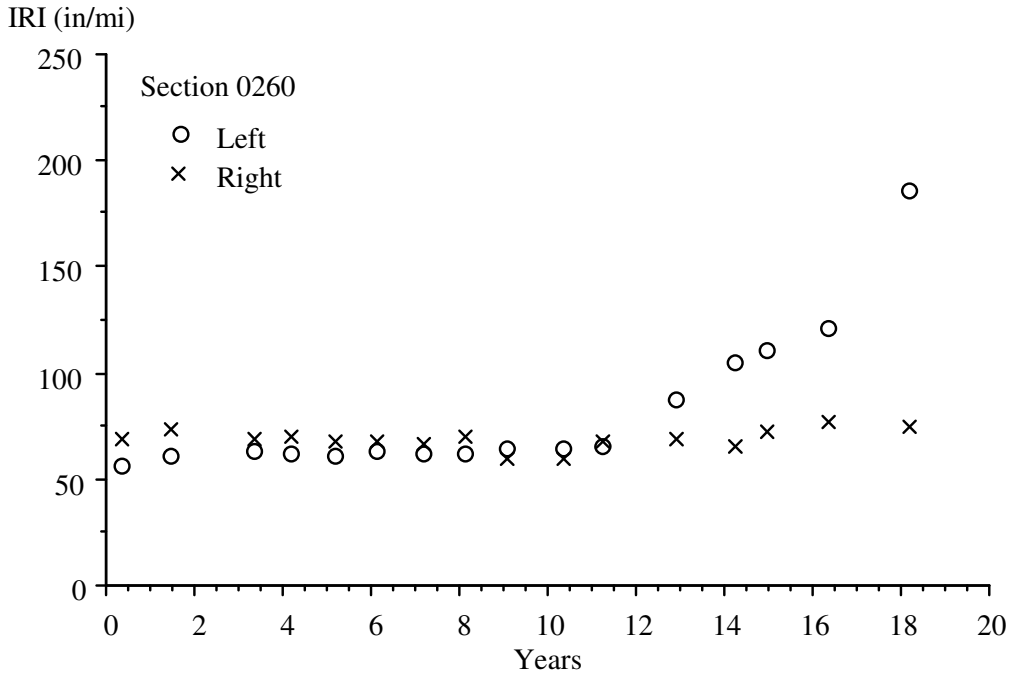

Figure 110. IRI Progression in Section 040260

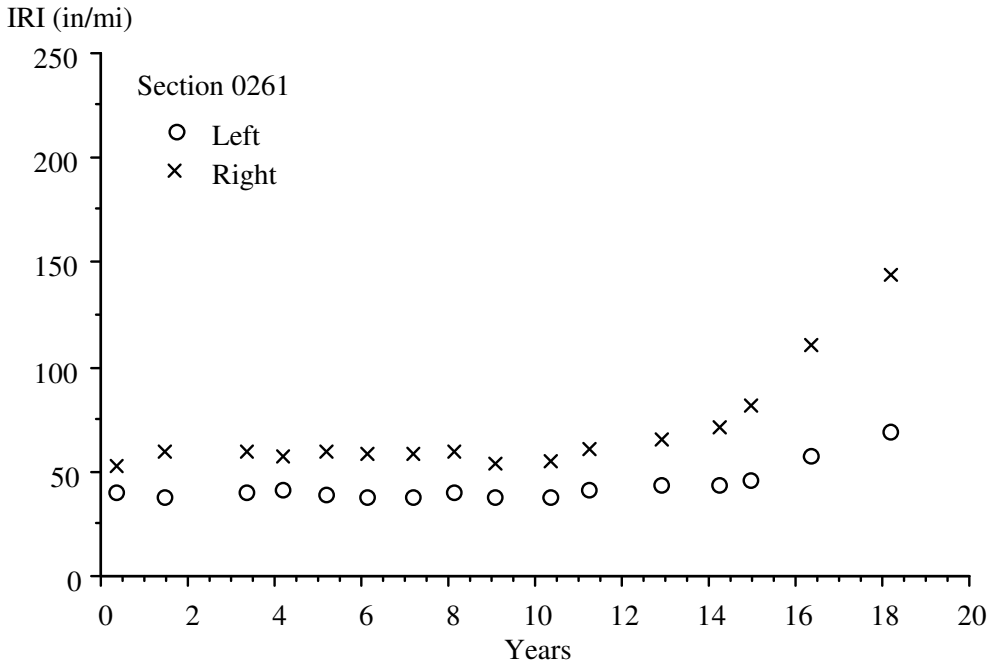

Figure 111. IRI Progression in Section 040261

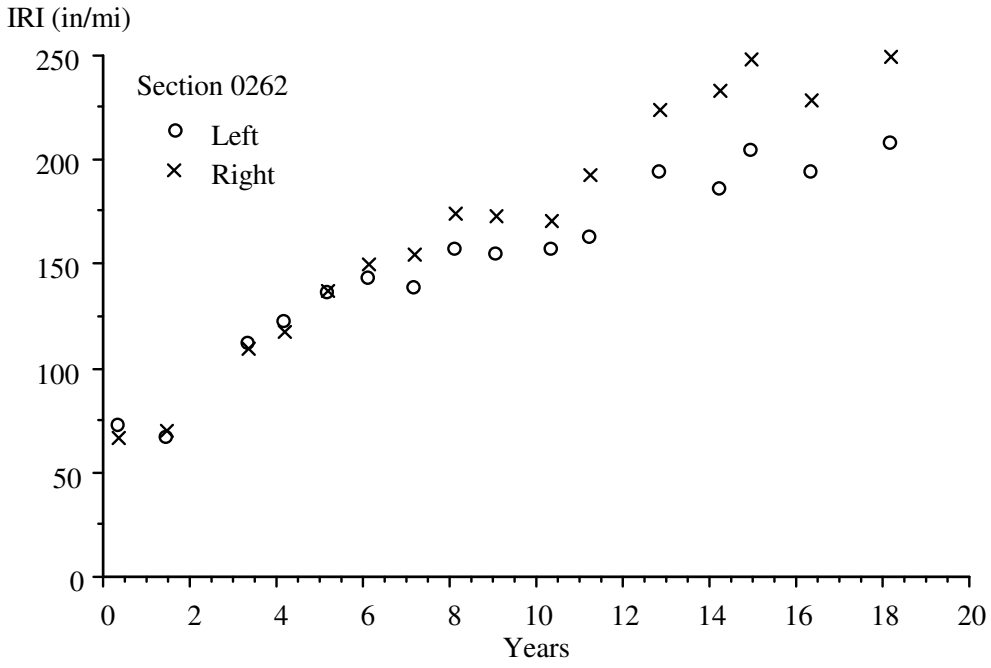

Figure 112. IRI Progression in Section 040262

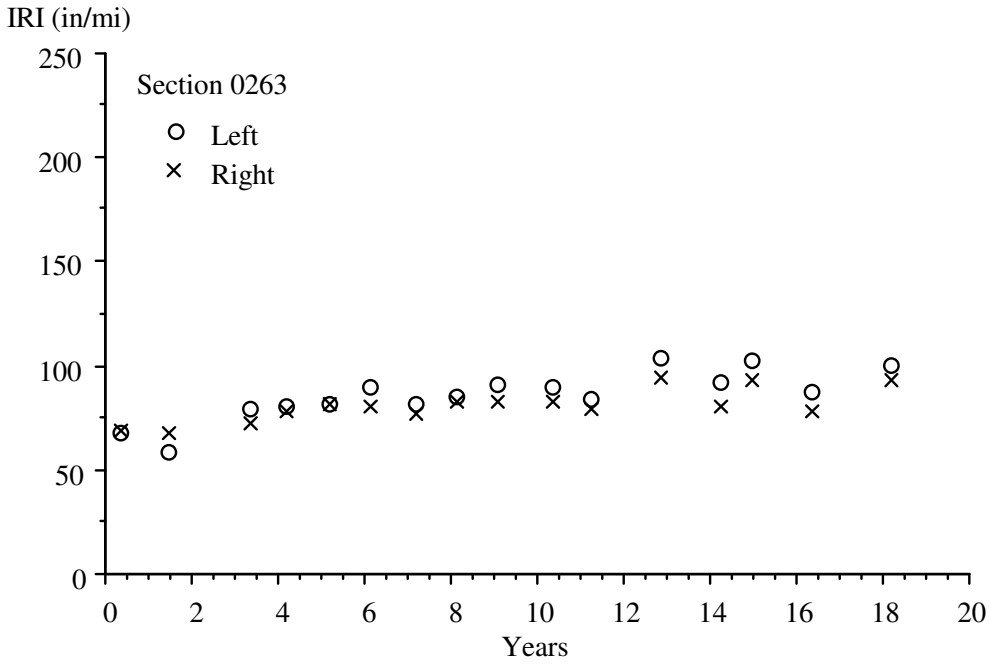

Figure 113. IRI Progression in Section 040263

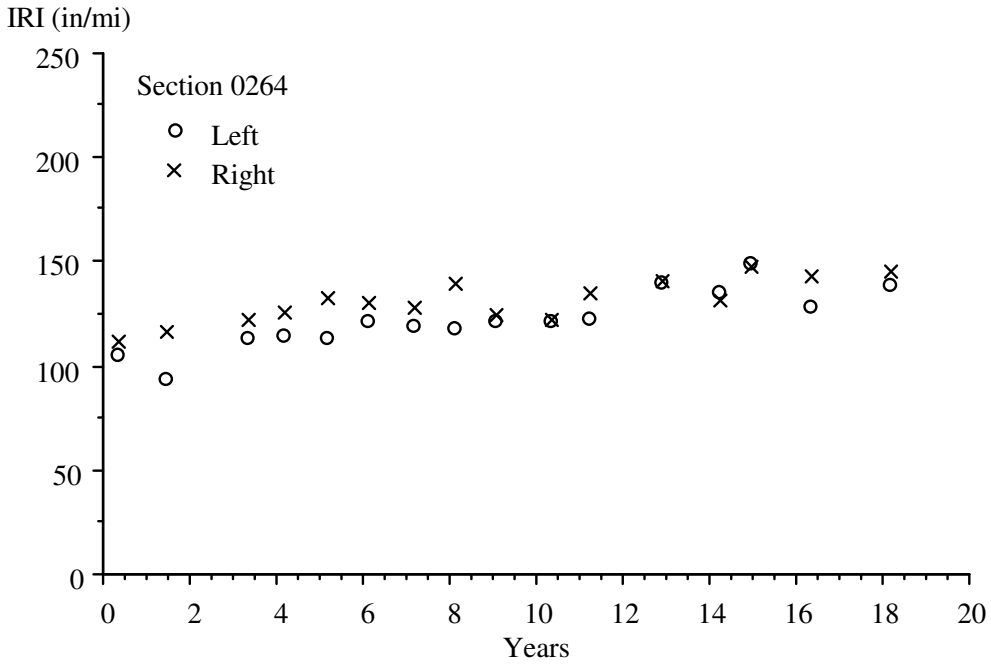

Figure 114. IRI Progression in Section 040264

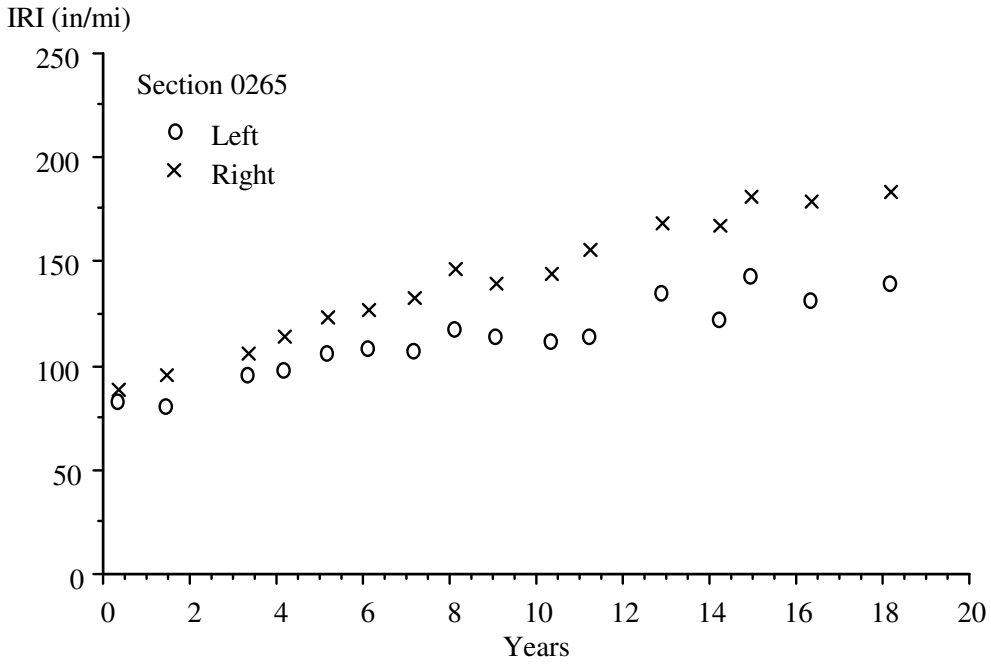

Figure 115. IRI Progression in Section 040265

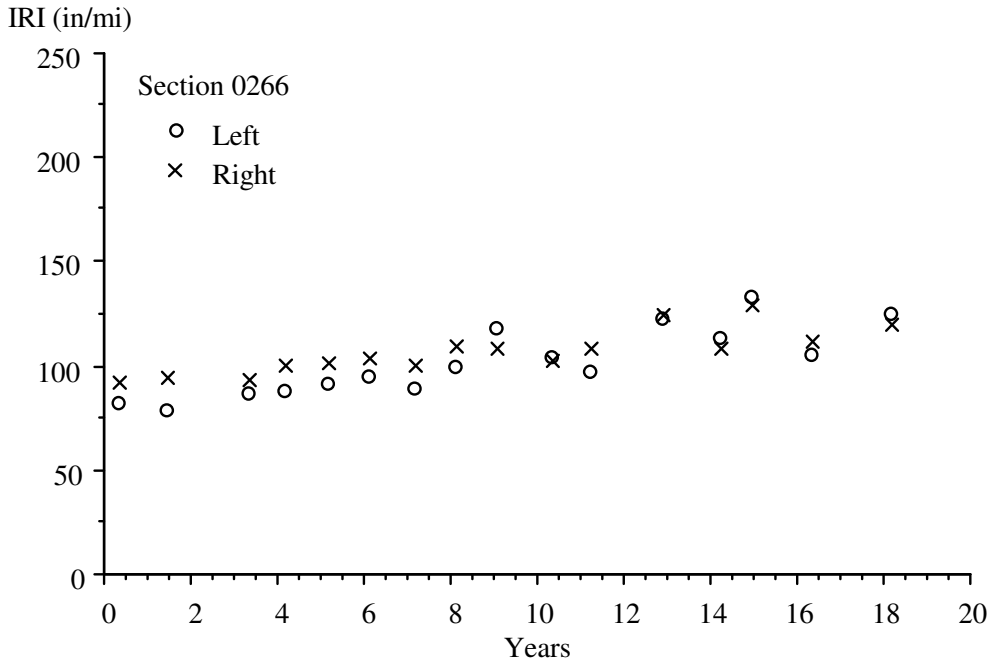

Figure 116. IRI Progression in Section 040266

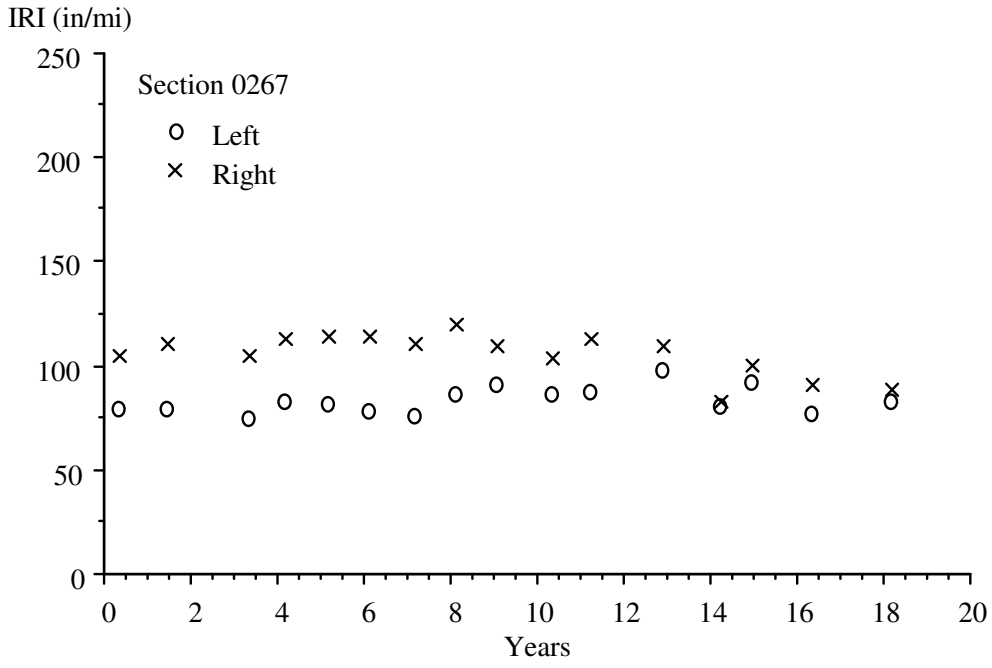

Figure 117. IRI Progression in Section 040267

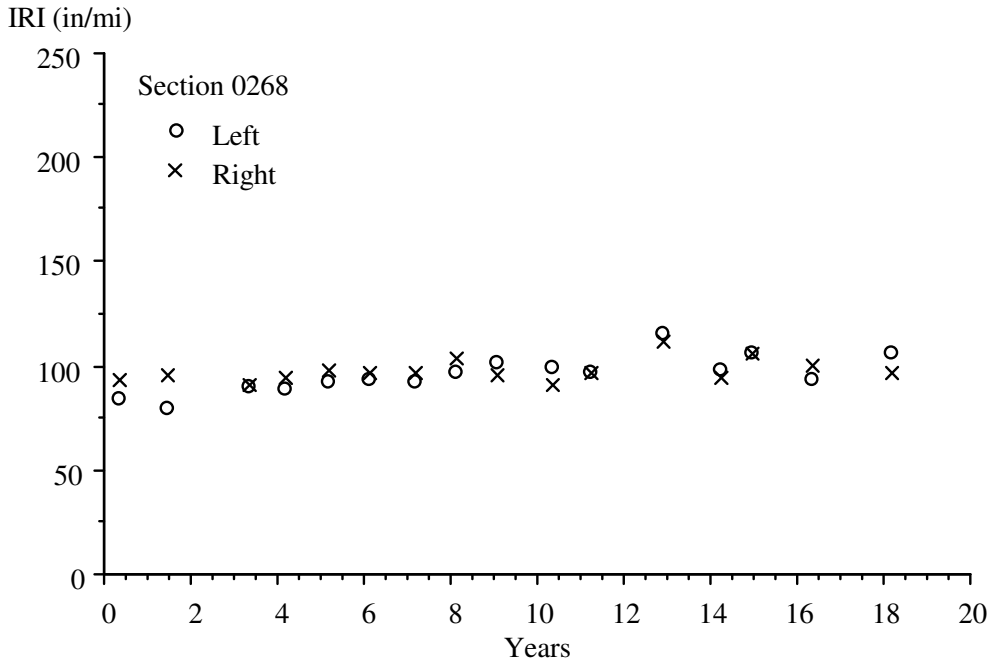

Figure 118. IRI Progression in Section 040268

TRADITIONAL PROFILE ANALYSES

A traditional profile analysis previously performed on the SPS-2 site (Karamihas and Senn 2012) applied typical diagnostic profile analyses, such as inspection of filtered elevation profile plots, roughness profile plots, and power spectral density plots, to explain the roughness, roughness distribution, and roughness progression of each section.

These analyses showed that slab curl and warp contributed to, and in some cases dominated, the roughness of many of the test sections. In addition, changes in curl and warp offered a possible explanation for the disorderly progression in roughness with time that occurred on some of the test sections. For example, Section 040215 exhibited a very unsteady progression in roughness with time, including large diurnal and seasonal changes in Years 4 through 6 and 8 through 12. More on the curl and warp analysis can be found in Appendix C.

The analyses described below are updates of the profile analyses previously performed and contain data collected from visit 16 (December 8, 2011). The analyses helped account for changes in slab curl and warp to determine what share of the roughness of each profile was due to slab effects.

This section provides findings from traditional profile analysis applied to the SPS-2 site. These tools helped study roughness, roughness distribution, and roughness progression of each section, including concentrated roughness linked pavement distress. These analyses included viewing filtered elevation profile plots, roughness profiles, and power spectral density (PSD) plots. Sayers and Karamihas (1996b

and 1998) provide tutorial demonstrations of these methods; Karamihas and Senn (2009 and 2012) applied them to other SPS sites in Arizona.

This section also provides observations pertinent to the IRI, but only on those sections where the analyses yielded noteworthy observations. The discussion of Section 040213 is longer than others to present several features of interest in the section and to provide detailed examples of phenomena that appeared on other sections.

Section 040213

A simple way to learn about the type of roughness that exists within a profile is to view the trace. However, certain key details of the profile are often not as obvious in a raw profile trace as they may be after the profile is filtered. Figure 119 shows the right side profile of Section 040213 in visit 03 (January 27, 1997). Several features are evident from this plot, but they are often much more obvious when plotted with filters.

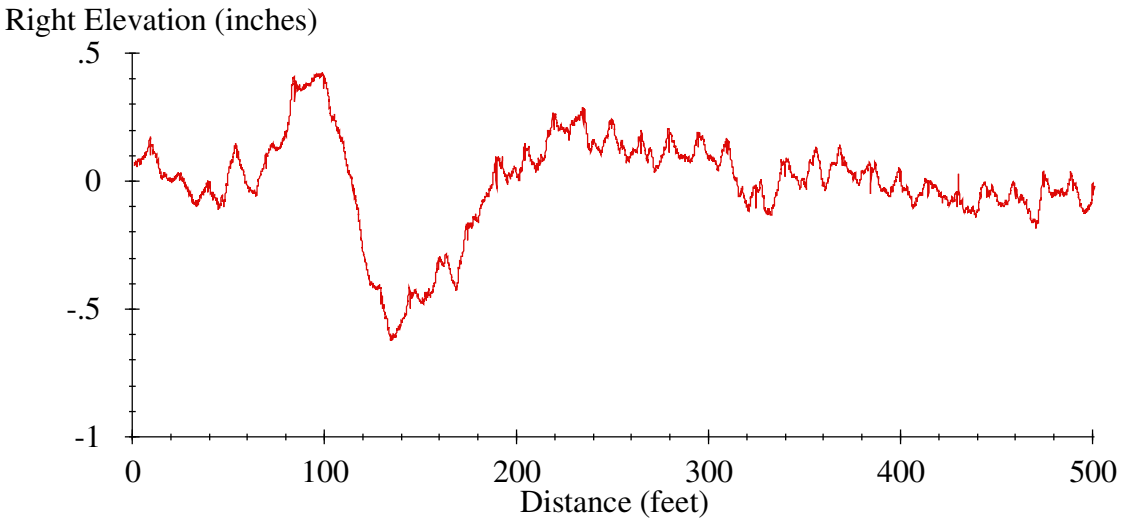

Figure 119. Raw Profile from Visit 03, Right Side of Section 040213

Figure 120 shows the profile from Figure 119 after various moving average filters were applied. Each filter helps examine a distinct feature of the roughness on Section 040213. The upper plot shows the profile after application of a smoothing filter with a 25-ft base length. The filter greatly reduces the contribution of deviations that occur over 25 ft and shorter, but preserves the trend. This plot shows a long bump followed by a long dip on both the left and right profiles throughout the monitoring history of Section 040213, and it consistently contributes to the overall IRI of the section. Together, the bump and dip make up a feature so long that the native filters applied to the profile during the measurement affect their shape, but preserve the roughness that affects the IRI most. For example, the largest change

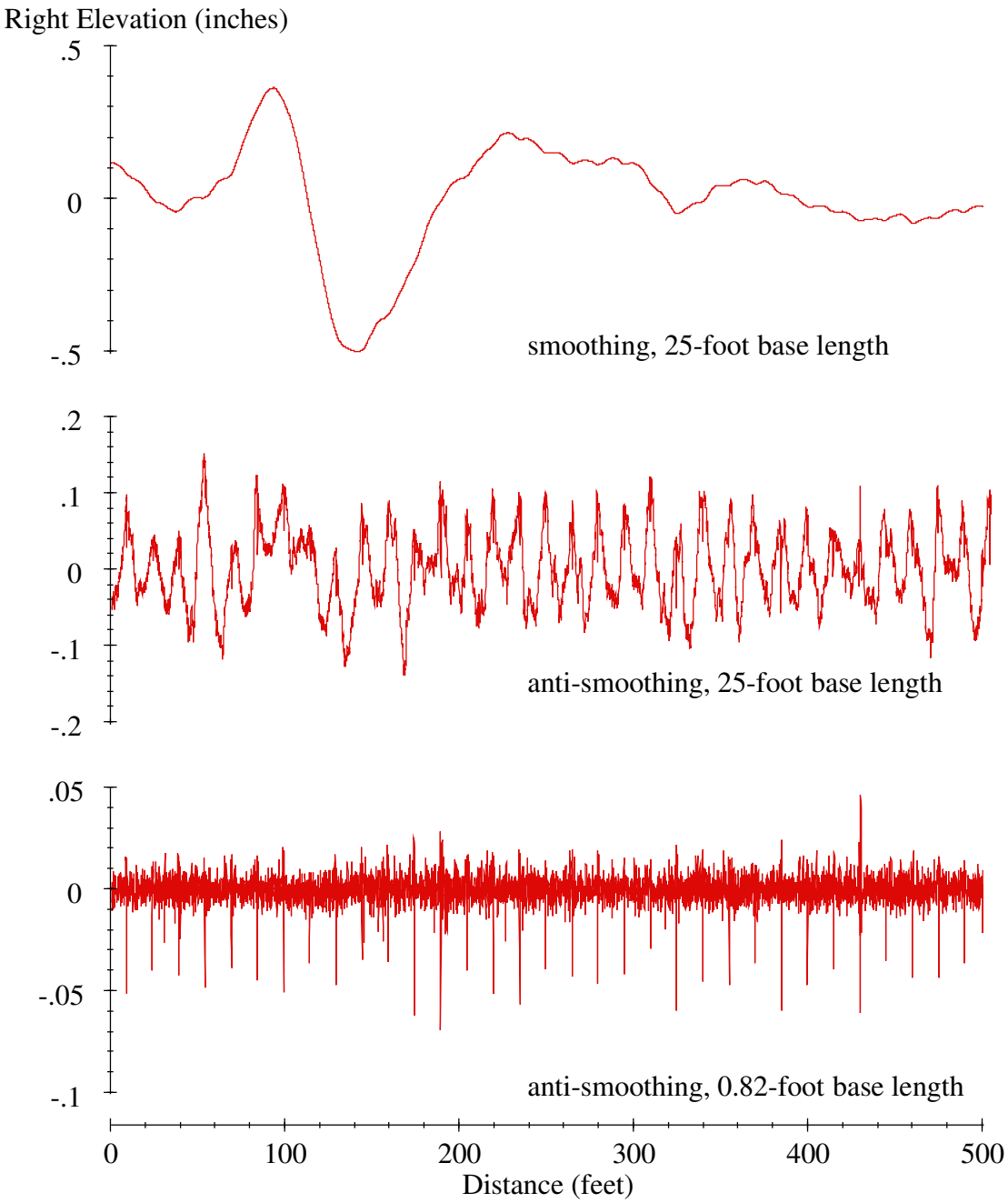

Figure 120. Filtered Profiles from Visit 03, Right Side of Section 040213

in this plot occurred between visit 08 (November 8, 2001) and 09 (October 30, 2002), when the high-pass filter applied by the profiler had changed (Perera and Kohn 2005).

The center plot shows the profile after application of an anti-smoothing filter with a base length of 25 ft. This filter greatly reduces the contribution of deviations that occur over 25 ft and longer. This eliminates the trend and makes the upward curl in the 15-ft-long slabs more obvious. Curl, as used in this report,

refers to the distortion of jointed concrete pavement slabs resulting from curling (typically associated with cyclic thermal gradients), warping (typically associated with the moisture gradient), and a small portion of built-in unevenness. In this plot, local peaks appear 15 ft apart, starting about 9 ft from the start of the section and ending about 489 ft from the start of the section. These represent the joints that surround 32 slabs. Even though the vertical scale is much smaller in the center plot than in the upper plot, the contribution to the IRI is much larger. For example, the IRI of the center trace in Figure 120 is 104.7 inches/mi, and the IRI of the upper trace is 26.6 inches/mi. Although the upper trace covers a larger vertical scale, the rapid reversals in the center trace create greater roughness.

The lower plot shows the profile after application of an anti-smoothing filter with a base length of 0.82 ft. Again, eliminating the longer wavelength content reduces the vertical range of the plot. This filter eliminates nearly all content affecting the IRI, but retains the narrow dips appearing at the joints.

Inspection of filtered elevation profiles showed that upward slab curl existed throughout the monitoring history of Section 040213 and that the level of curl was not consistent. Figure 121 shows part of the left-side profile traces from visits 12 (August 11, 2006) and 13 (December 30, 2007). The figure shows a distinct set of upwardly curled slabs. The figure also shows that the extent of curling at each slab is greater in visit 12 than in visit 13. The level of curl that appears on a pavement section is determined by a combination of diurnal, seasonal, and long-term effects. However, a change in temperature gradient may explain the difference in profile, since visit 12 occurred before sunrise and visit 13 after sunrise.

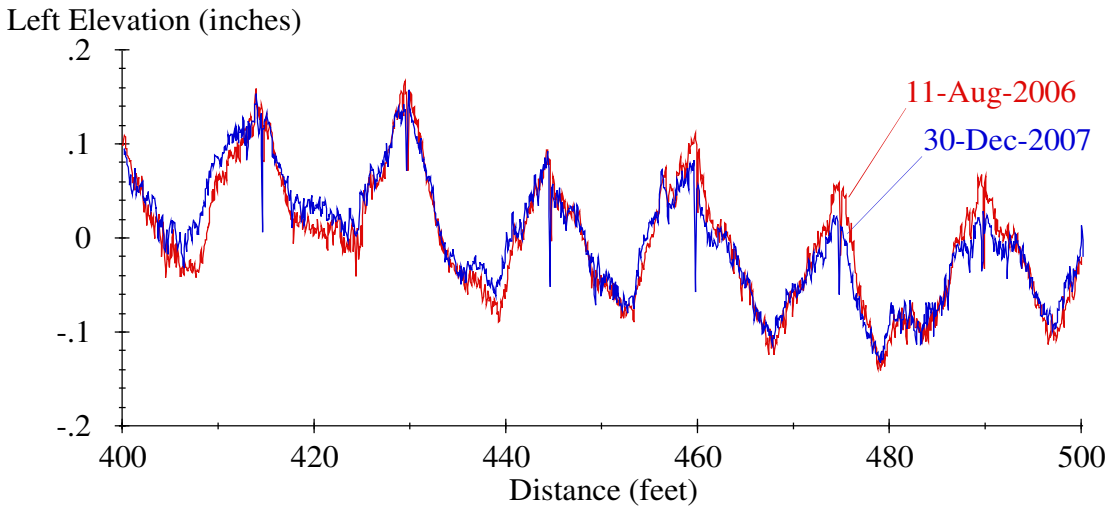

Figure 121. Changes In Curl in Section 040213

Over the 100 ft displayed in Figure 121, the IRI for the visit 12 (August 11, 2006) profile was 132.0 inches/mi, and the IRI for the visit 13 (December 30, 2007) profile was 106.0 inches/mi. Over the entire section, the difference in IRI was 25.6 inches/mi, which demonstrates the influence on the roughness of

a pavement section of a visually modest change in the curling within a profile. (See Figures 150 and 151 in Appendix C.)

A PSD plot provides an alternative way of comparing the severity of slab curl within a profile. Figure 122 shows a PSD plot for the two profiles featured in Figure 121. The plot is modified to show PSD of profile slope rather than elevation, and it uses wavelength as the ordinate axis instead of wave number (the reciprocal of wavelength). The plot displays spectral density in 24 bands per octave (i.e., 24 values for each increase in wavelength by a factor of 2, with uniform spacing along a logarithmic scale). The PSD plots for both visits include peaks at wavelengths of 15 ft, 7.5 ft, and 5 ft. The peak at 15 ft corresponds to the slab length. Additional peaks appear at 7.5 ft and 5 ft because the slabs do not curl into a sinusoidal profile. Instead, they curl into a shape that breaks down into an infinite series of sine waves that are as long as the slab, half as long, a third as long, etc.

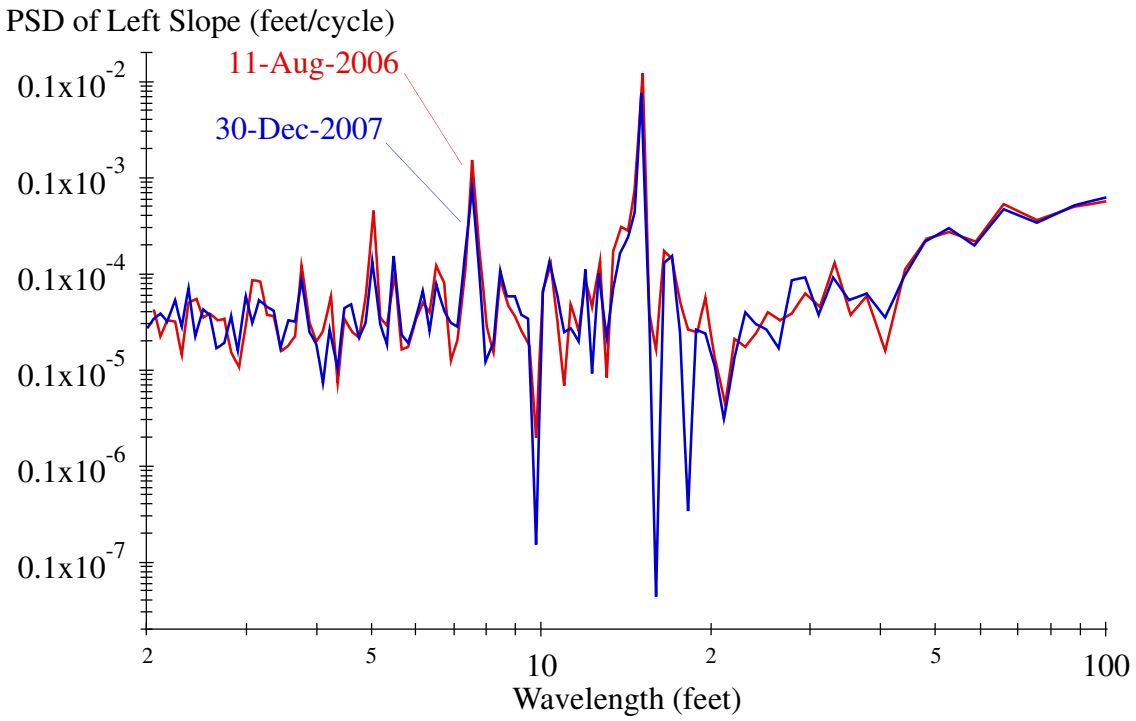

Figure 122. Slope Spectral Density of Section 040213

In Figure 122, values on the ordinate axis map directly to the characteristic length of known pavement features, such as joint spacing. The figure also shows that curling's influence on variations in profile slope stands out over other profile features. However, the nonstandard method of display in Figure 122 distorts the relative contribution of each waveband to the overall profile. Figure 123 provides a more standard display of PSD. The figure displays both axes on a linear scale and provides spectral density versus wave number. When the plots are displayed in this manner, the area under the curve for any

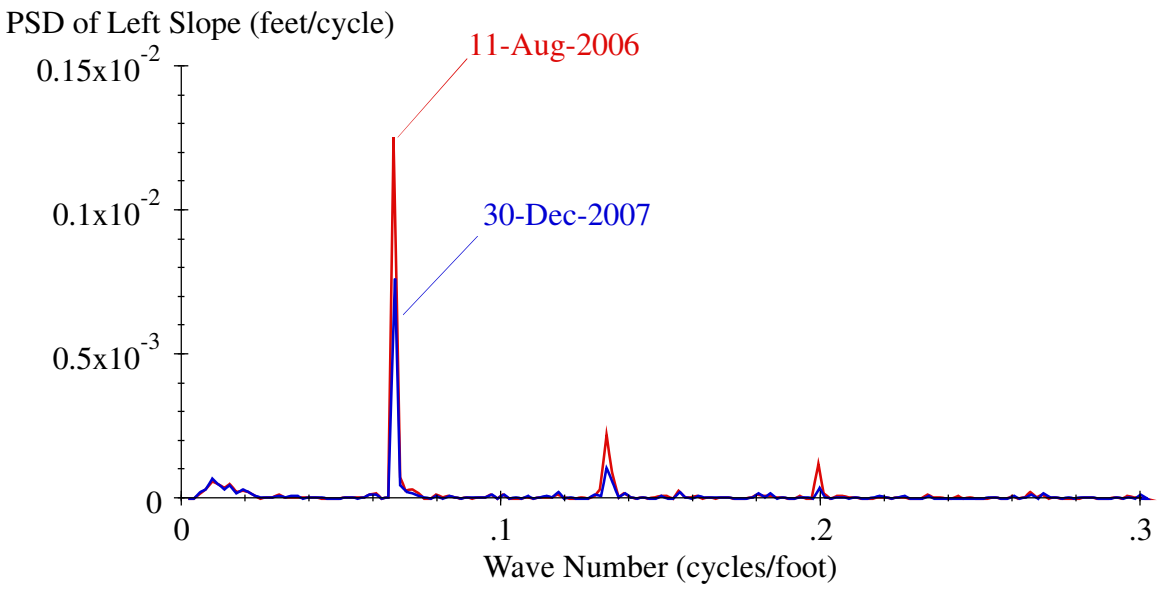

Figure 123. Slope Spectral Density of Section 040213, Linear Scaling

range of wave numbers is proportional to the contribution that range makes to the overall mean square. Over the range that affects the IRI, shown in Figure 123, slab curl dominates the roughness of the section in both visits. Figure 123 also provides a more representative view of the difference between visits 12 (August 11, 2006) and 13 (December 30, 2007). At a wave number of 0.066 cycles/ft, which corresponds to a wavelength of 15 ft, the plot for visit 12 has a value of 0.00125 ft/cycle and the plot for visit 13 has a value of 0.00076 ft/cycle. In terms of RMS, this waveband accounts for 28 percent more roughness in visit 12 than in visit 13.

Section 040213 developed distress in the later part of the monitoring history. Starting in visit 12 (August 11, 2006), narrow dips and groups of densely spaced narrow dips appeared in the right-side profiles. The right side profiles from visit 12 included narrow dips at 35 to 47 ft, 143 to 160 ft, 243 to 246 ft, 255 ft, and 317 to330 ft from the start of the section. These areas correspond to locations where the distress survey showed longitudinal cracking starting in 2004. Starting in 2008, longitudinal cracks appear either in or near the right side wheelpath over the first two thirds of the section. The cracks grow in width from 2008 onward, and some of them include missing material replaced by asphalt by 2011. Typically, the dips within the profile appear where the cracks wander into the center of the wheelpath.

Figure 124 shows three repeat profiles from the right side of Section 040213. The area from 143 to 160 ft includes several deep dips. The most severe features in this area appear with the same shape in all three measurements. However, some details of the profiles in this area are not perfectly repeated because they are caused by longitudinal cracks.

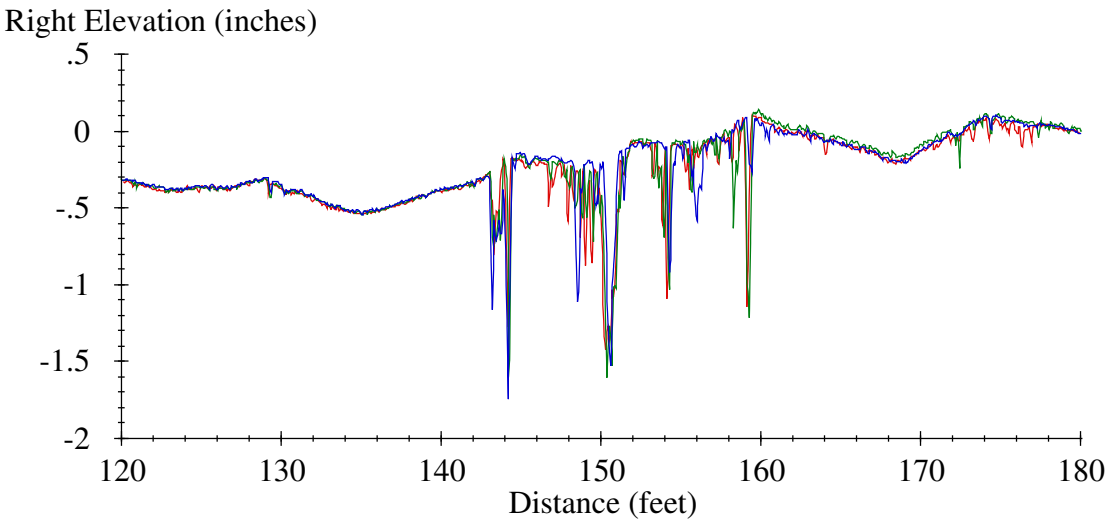

Figure 124. Right Elevation Profile, Three Repeats from Visit 12 of Section 040213

A roughness profile provides a way to quantify the severity of isolated disturbances in a profile, such as the dips shown in Figure 124. A roughness profile provides a continuous report of road roughness using a given segment length (Sayers 1990). Instead of summarizing the roughness by providing the IRI for an entire pavement section, the roughness profile shows the details of how IRI varies with distance along the section. It does this by displaying the IRI of every possible segment of a given base length along the pavement using a sliding window. Figure 125 shows the roughness profile using a 25-ft base length for the profiles shown in Figure 124. With a 25-ft base length, isolated roughness is easy to identify, and the area with the narrow dips stands out as much rougher than the surrounding area. The peak value in this area was about 600 to 700 inches/mi. Since this 25-ft-long area accounts for 1/20 of the section length, this area contributes 30 to 35 inches/mi to the overall IRI of the section for these repeat measurements.

One of the repeat measurements shown in Figure 125 also includes an area of higher roughness about 250 ft from the start of the section. This is another patch of dips on a longitudinal crack that only one pass detected because of small variations in the tracking position of the profiler.

Inspection of roughness profiles showed that the narrow dips at longitudinal cracks account for much of the increase in roughness after visit 11 (December 12, 2004), although the dips were less severe overall in visit 13 than in visit 12. By visit 15 (January 25, 2010), two additional areas of isolated roughness appeared along with the area shown in Figure 125.

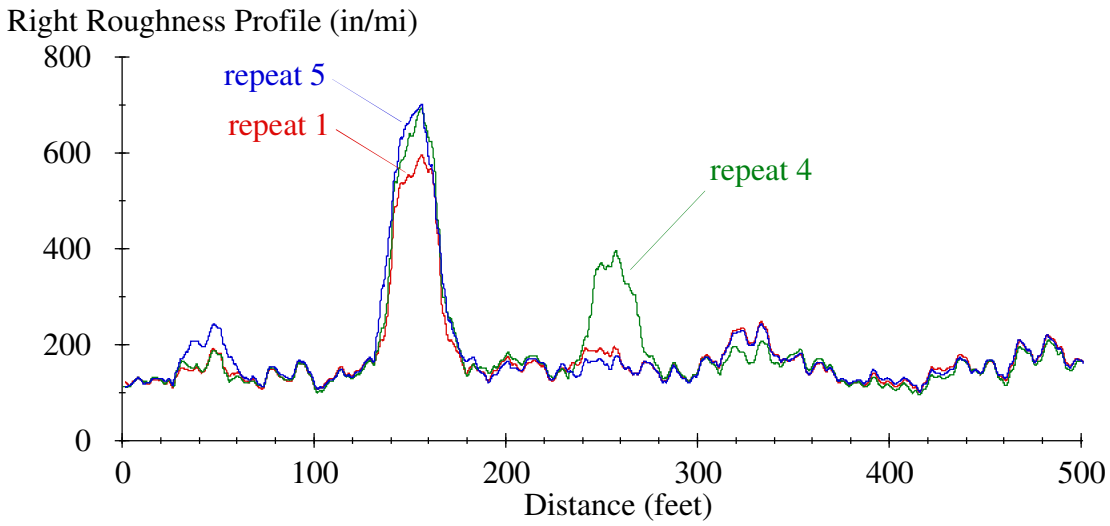

Figure 125. Right Roughness Profile, Three Repeats from Visit 12 of Section 040213

Section 040214

Section 040214 profiles included evidence of upward curl in the early visits. However, the slabs in the first half of the section gradually changed from upward curl to downward curl, and the upward curl diminished in the second half of the section over time. The slabs changed most aggressively between visit 04 (December 4, 1997) and visit 10 (February 4, 2004). Figure 126 shows right-side profiles from visit 01 (January 25, 1994) and visit 10 over the part of Section 040214 where all the slabs changed from upward to downward curl.

Distress surveys noted map cracking on the section starting in 1997, including low-severity map cracking throughout the section. By 2008, the distress surveys listed hig-severity map cracking in the first part of the section and map cracking in the wheelpaths throughout the section. The 2008 distress survey also noted a rough transition from asphalt to concrete pavement upstream of Section 040214; researchers proposed that the resulting dynamic loads imposed on the section may have contributed to the cracking. Figure 127 shows the profile leading to Section 040214 in visit 09 (October 30, 2002). The figure shows a distance of zero at the section start. The rough features 60 to 80 ft upstream of the section would indeed exacerbate truck dynamic loading. However, the role of dynamic loading in causing the map cracking is unclear.

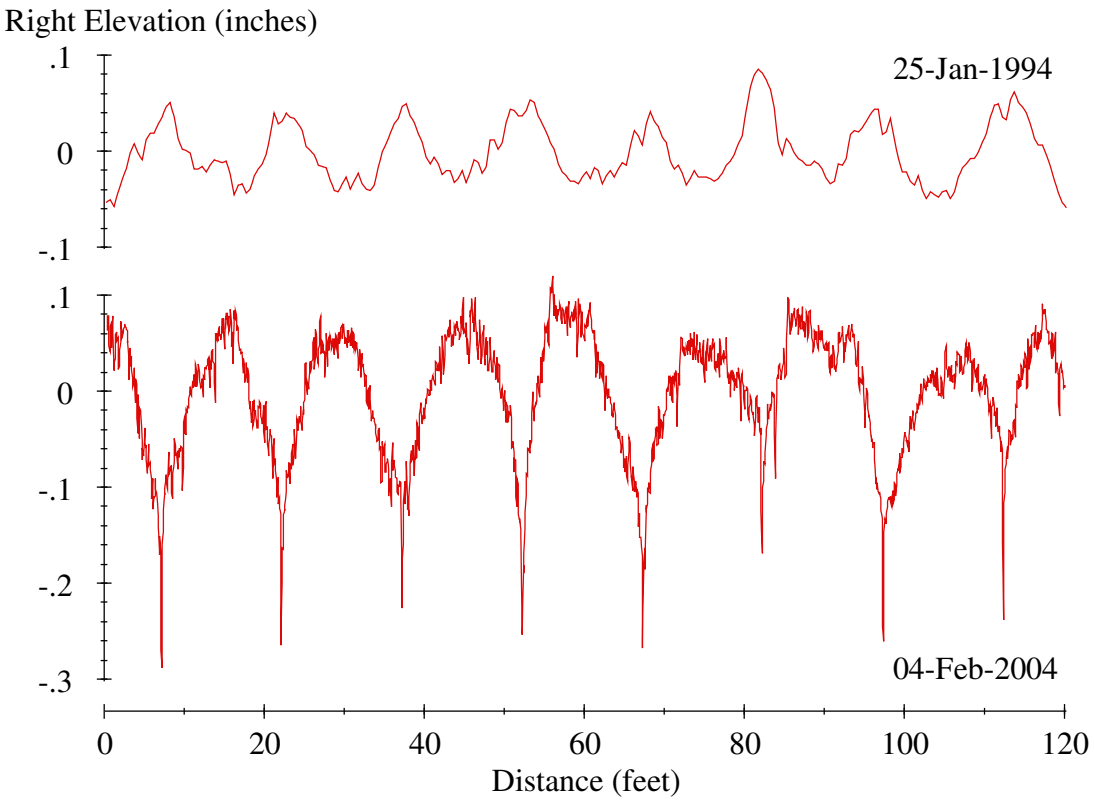

Figure 126. Right Elevation Profiles from Section 040214

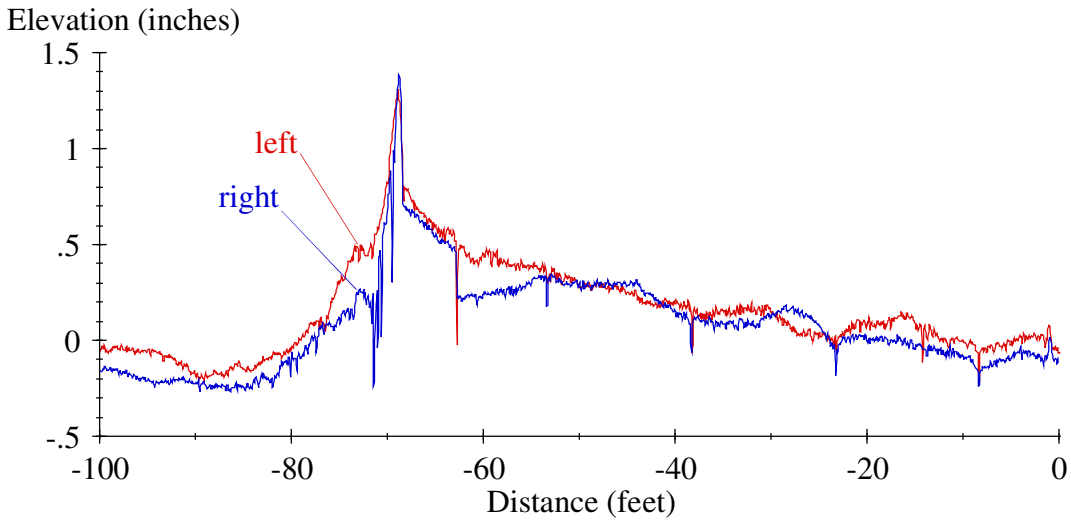

Figure 127. Profiles from Visit 09 Leading to Section 040214

Section 040215

Profile data for Section 040215 included measurements on 16 additional dates for the SMP; these data were collected early (typically in the morning) and late (typically in the afternoon). Together with the 15 routine visits, the data include 47 sets of repeat measurements, with measurements every season in 1998 and from winter 2001 through winter 2004. Plotting of filtered profiles and PSD functions revealed that changes in slab curl caused most of the sction's changes in roughness over time.

Figure 128 shows the PSD plot for profiles measured in visits S05 (July 9, 1998, 08:45) and S30 (July 15, 2004, 09:07). The spectral content for these two profiles is very similar. In addition, the roughness level is about equal over the range shown in the figure, except at wavelengths equal to the slab length (15 ft) and half the slab length (7.5 ft). The IRI for the earlier profile is 93.6 inches/mi, and the IRI for the later profile is 129.4 inches/mi. Figure 128 shows that changes in slab curl caused most of the difference. (See Figures 152 and 153 of Appendix C.)

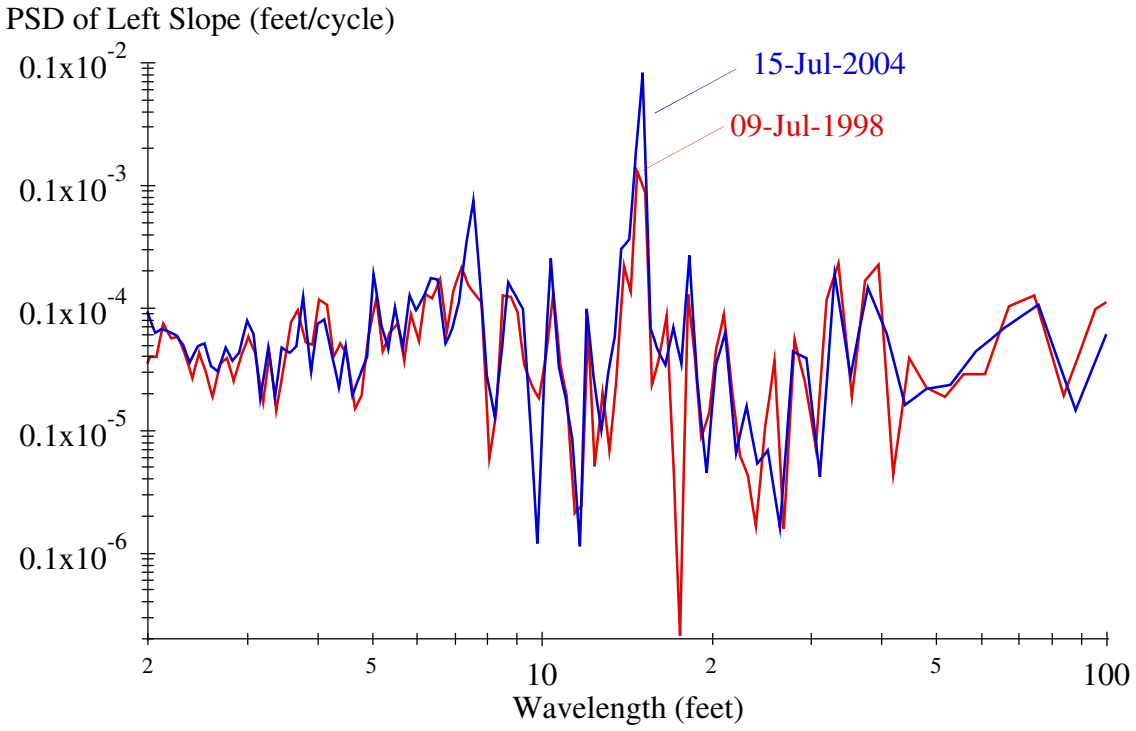

Figure 128. PSD Plots from Section 040215

PSD plots of profiles from the 47 visits showed the following:

- The overall level of slab curl increased over time, but the trend was not orderly.

- The overall level of curl was higher in visits 12 (August 11, 2006) and 14 (September 20, 2008) than in 11 (December 12, 2004), 13 (December 30, 2007), and 15 (January 25, 2010). Visits 12 and 14 occurred shortly after midnight, and visits 11, 13, and 15 occurred after sunrise.
- In many of the "paired" seasonal visits from the same date, the level of curl was higher in the early set of passes than on the following set of passes. This occurred in visits S01 through S20, S27, and S28, but not in visits S21-S26 and S29 through S30.
- Variations in IRI between visits followed the same trend as the severity of the peak value in the PSD plot at a wavelength of 15 ft.

Section 040216

No specific observations are provided for Section 040216.

Section 040217

The 1997 distress survey recorded longitudinal and transverse cracks, and the level of cracking increased throughout the rest of the monitoring period. The 2002 distress survey also listed map cracking throughout (the) section.

Narrow dips appeared in both the left and right profiles at positions in the middle third of some slabs starting in visit 09 (October 30, 2002). The dips appeared in locations where the distress surveys included transverse cracks, although not every transverse crack caused a dip. In visit 15 (January 25, 2010), the most severe dips appeared 30 ft (0 to 1.3 inches deep), 407 ft (0 to 0.9 inch deep), 466.5 ft (0 to 0.15 inch deep), and 481.5 ft (0 to 0.6 inch deep) from the start of the section in the left-side profiles and 42 to 45 ft (0 to 0.7 inch deep), 238 ft (0 to 0.4 inch deep), 450 ft (0 to 1.3 inches deep), and 478 ft (0 to 1.6 inches deep) from the start of the section in the right-side profiles. The construction report listed transverse cracking in the LCB 480 ft from the start of Section 040217 but not at the other locations (Szrot 1994). Inspection of roughness profiles showed that none of the dips caused the short (25-ft) interval IRI to exceed 2.5 times the section average.

Throughout the monitoring history, one slab along the right side of Section 040217 contributed twice as much to the roughness of the section as the others. Figure 129 shows the right-side profiles from visit 01 (January 25, 1994) and visit 14 (September 20, 2008). Joints appear within the plot 444.3 ft, 459.2 ft, 474.2 ft, and 489.3 ft from the start of the section. The slab that extends from 459.2 to 474.2 ft has upward curvature that will register as upward curling to an automated curling analysis based solely on slab profile. However, this slab's upward curvature may have another cause, since (1) no other slab on Section 040217 exhibited a similar level of curvature, (2) the overall curvature of this profile along this slab did not change significantly with time, and (3) the left-side profiles were relatively flat. The cause of the upward curvature here cannot be determined without additional information, and the curling analyses presented in this report depend more heavily on changes in slab shape with time than on the nominal profiles.

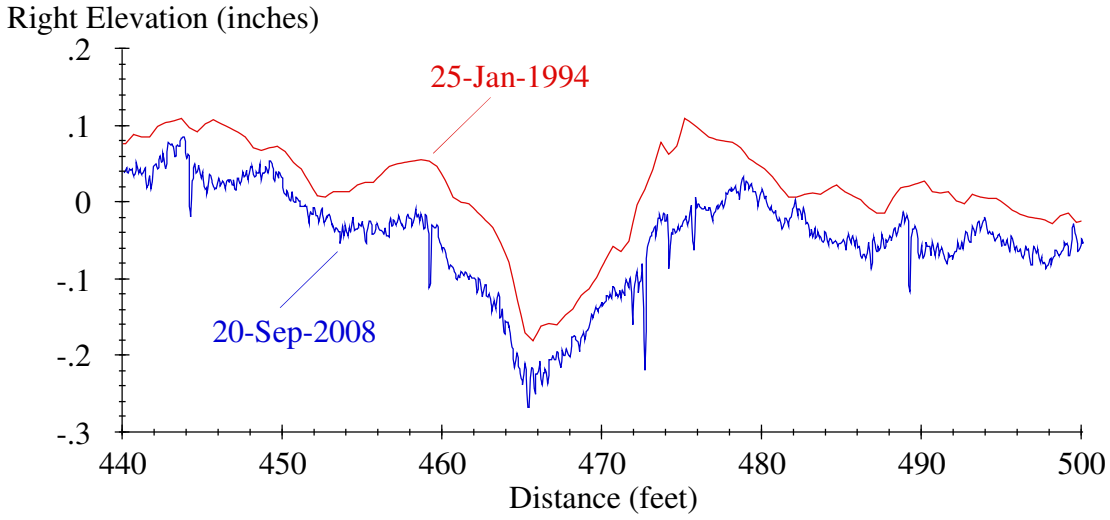

Figure 129. Right Elevation Profiles from Section 040217

Profiles from Section 040217 included noteworthy spectral content not caused by slab curl.

Figure 130 shows the PSD plot for the left profile from visit 08 (November 8, 2001) of Section 040217. Slab curl caused the spikes at 15 ft, 7.5 ft, and 5 ft. Another spike appears at about 33 ft that rivals the others in amplitude. The contractor who built the test pavements confirmed this was the approximate string line stake spacing. Content at this wavelength was strongest on Section 040217, but lesser peaks appear in PSD plots from Sections 040214, 040215, 040216, 040218, and 040220.

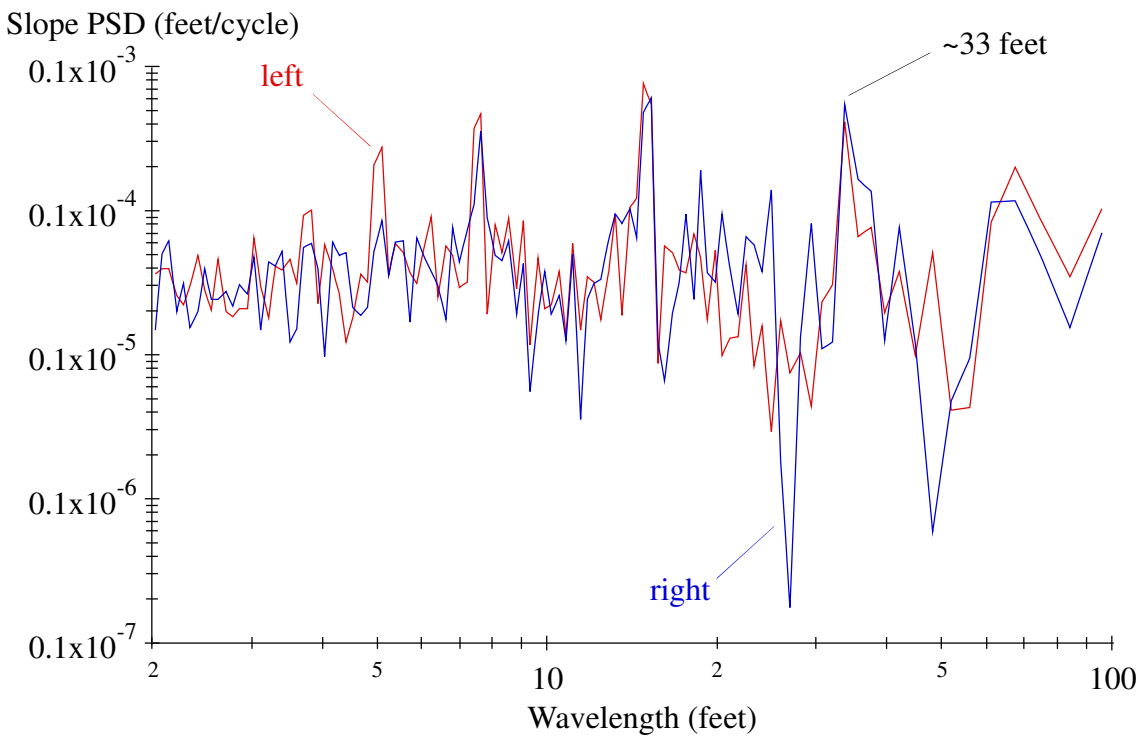

Figure 130. PSD Plots from Visit 08 of Section 040217

Section 040218

The construction report listed 11 transverse cracks in the LCB within the monitoring range of Section 040218 (Szrot 1994). Plotting of filtered profiles revealed no localized roughness and no systematic appearance of cracks in the surface layer.

Section 040219

Transverse cracks appeared in mid-slab positions on Section 040219 beginning in 2002 and on about half of the slabs by the end of the monitoring period. The profiles included narrow dips at some of these locations, particularly on the right side, starting in visit 09 (October 30, 2002). By visit 15 (January 25, 2010), narrow dips appeared intermittently in the right-side profiles 195 ft (0 to 0.15 inch deep), 258 ft (0 to 0.2 inch deep), 316 ft (0 to 0.9 inch deep), 384 ft (0 to 0.3 inch deep), 406 ft (0 to 0.8 inch deep), and 466 ft (0 to 0.4 inch deep) from the start of the section. Distress surveys also noted map cracking over most of the section by the end of the monitoring period, but the cracking was less obvious in the photos than on other sections.

Section 040220

Profiles of Section 040220 from visit 04 (December 4, 1997) included densely spaced positive and negative spikes at some joint locations (Figure 131). Similar disturbances appeared in the right-side

profiles at the joints about 70 ft, 115 ft, 175 ft, 220 ft, 325 ft, 384 ft, 430 ft, and 474 ft from the start of the section. These typically appeared in only one or two of the repeat measurements in visit 04 and sparingly in profiles from visit 05 (December 8, 1998) but not in any of the other visits. These disturbances did not correspond to anything noted in the distress survey, although a distress survey in 2003 noted seal damage at joints. The construction report listed 13 transverse cracks in the LCB within the monitoring range of Section 040220 (Szrot 1994). Plotting of filtered profiles revealed no localized roughness and no systematic appearance of cracks on the surface.

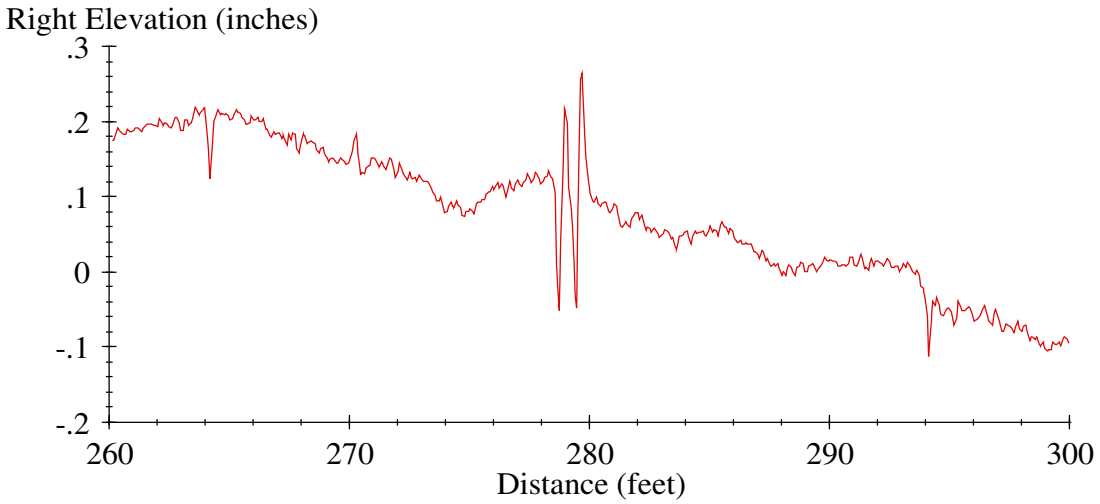

Figure 131. Visit 04 Profile from Section 040220

Section 040221

Distress surveys listed distress in the right wheelpath of a slab from 410 to 425 ft from the start of the section throughout the monitoring history and distress in neighboring slabs later in the monitoring period. In 1997, the survey noted severe aggregate loss. Every survey afterward showed scaling along the right side of that slab, and the survey in 2008 (including the photos) showed fiberglass patching at various locations. Figure 132 shows five repeat measurements of the right-side profile from visit 15 (January 25, 2010). The dip 421 ft from the start of the section caused localized roughness, and the slab from 410 to 425 ft from the start of the section contributed to the IRI three times as aggressively as the rest of the section.

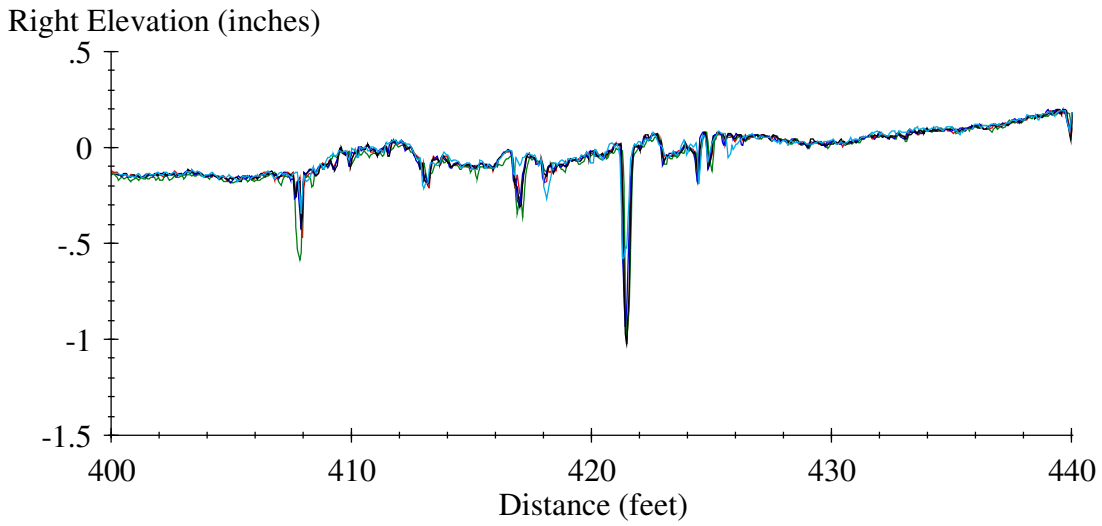

Figure 132. Right Elevation Profile, Five Repeats from Visit 15 of Section 040221

Section 040222

Some profiles from visits 14 (September 20, 2008) and 15 (January 25, 2010) included a narrow dip up to 0.7 inch deep at a joint 325 ft from the start of the section. Nothing in the distress surveys distinguished this joint from the others, and the dips did not increase the roughness of the section.

Section 040223

No specific observations are listed for Section 040223.

Section 040224

The left IRI value from visit 10 (February 4, 2004) was 114 inches/mi. This value stood out since the right IRI was 71 inches/mi, the left IRI from visit 09 (October 30, 2002) was 84 inches/mi, and the left IRI from visit 11 (December 12, 2004) was 70 inches/mi (Figure 152). As shown in Figure 133, a change in spectral content for wavelengths near 8 ft accounts for most of the difference. Although no other obvious explanation for this could be found, this content is most likely not caused by changes in slab curl since it only appears on the left side of the lane. The content within the PSD plot at a 15-ft wavelength was not affected strongly, and the high content for wavelengths near 8 ft is not as concentrated as the upper harmonics caused by slab curl in the PSD plots shown for other sections. Furthermore, the peaks and valleys of the approximately 8-ft-long waves do not align consistently with the joint locations.

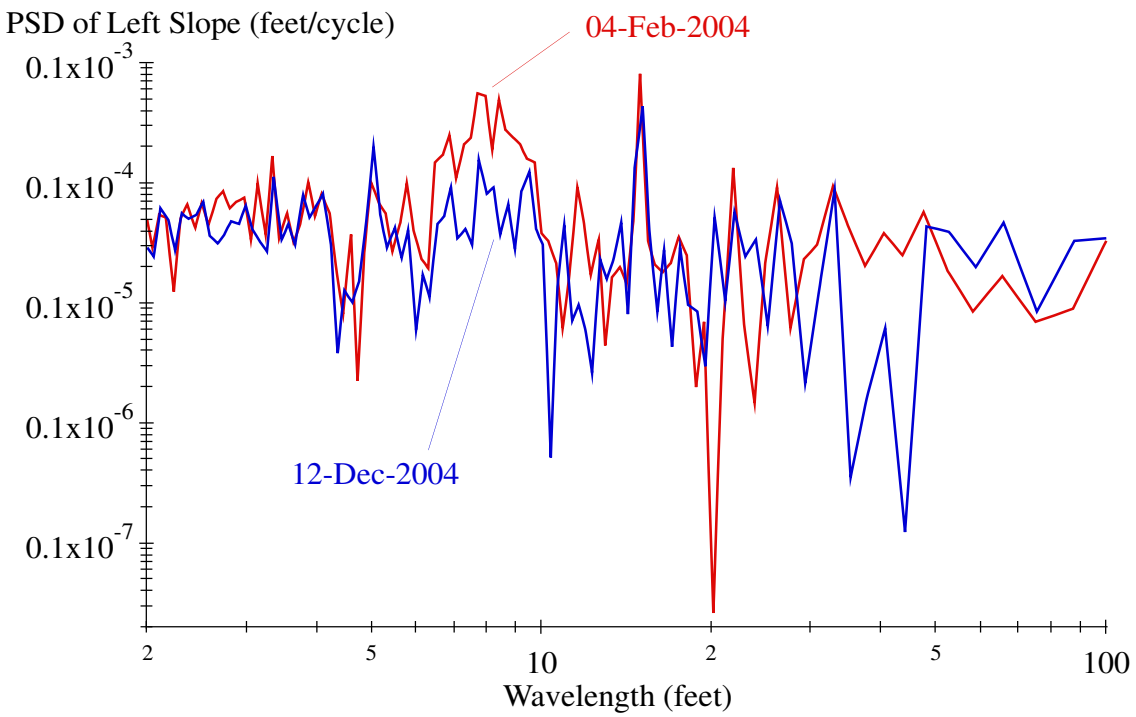

Figure 133. PSD of Left Slope from Section 040224

Section 040260

The distress surveys reported low-severity raveling on Section 040260 starting in 1995, and raveling in both wheelpaths with no qualification on severity starting in 2004. By 2008, the distress surveys reported significant distress in the left wheelpath and the photos showed fatigue, small potholes, patching, and pools of sealant in the left wheelpath. The distress increased in severity by 2010, including more visible cracking along the left wheelpath. These observations explain the steady rise in IRI of the left wheelpath starting 11 years after the experiment began.

Some areas within the profile showed clear evidence of surface distress. For example, the area from 50 to 70 ft from the start of the section often included patches of narrow dips. The dips appeared starting in visit 06 (November 15,1999) on the left side and in visit 11 (December 12, 2004) on the right side. The dips were not well-repeated when they first appeared. However, by the end of the monitoring period, the profile over this segment had a consistent shape, which included a narrow dip (0.7 inch deep) and a 3-ft-wide dip (nearly 0.2 inch deep).

A rough area present since construction exists about 350 ft from the start of the section. Figure 134 shows the roughness profile at various ages starting with the first profiling visit. The plot uses a 25-ft base length. The rough area progresses from a peak value of 118 inches/mi in visit 01 (January 25, 1994) to 735 inches/mi by visit 15 (January 25, 2010). Since the base length is equal to 1/20 of the section

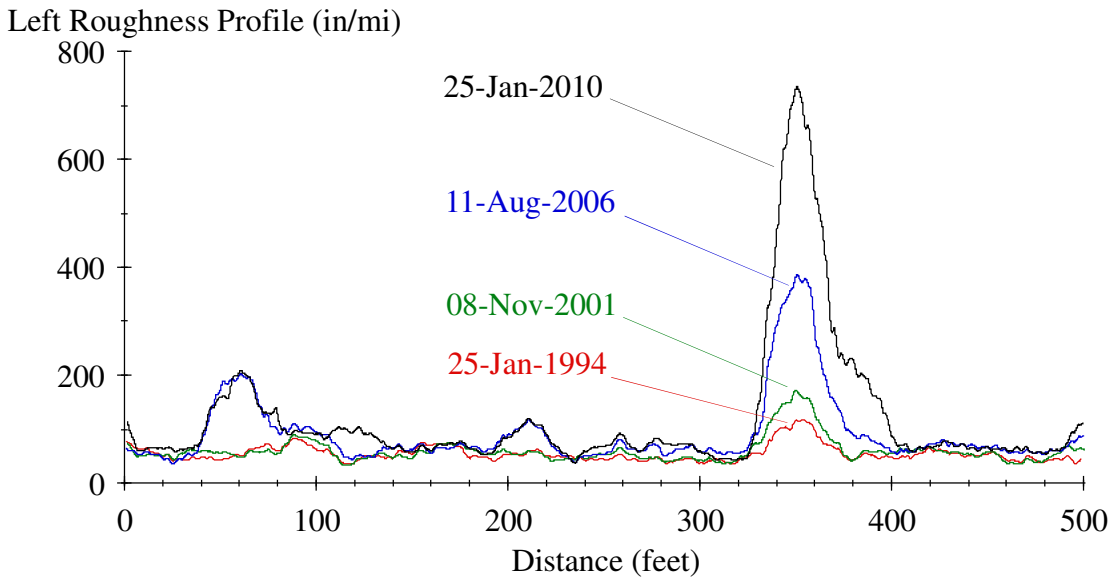

Figure 134. Left Roughness Profile from Section 040260

length, this represents a progression in the contribution to the overall IRI of the roughest area from 5.9 inches/mi to more than 36 inches/mi.

Figure 135 shows a profile from visit 01 (January 25, 1994) and visit 15 (January 25, 2010). The initial disturbance is visible in the plot, although distress was not recorded there until 2000. However, it is not clear whether the initial disturbance caused the roughness to progress by increasing the loading experienced at certain locations (i.e., a hot spot), or if the disturbance was evidence of structural defects at that location (i.e., a weak spot), or both. In either case, Figure 134 showed that the roughest area within Section 040260 at the start of its service life progressed to the roughest area much later in its service life. (The peak value would stand out in the plot from visit 01 if not for the large vertical scale needed in Figure 134 to accommodate the roughness in later visits.)

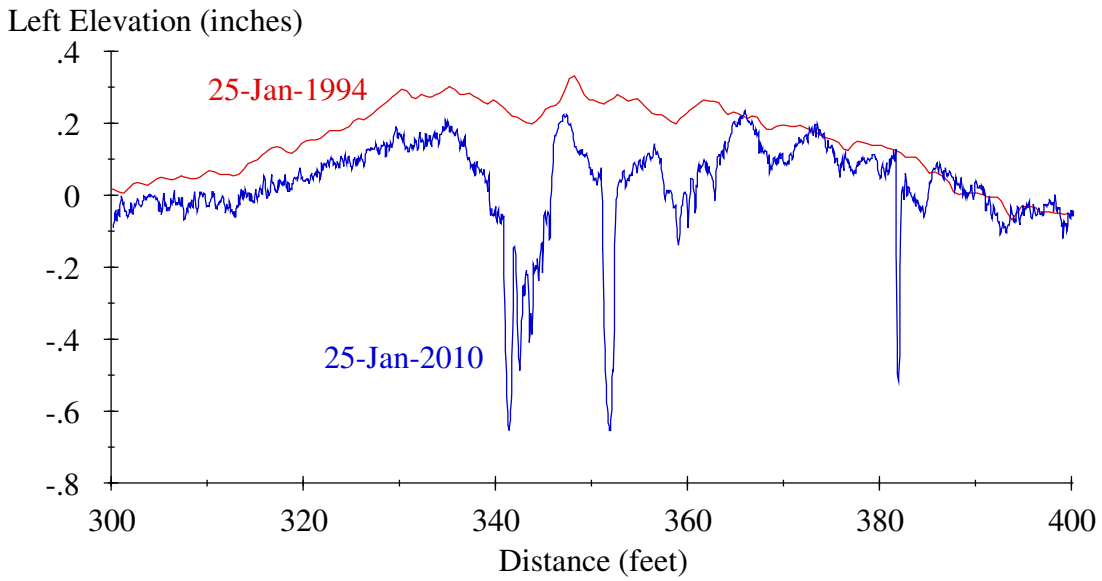

Figure 135. Left Elevation Profile of a Segment from Section 040260

Section 040261

Distress surveys recorded longitudinal cracking in some areas of Section 040261 starting in 1997 and transverse cracking at several locations after 2004. Dips appeared as depressions up to 5 ft wide with a narrow dip up to 1 ft wide in the majority of locations where the 2008 (and later) distress surveys showed transverse cracking. These appeared in the profiles starting with visit 11 (December 12, 2004), and they were prominent late in the experiment. These dips exacerbated the roughness progression. Localized roughness appeared about 325 ft from the start of the section late in the experiment where a pothole developed.

The 1997 distress survey recorded the presence of six cores along the right wheelpath near the end of the section. A longitudinal crack developed along the line of cores. This area was sealed, but the sealant eventually wore off. A series of bumps and dips appeared in the right-side profiles at that location throughout the monitoring history that grew in roughness.

Section 040262

Section 040262 faulted. Filtered profile plots showed that the faulting grew steadily throughout the experiment. Figure 136 shows five repeat profile measurements from a portion of Section 040262 in visit 15 (January 25, 2010). The figure shows a consistent level of faulting along the section and among the repeat measurements. Faulting caused much of the roughness on Section 040262 and its progression. Figure 137 shows a very short (8-ft) interval roughness profile for the same set of measurements covered in Figure 136. The figure shows the average contribution to the IRI of each 8-ft-long segment as a function of the segment midpoint. The figure demonstrates that contributions to the overall IRI of the section build up most aggressively at the joints.

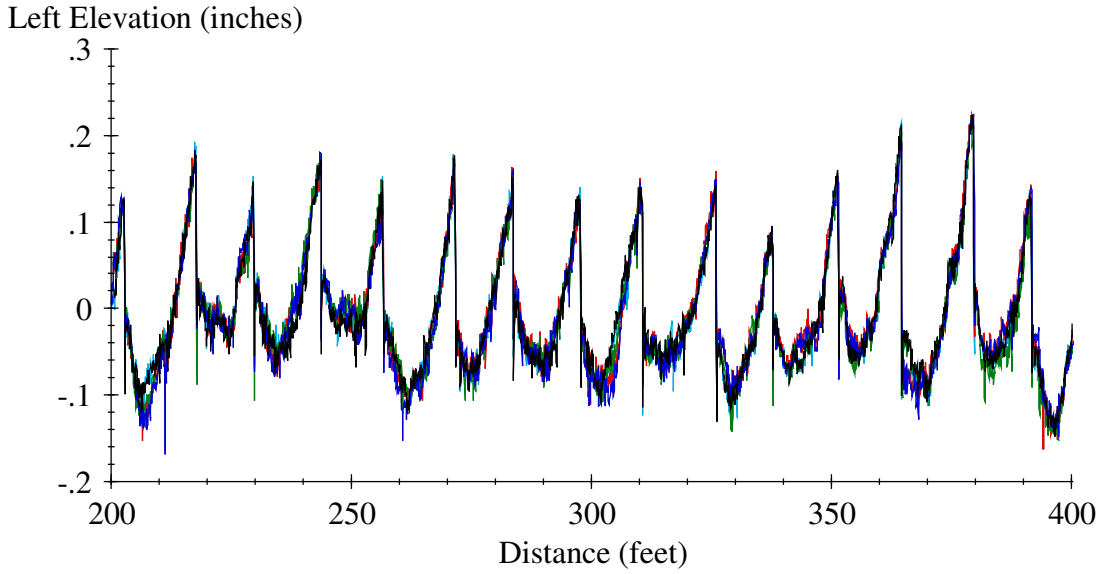

Figure 136. Left Elevation Profile from Visit 15 of Section 040262

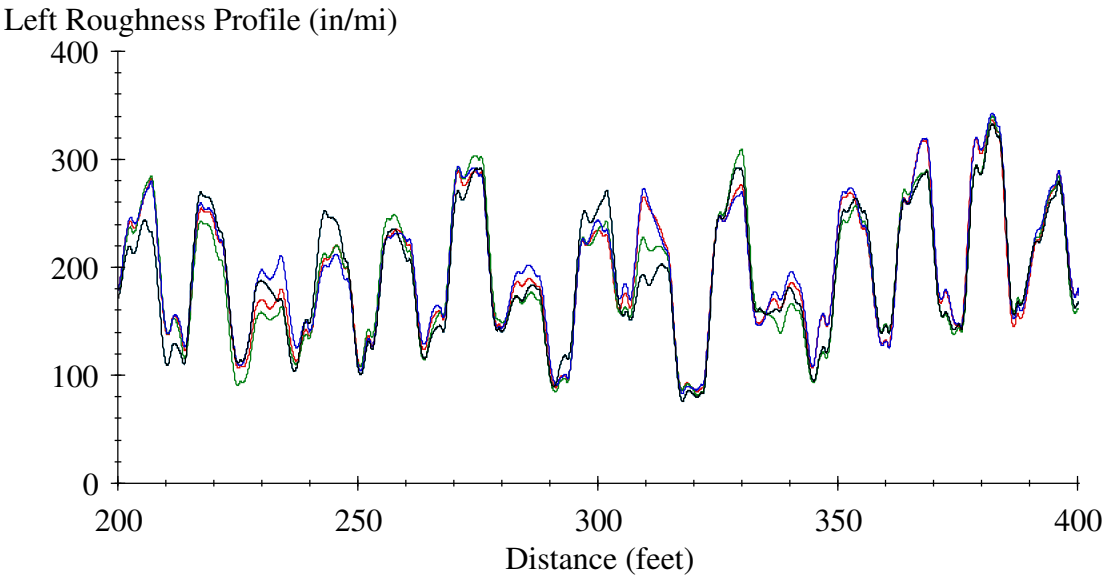

Figure 137. Left Roughness Profile from Visit 15 of Section 040262

Starting in visit 12 (August 11, 2006), the right-side profiles from Section 040262 included a narrow dip at the joint 83 ft from the start of the section and a swatch of narrow dips over a half slab from 129 to 137 ft from the start of the section. Both of these features appeared in areas where distress surveys

recorded longitudinal cracking. The roughness at joints caused by the faulting obscured the roughness of these dips.

Section 040263

Section 040263 developed very little faulting relative to the other test sections without dowels (040262, 040264, and 040265). In contrast, elevation profile plots showed a high level of slab curl.

Section 040264

All profiles from the right side of Section 040264 included a rise in elevation of more than 0.5 inch over a 7-ft distance starting 164 ft from the beginning of the section. The area that included this built-in feature was the roughest of the section throughout the experiment.

Section 040265

Section 040265 faulted. Filtered profile plots showed that the faulting grew steadily throughout the experiment. Like Section 040262, faulting on section 0265 caused a large portion of the roughness progression on Section 040265. Figure 138 shows the roughness profile for Section 040265 at various stages of the experiment. In this case, the roughness profile is plotted using a base length of 100 ft. Thus, every point along the lot represents the IRI of a segment of pavement that starts 50 ft upstream and ends 50 ft downstream of that location. The 100-ft base length shows the distribution of roughness throughout the section, but it is long enough to avoid local peaks caused by a single slab or joint.

Figure 138 demonstrates that, in the later visits, roughness was distributed evenly along the section because the magnitude of faulting was relatively consistent along the section. The figure also demonstrates that roughness continued to increase throughout the section over the entire experiment.

In the later visits, a patch of short wavelength chatter appeared in the left-side profile within the slab from 314 to 328 ft from the start of the section. Distress surveys recorded scaling over this area and irregular surface characteristics on the section. Portions of the section were diamond-ground in an effort to alter the surface texture.

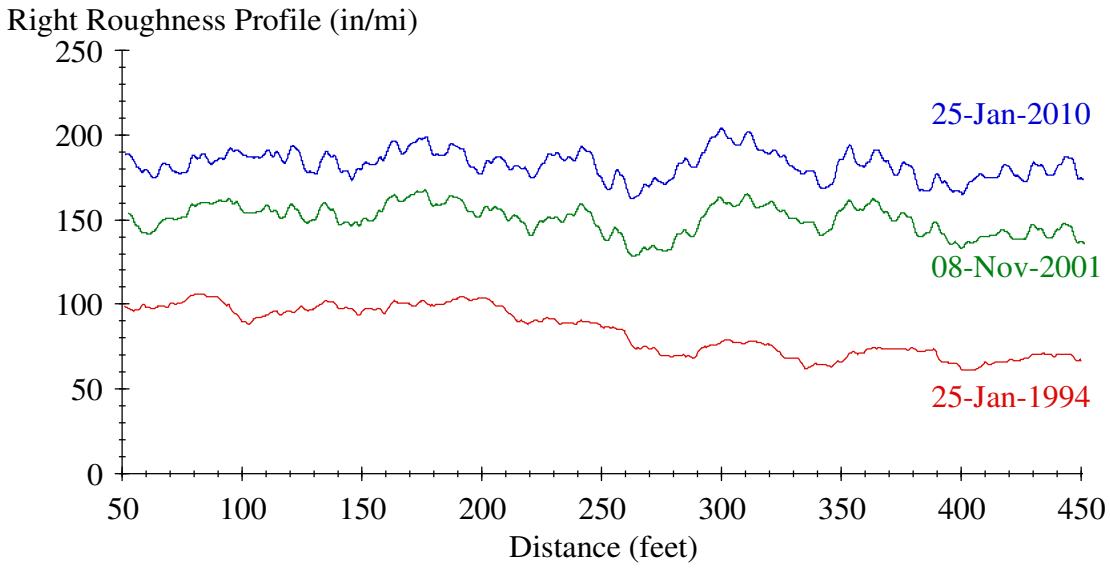

Figure 138. Right Roughness Profile from Section 040265

Section 040266

Section 040266 included a 60-ft long bump beginning 400 ft from the start of the section. The bump was more than 0.6 inch high throughout the monitoring history. On the left side, a narrow dip appeared 438 ft from the start of the section that grew in severity over time. The dip appeared at a joint where photos in the 2004 distress survey showed a gap in the sealant and some missing concrete at the aft side of the joint. PSD plots and filtered elevation profile plots showed that the curl on this section was more severe than it was on Sections 040267 and 040268.

Distress surveys indicated irregular surface characteristics on the section. Diamond grinding had been performed on the left wheelpath from 405 to 450 ft from the start of the section to adjust the texture. In the photos, it appeared the grinding barely submerged the existing texture. As such, the grinding did not affect the IRI.

Section 040267

A weigh-in-motion scale was installed within Section 040267 between visit 11 (December 12, 2004) and visit 12 (August 11, 2006). The scales appeared 206 ft from the start of the section on the left side and 194 ft from the start of the section on the right side. The portion of the section upstream of the scales received diamond grinding as part of the installation procedure. Diamond grinding reduced the IRI of the first 200 ft of the section by about 20 inches/mi on the right side but very little on the left side. Figure 139 shows the profile from visit 12 over a segment that includes the scale, which is about 0.1 inch above the surrounding pavement and as such, contributes some roughness to the section. The series of closely spaced peaks from 176 to 192 ft along the plot occurs in an area that includes the inductive loop and the approach slab.

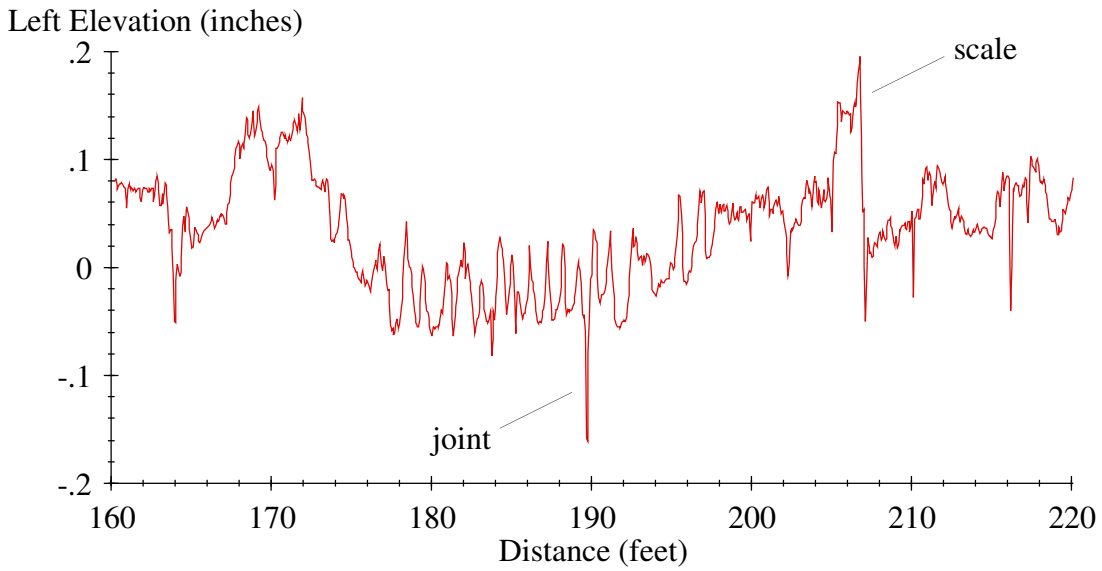

Figure 139. Weigh-in-Motion Scale On Section 040267

Section 040268

No specific observations are listed for Section 040268.

FAULTING ANALYSIS

Traditional profile analysis also revealed that faulting contributed heavily to the roughness of some of the test sections. A simple algorithm provided faulting estimates at each joint. This included an algorithm for finding the joints and a simple calculation of the difference in elevation downstream of the joint and the elevation upstream of the joint (Sayers et al. 1986).

To exclude the narrow dips at the joint from the calculation, the faulting algorithm excluded 6 inches of profile on either side of the joint and used the average elevation over 6 inches of profile on either side of the excluded area. In visit 01 (0.32 years) and visit 02 (1.42 years), only one profile point appeared within this range for the approach and leave slab. In later visits, the calculation included at least six points on either side of the joint.

All the test sections except 040262 and 040265 produced average faulting values of less than 0.05 inch throughout the experiment. As described above, Sections 040262 and 040265 faulted, the severity of faulting grew throughout the experiment, and the increase in IRI with time owed primarily to faulting. Figures 140 and 141 show the faulting estimates for the left and right profiles of these sections.

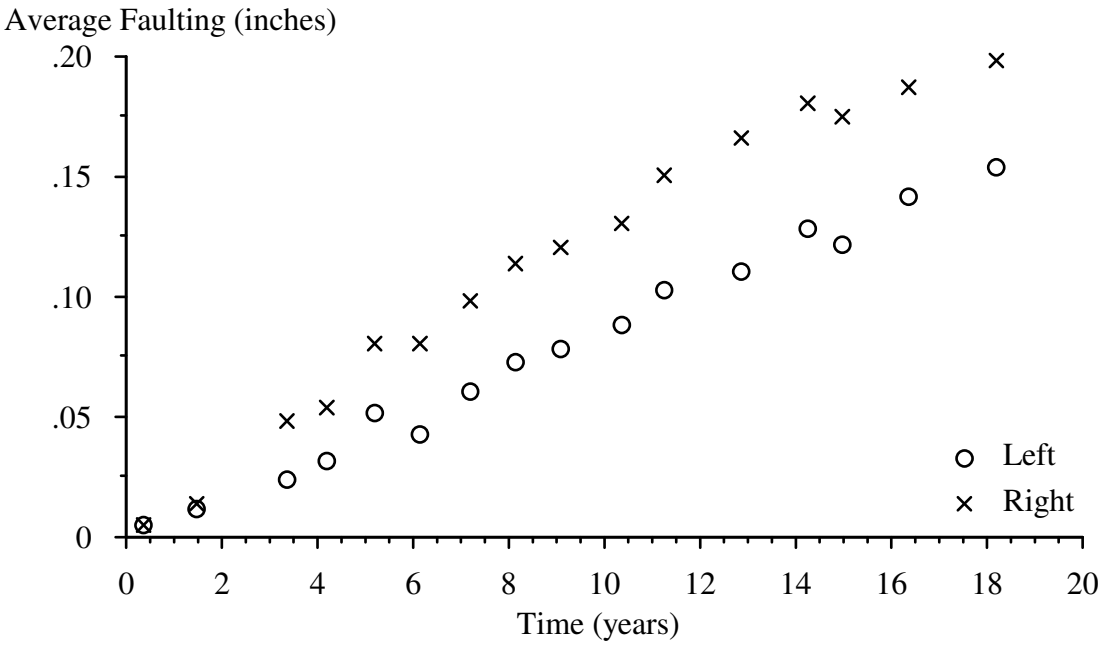

Figure 140. Faulting in Section 040262

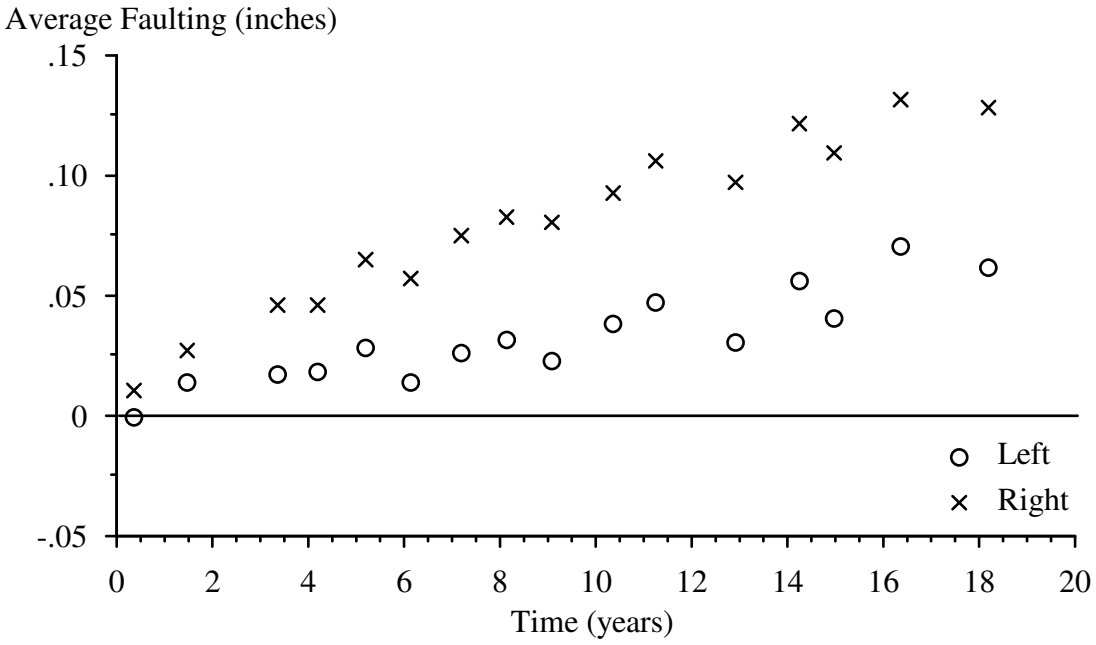

Figure 141. Faulting in Section 040265

PROFILE ANALYSIS KEY FINDINGS

Traditional profile analyses revealed roughness on some test sections caused by transverse and longitudinal cracking, and some localized roughness caused by built-in defects. However, spectral analysis and filtered profile plots showed that curl and warp contributed to, and in some cases dominated, the roughness on many of the test sections. In addition, the progression of roughness throughout the experiment often followed a disorderly trend because of diurnal and seasonal changes in slab curl and warp. Pseudo strain gradient (PSG) analysis also revealed the level of curl and warp increased overall throughout the life of the experiment, with commensurate increases in the IRI.

Low-Strength Core Sections

Table 42 summarizes results from the low-strength sections in the base experiment The table also provides the net change in IRI values for the left and right side, that is, the change in IRI from the initial visit (0.32 year) to the final visit (16.32 years); the net change in PSG value from the initial to the final visit; and the prevailing direction of curl in the final visit. For these test sections, a negative value indicates an increase in upward curl, and a positive value indicates a decrease in upward curl.

Table 42 shows that a strong relationship exists between the change in PSG and the change in IRI, even though the specific relationship depends on the pavement structural properties. (See Table 67.) For example, the highest change in PSG of the 11-inch-thick sections occurred on Section 040215, which showed the highest change in IRI. Further, Section 040217 (where the level of curl decreased) showed a net decrease in IRI also.

Table 42. Summary of Low-Strength Section Results

Section	040213	040217	040221	040215	040219	040223
PCC flexural strength (psi)	550	550	550	550	550	550
Surface layer thickness (inch)	8	8	8	11	11	11
Base type	DGAB	LCB	PATB	DGAB	LCB	PATB
Direction of curl	Up	Up	Up	Up	Up	Up
IRI change (inch/mi)						
Left	29	3	20	43	30	39
Right	130	-7	12	46	26	29
PSG change (με /inch)						
Left	-36	15	-21	-38	-14	-33
Right	-15	13	-16	-40	-8	-29
IRI change, curl removed (inch/mi)						
Left	-3	17	3	-5	10	-4
Right	92	5	-3	-3	11	-5

On the six low-strength test sections within the standard experiment, the correlation between IRI and PSG was very high. This permitted statistical analysis that isolated the portion of the overall roughness caused by curl and warp from the remainder of the roughness. With the influence of curl and warp removed, the balance of roughness often followed a much more orderly trend. This helped investigate other sources of roughness, such as distress, that were otherwise obscured by the influence of curl and warp. It also identified instances in which the roughness progressed solely due to changes in curl and warp, where the test section had not deteriorated despite the increase in overall IRI.

Table 42 also lists the change in IRI with the influence of curl removed. In this case, the balance of the roughness held steady throughout the monitoring period on Sections 040215, 040217, and 040221. This was also the case on Sections 040219 and 040223, with the exception of two left IRI values from years 9 and 10 that stood out as higher than the rest. Profile analysis showed that the additional roughness was isolated to the 8- to 11-ft wavelength range. Otherwise, the noncurl IRI on these sections held steady at a relatively low value, or increased slightly from an initially low value.

With the influence of curl and warp removed, the balance of the roughness on Section 040213 held steady throughout the experiment on the left side, but increased after 11 years on the left side. Patches of narrow dips, caused by longitudinal cracking, appeared in the left-side profiles in the second half of the monitoring period, and they caused localized roughness starting in year 12 of the experiment.

Some other observations from the low-strength sections include:

- Section 040213 included a long bump followed by a long dip in all profiles. This feature of the profile included a 0.9-inch transition from the peak of the bump to the lowest part of the dip over 40 ft of pavement.
- Section 040217 included transverse and longitudinal cracking starting in year 3 of the experiment. The transverse cracks caused narrow dips in the profiles at some mid-slab positions that increased in severity throughout the rest of the monitoring period.
- One of the slabs within Section 040221 experienced severe aggregate loss early in the experiment. The distress surveys listed scaling along the right side of the slab. This area and a few others were sealed with fiberglass by year 14. Yet the slab with the most severe aggregate loss caused localized roughness in the right-side profiles by the end of the monitoring period.

High-Strength Core Sections

Table 43 summarizes results from the high-strength sections. As a group, these sections exhibited a lesser increase in roughness. Like the low-strength group, the sections with the LCB either increased in roughness less than their counterparts with other base types or decreased in roughness while the others increased.

Table 43 lists the net change in PSG for each section. On Sections 040218, 040220, and 040222, a positive number indicates a reduction in upward curl. The IRI either reduced or held steady on these

sections. On Sections 040214 and 040216, a positive value of PSG change indicates a change from upward curl at the start of the experiment to downward curl at the end. On Section 040214, the transition toward downward curl was more aggressive on the first half of the section, and a group of slabs in the second half of the section maintained a reduced level of upward curl. In this case, the effect on IRI depends on the initial level of downward curl. On Section 040224, upward curl increased overall.

Table 43. Summary of High-Strength Section Results

Section	040214	040218	040222	040216	040220	040224
PCC flexural strength (psi)	900	900	900	900	900	900
Surface layer thickness (inch)	8	8	8	11	11	11
Base type	DGAB	LCB	PATB	DGAB	LCB	PATB
Direction of curl						
Initial (0.32 year)	Up	Up	Up	Up	Up	Up
Final (16.32 years)	Down	Up	Up	Down	Up	Up
IRI change (inch/mi)						
Left	17	-2	26	11	25	47
Right	14	-6	11	13	11	27
PSG change (με/inch)						
Left	96	42	-16	24	7	-26
Right	99	41	-7	24	-1	-23

Supplemental Sections

Table 44 summarizes the results from the supplemental sections. Sections 040262 to 040265 match the designs of Sections 040213, 040221, 040223, and 040215, respectively, with the exception that they are undoweled. All of the supplemental sections exhibited upward curl (on average) in the initial profiling visit (0.32 year) and the final visit (16.32 years), but some exhibited downward curl in the second visit (1.42 years). Sections 040262 and 040265 faulted, and the faulting progressed throughout the experiment from virtually none to an average value of about 0.15 inch on Section 040262 and 0.10 inch on Section 040265.

Table 44. Summary of Supplemental Section Results

Section	040262	040263	040264	040265	040266	040267	040268
PCC flexural strength (psi)	550	550	550	550	550	550	550
Surface layer thickness (inch)	8	8	8.5	8.5	12.5	11	8
Base type	DGAB	PATB	PATB	DGAB	DGAB	BTB	BTB
Direction of curl	Up	Up	Up	Up	Up	Up	Up
IRI change (inch/mi)							
Left	136	32	34	56	43	4	22
Right	183	24	33	95	27	-17	4
PSG change (με /inch)							
Left	-59	-20	-24	-37	-30	-15	-26
Right	-57	-32	-23	-37	-23	-12	-22

AC Sections

The IRI increased on Section 040260 by 64 inch/mi on the left side and 9 inch/mi on the right side. Two areas of localized roughness appeared on the left side of Section 040260 that account for the increase in IRI. These areas included small potholes, patching, longitudinal cracks, and pools of sealant.

The IRI increased on Section 040261 by 17 inch/mi on the left side and 58 inch/mi on the right side. Dips appeared at several transverse cracks starting 10 years into the experiment that exacerbated the roughness of the section in both wheelpaths. In addition, a distressed area on the right side developed into a pothole. This caused localized roughness in the final profiling visit.

CHAPTER 5. CONCLUSIONS AND RECOMMENDATIONS

ADOT initiated this analysis project to study the relative performance of the various SPS-2 design alternatives (including supplemental sections), which can provide a foundation for future design decisions. Surface distress, deflection, and profile data were used as the basis for performance and were each analyzed as part of the study.

The findings drawn from this evaluation must be considered carefully. Although the SPS-2 project offers a distinctive opportunity to directly compare the performance of various pavement structures while reducing the confounding effects of traffic loading, climate, and subgrade conditions, the experimental design did not offer replicate structures under the same conditions to verify findings. Conclusions drawn from this study are based on one set of in situ conditions; observations from other climate or loading scenarios may differ from those noted within this report. Therefore, findings reported may be unique to the conditions and construction of this site.

Considering this, the data captured at the project provides valuable insight into pavement design and performance. Following is a summary of lessons learned from the performance data collected at the SPS-2 site:

- The flexible sections perform quite similarly in all analyses. The sections exhibit remarkably constant response over time in deflection analysis, despite the large increase in distress. Subgrade support is similar to the rigid DGAB sections in the initial period, but does not decrease over time to the extent that it does for the rigid sections. The cracking and distress present for the two sections are strikingly similar and the combined (left and right) IRI progression is very similar. The similar performance of the AC supplemental sections indicates the conditions of the Arizona SPS-2 project have remained consistent.

- The State 406 BTB (Section 040268) performs better than the PATB (Section 040223) counterpart section in all measured deflection parameters. Roughness and distress performance between the two sections are rather similar. However, caution should be used because the comparison is based on only one pair of sections.

- The role of drained base sections (PATB) in improving pavement performance appears to be unclear in this study. This can be attributed to the relative dry conditions of the test site and the drainage efficiency of the materials used in the roadway.

- Deflection analysis determined that slabs on LCB had the greatest decline in stiffness. The transverse and longitudinal cracking formed on LCB sections corroborates the conclusion of slabs on LCB exhibiting poor performance. However, IRI progression exhibited by the section was less than other sections, and in some instances the IRI has improved.

- Roughness and roughness progression alone cannot be used to represent the health of a test section. Several LCB test sections did not exhibit changes in roughness in proportion to the amount of cracking.

- Spectral analysis and filtered plots showed that curl and warp contributed to, and in some cases dominated, the roughness of the test sections.
- Well-defined map cracking exists in multiple sections. Dynamic loading occurring just before Section 040214 may be a possible cause, however its role is unclear. Another association with the map cracking is the high-strength sections that are most affected also have the greatest decline in stiffness. Preliminary testing has determined ASR is not a major contributor.
- Thicker sections performed largely as expected under deflection and distress analysis. Thicker sections exhibited greater slab stiffness, subgrade support, and resistance to cracking.
- Wider 14-ft sections exhibit better LTE between joints, as well as the least lane-to-shoulder drop when compared to thinner 12-ft sections.
- Both undoweled DGAB sections (040262 and 040265) exhibit the most faulting in distress and profile monitoring. The undoweled DGAB sections have better LTE as measured by the JL test than the undoweled PATB sections. LTE as measured by the JA test is similar for both base types. This may indicate the formation of voids under the leave edge of the slab due to erosion of the DGAB material.

Based on these findings, the following recommendations are provided by the research team for consideration by ADOT:

- Most of the high-strength pavement test sections appeared to have experienced heavy map cracking. Preliminary testing has determined that ASR is not a major contributing factor. It is recommended that forensic analysis be performed to determine the factors contributing to this map cracking.
- The use of pavement condition indicators in addition to IRI typically provides a better assessment of pavement condition for network-level decision-making. However, careful consideration of warp and curl should be used when assessing rigid pavements.
- Continuing to monitor these test sections will provide deeper and more substantial findings. It is recommended that the interim findings of this report be re-evaluated when the pavement has reached the end of its service.

REFERENCES

American Association of State Highway and Transportation Officials (AASHTO). 1985. *AASHTO Guide for Design of Pavement Structures*. Vol. 2. Washington, D.C.: American Association of State Highway and Transportation Officials.

American Association of State Highway and Transportation Officials (AASHTO). 1993. *AASHTO Guide for Design of Pavement Structures.* Washington, D.C.: American Association of State Highway and Transportation Officials.

American Association of State Highway and Transportation Officials (AASHTO). 1998. *Supplement to the AASHTO Guide for Design of Pavement Structures.* Washington, D.C.: American Association of State Highway and Transportation Officials.

Chang, G. K., R. Rasmussen, D. Merritt, S. Garber, S. Karamihas. 2010. *Impact of Temperature Curling and Moisture Warping on Jointed Concrete Pavement Performance, Volume II: Data Analysis and Model Development.* Federal Highway Administration Contract DTFH61-02-C-00077. Washington, D.C.: Federal Highway Administration.

Evans, L. D. and A. Eltahan. 2000. *LTPP Profile Variability.* Publication FHWA-RD-00-113. McLean, VA: Federal Highway Administration.

Huang, Y. H. 1993. *Pavement Analysis and Design*. Upper Saddle River, NJ: Prentice Hall.

Karamihas, S. M. 2004. "Development of Cross Correlation for Objective Comparison of Profiles." *International Journal of Vehicle Design*, 36(2/3): 173–193.

Karamihas, S. M., T.D. Gillespie, S.D. Kohn, R.W. Perera. 1999. *Guidelines for Longitudinal Pavement Profile Measurement*. Report 454. Washington, D.C.: National Cooperative Highway Research Program.

Karamihas, S. M., T.D. Gillespie, S.M. Riley. 1995. "Axle Tramp Contribution to the Dynamic Wheel Loads of a Heavy Truck." *Proceedings of the 4th International Symposium on Heavy Vehicle Weights and Dimensions*. C. B. Winkler (ed.): 425–434.

Karamihas, S. M. and K. Senn. 2009. "Profile Analysis of Arizona Specific Pavement Studies 5 Project." *Transportation Research Record: Journal of the Transportation Research Board* 2095: 144–152.

Karamihas, S. M. and K. Senn. 2010. *Profile Analysis of the LTPP SPS-6 Site in Arizona*. Report UMTRI-2010-17. Ann Arbor, MI: University of Michigan Transportation Research Institute.

Karamihas, S. M. and K. Senn. 2012. *Curl and Warp Analysis of the LTPP SPS-2 Site in Arizona*. Publication FHWA-HRT-12-068. McLean, VA: Federal Highway Administration.

Miller, J. S. and W. Y. Bellinger. 2003. *Distress Identification Manual for the Long-Term Pavement Performance Program*. Revised fourth edition. Publication FHWA-RD-03-031. Washington, D.C.: Federal Highway Administration.

Perera, R. W. and S. D. Kohn. 2005. *Quantification of Smoothness Index Differences Related to Long-Term Pavement Performance Equipment Type*. Publication FHWA-HRT-05-054. McLean, VA: Federal Highway Administration: 2005.

Rada, G. R., C. L. Wu, R. K. Bhandari, A. R. Shekharan, G. E. Elkins, J. S. Miller. 1999. *Study of LTPP Distress Data Variability*. Publication FHWA-RD-99-074, FHWA-RD-99-075. Washington, D.C.: Federal Highway Administration.

Sayers, M. W. 1989. "Two Quarter-Car Models for Defining Road Roughness: IRI and HRI." *Transportation Research Record: Journal of the Transportation Research Board* 1215: 165–172.

Sayers, M. W. 1990. "Profiles of Roughness." *Transportation Research Record: Journal of the Transportation Research Board* 1260: 106–111.

Sayers, M. W., T. D. Gillespie, C. A. V. Queiroz. 1986. "The International Road Roughness Experiment." World Bank Technical Paper Number 45. *Transportation Research Record: Journal of the Transportation Research Board*.

Sayers, M. W. and S. M. Karamihas. 1996a. "Estimation of Rideability by Analyzing Longitudinal Road Profile." *Transportation Research Record: Journal of the Transportation Research Board* 1536: 110–116.

Sayers, M. W. and S. M. Karamihas. 1996b. *Interpretation of Road Roughness Profile Data*. Publication FHWA-RD-96-101. Washington, D.C.: Federal Highway Administration.

Szrot, Robert B. 1994. *Specific Pavement Studies Construction Report for Experiment SPS-2 Strategic Study of Structural Factors for Rigid Pavement Ehrenberg-Phoenix Highway, Maricopa County, Arizona*. Unpublished construction report. Phoenix: Arizona Department of Transportation.

Yu, H. T., K. Smith, M. I. Darter. 1995. *Field and Analytical Evaluation of the Effects of Tied PCC Shoulders and Widened Slabs on Performance of JPCP*. Publication CDOT-DTD-R-95-18. Denver: Colorado Department of Transportation.

Zollinger, S. Lee, J. Puccinelli, and N. Jackson. 2008. *LTPP Computed Parameter: Moisture Content*. Publication FHWA-HRT-08-035. McLean, VA: Federal Highway Administration.

APPENDIX A: DATA QUALITY SCREENING

Researchers performed a screening process to select five repeat profile measurements from each visit of each section. The five measurements among the group of either five, seven, or nine available runs were selected that exhibited the best agreement with each other. In this case, agreement between any two measurements was judged by cross correlating them after applying the IRI filter (Karamihas 2004). In this method, the output signals are compared instead of the overall index. High correlation by this method requires that the overall roughness is in agreement, as well as the details of the profile shape that affect the IRI. The IRI filter was applied before correlation in this case for several reasons:

- Direct correlation of unfiltered profiles places a premium on long wavelength content, but ignores much of the contribution of short wavelength content.
- Correlation of IRI filter output emphasizes profile features in (approximate) proportion to their effect on the overall roughness.
- Correlation of IRI filter output provides a good trade-off between emphasizing localized rough features at distressed areas in the pavement and placing too much weight on the very short-duration, narrow features (spikes) that are not likely to agree between measurements. This is because the IRI filter amplifies short wavelength content, but attenuates macrotexture, megatexture, and spikes.
- A relationship has been demonstrated between the cross correlation level of IRI filter output and the expected agreement in overall IRI (Karamihas 2004).

This method was performed with a special provision for correcting modest longitudinal distance measurement errors.

Each comparison between profiles produced a single value that summarized their level of agreement. When nine repeat profile measurements were available, they produced 36 correlation values. Any subgroup of five measurements could be summarized by averaging the appropriate 10 correlation values. The subgroup that produced the highest average was selected, and the other repeats were excluded from the analyses discussed in this report. When the number of available profiles was either seven or nine, the number of measurements that were excluded was either two or four. Tables 45 through 65 list the selected repeats for each visit of each section, and the composite correlation level produced by them.

This process of selecting five repeat measurements from a larger group is similar to the practice within the LTPP study except that it uses composite agreement in profile rather than the overall index value. The correlation levels listed in Tables 45 through 65 provide a repeatability score and appraise the agreement between profile measurements for each visit of each section. When two profiles produce a correlation level above 0.82, their IRI values are expected to agree within 10 percent most (95 percent) of the time. Above this threshold, the agreement between profiles is usually acceptable for studying the

influence of distresses on profile. When two profiles produce a correlation level above 0.92, they are expected to agree within 5 percent most of the time. Above this threshold, the agreement between profiles is good. Correlation above 0.92 often depends on consistent lateral tracking of the profiler, and may be very difficult to achieve on highly distressed surfaces. Note that the IRI values in this report will be the average of five observations, which will tighten the tolerance even further.

Table 45. Selected Repeats of Section 040213

Visit	Repeat Numbers					Composite Correlation
01	2	3	6	7	8	0.935
02	2	5	6	7	9	0.902
03	1	3	5	6	8	0.971
04	1	3	4	5	7	0.953
05	1	2	5	6	7	0.965
06	1	3	4	5	6	0.963
07	4	5	6	7	9	0.948
08	1	2	4	7	9	0.936
09	1	3	4	5	7	0.948
10	1	2	6	7	8	0.947
11	2	3	4	7	9	0.900
12	1	4	5	7	8	0.853
13	1	2	3	4	5	0.812
14	1	3	4	5	6	0.771
15	1	4	5	7	9	0.769
16	1	4	6	7	9	0.793

Table 46. Selected Repeats of Section 040214

Visit	Repeat Numbers					Composite Correlation
01	2	3	5	6	8	0.909
02	2	4	6	7	8	0.822
03	2	3	4	5	8	0.912
04	1	3	4	5	7	0.900
05	1	3	4	5	6	0.903
06	2	3	4	6	7	0.926
07	1	2	5	6	8	0.953
08	1	2	5	6	7	0.950
09	1	3	5	6	8	0.937
10	2	3	5	6	8	0.935
11	3	5	6	7	8	0.924
12	2	3	4	7	8	0.945
13	4	5	6	8	9	0.959
14	1	3	4	7	8	0.927
15	2	4	5	6	9	0.955
16	1	2	4	5	7	0.941

Table 47. Selected Repeats of Section 040215

Visit	Repeat Numbers					Composite Correlation
01	1	3	4	5	8	0.930
02	1	3	5	7	8	0.920
03	5	6	7	8	9	0.962
04	1	3	4	5	7	0.922
05	1	2	4	6	7	0.967
06	1	2	4	6	7	0.955
07	1	3	4	8	9	0.976
08	4	5	6	7	9	0.987
09	3	5	6	7	8	0.943
10	1	3	5	8	9	0.933
11	1	2	3	5	7	0.948
12	2	4	5	6	7	0.981
13	2	3	4	7	9	0.976
14	1	2	7	8	9	0.969
15	2	3	4	5	8	0.965
16	1	3	4	7	8	0.971
S01	2	3	4	5	7	0.936
S02	1	2	3	4	5	0.966
S03	1	2	3	4	5	0.955
S04	1	2	3	4	5	0.921
S05	1	2	3	4	5	0.937
S06	1	2	3	4	5	0.959
S07	1	2	3	4	5	0.936

Table 47. Selected Repeats of Section 040215 (cont.)

Visit	Repeat Numbers					Composite Correlation
S08	2	3	4	5	6	0.959
S09	1	2	3	4	7	0.977
S10	1	3	4	5	9	0.972
S11	2	3	5	6	7	0.979
S12	1	2	3	6	8	0.983
S13	1	3	4	5	7	0.979
S14	2	3	5	6	7	0.965
S15	4	5	6	7	9	0.960
S16	1	2	3	4	5	0.965
S17	1	2	3	4	6	0.976
S18	1	4	7	8	9	0.947
S19	2	3	5	6	9	0.963
S20	2	4	6	7	9	0.960
S21	1	3	4	5	6	0.972
S22	3	4	6	7	9	0.975
S23	3	4	5	8	9	0.964
S24	1	4	5	6	9	0.957
S25	1	2	4	7	9	0.975
S26	1	2	4	5	6	0.973
S27	1	2	3	8	9	0.972
S28	4	6	7	8	9	0.961
S29	1	2	3	4	8	0.973
S30	2	4	6	7	8	0.978
S31	3	4	6	7	8	0.978
S32	1	2	3	4	6	0.976

Table 48. Selected Repeats of Section 040216

Visit	Repeat Numbers					Composite Correlation
01	3	5	6	8	9	0.922
02	3	5	7	8	9	0.892
03	1	2	3	5	7	0.927
04	1	2	4	5	6	0.930
05	1	2	3	5	6	0.951
06	2	3	4	5	6	0.948
07	2	3	4	6	9	0.968
08	2	3	4	6	8	0.957
09	1	2	4	5	8	0.930
10	1	3	4	6	7	0.937
11	2	4	5	6	9	0.910
12	1	4	6	7	8	0.949
13	2	4	7	8	9	0.954
14	2	3	6	8	9	0.938
15	1	2	3	4	8	0.948
16	3	4	5	7	8	0.960

Table 49. Selected Repeats of Section 040217

Visit	Repeat Numbers					Composite Correlation
01	4	6	7	8	9	0.925
02	1	4	5	6	8	0.876
03	3	4	6	8	9	0.951
04	2	3	4	6	7	0.916
05	1	2	3	6	7	0.915
06	1	2	4	5	7	0.939
07	4	5	6	8	9	0.963
08	1	2	3	6	9	0.957
09	1	2	3	4	5	0.921
10	1	2	3	7	9	0.907
11	1	2	6	7	9	0.875
12	1	3	5	6	7	0.957
13	2	3	4	6	9	0.911
14	1	2	5	7	9	0.933
15	1	5	6	7	9	0.838
16	4	5	6	8	9	0.886

Table 50. Selected Repeats of Section 040218

Visit	Repeat Numbers					Composite Correlation
01	1	2	5	7	9	0.898
02	2	4	5	8	9	0.818
03	1	3	6	7	9	0.909
04	1	3	4	5	7	0.891
05	1	2	3	4	5	0.888
06	2	3	4	6	7	0.923
07	1	2	3	6	9	0.944
08	1	3	4	7	8	0.951
09	2	3	5	6	7	0.892
10	1	2	4	7	9	0.906
11	1	2	3	6	7	0.889
12	4	5	6	7	9	0.928
13	2	3	6	8	9	0.931
14	1	3	7	8	9	0.947
15	1	3	6	7	8	0.921
16	1	3	4	5	7	0.962

Table 51. Selected Repeats of Section 040219

Visit	Repeat Numbers					Composite Correlation
01	3	5	6	7	9	0.902
02	1	2	5	6	8	0.870
03	2	4	7	8	9	0.931
04	1	3	4	6	7	0.920
05	1	2	3	5	7	0.928
06	2	3	4	6	7	0.942
07	2	4	6	8	9	0.955
08	1	2	5	6	8	0.954
09	1	2	3	7	9	0.923
10	1	2	5	6	8	0.932
11	4	5	6	7	8	0.936
12	1	4	6	7	8	0.970
13	2	3	4	8	9	0.954
14	1	3	4	5	6	0.951
15	4	5	6	7	9	0.931
16	2	5	6	7	9	0.959

Table 52. Selected Repeats of Section 040220

Visit	Repeat Numbers					Composite Correlation
01	5	6	7	8	9	0.910
02	3	4	5	6	9	0.871
03	1	2	6	7	8	0.917
04	1	3	4	6	7	0.898
05	2	3	4	6	7	0.950
06	1	2	5	6	7	0.950
07	1	2	5	7	9	0.935
08	2	3	4	5	6	0.958
09	1	2	3	6	8	0.915
10	2	3	4	6	7	0.929
11	1	2	5	6	9	0.938
12	3	4	6	7	8	0.936
13	2	3	6	7	9	0.932
14	2	4	5	6	7	0.944
15	1	3	6	8	9	0.936
16	3	5	6	7	8	0.959

Table 53. Selected Repeats of Section 040221

Visit	Repeat Numbers					Composite Correlation
01	1	4	6	8	9	0.890
02	4	6	7	8	9	0.838
03	1	2	4	6	9	0.901
04	1	2	4	5	6	0.882
05	1	2	3	5	6	0.936
06	1	2	4	5	7	0.946
07	1	2	5	6	9	0.932
08	1	5	6	8	9	0.946
09	1	5	6	7	8	0.825
10	1	3	4	6	8	0.861
11	2	4	5	6	7	0.857
12	3	4	5	6	7	0.943
13	1	2	3	5	6	0.907
14	1	2	3	4	6	0.949
15	2	5	7	8	9	0.934
16	3	4	6	7	9	0.919

Table 54. Selected Repeats of Section 040222

Visit	Repeat Numbers					Composite Correlation
01	4	5	6	8	9	0.898
02	1	4	5	6	7	0.816
03	1	3	5	6	9	0.942
04	1	3	5	6	7	0.857
05	2	3	4	6	7	0.929
06	2	3	4	5	7	0.920
07	2	4	5	6	8	0.943
08	2	4	5	7	8	0.948
09	1	2	4	6	7	0.900
10	1	2	3	5	6	0.880
11	2	3	4	6	8	0.853
12	2	3	6	7	8	0.935
13	2	3	5	6	9	0.931
14	2	3	4	6	7	0.914
15	2	6	7	8	9	0.910
16	1	3	6	7	9	0.943

Table 55. Selected Repeats of Section 040223

Visit	Repeat Numbers					Composite Correlation
01	1	2	6	7	9	0.892
02	1	3	4	8	9	0.893
03	4	5	6	7	9	0.934
04	3	4	5	6	7	0.948
05	1	2	3	6	7	0.943
06	1	2	3	4	6	0.953
07	1	2	3	6	8	0.956
08	3	4	5	6	9	0.960
09	3	6	7	8	9	0.949
10	1	2	3	5	8	0.914
11	5	6	7	8	9	0.946
12	2	4	5	6	9	0.972
13	2	3	4	8	9	0.956
14	3	5	6	8	9	0.965
15	3	4	6	8	9	0.951
16	1	2	3	5	8	0.968

Table 56. Selected Repeats of Section 040224

Visit	Repeat Numbers					Composite Correlation
01	3	4	6	8	9	0.894
02	4	5	6	8	9	0.837
03	2	3	4	6	7	0.907
04	1	2	3	4	5	0.863
05	1	2	3	6	7	0.873
06	2	3	5	6	7	0.921
07	2	3	5	6	7	0.940
08	2	4	6	7	8	0.932
09	1	2	4	5	8	0.917
10	2	4	6	8	9	0.960
11	1	2	4	7	9	0.873
12	1	2	6	7	8	0.939
13	5	6	7	8	9	0.950
14	3	6	7	8	9	0.905
15	1	2	3	5	9	0.918
16	3	6	7	8	9	0.966

Table 57. Selected Repeats of Section 040260

Visit	Repeat Numbers					Composite Correlation
01	1	2	3	4	7	0.939
02	3	5	6	8	9	0.899
03	1	2	5	6	8	0.932
04	3	4	5	6	7	0.885
05	1	2	4	5	7	0.921
06	2	4	5	6	7	0.920
07	1	3	4	6	9	0.952
08	2	3	6	7	9	0.962
09	1	3	4	6	8	0.921
10	1	2	5	7	8	0.897
11	1	2	5	6	7	0.837
12	1	3	4	6	8	0.889
13	1	3	5	6	8	0.799
14	1	2	3	4	6	0.882
15	1	3	4	5	6	0.866
16	1	3	4	8	9	0.900

Table 58. Selected Repeats of Section 040261

Visit	Repeat Numbers					Composite Correlation
01	3	5	6	8	9	0.916
02	2	4	6	7	9	0.872
03	5	6	7	8	9	0.910
04	1	3	5	6	7	0.857
05	3	4	5	6	7	0.926
06	1	2	4	5	7	0.896
07	3	4	5	6	7	0.937
08	1	3	4	5	7	0.940
09	1	2	3	4	9	0.866
10	1	2	5	6	7	0.860
11	1	4	5	6	7	0.766
12	4	5	6	8	9	0.882
13	2	3	4	7	8	0.893
14	1	2	3	6	7	0.877
15	1	2	3	5	9	0.922
16	3	5	7	8	9	0.890

Table 59. Selected Repeats of Section 040262

Visit	Repeat Numbers					Composite Correlation
01	4	5	6	8	9	0.867
02	1	4	5	7	9	0.859
03	2	3	5	6	7	0.965
04	2	3	4	5	7	0.969
05	1	2	3	4	5	0.981
06	2	3	4	5	6	0.980
07	2	5	6	8	9	0.981
08	2	3	5	6	7	0.986
09	1	2	3	4	6	0.976
10	2	3	4	6	7	0.975
11	2	3	4	6	7	0.978
12	1	4	5	8	9	0.982
13	2	3	5	7	9	0.949
14	1	4	7	8	9	0.959
15	1	2	5	8	9	0.974
16	2	5	7	8	9	0.943

Table 60. Selected Repeats of Section 040263

Visit	Repeat Numbers					Composite Correlation
01	3	6	7	8	9	0.839
02	1	6	7	8	9	0.813
03	1	2	3	5	9	0.940
04	1	2	3	4	5	0.936
05	2	3	4	5	7	0.939
06	1	2	3	4	6	0.942
07	1	3	5	7	9	0.947
08	2	3	5	7	9	0.944
09	2	5	6	7	8	0.884
10	1	2	4	5	9	0.932
11	1	2	4	5	7	0.855
12	2	3	4	6	7	0.949
13	2	4	5	6	8	0.941
14	2	3	5	7	8	0.939
15	2	3	4	5	6	0.899
16	2	4	6	7	9	0.944

Table 61. Selected Repeats of Section 040264

Visit	Repeat Numbers					Composite Correlation
01	2	3	4	5	8	0.906
02	1	5	6	7	8	0.931
03	1	2	4	6	8	0.938
04	2	3	4	5	6	0.940
05	2	3	5	6	7	0.964
06	1	2	3	6	7	0.951
07	1	2	5	6	8	0.962
08	1	4	5	6	7	0.969
09	1	3	4	7	8	0.904
10	3	4	5	7	8	0.894
11	1	2	4	5	6	0.911
12	1	3	6	8	9	0.968
13	2	4	6	8	9	0.946
14	1	2	4	6	7	0.962
15	1	2	3	4	5	0.937
16	3	6	7	8	9	0.962

Table 62. Selected Repeats of Section 040265

Visit	Repeat Numbers					Composite Correlation
01	1	2	4	5	8	0.915
02	4	5	6	7	9	0.879
03	1	3	4	6	7	0.958
04	3	4	5	6	7	0.927
05	1	4	5	6	7	0.950
06	1	2	4	6	7	0.937
07	2	4	6	7	8	0.976
08	2	3	4	5	6	0.965
09	2	3	4	5	7	0.923
10	3	6	7	8	9	0.935
11	2	4	5	6	7	0.916
12	2	3	7	8	9	0.974
13	3	4	6	8	9	0.966
14	1	2	4	6	7	0.962
15	1	2	3	6	7	0.977
16	1	4	5	6	9	0.971

Table 63. Selected Repeats of Section 040266

Visit	Repeat Numbers					Composite Correlation
01	1	4	6	7	9	0.886
02	1	2	3	5	6	0.885
03	1	2	7	8	9	0.941
04	1	2	3	4	6	0.901
05	1	2	3	4	6	0.972
06	1	2	3	5	6	0.943
07	1	4	6	7	8	0.958
08	2	3	4	5	6	0.963
09	3	4	7	8	9	0.902
10	1	3	5	7	8	0.949
11	1	4	5	7	9	0.934
12	1	2	5	6	9	0.947
13	1	2	4	5	8	0.960
14	1	3	4	5	8	0.950
15	1	3	4	5	6	0.937
16	2	4	5	7	9	0.955

Table 64. Selected Repeats of Section 040267

Visit	Repeat Numbers					Composite Correlation
01	1	3	6	7	9	0.888
02	4	5	6	7	8	0.878
03	4	5	6	8	9	0.919
04	1	2	3	4	6	0.872
05	1	2	4	5	6	0.921
06	2	3	4	5	7	0.949
07	1	2	3	7	9	0.955
08	1	4	6	7	9	0.960
09	2	3	5	6	8	0.874
10	2	3	5	7	9	0.930
11	1	2	5	6	7	0.926
12	1	2	4	6	9	0.869
13	1	4	6	7	8	0.878
14	1	2	4	5	6	0.907
15	1	2	3	4	6	0.909
16	5	6	7	8	9	0.893

Table 65. Selected Repeats of Section 040268

Visit	Repeat Numbers					Composite Correlation
01	1	2	5	6	9	0.851
02	1	3	5	6	8	0.813
03	4	5	7	8	9	0.919
04	1	2	4	6	7	0.863
05	1	2	4	5	6	0.904
06	2	3	5	6	7	0.956
07	1	3	4	8	9	0.932
08	2	3	6	7	9	0.947
09	1	2	3	5	6	0.831
10	1	5	6	8	9	0.924
11	3	4	6	7	9	0.875
12	2	3	6	7	8	0.939
13	3	4	5	7	9	0.931
14	1	2	5	6	9	0.883
15	2	3	4	6	9	0.873
16	2	5	6	8	9	0.939

Only nine of the 347 sets of selected repeat measurements listed in Tables 45 through 65 exhibited composite correlation below 0.82. Measurements of Sections 040215 and 040262 produced the highest repeatability scores, whereas some profiles from visit 02 and the later visits of Section 040213 produced the lowest scores. Fortunately, correlation was never low enough to impede the automated synchronization process. However, low repeatability scores prompted inspection of profile plots to help identify the cause.

In visit 02, most of the profiles included short wavelength content that was not correlated between repeat measurements. The effect was greatest in Sections 040214, 040218, 040222, 040263, and 040268. This was probably caused by coarse surface texture, but that cannot be verified.

Other observations follow:

- Section 040213, Visit 13-15: The right-side profiles of these visits included deep, narrow dips, or patches of narrow dips that appeared in some areas in each profile, but with inconsistent size and placement.

- Section 040260 (an AC section), Later Visits: Agreement between profiles was diminished by patches of uncorrelated deep, narrow dips in the left profiles from 50 to 65 ft from the start of the section, and 330 to 360 ft from the start of the section.

- Section 040261 (an AC section), Visit 11: Localized roughness appeared from 474 to 479 ft from the start of the profile on the right side in four of the five profiles, and with inconsistent shape and placement on the left side from 355 to 375 ft from the start of the section. Visits 09 and 10 also included inconsistent measurement of these features.

- Section 040267 and 040268, Visit 09: The short wavelength content from these visits did not agree well, and the profiles included some extraneous narrow dips.

APPENDIX B: ROUGHNESS VALUES

This appendix lists the left IRI, right IRI, mean roughness index (MRI), HRI, and RN values for each visit of each section. The roughness values are the average for five repeat runs. The five runs were selected from a group of as many as nine by automated comparison of profiles, as described in Appendix A. Values of standard deviation are also provided for left and right IRI to reveal cases of high variability among the five measurements. However, the screening procedure used to select five repeats usually helped reduce the level of scatter.

The discussion of roughness in the report emphasizes the left and right IRI. Nevertheless, the other indexes do provide useful additional information. MRI is simply the average of the left and right IRI value. HRI is calculated by converting the IRI filter into a half-car model (Sayers 1989). This is done by collapsing the left and right profiles into a single profile in which each point is the average of the corresponding left and right elevation. The IRI filter is then applied to the resulting signal. The HRI is very similar to the IRI except that side-to-side deviations in profile are eliminated. The result is that the HRI value for a pair of profiles will always be lower than the corresponding MRI value. Comparing the HRI and MRI value provides a crude indication of the significance of roll (i.e., side-by-side variation in profile) to the overall roughness. When HRI is low compared to MRI, roll is significant. This is common among asphalt pavements (Karamihas et al. 1995). Certain types of pavement distress, such as longitudinal cracking, may also cause significant differences between HRI and MRI.

Figure 142 compares the HRI to MRI for the profile measurements on PCC sections. This includes 1,585 pairs of roughness values and excludes AC Sections 040260 and 040261. The figure shows a best fit line with a zero intercept and a line of equality. The slope of the line is 0.914. A typical range for concrete pavement is 0.90 through 0.95. Note that a better linear fit was found without forcing a zero intercept. A simple linear fit produced a slope of about 0.979 and an intercept of about -6.9 inches/mi.

RN has shown a closer relationship to road user opinion than the other indexes (Sayers 1996a). As such, it may help distinguish the segments from each other by ride quality. Further, the effect on RN may help quantify the impact of that distress on ride when the roughness of a section is dominated by a particular type of distress. In particular, a very low RN value coupled with moderate IRI values indicates a high level of short wavelength roughness and potential sensitivity to narrow dips and measurement errors caused by coarse surface texture.

Table 66 provides the roughness values, including the date of each measurement and the time (in years) since the site was opened to traffic.

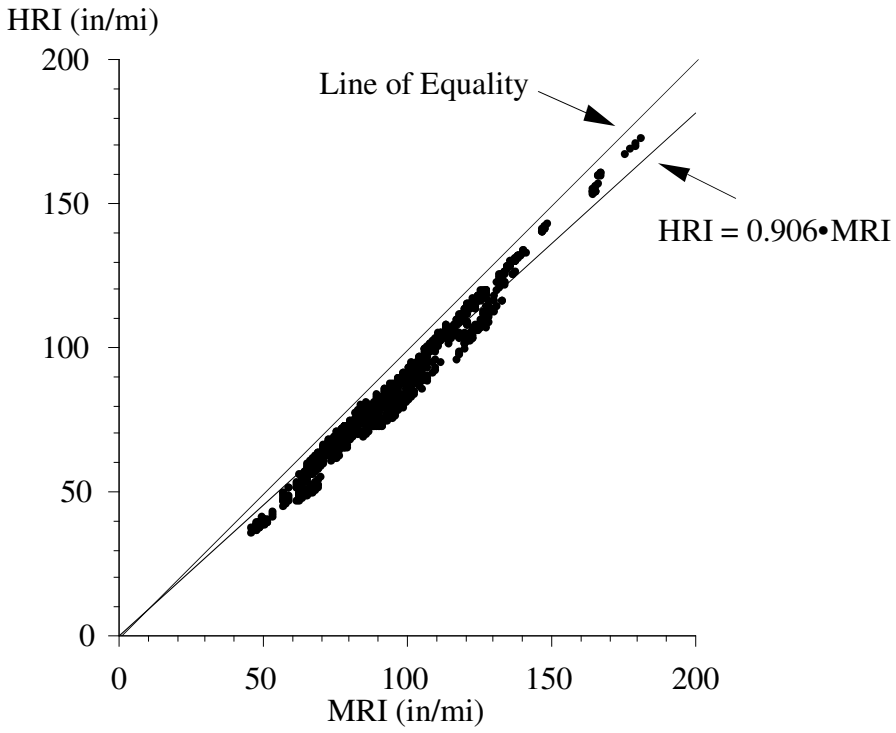

Figure 142. Comparison of HRI to MRI

Table 66. Roughness Values

Section	Date	Years	Left IRI (inch/mi)		Right IRI (inch/mi)		MRI	HRI	RN
			Avg.	St. Dev.	Avg.	St. Dev.	(inch/mi)	(inch/mi)	
0213	25-Jan-94	0.32	91	1.7	97	1.5	94	86	3.63
0213	5-Mar-95	1.42	72	1.0	83	1.7	78	69	3.75
0213	27-Jan-97	3.32	103	0.9	110	1.1	107	101	3.53
0213	4-Dec-97	4.18	104	2.6	117	2.0	111	105	3.50
0213	8-Dec-98	5.19	108	1.1	117	1.5	112	107	3.46
0213	15-Nov-99	6.12	118	0.7	131	1.0	124	118	3.33
0213	30-Nov-00	7.16	107	1.1	119	1.4	113	106	3.42
0213	8-Nov-01	8.10	118	1.2	133	1.5	125	119	3.29
0213	30-Oct-02	9.08	124	0.6	119	2.4	122	116	3.36
0213	4-Feb-04	10.34	110	1.4	105	3.3	108	101	3.48
0213	12-Dec-04	11.20	103	1.2	117	3.2	110	103	3.32
0213	11-Aug-06	12.86	139	1.0	177	5.5	158	149	2.39
0213	30-Dec-07	14.25	114	0.8	147	6.9	131	121	2.56
0213	20-Sep-08	14.97	127	1.0	166	6.8	147	136	2.56
0213	25-Jan-10	16.32	111	1.3	198	3.5	155	140	2.00
0214	25-Jan-94	0.32	85	1.9	80	1.9	83	80	3.65
0214	5-Mar-95	1.42	55	0.5	59	1.7	57	50	3.78
0214	27-Jan-97	3.32	76	3.2	64	2.6	70	65	3.80
0214	4-Dec-97	4.18	70	2.6	69	1.9	70	65	3.79
0214	8-Dec-98	5.19	67	3.3	68	0.9	68	62	3.80
0214	15-Nov-99	6.12	85	2.0	71	1.8	78	71	3.70
0214	30-Nov-00	7.16	81	0.8	71	1.2	76	70	3.68
0214	8-Nov-01	8.10	79	2.5	79	0.5	79	73	3.62
0214	30-Oct-02	9.08	94	3.4	78	1.0	86	78	3.47
0214	4-Feb-04	10.34	101	3.1	87	1.4	94	85	3.38

Table 66. Roughness Values (cont.)

Section	Date	Years	Left IRI (inch/mi)		Right IRI (ich/mi)		MRI	HRI	RN
			Avg	St. Dev.	Avg.	St. Dev.	(inch/ mi)	(inch/ mi)	
0214	12-Dec-04	11.20	80	2.9	83	1.0	81	75	3.46
0214	13-Aug-06	12.87	81	1.9	83	0.8	82	75	3.44
0214	30-Dec-07	14.25	102	1.3	93	1.8	97	90	3.31
0214	20-Sep-08	14.97	96	3.0	85	1.7	91	84	3.39
0214	25-Jan-10	16.32	100	2.0	99	0.9	100	94	3.27
0215	25-Jan-94	0.32	89	0.8	91	1.4	90	80	3.66
0215	5-Mar-95	1.42	82	0.9	97	3.2	89	80	3.61
0215	27-Jan-97	3.32	98	0.7	102	1.4	100	91	3.60
0215	4-Dec-97	4.18	100	3.6	105	2.2	103	94	3.52
0215	15-Jan-98	4.29	89	0.8	101	2.3	95	86	3.61
0215	15-Jan-98	4.29	87	0.7	103	0.9	95	87	3.61
0215	13-Apr-98	4.53	92	0.9	99	1.7	96	86	3.60
0215	13-Apr-98	4.53	91	1.2	98	1.6	95	85	3.60
0215	9-Jul-98	4.77	96	1.7	107	2.3	101	91	3.54
0215	9-Jul-98	4.77	93	0.7	105	1.9	99	88	3.54
0215	30-Sep-98	5.00	105	1.1	114	2.3	109	100	3.47
0215	30-Sep-98	5.00	99	2.3	112	1.6	105	96	3.48
0215	8-Dec-98	5.19	109	1.2	110	2.1	109	101	3.46
0215	15-Nov-99	6.12	114	1.9	123	1.5	118	110	3.41
0215	30-Nov-00	7.16	111	0.5	119	1.4	115	106	3.44
0215	8-Nov-01	8.10	121	0.5	126	0.7	124	116	3.34
0215	9-Dec-01	8.19	125	0.3	129	0.6	127	120	3.32
0215	9-Dec-01	8.19	116	0.9	120	0.6	118	111	3.42
0215	24-Jan-02	8.31	122	1.2	127	0.9	124	117	3.34
0215	24-Jan-02	8.31	112	0.3	120	1.1	116	108	3.43
0215	15-Mar-02	8.45	130	1.2	133	1.3	132	125	3.27
0215	15-Mar-02	8.45	117	0.7	122	2.8	119	112	3.40
0215	9-Oct-02	9.02	140	1.3	132	3.0	136	130	3.24
0215	9-Oct-02	9.02	121	1.4	123	1.4	122	116	3.35
0215	30-Oct-02	9.08	131	6.1	122	1.1	127	119	3.33
0215	20-Dec-02	9.22	137	0.8	131	1.3	134	128	3.25
0215	20-Dec-02	9.22	125	4.4	120	1.6	123	115	3.37
0215	7-Mar-03	9.43	124	1.5	119	2.1	122	115	3.35
0215	7-Mar-03	9.43	112	0.7	112	2.0	112	105	3.45
0215	25-Jul-03	9.81	121	0.3	130	1.2	126	119	3.32
0215	25-Jul-03	9.81	119	1.0	126	1.0	122	115	3.33
0215	24-Nov-03	10.15	124	1.7	127	0.9	125	119	3.29
0215	24-Nov-03	10.15	117	1.2	120	2.2	118	112	3.39
0215	14-Dec-03	10.20	119	0.8	126	1.0	122	115	3.32
0215	14-Dec-03	10.20	115	1.4	119	0.6	117	110	3.39
0215	4-Feb-04	10.34	130	3.3	118	2.4	124	116	3.35
0215	22-Apr-04	10.56	133	0.4	139	2.1	136	129	3.22
0215	22-Apr-04	10.56	118	1.1	121	1.6	120	113	3.36
0215	15-Jul-04	10.79	132	1.3	142	1.7	137	131	3.21
0215	15-Jul-04	10.79	129	0.3	135	0.9	132	126	3.24
0215	9-Sep-04	10.94	135	0.1	145	0.7	140	134	3.18
0215	9-Sep-04	10.94	132	0.7	142	1.6	137	131	3.19
0215	12-Dec-04	11.20	108	1.9	120	1.3	114	107	3.39

Table 66. Roughness Values (cont.)

Section	Date	Years	Left IRI (inch/mi)		Right IRI (inch/mi)		MRI	HRI	RN
			Avg.	St. Dev.	Avg.	St. Dev.	(inch/ mi)	(inch/ mi)	
0215	13-Aug-06	12.87	135	0.6	141	0.9	138	133	3.18
0215	30-Dec-07	14.25	122	0.5	123	1.0	123	116	3.32
0215	20-Sep-08	14.97	134	0.9	142	1.6	138	132	3.18
0215	25-Jan-10	16.32	124	1.5	129	1.0	126	119	3.28
0216	25-Jan-94	0.32	90	2.4	87	2.3	89	81	3.57
0216	5-Mar-95	1.42	83	1.5	89	1.8	86	75	3.54
0216	27-Jan-97	3.32	87	3.7	84	0.8	86	76	3.65
0216	4-Dec-97	4.18	86	0.7	85	2.5	85	76	3.61
0216	8-Dec-98	5.19	88	0.9	87	1.8	88	78	3.59
0216	15-Nov-99	6.12	93	2.7	86	0.6	89	79	3.63
0216	30-Nov-00	7.16	85	1.3	88	0.7	87	78	3.65
0216	8-Nov-01	8.10	85	1.2	91	1.3	88	78	3.62
0216	30-Oct-02	9.08	98	3.9	92	1.3	95	80	3.52
0216	4-Feb-04	10.34	99	3.2	99	1.6	99	84	3.47
0216	12-Dec-04	11.20	88	1.6	99	2.7	94	85	3.50
0216	13-Aug-06	12.87	88	1.4	99	1.5	94	85	3.49
0216	30-Dec-07	14.25	98	1.6	101	1.5	99	88	3.44
0216	20-Sep-08	14.97	100	2.8	97	0.4	99	85	3.47
0216	25-Jan-10	16.32	93	1.0	105	1.8	99	90	3.42
0217	25-Jan-94	0.32	93	0.5	82	1.1	87	79	3.59
0217	5-Mar-95	1.42	61	1.5	70	2.1	65	56	3.81
0217	27-Jan-97	3.32	83	0.7	78	1.3	80	71	3.76
0217	4-Dec-97	4.18	79	3.7	80	2.6	79	72	3.78
0217	8-Dec-98	5.19	82	3.2	78	2.8	80	72	3.76
0217	15-Nov-99	6.12	93	2.2	81	0.9	87	77	3.73
0217	30-Nov-00	7.16	85	1.6	75	0.6	80	70	3.81
0217	8-Nov-01	8.10	87	2.2	77	1.7	82	74	3.78
0217	30-Oct-02	9.08	87	1.5	74	0.8	80	70	3.73
0217	4-Feb-04	10.34	88	3.3	66	1.4	77	65	3.79
0217	12-Dec-04	11.20	84	4.3	74	2.0	79	69	3.75
0217	11-Aug-06	12.86	105	1.7	89	2.1	97	89	3.62
0217	30-Dec-07	14.25	80	2.5	74	1.6	77	66	3.60
0217	20-Sep-08	14.97	110	3.5	82	1.9	96	86	3.61
0217	25-Jan-10	16.32	81	1.6	75	3.0	78	68	3.26
0218	25-Jan-94	0.32	92	3.7	85	1.9	88	83	3.54
0218	5-Mar-95	1.42	65	1.3	59	1.6	62	53	3.74
0218	27-Jan-97	3.32	74	1.5	56	0.4	65	58	3.81
0218	4-Dec-97	4.18	73	1.4	61	2.0	67	60	3.77
0218	8-Dec-98	5.19	74	0.9	60	1.2	67	60	3.77
0218	15-Nov-99	6.12	79	1.9	65	0.7	72	65	3.77
0218	30-Nov-00	7.16	72	1.1	60	0.7	66	58	3.82
0218	8-Nov-01	8.10	71	1.0	62	0.6	67	59	3.82
0218	30-Oct-02	9.08	85	4.7	56	0.9	70	63	3.75
0218	4-Feb-04	10.34	82	3.2	56	1.3	69	61	3.76
0218	12-Dec-04	11.20	72	1.4	64	2.1	68	59	3.76
0218	13-Aug-06	12.87	77	1.1	71	0.8	74	66	3.70
0218	30-Dec-07	14.25	83	2.5	68	1.7	76	67	3.70
0218	20-Sep-08	14.97	80	1.2	76	0.8	78	69	3.66

Table 66. Roughness Values (cont.)

Section	Date	Years	Left IRI (inch/mi)		Right IRI (inch/mi)		MRI	HRI	RN
			Avg.	St. Dev.	Avg.	St. Dev.	(inch/ mi)	(inch/ mi)	
0218	25-Jan-10	16.32	78	1.4	70	1.3	74	65	3.68
0219	25-Jan-94	0.32	78	1.5	90	2.1	84	75	3.60
0219	5-Mar-95	1.42	67	1.1	84	1.4	76	66	3.63
0219	27-Jan-97	3.32	77	1.6	95	1.3	86	78	3.68
0219	4-Dec-97	4.18	88	3.9	97	1.6	92	84	3.63
0219	8-Dec-98	5.19	84	3.8	102	1.6	93	86	3.63
0219	15-Nov-99	6.12	89	2.5	105	2.3	97	90	3.59
0219	30-Nov-00	7.16	79	0.4	101	1.2	90	82	3.67
0219	8-Nov-01	8.10	87	1.8	110	3.2	99	92	3.59
0219	30-Oct-02	9.08	100	1.6	102	1.6	101	92	3.53
0219	4-Feb-04	10.34	101	4.4	98	1.6	100	91	3.52
0219	12-Dec-04	11.20	91	2.8	111	2.0	101	94	3.54
0219	13-Aug-06	12.87	117	1.5	136	1.4	127	121	3.24
0219	30-Dec-07	14.25	90	1.2	102	1.0	96	89	3.54
0219	20-Sep-08	14.97	118	2.4	135	3.3	126	121	3.29
0219	25-Jan-10	16.32	98	2.7	114	1.5	106	99	3.42
0220	25-Jan-94	0.32	77	2.1	80	1.8	78	74	3.70
0220	5-Mar-95	1.42	66	1.4	72	1.2	69	62	3.74
0220	27-Jan-97	3.32	66	3.6	72	1.7	69	64	3.87
0220	4-Dec-97	4.18	70	1.8	73	1.6	71	67	3.84
0220	8-Dec-98	5.19	69	0.6	73	1.4	71	67	3.86
0220	15-Nov-99	6.12	69	1.0	77	1.4	73	68	3.85
0220	30-Nov-00	7.16	77	4.7	69	1.3	73	68	3.86
0220	8-Nov-01	8.10	68	1.0	78	0.5	73	67	3.86
0220	30-Oct-02	9.08	82	2.1	69	1.2	76	71	3.77
0220	4-Feb-04	10.34	89	4.5	69	0.5	79	73	3.75
0220	12-Dec-04	11.20	73	1.6	80	1.9	77	71	3.75
0220	13-Aug-06	12.87	75	1.8	82	1.0	79	73	3.71
0220	30-Dec-07	14.25	86	1.9	85	1.6	85	80	3.63
0220	20-Sep-08	14.97	91	2.2	79	0.8	85	80	3.63
0220	25-Jan-10	16.32	80	2.4	83	1.7	82	76	3.65
0221	25-Jan-94	0.32	73	1.9	73	1.7	73	65	3.72
0221	5-Mar-95	1.42	56	0.7	60	1.4	58	48	3.82
0221	27-Jan-97	3.32	78	1.6	78	0.4	78	71	3.76
0221	4-Dec-97	4.18	82	3.3	84	2.3	83	77	3.59
0221	8-Dec-98	5.19	85	2.8	82	1.7	83	77	3.66
0221	15-Nov-99	6.12	85	1.8	88	1.0	86	79	3.61
0221	30-Nov-00	7.16	76	1.2	82	1.6	79	71	3.62
0221	8-Nov-01	8.10	84	2.0	85	0.9	85	79	3.63
0221	30-Oct-02	9.08	90	6.3	77	2.4	84	77	3.46
0221	4-Feb-04	10.34	76	1.3	74	3.8	75	67	3.63
0221	12-Dec-04	11.20	79	2.9	80	1.3	79	72	3.61
0221	11-Aug-06	12.86	100	0.9	99	0.9	100	94	3.43
0221	30-Dec-07	14.25	81	1.3	81	1.6	81	74	3.52
0221	20-Sep-08	14.97	96	1.3	94	1.8	95	88	3.43
0221	25-Jan-10	16.32	82	1.3	84	1.5	83	76	3.40
0222	25-Jan-94	0.32	72	1.1	71	1.7	72	65	3.74
0222	5-Mar-95	1.42	58	1.4	56	1.1	57	47	3.82

Table 66. Roughness Values (cont.)

Section	Date	Years	Left IRI (inch/mi)		Right IRI (inch/mi)		MRI	HRI	RN
			Avg.	St. Dev.	Avg.	St. Dev.	(inch/mi)	(inch/mi)	
0222	15-Nov-99	6.12	79	2.5	64	0.8	72	64	3.78
0222	27-Jan-97	3.32	72	0.9	55	0.7	64	55	3.85
0222	4-Dec-97	4.18	64	2.8	63	1.8	63	55	3.82
0222	8-Dec-98	5.19	66	0.4	63	1.3	64	56	3.80
0222	30-Nov-00	7.16	77	1.9	60	0.4	69	61	3.83
0222	8-Nov-01	8.10	68	1.6	64	0.8	66	57	3.84
0222	30-Oct-02	9.08	88	4.3	57	0.7	73	64	3.73
0222	4-Feb-04	10.34	87	6.3	58	1.1	72	64	3.72
0222	12-Dec-04	11.20	69	3.1	66	0.9	67	58	3.77
0222	13-Aug-06	12.87	72	0.8	73	1.7	73	63	3.75
0222	30-Dec-07	14.25	91	2.3	69	0.9	80	73	3.67
0222	20-Sep-08	14.97	78	2.1	75	1.5	76	69	3.69
0222	25-Jan-10	16.32	76	1.7	70	1.7	73	64	3.72
0223	25-Jan-94	0.32	73	1.5	81	3.1	77	66	3.70
0223	5-Mar-95	1.42	69	0.9	79	1.3	74	63	3.68
0223	27-Jan-97	3.32	80	1.5	85	1.2	82	71	3.69
0223	4-Dec-97	4.18	83	0.7	88	1.4	85	76	3.69
0223	8-Dec-98	5.19	89	2.2	92	1.5	90	82	3.64
0223	15-Nov-99	6.12	89	1.7	95	1.4	92	84	3.62
0223	30-Nov-00	7.16	82	1.3	94	0.8	88	79	3.66
0223	8-Nov-01	8.10	87	1.8	99	1.1	93	85	3.61
0223	30-Oct-02	9.08	108	1.3	88	0.9	98	90	3.56
0223	4-Feb-04	10.34	117	5.8	86	1.1	101	93	3.52
0223	12-Dec-04	11.20	91	2.5	98	1.3	95	87	3.54
0223	13-Aug-06	12.87	111	1.5	120	1.3	116	109	3.37
0223	30-Dec-07	14.25	97	1.6	96	2.2	96	90	3.51
0223	20-Sep-08	14.97	122	2.5	118	0.8	120	115	3.35
0223	25-Jan-10	16.32	101	2.9	102	1.2	102	95	3.47
0224	25-Jan-94	0.32	65	0.5	67	1.7	66	61	3.80
0224	5-Mar-95	1.42	60	1.8	71	3.6	66	60	3.74
0224	27-Jan-97	3.32	73	3.2	69	0.8	71	66	3.84
0224	4-Dec-97	4.18	64	5.5	71	2.3	67	61	3.84
0224	8-Dec-98	5.19	64	5.5	75	3.3	69	64	3.83
0224	15-Nov-99	6.12	80	5.2	71	1.5	76	71	3.83
0224	30-Nov-00	7.16	83	4.3	69	0.4	76	72	3.84
0224	8-Nov-01	8.10	66	3.3	77	0.8	72	66	3.82
0224	30-Oct-02	9.08	84	2.7	72	0.9	78	72	3.77
0224	4-Feb-04	10.34	114	2.1	71	1.0	93	86	3.65
0224	12-Dec-04	11.20	70	5.0	79	1.7	75	69	3.78
0224	13-Aug-06	12.87	78	3.6	74	1.1	76	72	3.78
0224	30-Dec-07	14.25	79	1.7	77	0.9	78	74	3.75
0224	20-Sep-08	14.97	89	6.6	78	1.2	83	78	3.72
0224	25-Jan-10	16.32	85	5.2	84	1.7	84	80	3.70
0260	25-Jan-94	0.32	57	0.3	69	1.8	63	50	3.89
0260	5-Mar-95	1.42	62	0.5	75	2.8	68	54	3.75
0260	27-Jan-97	3.32	64	0.9	70	2.6	67	51	3.84
0260	4-Dec-97	4.18	62	1.5	70	1.3	66	52	3.73
0260	8-Dec-98	5.19	61	1.8	69	1.6	65	50	3.77

Table 66. Roughness Values (cont.)

Section	Date	Years	Left IRI (inch/mi)		Right IRI (inch/mi)		MRI	HRI	RN
			Avg.	St. Dev.	Avg.	St. Dev.	(inch/ mi)	(inch/ mi)	
0260	15-Nov-99	6.12	63	1.4	68	1.4	66	51	3.84
0260	30-Nov-00	7.16	62	0.8	68	0.8	65	51	3.86
0260	8-Nov-01	8.10	62	0.5	70	1.4	66	51	3.82
0260	30-Oct-02	9.08	64	1.2	60	0.7	62	48	3.85
0260	4-Feb-04	10.34	65	1.6	60	2.1	63	49	3.82
0260	12-Dec-04	11.20	66	1.9	69	0.6	67	52	3.64
0260	13-Aug-06	12.87	88	2.7	70	2.4	79	61	3.36
0260	30-Dec-07	14.25	105	6.8	66	2.2	86	69	2.76
0260	20-Sep-08	14.97	111	3.8	72	2.0	92	74	2.78
0260	25-Jan-10	16.32	121	3.1	78	1.3	99	78	2.50
0261	25-Jan-94	0.32	40	0.4	53	1.5	47	39	4.05
0261	5-Mar-95	1.42	38	0.7	60	1.8	49	40	3.99
0261	27-Jan-97	3.32	40	0.5	60	1.4	50	40	3.85
0261	4-Dec-97	4.18	41	0.4	58	2.2	50	40	3.89
0261	8-Dec-98	5.19	39	0.9	60	1.0	50	40	3.84
0261	15-Nov-99	6.12	39	1.1	59	1.3	49	39	3.87
0261	30-Nov-00	7.16	38	0.4	59	0.8	48	40	3.82
0261	8-Nov-01	8.10	40	0.5	60	0.7	50	40	3.80
0261	30-Oct-02	9.08	38	0.6	55	1.7	46	38	4.02
0261	4-Feb-04	10.34	39	0.3	55	1.3	47	37	3.92
0261	12-Dec-04	11.20	42	2.5	62	1.0	52	42	3.86
0261	13-Aug-06	12.87	44	1.0	66	1.3	55	44	3.76
0261	30-Dec-07	14.25	44	0.6	72	3.1	58	48	3.51
0261	20-Sep-08	14.97	47	1.0	82	3.4	65	52	3.32
0261	25-Jan-10	16.32	57	0.8	111	2.5	84	69	2.83
0262	25-Jan-94	0.32	72	1.0	67	1.3	70	62	3.76
0262	5-Mar-95	1.42	67	0.6	70	1.3	69	59	3.71
0262	27-Jan-97	3.32	112	1.0	110	1.3	111	105	3.44
0262	4-Dec-97	4.18	122	1.3	118	1.4	120	115	3.35
0262	8-Dec-98	5.19	137	1.3	138	0.4	137	132	3.14
0262	15-Nov-99	6.12	144	0.6	150	1.1	147	142	3.08
0262	30-Nov-00	7.16	139	1.4	155	1.1	147	141	3.02
0262	8-Nov-01	8.10	158	0.3	175	0.5	166	161	2.84
0262	30-Oct-02	9.08	155	0.8	174	1.4	165	156	2.79
0262	4-Feb-04	10.34	158	0.8	171	1.5	164	154	2.73
0262	12-Dec-04	11.20	163	2.3	193	1.8	178	170	2.60
0262	11-Aug-06	12.86	195	0.8	225	0.8	210	201	2.33
0262	30-Dec-07	14.25	186	2.1	234	4.5	210	199	1.80
0262	20-Sep-08	14.97	204	0.6	249	3.9	227	215	1.76
0262	25-Jan-10	16.32	195	1.0	229	3.8	212	202	2.13
0263	25-Jan-94	0.32	68	0.8	70	1.8	69	61	3.67
0263	5-Mar-95	1.42	59	1.9	68	1.4	64	53	3.65
0263	27-Jan-97	3.32	80	0.7	73	0.7	77	69	3.76
0263	4-Dec-97	4.18	81	1.5	79	2.1	80	72	3.67
0263	8-Dec-98	5.19	82	1.2	82	2.3	82	74	3.67
0263	15-Nov-99	6.12	90	0.3	81	1.3	85	77	3.69
0263	30-Nov-00	7.16	82	1.7	78	1.6	80	72	3.75
0263	8-Nov-01	8.10	86	2.4	83	0.3	85	77	3.69

Table 66. Roughness Values (cont.)

Section	Date	Years	Left IRI (in/mi)		Right IRI (in/mi)		MRI	HRI	RN
			Avg.	St. Dev.	Avg.	St. Dev.	(inch/ mi)	(inch/ mi)	
0263	30-Oct-02	9.08	92	2.6	83	1.4	88	78	3.58
0263	4-Feb-04	10.34	90	1.7	83	1.8	87	75	3.58
0263	12-Dec-04	11.20	84	3.9	80	1.9	82	73	3.62
0263	11-Aug-06	12.86	104	1.4	95	2.0	100	92	3.50
0263	30-Dec-07	14.25	92	2.1	81	1.8	87	78	3.58
0263	20-Sep-08	14.97	103	2.4	93	1.9	98	89	3.50
0263	25-Jan-10	16.32	88	1.4	79	1.4	83	75	3.59
0264	25-Jan-94	0.32	105	1.9	113	2.4	109	93	3.37
0264	5-Mar-95	1.42	93	1.5	117	2.2	105	89	3.41
0264	27-Jan-97	3.32	113	1.4	122	2.6	118	98	3.34
0264	4-Dec-97	4.18	115	2.4	126	1.1	120	103	3.32
0264	8-Dec-98	5.19	114	2.1	133	1.7	123	106	3.30
0264	15-Nov-99	6.12	121	1.8	130	2.5	126	108	3.27
0264	30-Nov-00	7.16	119	0.7	129	2.7	124	107	3.28
0264	8-Nov-01	8.10	119	1.6	140	3.2	129	113	3.26
0264	30-Oct-02	9.08	122	4.7	125	1.0	123	108	3.26
0264	4-Feb-04	10.34	121	5.3	123	3.5	122	107	3.26
0264	12-Dec-04	11.20	123	4.7	135	4.4	129	114	3.19
0264	13-Aug-06	12.87	140	1.5	141	0.5	141	126	3.10
0264	30-Dec-07	14.25	135	1.6	132	2.7	134	119	3.12
0264	20-Sep-08	14.97	150	1.7	148	1.5	149	135	3.04
0264	25-Jan-10	16.32	128	3.6	144	3.5	136	122	3.13
0265	25-Jan-94	0.32	84	2.1	89	2.3	86	72	3.55
0265	5-Mar-95	1.42	81	2.0	96	2.1	89	73	3.50
0265	27-Jan-97	3.32	96	1.9	106	0.7	101	88	3.44
0265	4-Dec-97	4.18	99	2.6	115	3.2	107	94	3.37
0265	8-Dec-98	5.19	107	2.0	123	2.1	115	104	3.27
0265	15-Nov-99	6.12	109	1.4	128	1.0	118	106	3.29
0265	30-Nov-00	7.16	107	0.7	133	0.7	120	109	3.21
0265	8-Nov-01	8.10	118	1.6	146	0.5	132	122	3.11
0265	30-Oct-02	9.08	114	2.3	141	0.8	127	114	3.12
0265	4-Feb-04	10.34	112	2.1	145	3.5	129	116	3.05
0265	12-Dec-04	11.20	114	2.0	156	3.8	135	125	2.97
0265	13-Aug-06	12.87	136	1.4	168	1.4	152	143	2.90
0265	30-Dec-07	14.25	123	1.0	168	1.4	146	134	2.82
0265	20-Sep-08	14.97	143	1.6	182	1.5	163	154	2.79
0265	25-Jan-10	16.32	133	1.1	180	0.6	156	145	2.75
0266	25-Jan-94	0.32	82	1.2	93	1.8	87	78	3.54
0266	5-Mar-95	1.42	79	1.1	95	2.4	87	78	3.57
0266	27-Jan-97	3.32	87	1.5	94	0.4	90	79	3.65
0266	4-Dec-97	4.18	88	1.5	100	3.2	94	86	3.63
0266	8-Dec-98	5.19	91	1.6	102	0.5	97	89	3.60
0266	15-Nov-99	6.12	95	3.5	104	0.8	99	89	3.58
0266	30-Nov-00	7.16	89	0.7	101	0.7	95	87	3.62
0266	8-Nov-01	8.10	99	1.1	110	1.0	105	97	3.53
0266	30-Oct-02	9.08	118	5.2	108	0.9	113	104	3.39
0266	4-Feb-04	10.34	104	1.0	103	0.9	103	93	3.44
0266	12-Dec-04	11.20	98	1.9	109	2.1	103	96	3.47

Table 66. Roughness Values (cont.)

Section	Date	Years	Left IRI (inch/mi)		Right IRI (inch/mi)		MRI	HRI	RN
			Avg.	St. Dev.	Avg.	St. Dev.	(inch/ mi)	(inch/ mi)	
0266	13-Aug-06	12.87	122	3.5	125	1.9	123	116	3.28
0266	30-Dec-07	14.25	114	1.6	109	1.1	111	102	3.35
0266	20-Sep-08	14.97	133	0.6	129	0.8	131	123	3.21
0266	25-Jan-10	16.32	106	1.7	112	1.1	109	102	3.39
0267	25-Jan-94	0.32	80	1.7	106	2.0	93	78	3.39
0267	5-Mar-95	1.42	79	0.9	112	4.2	95	79	3.38
0267	27-Jan-97	3.32	75	2.2	106	1.4	90	75	3.61
0267	4-Dec-97	4.18	83	5.4	113	3.0	98	83	3.52
0267	8-Dec-98	5.19	82	1.8	115	1.7	99	84	3.49
0267	15-Nov-99	6.12	78	0.8	114	1.9	96	83	3.57
0267	30-Nov-00	7.16	76	0.3	111	1.0	94	82	3.56
0267	8-Nov-01	8.10	86	2.7	120	1.8	103	90	3.44
0267	30-Oct-02	9.08	92	6.2	110	2.7	101	86	3.44
0267	4-Feb-04	10.34	86	1.0	104	1.1	95	82	3.45
0267	12-Dec-04	11.20	88	1.6	114	1.4	101	89	3.40
0267	13-Aug-06	12.87	98	1.8	110	1.9	104	92	3.29
0267	30-Dec-07	14.25	81	1.2	84	1.2	82	71	3.53
0267	20-Sep-08	14.97	92	1.5	101	1.5	97	87	3.42
0267	25-Jan-10	16.32	77	2.0	91	1.7	84	74	3.45
0268	25-Jan-94	0.32	85	2.0	94	0.5	89	73	3.39
0268	5-Mar-95	1.42	80	1.5	96	3.7	88	72	3.36
0268	27-Jan-97	3.32	91	1.2	92	1.2	91	75	3.53
0268	4-Dec-97	4.18	89	3.9	95	2.5	92	76	3.48
0268	8-Dec-98	5.19	93	3.2	98	3.0	95	79	3.45
0268	15-Nov-99	6.12	94	1.6	98	1.6	96	79	3.52
0268	30-Nov-00	7.16	92	0.5	97	1.9	95	78	3.48
0268	8-Nov-01	8.10	97	1.1	104	2.1	101	84	3.42
0268	30-Oct-02	9.08	102	4.7	96	2.8	99	84	3.40
0268	4-Feb-04	10.34	99	0.6	91	1.9	95	80	3.39
0268	12-Dec-04	11.20	97	3.5	98	2.1	97	80	3.35
0268	13-Aug-06	12.87	116	0.6	112	2.1	114	100	3.26
0268	30-Dec-07	14.25	99	2.2	94	1.3	97	80	3.40
0268	20-Sep-08	14.97	106	3.2	107	2.4	107	93	3.32
0268	25-Jan-10	16.32	94	2.1	100	0.8	97	80	3.33

APPENDIX C: WARP AND CURL ANALYSIS

The information contained in this appendix is an update of *SpecificPavement Studies Construction Report for Experiment SPS-2 Strategic Study of Structural Factors for Rigid Pavement Ehrenberg-Phoenix Highway, Maricopa County, Arizona* (Szrot 1994). The updated information from the 2011 testing did not impact the observations and conclusions from the FHWA report. This study applied algorithms for estimating the level of curl and warp present in the pavement and its effect on surface roughness. The algorithms included slab-by-slab quantification of curl and warp throughout the monitoring history of the site. The analysis framework for this was established in a recent Federal Highway Administration (FHWA) study of seasonal and diurnal changes in jointed concrete pavement roughness (Chang et al. 2010). This method applies Westergaard's theory to establish the likely shape of a curled slab and a curve-fitting algorithm to quantify the level of curling in each slab.

The study related aggregated measurements of curl and warp within each profile measurement to the IRI. The observed statistical relationship between changes in curl and warp and changes in IRI for a given section provided a way to distinguish the long-term roughness caused by distress from short-term and long-term changes in roughness associated with curl and warp.

Statistical analysis segregated the portion of roughness caused by curl and warp within a profile from the rest of the irregularities. The levels of curl and warp present within each profile were estimated using slab-by-slab analysis of local profile segments. The procedure quantifies the level of curl and warp on each slab using a PSG, the gross strain gradient required to deform a slab into the shape that appears within the measured slab profile from a flat baseline.

The PSG value for each slab was derived using a curve fit between the measured profile and an expected curled slab shape using the Westergaard equation, which requires estimates of pavement mechanical properties (summarized by the radius of relative stiffness). As such, the idealized slab shape for each test section was different. Estimates of these properties were developed using the LTPP database.

Identifying the slab boundaries and the methodology for estimating PSG for each slab, given the measured profile and pavement mechanical properties, can be found in *the Curl and Warp Analysis of the LTPP SPS-2 Site in Arizona* (Karamihas and Senn 2012). Figure 143 shows some results for a left-side profile of Section 040213 collected in visit 09 (October 30, 2002). The figure shows the PSG value for each slab along the profile, where slabs 0 and 33 straddle the boundaries of the section. (Slabs -1 and 34 are outside the boundaries.) The figure shows PSG in units of micro strain per inch. The negative values indicate upward curl, which means that the slab edges have higher elevation than the center.

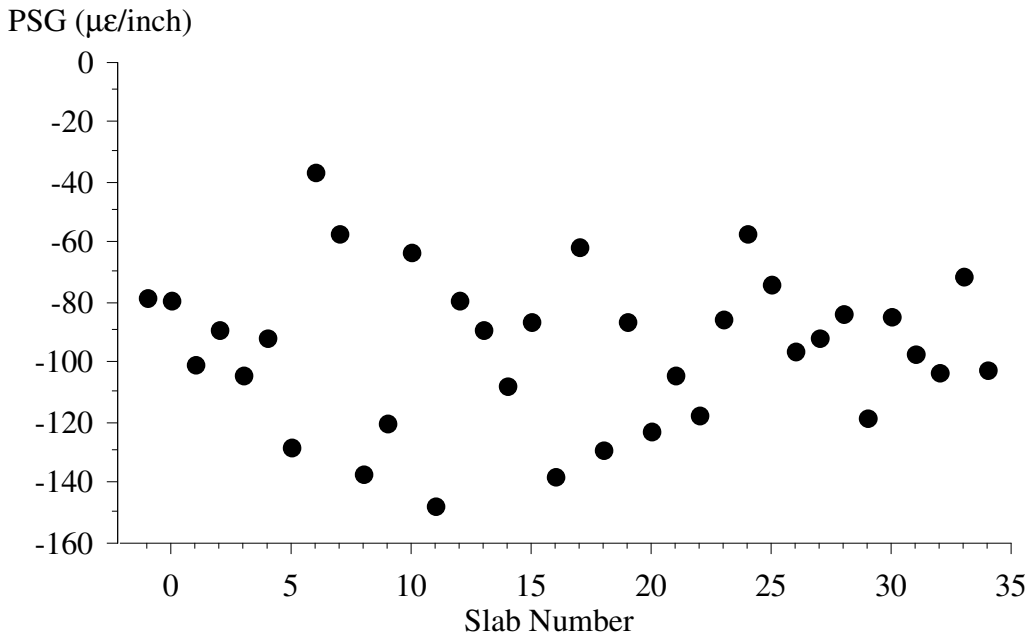

Figure 143. Left Profile PSG Values from Visit 09 of Section 040213

Figure 143 provides an example of the variation in upward curl along the left profile of Section 040213. For the purposes of examining trends over time, the average PSG value summarizes the overall curl and warp observed for the entire section. The average PSG value is -95.5 με /inch for the profile featured in Figure 143. This is a weighted average where the PSG of each slab contributes to the section average in proportion to the length that appears within the section. Thus, the PSG of slabs -1 and 34 do not affect the average, and the PSG of slabs 0 and 33 influence the average less than slabs 1 through 32.

The average PSG values are further averaged over the five repeat measurements. For example, the five left-side profiles of Section 040213 from visit 09 (October 30, 2002) yielded sectionwide average PSG values of -95.5 to -93.0 με /inch, with an average value of -94.5 με /inch. Unless otherwise specified, the PSG values provided from this point are averaged over five repeat profile measurements.

PSG Progression

Figure 144 shows the variation in average PSG for the left side of Section 040213 throughout the experiment. The value of -94.5 με /inch, discussed above for visit 09, appears on the plot 9.08 years into the experiment.

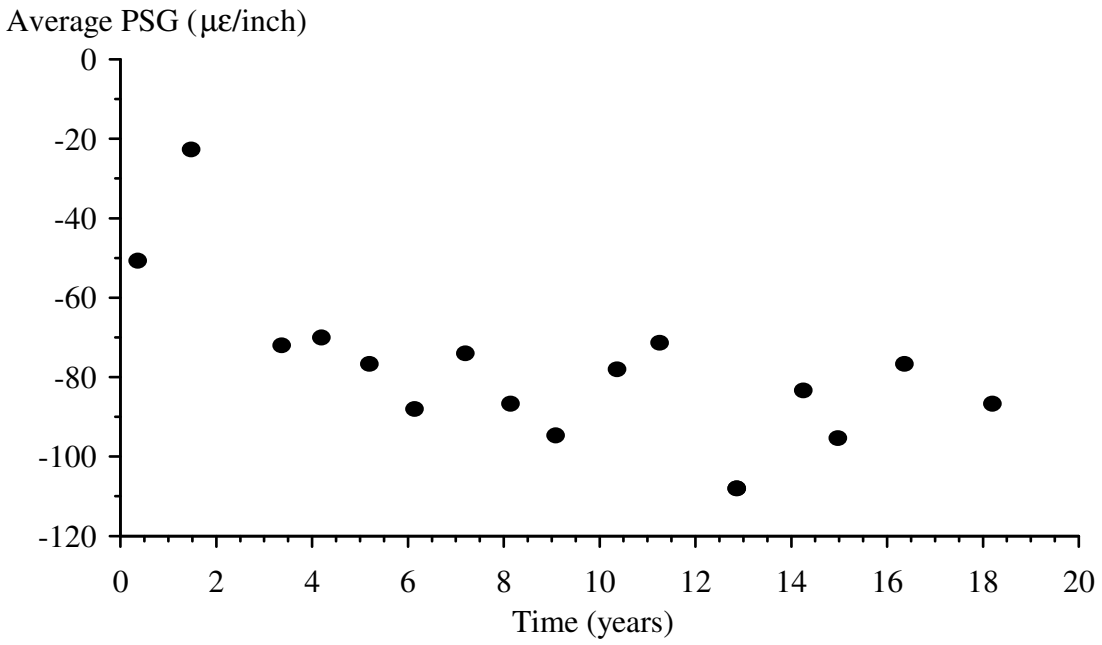

Figure 144. Average PSG vs. Time, Left Side of Section 040213

The data in Figure 144 provide a way to examine the gross changes in curl and warp over time for the left profile of Section 040213. The levels of downward curl for the left profile and the left IRI, shown in

Figure 98, follow a similar trend for Section 040213. For example:

- Curling is more severe in visit 01 (0.32 year) than in visit 02 (1.42 years), and the IRI is higher in visit 01 than in visit 02.
- Curling is more severe in visit 09 (9.08 years) than in the two visits before and the two visits after, and the IRI is higher in visit 09 than in the two visits before and the two visits after.
- Curling is greater in visits 12 (12.86 years) and 14 (14.97 years) than in visits 11 (11.20 years), 13 (14.25 years), and 15 (16.32 years); and the IRI is higher in visits 12 and 14 than in visits 11, 13 and 15.

Indeed, the variations in absolute average IRI over time imitate many of the details of the variations in PSG over time for the left side of Section 040213.

Inspection of PSG values versus time showed a similar relationship between PSG and IRI over most of the test sections in the experiment. In some cases, variation in PSG was proportional to variation in IRI, but only over the early part of the experiment and eras of the pavement life where distress remained constant. The following section examines the relationship between PSG and IRI in detail.

Several trends in the variation of PSG over time existed on multiple sections that help explain the disorderly progression in IRI shown in Figures 98 through 118. First, like Section 040213, the upward curl was much more severe in visit 01 (January 25, 1994) than in visit 02 (March 5, 1995) on many of the test sections, or the PSG reversed from negative (upward curl) in visit 01 to positive (downward curl) in visit 02. Visit 01 was conducted at about 6 a.m. and visit 02 was conducted at 11 a.m.

Second, PSG values were more negative in visits 12 (August 11, 2006) and 14 (September 20, 2008) than in visits 11 (December 12, 2004), 13 (December 30, 2007), and 15 (January 25, 2010) on Sections 040213, 040215-040219, 040220, 040222, and 040262-042068. This indicates a decrease in upward curling in visits 11, 13, and 15 as compared to visits 12 and 14. Visits 12 and 14 occurred shortly after midnight, and visits 11, 13, and 15 occurred after sunrise. Section 040214 also exhibited a decrease in downward curl in visits 12 and 14.

Third, Sections 040215, 040219, 040223, 040224, and 040264-040266 exhibited a net increase in the magnitude of upward curl over the life of the experiment. The trend was not orderly on any of the test sections, and it typically included the short-term variations discussed above for visits 01 and 02 and visits 11 through 15. Figure 145 provides an example for Section 040223. The figure shows the average PSG for the left- and right-side profiles of each visit. Diurnal cycles in temperature and sunlight explain the short-term variations in PSG, but not the increasing upward curl over the life of the experiment.

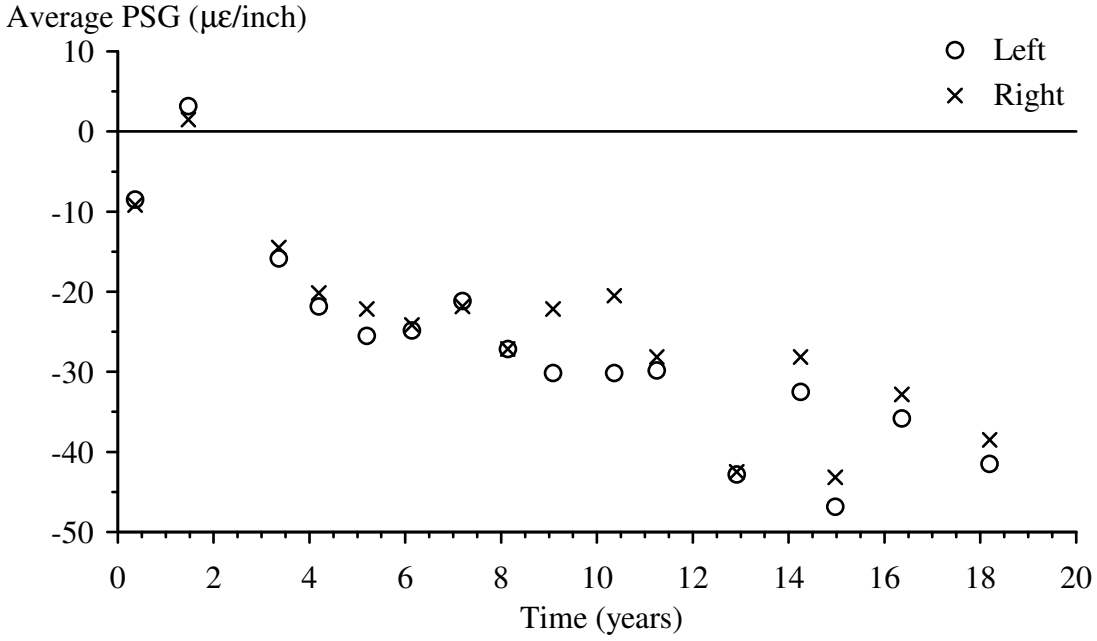

Figure 145. Average PSG vs. Time in Section 040223

In contrast to the rest of the test sections, Section 040214 exhibited a trend from upward curl at the start of the experiment to increasingly downward curl at the end. As shown in Figure 146, the PSG values increase the most aggressively in years 4 through 10 from negative to positive. Figure 147 shows that the slabs curled upward throughout the section in visit 01 (0.32 year). However, the trend toward downward curl is strongest near the start of the section in visit 10 (10.34 years) and becomes increasingly weak toward the end of the section. A decrease in severity of map cracking from the beginning to the end of the section may explain this trend.

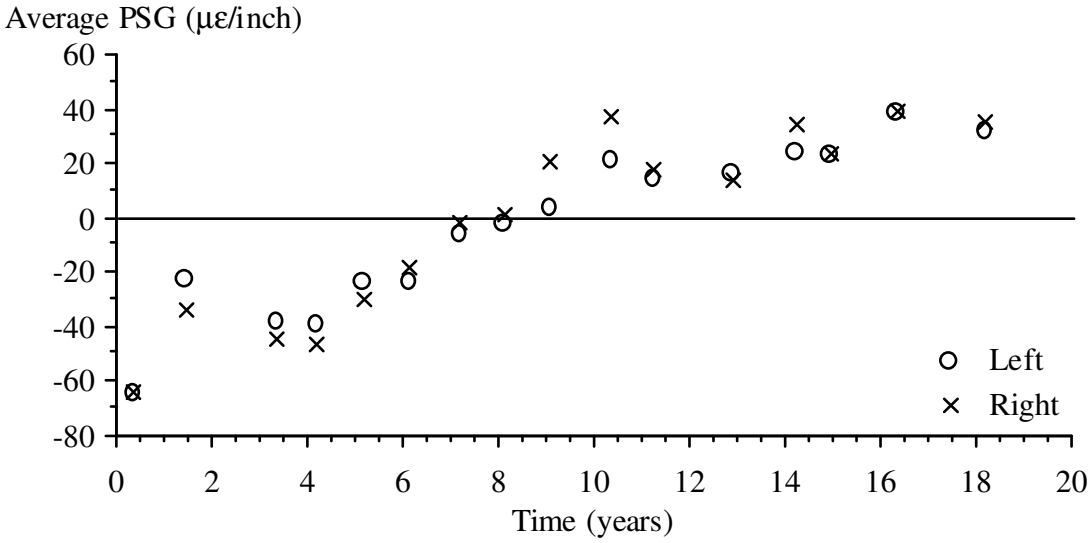

Figure 146. Average PSG vs. Time in Section 040214

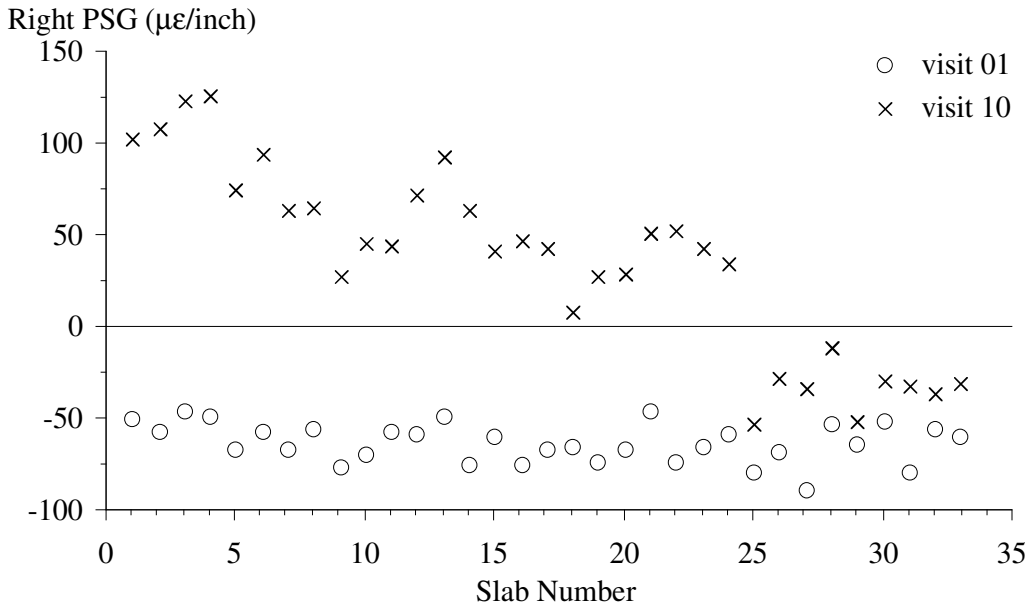

Figure 147. Right PSG Values from Visits 01 and 10 of Section 040214

Relationship Between PSG and IRI

This section addresses the penalty to the IRI caused by curling. On the low-strength sections, a very strong statistical relationship was found between variations in PSG and variations in IRI. Using this relationship, the roughness caused by slab curl was separated from the roughness caused by other sources. This provided a way to look for increases in IRI caused by surface deterioration, without the erratic changes caused by variations in curl and warp over time. This also provided a way to directly estimate the potential improvement in IRI that is possible with a reduction in slab curl.

Originally, the study sought to relate PSG to IRI theoretically. For example, an artificial profile constructed using a pattern of 15-ft-long slabs with profiles equivalent to the Westergaard equation increases in IRI by 1.74 inch/mi per 1 με/inch increases in PSG when the radius of relative stiffness is 39.37 inches. However, statistical observations using measured profiles showed that the variation in IRI with PSG was roughly three-quarters as large because more roughness appeared at transitions between slabs in the theoretical profile, where the slope break between slabs was sharper. In the measured profiles the slope at slab ends was not as large as in the model, most likely due to the influence of dowel bars and slab weight, which were not included in the model that produced the theoretical slab profile.

Instead, the statistical relationship between IRI and PSG was derived using detailed profile measurements collected for the FHWA project Inertial Profile Data for Pavement Performance Analysis (Chang et al. 2010). Measurements from the FHWA project include 124 profiles of Sections 040213 through 040224 collected over a one-year cycle. The measurements include four seasonal visits (August 17, 2003; December 13, 2003; March 9, 2004; July 3, 2004), and four rounds of measurement per visit (before sunrise, after sunrise, mid-afternoon, and after sunset). Seven or more repeat profiles were collected in each of the 16 rounds of measurement. One of the data collection rounds commenced less than 11 hours after LTPP visit 11 (December 12, 2003).

Overall, the FHWA profile measurements occurred throughout a diverse mix of ground temperature, air temperature, weather, and intensity of solar radiation. Thus, large changes were observed in curl and warp without large changes in other surface conditions that affect the IRI, such as distress. Unfortunately, the profiles from the FHWA project did not cover Sections 040260 through 040268.

Figure 148 shows the relationship between IRI and PSG on the left side of Section 040215 using the FHWA data set. The figure shows a distinct IRI-PSG pair for each of 122 passes by the profiler. A least-squares linear fit indicates that the IRI will change 1.3754 inch/mi per με /inch of change in PSG, with a standard estimate of error (SEE) of 2.23 inch/mi. The close relationship observed here depends on using measurements collected over a relatively short portion of the pavement life so that changes do not occur because of other contributors to the IRI, such as surface distress. The high correlation also owes to the large range of observed PSG values. Figure 148 provides noteworthy insight into the contribution of curl and warp to the roughness of Section 040215. The PSG values for the left side covered a range of 30 to 55 με/inch in just one year, and the IRI exhibited a commensurate variation of 38 inch/mi. Further,

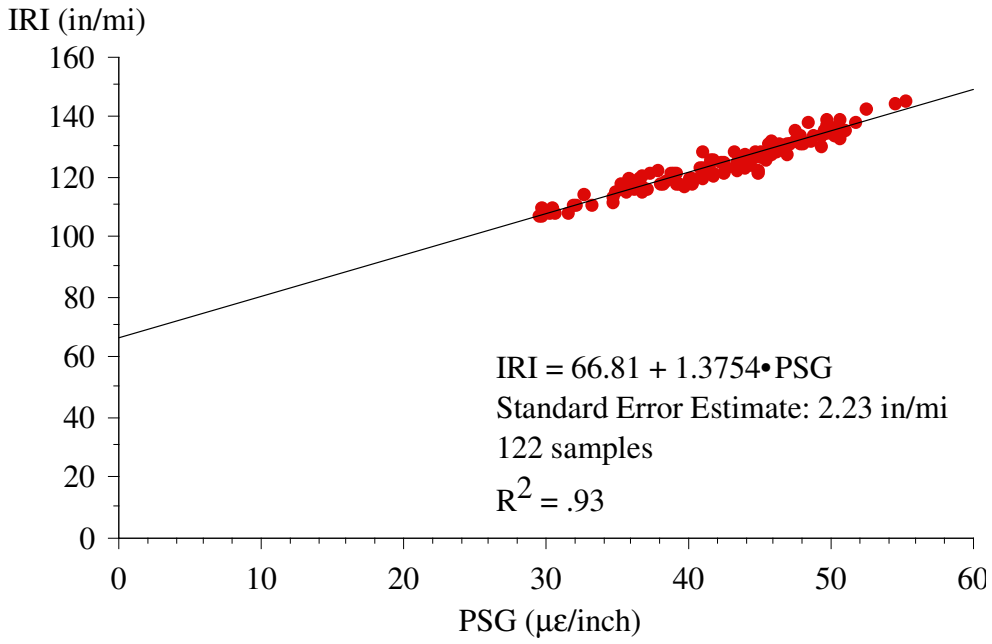

Figure 148. IRI vs. PSG from FHWA Data, Section 040215, Right Side

the plot suggests that if the apparent curl were eliminated, the IRI of the right-side profiles would be about 67 inch/mi, which is less than half of the peak value.

Linear regression of IRI against PSG demonstrated a similar level of correlation for the low-strength test sections in the standard experiment. Table 67 lists the slope, intercept, SEE, and correlation coefficient for the left- and right-side profiles of these sections. The test sections are grouped by surface layer thickness to illustrate the similarity in the IRI-PSG slope among structurally similar pavements. A similar dependence of the slope on radius of relative stiffness appeared in the theoretical calculations. This is, at a higher radius of relative stiffness, the IRI is higher for the same strain gradient in an artificial profile constructed using the Westergaard equation. The consistency between this trend and the influence of radius of relative stiffness on the IRI-PSG slope derived empirically is a sign that the Westergaard equation may have been an appropriate choice of an idealized profile on the low-strength test sections.

For Section 040215, the dependence of IRI on PSG was also characterized using LTPP data. This was possible because the section is in the SMP, and data collected from November 2001 through December 2004 included three regular profiling visits and 24 seasonal visits. Figure 149 shows the linear regression for IRI against PSG for the 135 associated profiler passes. The slope, intercept, and SEE are all exceptionally similar to the observations from the FHWA data. For the left side, the LTPP data produced a slope of 1.442 inch/mi per inch.

Table 67. Regression Results for IRI and PSG on Low-Strength Test Sections

Section	Side	Slope ((inch/mi)/(με/inch))	Intercept (inch/mi)	SEE (inch/mi)	R^2
040213	Left	0.8969	39.97	1.19	0.99
	Right	0.8859	48.95	4.64	0.86
040217	Left	1.0511	50.90	2.51	0.96
	Right	1.1348	42.11	2.15	0.96
040221	Left	0.8307	42.03	3.60	0.90
	Right	0.9346	36.00	2.52	0.96
040215	Left	1.3182	60.40	1.84	0.95
	Right	1.3754	66.81	2.23	0.93
040219	Left	1.4938	52.02	4.02	0.92
	Right	1.5094	69.97	2.17	0.98
040223	Left	1.3995	52.27	2.83	0.94
	Right	1.3686	60.36	2.14	0.96

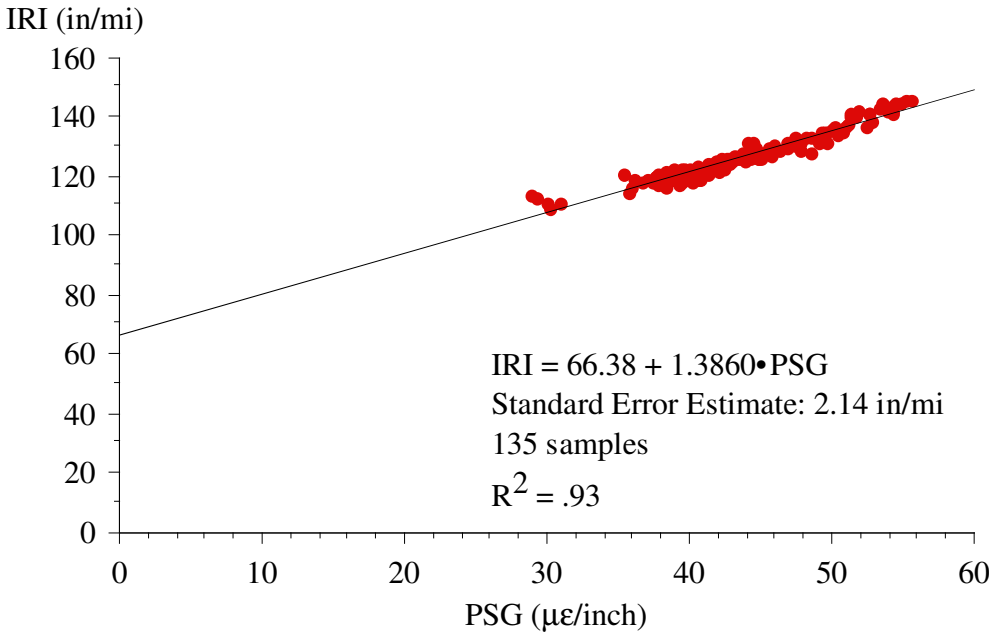

Figure 149. IRI vs. PSG from LTPP SMP Data, Section 040215, Right Side

The agreement between Figures 148 and 149 demonstrates that the IRI-PSG relationship derived from one data set may be applied to data from another, so long as appropriate measurement practices are followed. An analytical procedure with this quality is called transportable in the classic road roughness literature (Sayers et al. 1986). The consistency between data sets also indicates that the SMP produced sufficient data to investigate the IRI-PSG relationship, and other rigid SMP test sections may also produce sufficient data for this analysis.

Unfortunately, the regression for the high-strength sections often produced low correlation. Table 66 lists the statistics produced by the FHWA data set for the high-strength sections. In some cases, the low

overall range in PSG values over the 16 rounds of testing caused low correlation to the IRI. The curl and warp also caused only a small share of the overall roughness on many of the high-strength sections, which often led to poor curve fits in the slab-by-slab analysis. High correlation (and low SEE) existed for the right-side profiles on Sections 040218, 040220, and 040222. However, the variations in IRI over the monitoring period were low relative to the SEE for these sections as compared to the low-strength sections.

Table 68. Regression Results for IRI and PSG on High-Strength Test Sections

Section	Side	Slope ((inch/mi)/(με/inch))	Intercept (inch/mi)	SEE (inch/mi)	R^2
040214	Left	0.3726	74.32	5.85	0.02
	Right	0.8089	44.30	1.87	0.72
040218	Left	0.2879	71.08	3.39	0.19
	Right	1.0129	41.36	2.07	0.90
040222	Left	0.5281	60.37	4.85	0.72
	Right	0.7001	41.51	2.29	0.96
040216	Left	3.3459	49.39	3.80	0.54
	Right	0.8603	82.18	2.12	0.21
040220	Left	0.8482	65.20	5.86	0.18
	Right	1.1765	53.60	2.04	0.88
040224	Left	0.6488	69.75	7.43	0.26
	Right	0.5674	65.18	2.15	0.80

Effect of Curling on the IRI

For the low-strength sections, the relationship between IRI and PSG was sufficiently good to support empirical estimates of the contribution curl and warp make to each IRI value. This is done by obtaining the absolute average PSG value for a given visit of a given section, applying the slope from Table 67 to it, and subtracting the result from the raw IRI value. (Graphically, this is equivalent to placing a point in the appropriate location on an IRI versus PSG plot, such as the one shown in Figure 148, and using the IRI-PSG slope to project the point to the IRI axis.)

The product of the PSG and the slope from Table 67 is the portion of the IRI associated with curl, warp, and other profile features that consistently appear with the same shape as the Westergaard equation. The balance is the roughness linked to other sources, such as built-in defects and surface distress. Figures 150 through 161 provide the results of this method for the low-strength test sections.

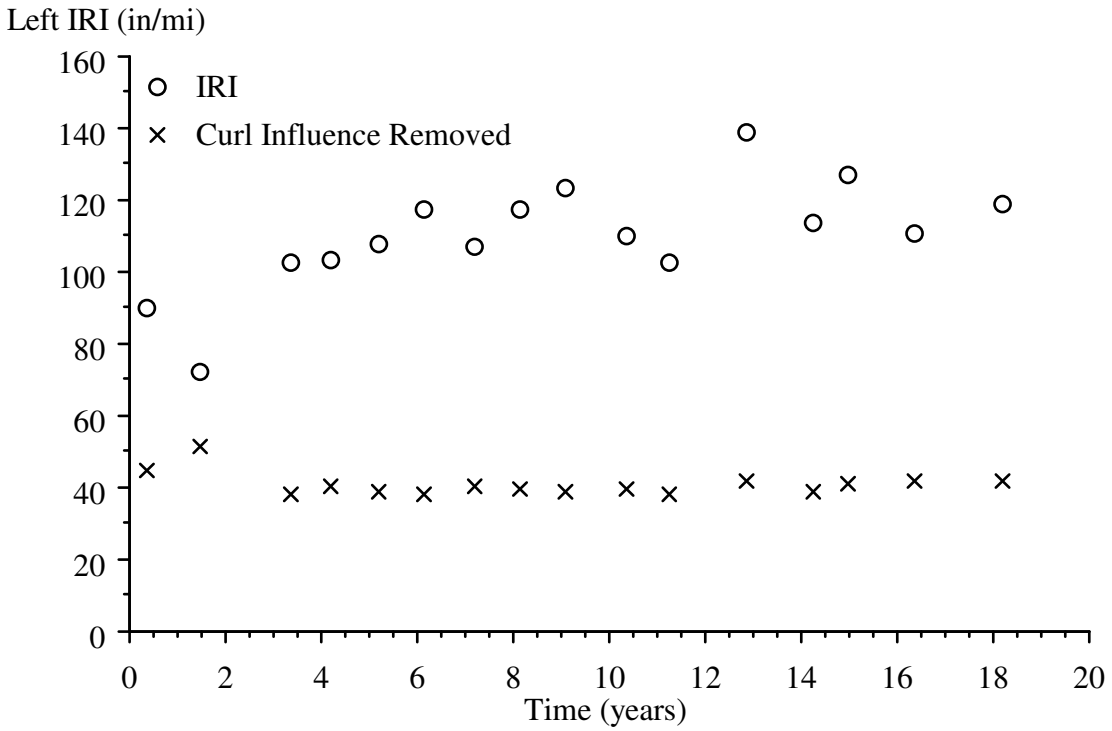

Figure 150. Left IRI Progression in Section 040213

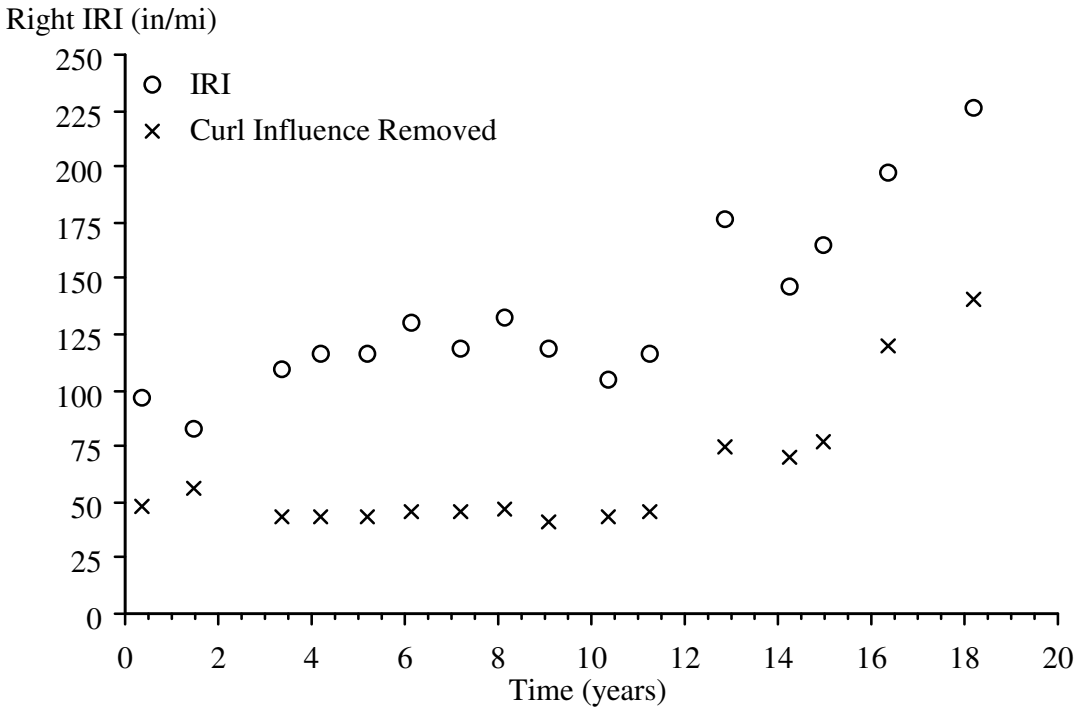

Figure 151. Right IRI Progression in Section 040213

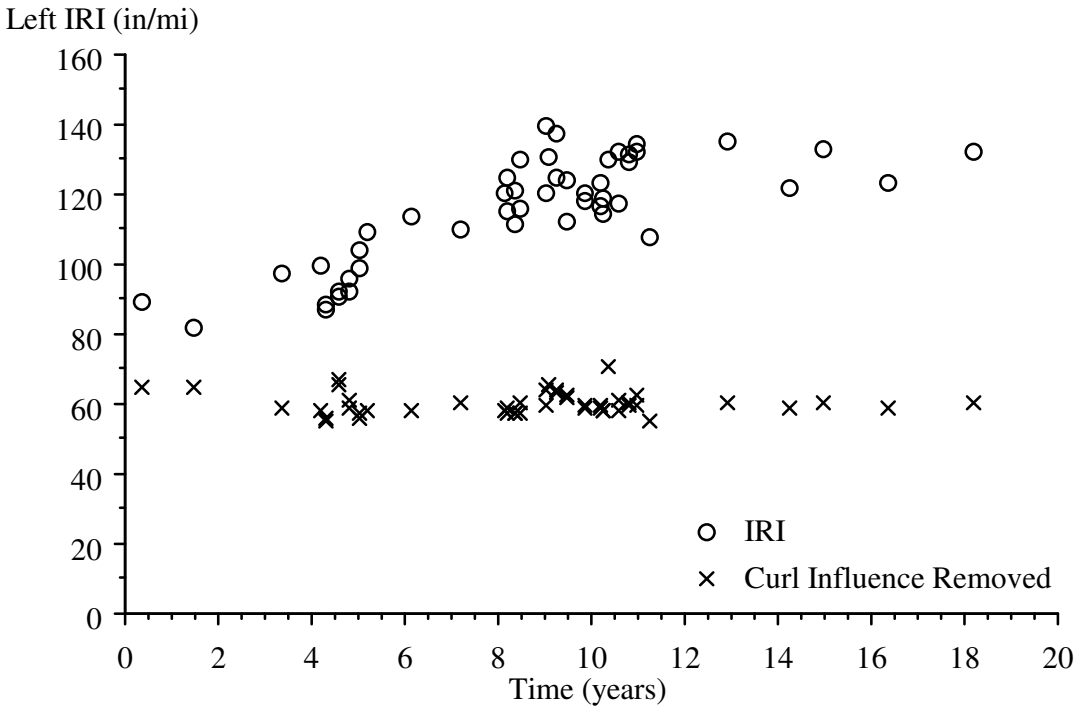

Figure 152. Left IRI Progression in Section 040215

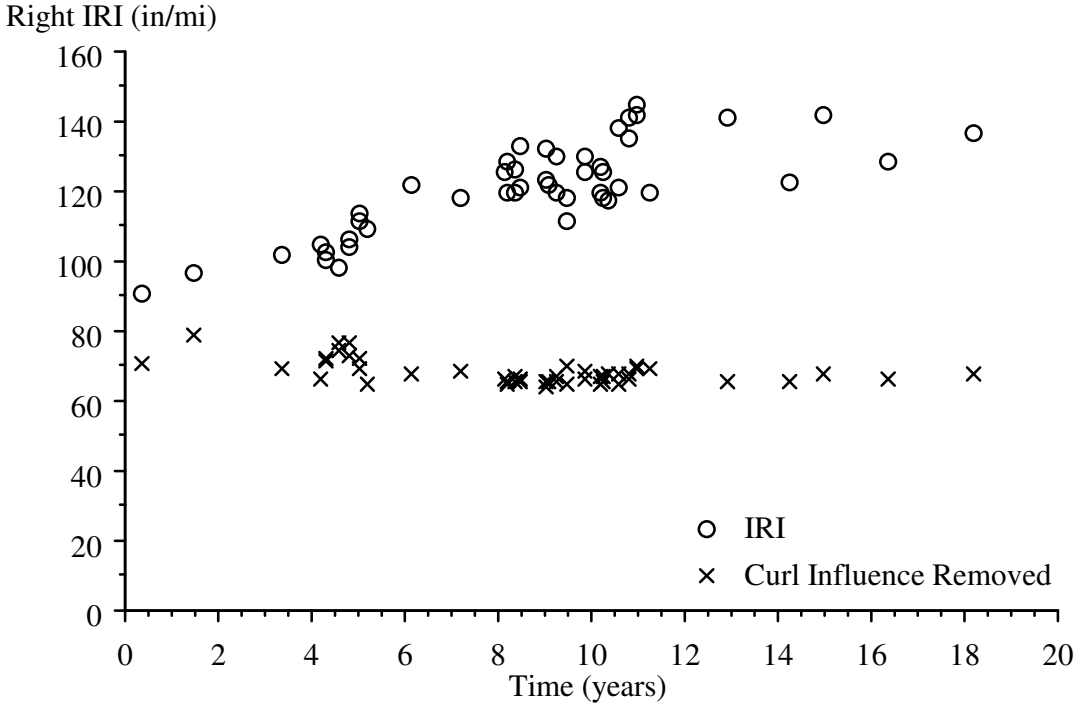

Figure 153. Right IRI Progression in Section 040215

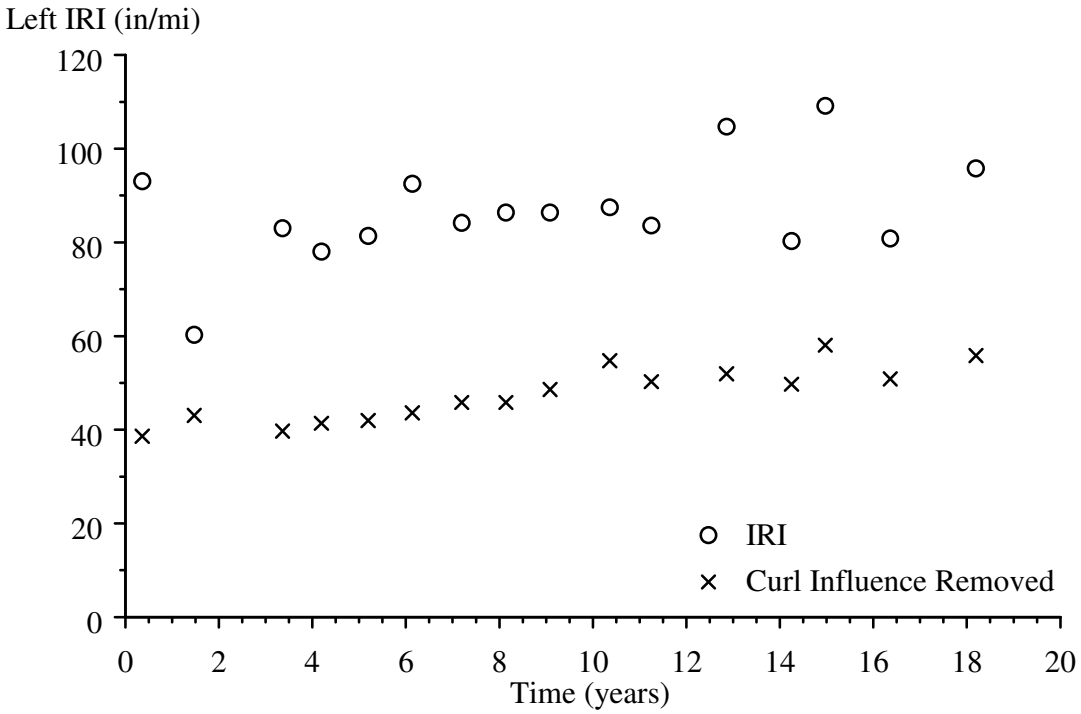

Figure 154. Left IRI Progression in Section 040217

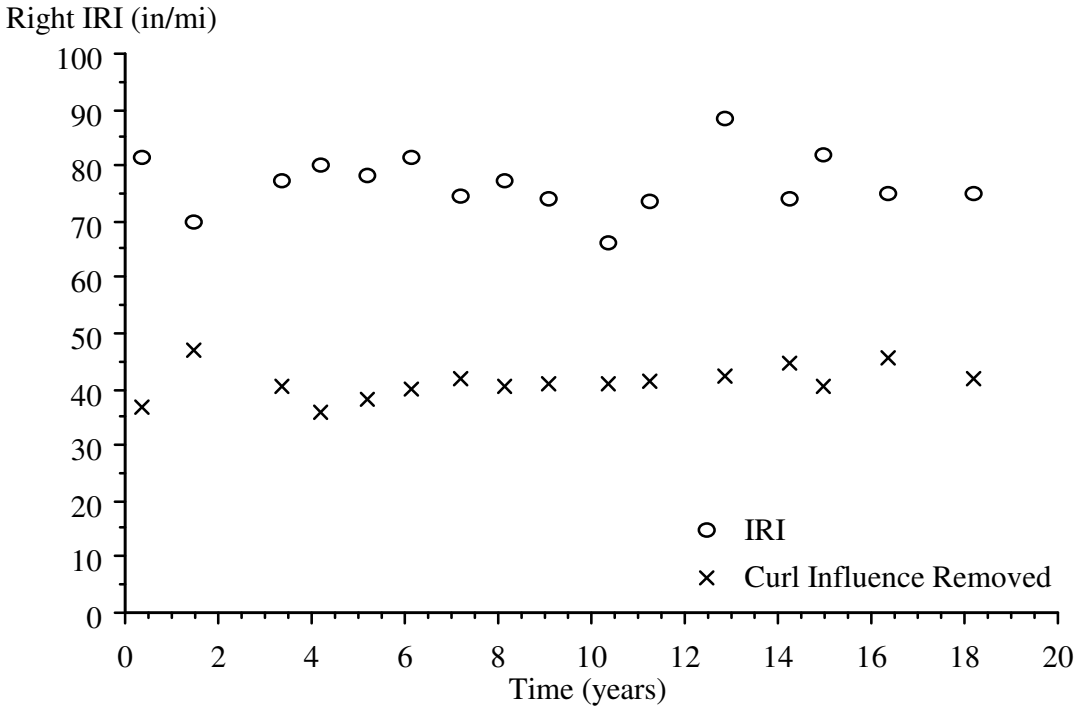

Figure 155. Right IRI Progression in Section 040217

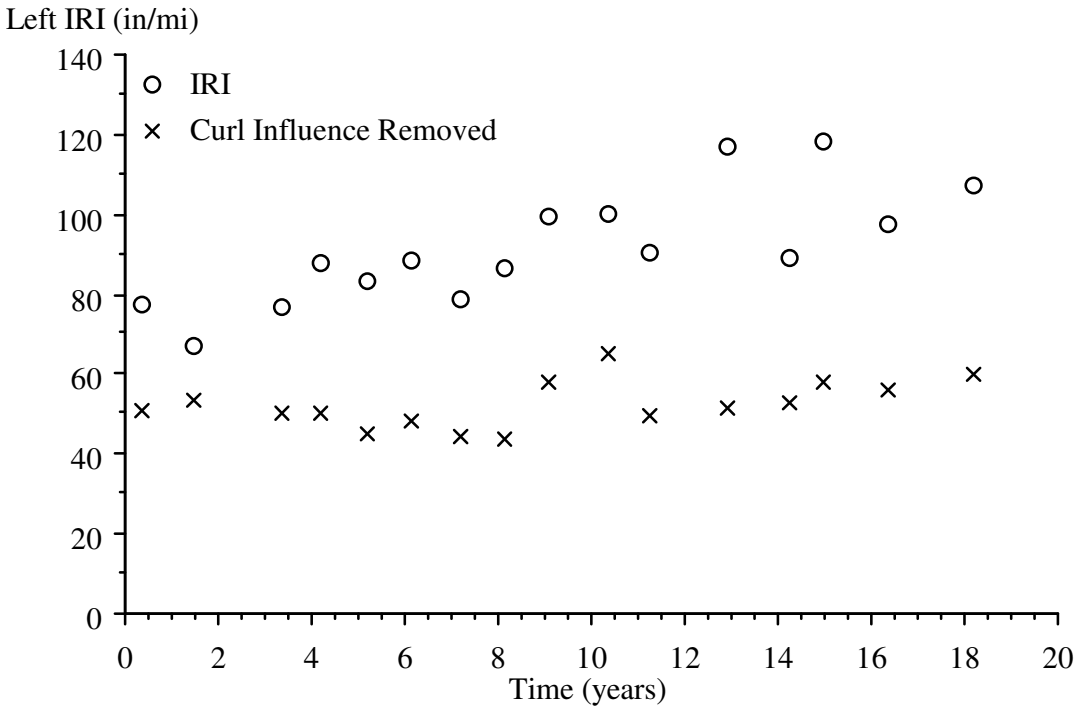

Figure 156. Left IRI Progression in Section 040219

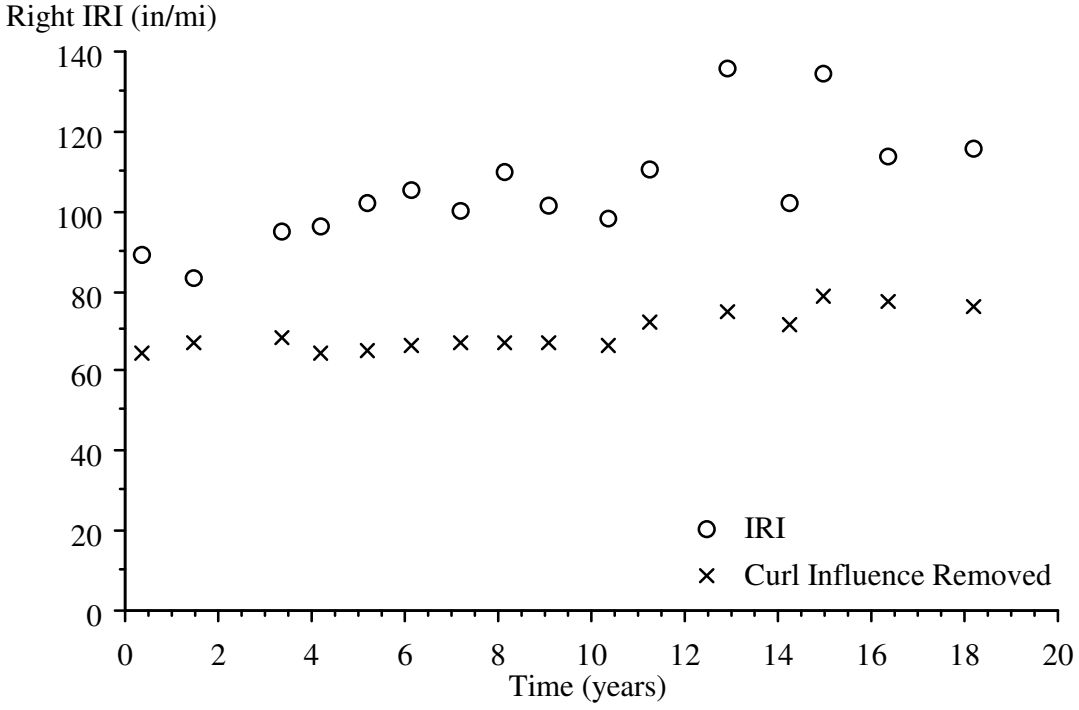

Figure 157. Right IRI Progression in Section 040219

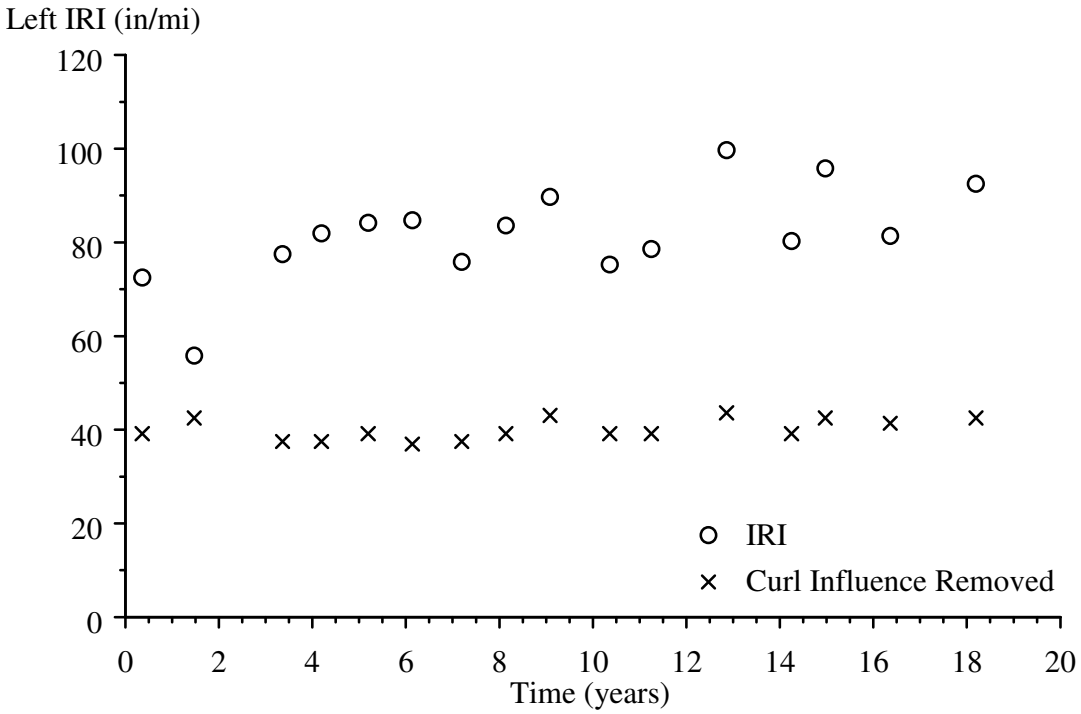

Figure 158. Left IRI Progression in Section 040221

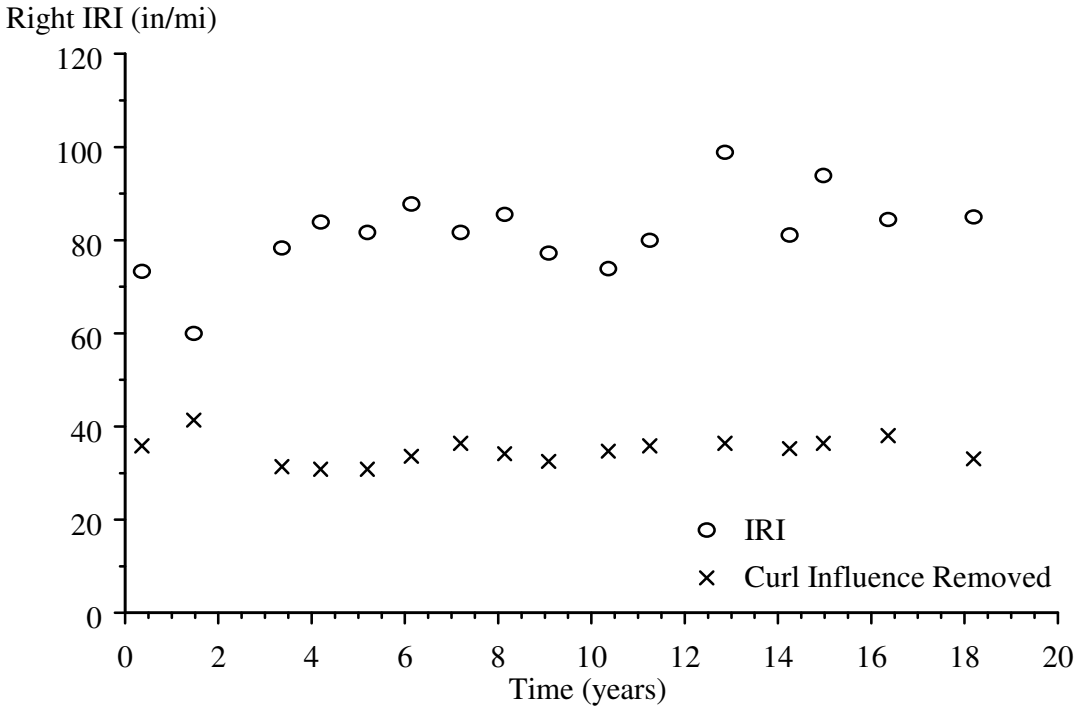

Figure 159. Right IRI Progression in Section 040221

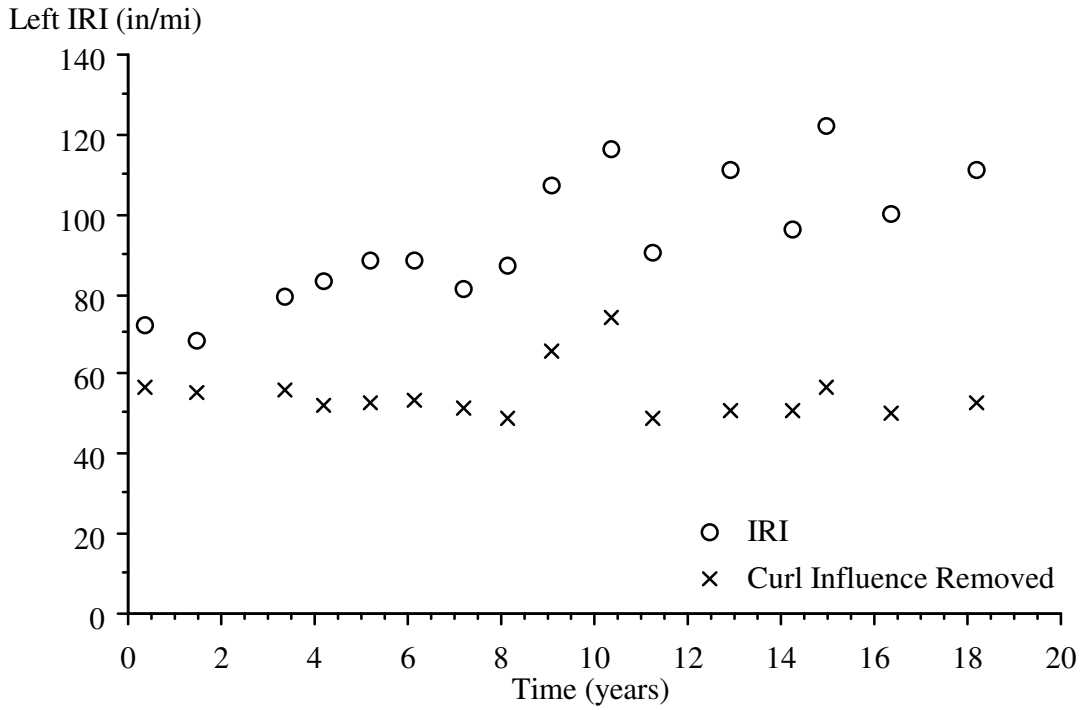

Figure 160. Left IRI Progression in Section 040223

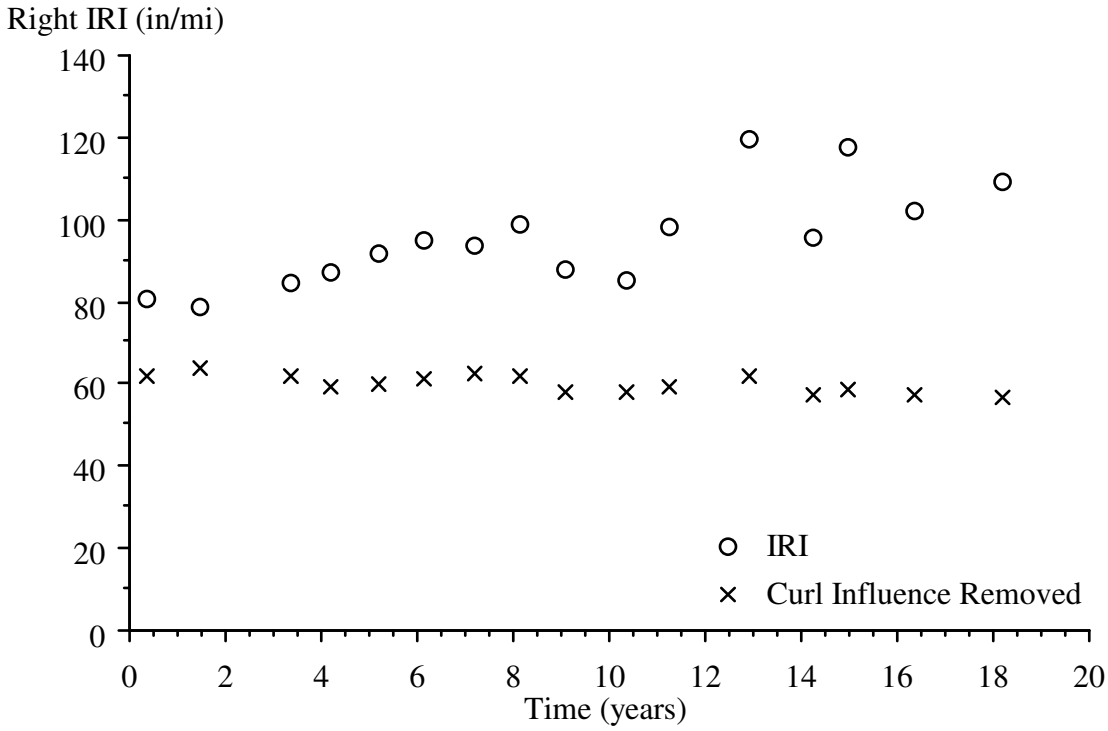

Figure 161. Right IRI Progression in Section 040223

This analysis depends on some key assumptions. First, the idealized slab shape must be an appropriate choice. If so, the individual curve fits for slab profiles will have high quality, as seen in Figure 162, which shows a sample curve fit for a slab on Section 040215. Second, empirical derivation of IRI-PSG slope requires measurements over a large range of PSG values. Third, these analyses used the average absolute PSG value as a basis for comparison to the IRI. As such, the quality of the relationship breaks down for test sections where some slabs curl upward and others curl downward. This was often the case in visit 02 (1.42 years). Lastly, the method may overestimate the influence of curl and warp on the IRI if other roughness is present that appears consistently as a pattern with the same characteristic length as the joint spacing. It is important to monitor the quality of the curve fits and qualitatively look for potential features of this type.

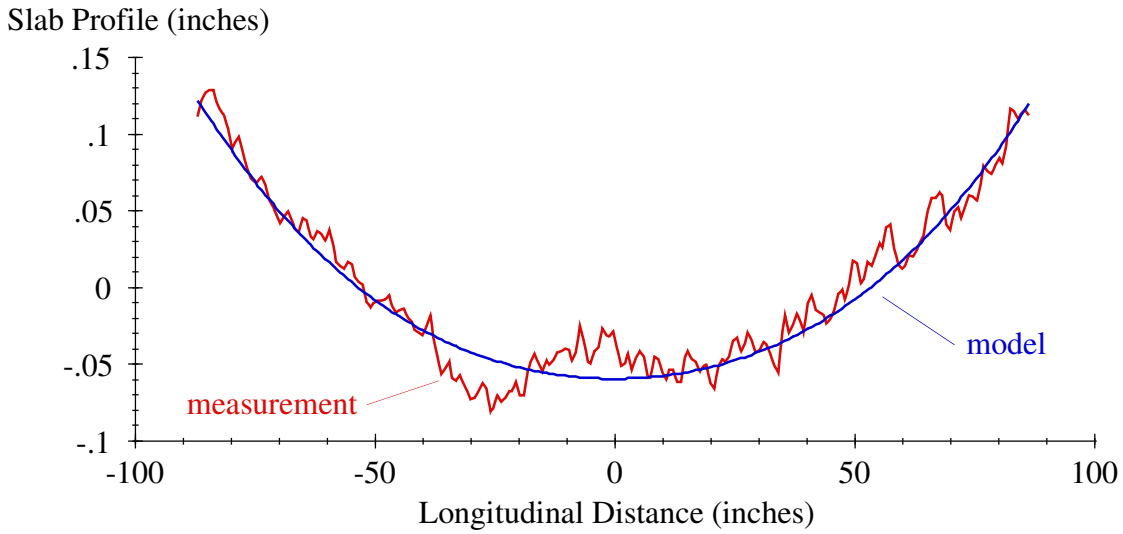

Figure 162. Curve Fit from Section 040215

Figures 150 and 151 provide sample results for Section 040213. The figures show the progression in left and right IRI, respectively, and the portion of the IRI that remained after removing the influence of curl and warp. On Section 040213, the overall IRI values increase over time, but they are erratic. This analysis shows that without curl and warp, the roughness on the left side is steady throughout the experiment, and the roughness on the right side is steady over the first 11 years of the experiment.

Since longitudinal cracking caused the increase in IRI on the right side after 11 years (see the Traditional Profile Analyses section in Chapter 4 of this report), it also contributes to the roughness in the plot after removing the influence of curl and warp. The right side of Section 040213 provides an example of using the IRI-PSG relationship to distinguish the roughness progression caused by curl and warp from the roughness progression caused by surface distress.

Figures 152 and 153 provide sample results for Section 040215, including the seasonal visits. Like Section 040213, the raw IRI values increase erratically on Section 040215, with the additional scatter caused by IRI values that differ between morning and afternoon passes. For example, seasonal visits S11 and S12 (8.31 years) produce an IRI on the left side of 121.8 inches/mi at 10 a.m. and 111.6 inches/mi at 3 p.m., respectively. With the influence of curl and warp removed, these values changed to 58.0 inches/mi and 57.7 inches/mi, respectively.

With the influence of curl and warp removed, the IRI values for Section 040215 progress much less erratically. Further, the overall IRI level holds steady over the experiment. This suggests that the long-term increase in upward curl and warp caused the net increase in raw IRI of 35 inches/mi on the left side and 39 inches/mi on the right side.

Figures 154 through 161 show the results for Sections 040217, 040219, 040221, and 040223. These sections also exhibit erratic changes in IRI caused by curl and warp. With the influence of curl and warp removed, the IRI values are much lower and either increase slowly or hold steady throughout the experiment, with two obvious exceptions. On the left side of Sections 040219 and 040223, the IRI values are much higher in visits 09 (9.08 years) and 10 (10.34 years) than in the previous and following visits, even after removing the influence of curl and warp (see Figures 156 and 160) because other factors caused the increased roughness.

On both sections, spectral analysis for the left-side profiles revealed additional content in the 8- to 11-ft wavelength range in visits 09 (9.08 years) and 10 (10.34 years) that did not appear in other visits. This phenomenon appeared prominently on Sections 040214, 040216, 040218, 040219, 040223, and 040224 and to a lesser extent on Sections 040215, 040217, 040220, and 040222. In many cases, this effect increased the IRI of some repeat measurements, but not all of them. The Traditional Profile Analyses section in Chapter 4 of this report provides an example for Section 040224, where the effect was strongest. On many of these sections, the IRI progression plots (Figures 98 through 118) or the standard deviation of IRI for the left side (Appendix B) showed some evidence of this, but the influence of curl and warp obscured the effect. The source of additional roughness in the 8- to 11-ft wavelength range is unclear, but the affected test sections all appear as a group along the site.